

**DEVELOPMENT OF THIN-FILM  
COMPOSITE MEMBRANES  
INCORPORATED WITH GRAPHENE  
OXIDE AND DERIVATIVES FOR  
FORWARD OSMOSIS PROCESSES**

**by Nawshad Akther**

Thesis submitted in fulfilment of the requirements for  
the degree of

**Doctor of Philosophy**

under the supervision of Prof. Hokyong Shon and Dr.  
Sherub Phuntsho

University of Technology Sydney  
Faculty of Engineering and Information Technology

September 2020

## **CERTIFICATE OF ORIGINAL AUTHORSHIP**

I, **Nawshad Akther**, declare that this thesis is submitted in fulfilment of the requirements for the award of **Doctor of Philosophy**, in the **School of Civil and Environmental Engineering/ Faculty of Engineering and Information Technology** at the University of Technology Sydney.

This thesis is wholly my own work unless otherwise referenced or acknowledged. In addition, I certify that all information sources and literature used are indicated in the thesis.

This document has not been submitted for qualifications at any other academic institution.

This research is supported by the Australian Government Research Training Program.

Production Note:

Signature of Student: Signature removed prior to publication.

(Nawshad Akther)

Date: 4<sup>th</sup> September 2020

# DEDICATION

This thesis is dedicated wholeheartedly to:

My beloved parents, Zinnat and Jahangir,  
who have always supported me, showed me the power of education and been the source  
of my inspiration,

and

My husband, Ashique,  
for having my back, motivating me and sharing the path with me.

## **ACKNOWLEDGEMENTS**

I would like to express my deepest gratitude to those who have supported me along this long but fulfilling journey towards the completion of my PhD thesis.

Foremost, I would like to express my heartfelt gratitude to my principal supervisor, Prof. Hokyong Shon, for his great mentorship, professional advice, encouragement, endless support and bringing out the best in me throughout my PhD study. I would also like to convey my gratitude to my co-supervisor, Dr. Sherub Phuntsho, for his insightful comments and valuable feedback during my study. Their consistent guidance and support throughout my PhD study have been invaluable, motivated me to grow as a researcher and give my best towards the completion of this thesis.

Besides my supervisors, I would like to acknowledge the support I received from the external collaborators who provided me with the opportunity to work with them. I would like to thank Prof. Hideto Matsuyama and Prof. Tomohisa Yoshioka for inviting me to work as a Visiting Researcher at Kobe University and use their laboratories and research facilities at the Research Center for Membrane and Film Technology. I further acknowledge Prof. Noreddine Ghaffour at King Abdullah University of Science and Technology (KAUST), Prof. Yuan Chen at The University of Sydney, A/Prof. Tae-Hyun Bae at Korea Advanced Institute of Science and Technology (KAIST) and Claus Helix-Nielsen at the Technical University of Denmark for their collaboration and support in my research work. I also appreciate Shengyao Wang and Yuki Kawabata at Kobe University, Ziwen Yuan at The University of Sydney, Victoria Sanahuja-Embuena and Radosław Górecki at the Technical University of Denmark for their contribution to my collaboration research projects.

Moreover, I am grateful to Dr. Sungil Lim for developing my membrane fabrication skills and Dr. Md. Johir and Dr. Niren Pathak for their assistance in the laboratory. My heartfelt appreciation goes to my friends in UTS and everyone in the NanoMemPro group, especially Van Huy Tran, Minwei Yao, Syed Muztuza Ali, Pema Dorji and Mukit Hossain for making my time enjoyable and helping me keep up my momentum during the entire course of my PhD journey.

I want to acknowledge the full financial support that I received from the Australian Government Research Training Program (RTP) to complete my PhD study.

Finally, I would like to thank my parents and my father-in-law for making me recognize the importance of education and hard work, making my academic journey a success, motivating me to pursue my dreams and be independent. I want to express my deep appreciation for the continuous support and encouragement that I have received from my brothers, Javed and Abed. I am grateful to my husband, Ashique, for believing in my ability to succeed and fulfil my dreams and for his enduring optimism despite the challenges we confronted during my PhD journey. Without his support, cooperation and motivation, it would have been difficult to accomplish my research goals.

## LIST OF PUBLICATIONS

This list includes journal articles that have been prepared during the PhD candidature, which are either \*part of or \*\*not part of the thesis.

1. \*\*Akther, N., Lim, S., Tran, V.H., Phuntsho, S., Yang, Y., Bae, T.-H., Ghaffour, N. & Shon, H.K. 2019, 'The effect of Schiff base network on the separation performance of thin film nanocomposite forward osmosis membranes', *Separation and Purification Technology*, vol. 217, pp. 284-93.
2. \*Akther, N., Phuntsho, S., Chen, Y., Ghaffour, N. & Shon, H.K. 2019, 'Recent advances in nanomaterial-modified polyamide thin-film composite membranes for forward osmosis processes', *Journal of Membrane Science*, vol. 584, pp. 20-45.  
**(Chapter 2)**
3. \*\*Yao, M., Ren, J., Akther, N., Woo, Y.C., Tijing, L.D., Kim, S.-H. & Shon, H.K. 2019, 'Improving membrane distillation performance: Morphology optimization of hollow fiber membranes with selected non-solvent in dope solution', *Chemosphere*, vol. 230, pp. 117-26.
4. \*\*Tran, V.H., Lim, S., Han, D.S., Pathak, N., Akther, N., Phuntsho, S., Park, H. & Shon, H.K. 2019, 'Efficient fouling control using outer-selective hollow fiber thin-film composite membranes for osmotic membrane bioreactor applications', *Bioresource Technology*, vol. 282, pp. 9-17.
5. \*\*Lim, S., Tran, V.H., Akther, N., Phuntsho, S. & Shon, H.K. 2019, 'Defect-free outer-selective hollow fiber thin-film composite membranes for forward osmosis applications', *Journal of Membrane Science*, vol. 586, pp. 281-91.
6. \*Akther, N., Yuan, Z., Chen, Y., Lim, S., Phuntsho, S., Ghaffour, N., Matsuyama, H. & Shon, H.K. 2020, 'Influence of graphene oxide lateral size on the properties

and performances of forward osmosis membrane’, *Desalination*, vol. 484, p. 114421.

**(Chapter 5)**

7. \*\*Lim, S., Park, K.H., Tran, V.H., Akther, N., Phuntsho, S., Choi, J.Y. & Shon, H.K. 2020, ‘Size-controlled graphene oxide for highly permeable and fouling-resistant outer-selective hollow fiber thin-film composite membranes for forward osmosis’, *Journal of Membrane Science*, vol. 609, p. 118171.
8. \*Akther, N., Ali, S.M., Phuntsho, S. & Shon, H.K. 2020, ‘Surface modification of thin-film composite forward osmosis membranes with polyvinyl alcohol–graphene oxide composite hydrogels for anti-fouling properties’, *Desalination*, vol. 491, p. 114591. **(Chapter 4)**
9. \*\*Lim, S., Akther, N., Tran, V.H., Bae, T.-H., Phuntsho, S., Merenda, A., Dumée, L.F. & Shon, H.K. 2020, ‘Covalent organic framework incorporated outer-selective hollow fiber thin-film nanocomposite membranes for osmotically driven desalination’, *Desalination*, vol. 485, p. 114161.
10. \*\*Shen, Q., Lin, Y., Kawabata, Y., Jia, Y., Zhang, P., Akther, N., Guan, K., Yoshioka, T., Shon, H.K., Matsuyama, H. 2020, ‘Engineering heterostructured thin-film nanocomposite membrane with functionalized graphene oxide quantum dots (GOQD) for highly efficient reverse osmosis’, *ACS Applied Materials & Interfaces*, vol. 12, no. 34, pp. 38662-73.
11. \*\*Daer, S †, Akther, N. †, Wei, Q., Shon, H.K. & Hasan, S.W. 2020, ‘Influence of silica nanoparticles on the desalination performance of forward osmosis polybenzimidazole membranes’, *Desalination*, vol. 491, p. 114441.
12. \*\*Akther, N., Lin, Y., Matsuyama, H., Phuntsho, S., Ghaffour, N. & Shon, H.K. 2020, ‘In situ coating of ultrathin silica layer on polyamide thin-film composite

forward osmosis membranes for enhanced separation and anti-fouling properties’, accepted in *Journal of Membrane Science*.

13. \***Akther, N.**, Sanahuja-Embuela, V., Górecki, R., Phuntsho, S., Helix-Nielsen, C. & Shon, H.K. 2020, ‘Employing the synergistic effect between aquaporin nanostructures and graphene oxide for enhanced separation performance of thin-film nanocomposite forward osmosis membranes’, *Desalination*, vol. 498, p. 114795 (**Chapter 6**)
14. \***Akther, N.**, Kawabata, Y., Lim, S., Yoshioka, T., Matsuyama, H., Phuntsho, S. & Shon, H.K. 2020, ‘Effect of graphene oxide quantum dots on the interfacial polymerization of a thin-film nanocomposite forward osmosis membrane: An experimental and molecular dynamics study’, *Journal of Membrane Science*, vol. 630, p. 119309 (**Chapter 7**)



## CONFERENCE PRESENTATIONS

Some parts of this study have been presented in conferences as listed below:

1. **Akther, N.**, Lim, S., Tran, V.H., Phuntsho, S., Bae, T.-H, Ghaffour, N. & Shon, H.K. ‘Covalent organic frameworks-based thin-film nanocomposite membranes for forward osmosis processes’, The 11th conference on the Aseanian Membrane Society, AMS11, July 3–6, Brisbane, Australia, 2018.
2. Lim, S., Tran, V.H., **Akther, N.**, Phuntsho, S. & Shon, H.K. ‘Preparation of outer-selective thin-film composite hollow fiber membranes with high performance and fouling resistance for forward osmosis applications’, The 11th conference on the Aseanian Membrane Society, AMS11, July 3–6, Brisbane, Australia, 2018.
3. Shon, H.K. & **Akther, N.** ‘Carbon-based nanomaterial incorporated FO membranes’, International Workshop for Membrane at Kobe University in 2019 (iWMK2019), November 18-19, Kobe, Japan, 2019.
4. **Akther, N.**, Phuntsho, S. & Shon, H.K. ‘Influence of graphene oxide lateral size on the properties and performances of forward osmosis membrane’, 4th International Conference on Desalination using Membrane Technology (MEMDES), December 1-4, Perth, Australia, 2019.
5. **Akther, N.**, Sanahuja-Embuela, V., Górecki, R., Phuntsho, S., Helix-Nielsen, C. & Shon, H.K. ‘Employing the synergistic effect between aquaporin nanostructures and graphene oxide for enhanced separation performance of thin-film nanocomposite forward osmosis membranes’, Membrane Society of Australasia (MSA) Annual General Meeting and Conference, November 23-24, Clayton, Victoria, 2020.

## **PREFACE**

This doctoral thesis is prepared in a “Thesis by compilation” format according to the “Graduate Research Candidature Management, Thesis Preparation and Submission Procedures, 2019” of the University of Technology Sydney. It comprises of the articles that have been published or submitted for publication.

This thesis contains one published review paper in Chapter 2 and four original research articles in Chapters 4 through 7, three of which are published and one accepted for publication. The authorship of these works has been decided after discussing with the supervisory team.

**Chapter 2** comprises of the following article:

Akther, N., Phuntsho, S., Chen, Y., Ghaffour, N. & Shon, H.K. 2019, ‘Recent advances in nanomaterial-modified polyamide thin-film composite membranes for forward osmosis processes’, *Journal of Membrane Science*, vol. 584, pp. 20-45.

**Chapter 4** includes the following article:

Akther, N., Ali, S.M., Phuntsho, S. & Shon, H.K. 2020, ‘Surface modification of thin-film composite forward osmosis membranes with polyvinyl alcohol–graphene oxide composite hydrogels for anti-fouling properties’, *Desalination*, vol. 491, p. 114591.

**Chapter 5** is based on the following technical paper:

Akther, N., Yuan, Z., Chen, Y., Lim, S., Phuntsho, S., Ghaffour, N., Matsuyama, H. & Shon, H.K. 2020, ‘Influence of graphene oxide lateral size on the properties and performances of forward osmosis membrane’, *Desalination*, vol. 484, p. 114421.

**Chapter 6** is published in *Desalination*:

Akther, N., Sanahuja-Embuela, V., Górecki, R., Phuntsho, S., Helix-Nielsen, C. & Shon, H.K. 2021, 'Employing the synergistic effect between aquaporin nanostructures and graphene oxide for enhanced separation performance of thin-film nanocomposite forward osmosis membranes', *Desalination*, vol. 498, p. 114795.

**Chapter 7** is published in *Journal of Membrane Science*:

Akther, N., Kawabata, Y., Lim, S., Yoshioka, T., Phuntsho, S., Matsuyama, H. & Shon, H.K. 2021, 'Effect of graphene oxide quantum dots on the interfacial polymerization of a thin-film nanocomposite forward osmosis membrane: An experimental and molecular dynamics study', *Journal of Membrane Science*, vol. 630, p. 119309.

## LIST OF ABBREVIATIONS

AAPTS	1-(2-amino-ethyl)-3-aminopropyl] trimethoxysilane
AFM	Atomic force microscopy
Ag	Silver
AgNP	Silver nanoparticles
AL-DS	Active layer oriented towards draw solution
AL-FS	Active layer oriented towards feed solution
Al <sub>2</sub> O <sub>3</sub>	Aluminium oxide
AQN	Aquaporin Z reconstituting nanostructures
AqpZ	Aquaporin Z
ASP	Alternate soaking process
BP	Bucky paper
BSA	Bovine serum albumin
CaCO <sub>3</sub>	Calcium carbonate
CFV	Cross-flow velocity
CN	Graphitic carbon nitride
CNT	Carbon nanotube
CTA	Cellulose triacetate
DA	Dopamine
DI	De-ionized water
DS	Draw solution
ECP	External concentration polarisation
Fe <sub>3</sub> O <sub>4</sub>	Iron (III) oxide
FO	Forward osmosis
FRR	flux recovery ratio

FS	Feed solution
FTIR	Fourier transform infrared spectroscopy
GA	Glutaraldehyde
GO	Graphene oxide
GQD	Graphene/ graphene oxide/ carbon quantum dot
HA	Humic acid
HF	Hollow fiber
HTI	Hydration technologies Inc.
HNT	Halloysite nanotube
ICP	Internal concentration polarisation
INT	Imogolite nanotube
IEP	Isoelectric point
IP	Interfacial polymerization
ISHF	Inner-selective hollow fiber
LbL	Layer-by-layer
LDH	Layered double hydroxide
MD	Molecular dynamics/ Membrane distillation
MOF	Metal-organic framework
MPD	1,2-phenylenediamine
NaCl	Sodium chloride
NF	Nanofiltration
NIPS	Non-solvent induced phase separation
NMP	1-methyl-2-pyrrolidone
NP	Nanoparticles
OMBR	Osmotic membrane bioreactor
OSHF	Outer-selective hollow fiber
PA	Polyamide

PAN	Polyacrylonitrile
pDA	Polydopamine
PEG	Polyethylene glycol
PEG-PPG-PEG	Poly(ethylene glycol)-block-poly(propylene glycol)-block-poly(ethylene glycol)
PES	Poly(ethersulfone)
PEI	Polyethylenimine
PET	Polyester
PI	Phase inversion
PMA	Poly(ether monoamine)
PRO	Pressure-retarded osmosis
PLL	Poly L-Lysine
PMR	Photocatalytic membrane reactor
PSf	Polysulfone
PV	Pervaporation
PVA	Polyvinyl alcohol
PVDF	Polyvinylidene fluoride
PVP	Polyvinylpyrrolidone
rGO	Reduced graphene oxide
RO	Reverse osmosis
SA	Sodium alginate
SDS	Sodium dodecyl sulfate
SEM	Scanning electron microscope
SiO <sub>2</sub>	Silica
TDS	Total dissolved solids
TEA	Triethylamine
TFC	Thin-film composite

TFC-P	PVA hydrogel-coated TFC membrane
TFC-PGO	PVA-GO hydrogel-coated TFC membrane
TFN	Thin-film nanocomposite
TiO <sub>2</sub>	Titanium oxide
TMC	Trimesoyl chloride
TNT	Titanate nanotubes
TSB	Tryptic soy broth
UF	Ultrafiltration
UiO-66	Zirconium (IV) carboxylate metal organic framework
VAIP	Vacuum-assisted interfacial polymerization
Zn <sub>2</sub> GeO <sub>4</sub>	Zinc germinate
ZnO	Zinc oxide
ZSCSNP	ZnO-SiO <sub>2</sub> core-shell nanoparticles

## NOMENCLATURE

Symbol	Meaning	Unit
$\Delta C$	Concentration difference across the selective layer of the membrane	$\text{mg}\cdot\text{L}^{-1}$
$\Delta C_{FS}$	Change in the feed solution concentration after an interval of $\Delta t$	$\text{mg}\cdot\text{L}^{-1}$
$\Delta P$	Transmembrane pressure	Pa
$\Delta t$	Time interval	h
$\Delta V_{FS}$	Change in the feed solution volume during the performance test	L
$\mu$	Solution viscosity	$\text{Pa}\cdot\text{s}$
$\chi_{CL}$	Theoretical cross-linking degree	%
$A$	Pure water permeability coefficient	$\text{L}\cdot\text{m}^{-2}\cdot\text{h}^{-1}\cdot\text{bar}^{-1}$
$A_m$	Effective area of membrane	$\text{m}^2$
$B$	Solute permeability coefficient	$\text{L}\cdot\text{m}^{-2}\cdot\text{h}^{-1}$
$B/A$	Intrinsic membrane selectivity	bar
$C_{FS}$	Bulk feed solution concentration	$\text{mol}\cdot\text{L}^{-1}$
$C_{DS}$	Bulk draw solution concentration	$\text{mol}\cdot\text{L}^{-1}$
$D$	Diffusion coefficient	$\text{m}^2\cdot\text{s}^{-1}$
$F$	Osmotic pressure across the membrane	Pa
$J_s$	Reverse solute flux	$\text{g}\cdot\text{m}^{-2}\cdot\text{h}^{-1}$ (gMH)
$J_w$	Water flux	$\text{L}\cdot\text{m}^{-2}\cdot\text{h}^{-1}$ (LMH)
$J_{w,0}$	Baseline water flux	$\text{L}\cdot\text{m}^{-2}\cdot\text{h}^{-1}$
$J_w/J_{w,0}$	Normalized flux	---
$M$	Molar concentration	$\text{mol}\cdot\text{L}^{-1}$
$MSD$	Mean square displacement	---



$MW_{CL}$	Molecular weight of the cross-linking agent	$\text{g}\cdot\text{mol}^{-1}$
$MW_{PVA\ unit}$	Molecular weight of one PVA unit	$\text{g}\cdot\text{mol}^{-1}$
$N_{ion}$	Ionization number in water	---
$R$	Overall hydraulic resistance against the water permeation	$\text{m}^{-1}$
$R_a$	Mean value of membrane surface roughness	nm
$R_f$	Foulant resistance	$\text{m}^{-1}$
$R_g$	Universal gas constant	$\text{Pa}\cdot\text{K}^{-1}\cdot\text{mol}^{-1}$
$R_m$	Membrane resistance	$\text{m}^{-1}$
$R_{max}$	Maximum value of membrane surface roughness	nm
$R_q$	Root mean square value of membrane surface roughness	nm
$S$	Structural parameter	$\mu\text{m}$
$SRSF (J_s/J_w)$	Specific reverse solute flux	$\text{g}\cdot\text{L}^{-1}$
$T$	Solution temperature	K
$V_{FS}$	Feed solution volume	L
$W_{CL}$	Weight of cross-linking agent	g
$W_{PVA}$	Weight of PVA	g

# TABLE OF CONTENTS

LIST OF PUBLICATIONS .....	vi
CONFERENCE PRESENTATIONS .....	ix
PREFACE .....	x
LIST OF ABBREVIATIONS .....	xii
NOMENCLATURE.....	xvi
ABSTRACT.....	xxix
1. CHAPTER 1 Introduction.....	2
1.1 Research background.....	2
1.2 Research motivation .....	3
1.3 Research aim.....	5
1.4 Research objectives and scope.....	5
1.5 Thesis organization.....	7
2. CHAPTER 2 Literature review .....	13
Abstract .....	13
2.1 Introduction.....	14
2.2 Nanomaterial-modified PA active layers.....	21
2.2.1 Zeolites and silica .....	25
2.2.2 Carbon nanotubes and graphene oxide.....	26
2.2.3 Other carbon-based nanomaterials .....	31
2.2.4 Titanate and halloysite nanotubes .....	32
2.2.5 Porous coordination polymers.....	35
2.2.6 Issues and challenges of nanomaterial-modified PA layers.....	37
2.3 Nanomaterial-coated PA layer surfaces.....	38
2.3.1 Carbon nanotubes and graphene oxide.....	39
2.3.2 Silver nanoparticles and nanocomposites.....	43
2.3.3 Membrane surface mineralization .....	46
2.3.4 Issues and challenges of nanomaterial-coated PA layer surfaces .....	49
2.4 Nanomaterial-modified substrates .....	50
2.4.1 Zeolites, silica and zinc oxide .....	55
2.4.2 Carbon nanotubes and graphene oxide.....	57
2.4.3 Titanium oxide .....	61

2.4.4	Other nanomaterials .....	62
2.4.5	Issues and challenges of nanomaterial-modified substrates .....	66
2.5	Nanomaterial interlayer .....	67
2.5.1	Carbon nanotubes and graphene oxide .....	68
2.5.2	Porous coordination polymers .....	70
2.5.3	Issues and challenges of nanomaterial interlayer .....	70
2.6	Implications and future perspectives .....	71
2.7	Conclusions .....	75
3.	CHAPTER 3 General experimental methods .....	78
3.1	Introduction .....	78
3.2	PA TFC FO membrane fabrication .....	78
3.2.1	TFC FO flat-sheet membranes preparation .....	78
3.2.1.1	Flat-sheet membrane substrate .....	78
3.2.1.2	PA selective layer .....	79
3.2.2	TFC FO OSHF membranes preparation .....	80
3.2.2.1	HF membrane substrate .....	80
3.2.2.2	OSHF modulation and PA selective layer formation .....	82
3.3	Membrane characterisation .....	83
3.3.1	Membrane cross-section and surface morphology .....	84
3.3.2	Membrane surface roughness .....	84
3.3.3	Membrane surface chemistry .....	85
3.3.4	Membrane hydrophilicity .....	85
3.3.5	Membrane surface charge .....	85
3.4	Membrane performance evaluation .....	86
3.4.1	FO experimental setup .....	86
3.4.2	FO membrane performance .....	87
3.4.3	Membrane intrinsic transport parameters .....	88
4.	CHAPTER 4 Surface modification of thin-film composite forward osmosis membranes with polyvinyl alcohol–graphene oxide composite hydrogels for antifouling properties .....	91
	Abstract .....	91
4.1	Introduction .....	92
4.2	Materials and methods .....	95
4.2.1	Chemicals .....	95

4.2.2	Hydrogel preparation and coating on PA TFC membrane.....	95
4.2.3	Membrane characterisation .....	97
4.2.4	Membrane performance evaluation.....	98
4.2.5	Membrane fouling test.....	99
4.2.6	Foulant resistance evaluation .....	99
4.2.7	Static bacterial adhesion test .....	100
4.3	Results and discussion .....	100
4.3.1	Membrane characterisation .....	100
4.3.2	Membrane performance evaluation.....	107
4.3.3	Membrane fouling study .....	111
4.3.4	Membrane foulant resistance.....	114
4.3.5	Bacterial anti-adhesion performance.....	115
4.4	Conclusions.....	118
4.5	Supporting Information.....	118
4.5.1	Membrane surface roughness .....	118
4.5.2	Foulant resistance evaluation .....	119
	CRedit authorship contribution statement .....	121
	Declaration of competing interest.....	122
	Acknowledgement.....	122
5.	CHAPTER 5 Influence of graphene oxide lateral size on the properties and performances of forward osmosis membrane .....	126
	Abstract .....	126
5.1	Introduction.....	127
5.2	Materials and methods .....	130
5.2.1	Chemicals .....	130
5.2.2	Graphene oxide preparation .....	130
5.2.3	TFC and TFN membrane fabrication .....	131
5.2.3.1	Membrane substrate.....	131
5.2.3.2	PA selective layer .....	131
5.2.4	Graphene oxide and membrane characterisation.....	132
5.2.5	Membrane performance evaluation.....	133
5.2.6	Membrane fouling test.....	134
5.3	Results and discussion .....	135
5.3.1	GO characterisation.....	135

5.3.2	Membrane characterisation .....	137
5.3.3	Membrane performance evaluation .....	144
5.3.4	Membrane fouling study .....	148
5.3.5	Benchmarking membrane performance .....	152
5.4	Conclusions.....	153
	CRedit authorship contribution statement .....	154
	Declaration of competing interest .....	154
	Acknowledgement.....	155
6.	<b>CHAPTER 6 Employing the synergistic effect between aquaporin nanostructures and graphene oxide for enhanced separation performance of thin-film nanocomposite forward osmosis membranes.....</b>	<b>159</b>
	Abstract .....	159
6.1	Introduction.....	160
6.2	Materials and methods .....	163
6.2.1	Chemicals .....	163
6.2.2	TFC and TFN membrane fabrication .....	164
6.2.3	Membrane characterisation .....	165
6.2.4	Membrane performance evaluation.....	166
6.3	Results and discussion .....	166
6.3.1	Membrane characterisation .....	166
6.3.2	Membrane performance evaluation.....	174
6.4	Conclusions.....	177
6.5	Supporting Information.....	178
6.5.1	Membrane surface roughness .....	178
	CRedit authorship contribution statement .....	179
	Declaration of competing interest .....	179
	Acknowledgement.....	179
7.	<b>CHAPTER 7 Effect of graphene oxide quantum dots on the interfacial polymerization of a thin-film nanocomposite forward osmosis membrane: An experimental and molecular dynamics study .....</b>	<b>183</b>
	Abstract .....	183
	Introduction .....	184
7.1	Materials and methods .....	188
7.1.1	Chemicals .....	188

7.1.2	HF membrane substrate development .....	189
7.1.3	OSHF TFC and TFN membrane development.....	189
7.1.4	Membrane characterisation .....	190
7.1.5	Membrane performance evaluation .....	191
7.1.6	Molecular dynamics simulation .....	191
7.1.6.1	Simulation cell of water-hexane interface .....	192
7.1.6.2	Simulation cell of water-PA interface .....	193
7.2	Results and discussion .....	195
7.2.1	Membrane characterisation .....	195
7.2.2	Membrane performance evaluation.....	199
7.2.3	Molecular dynamics simulation .....	203
7.2.3.1	Water-hexane interface simulation .....	203
7.2.3.2	Water-PA interface simulation .....	205
7.3	Conclusions.....	207
7.4	Supporting Information.....	208
7.4.1	Molecular dynamics simulation .....	208
	CRedit authorship contribution statement .....	209
	Declaration of competing interest .....	210
	Acknowledgement.....	210
8.	CHAPTER 8 Conclusions and recommendations.....	212
8.1	Conclusions.....	212
8.2	Recommendations.....	216
	References .....	218

## LIST OF FIGURES

<b>Fig. 1.1</b> Thesis structure on the development of GO-modified PA TFC membranes for FO processes. ....	6
<b>Fig. 2.1</b> Number of publications related to nanomaterial-modified PA TFC FO membranes (Retrieved from Web of Science on 14 <sup>th</sup> March 2019). ....	18
<b>Fig. 2.2</b> Schematic illustrations demonstrating typical structures of nanomaterial-incorporated PA TFC membranes: a) TFN membrane, b) TFC membrane with nanomaterial-coated PA layer surface, c) TFC membrane with nanocomposite substrate and d) TFC membrane with nanomaterial interlayer. ....	20
<b>Fig. 2.3</b> Typical steps involved in the fabrication of a TFN membrane through the IP process. Nanomaterials are uniformly-dispersed either in the MPD aqueous or TMC organic solution for the formation of nanocomposite PA layer. ....	22
<b>Fig. 2.4</b> Schematic illustration of the interaction between amine-functionalized titanate nanotube and polyamide (adapted from (Emadzadeh et al. 2015)). ....	34
<b>Fig. 2.5</b> Illustration of the steps involved in the modification of PA TFC membrane surface with silver-PEGylated dendrimer nanocomposite structure (Zhang, Qiu, et al. 2013). ....	44
<b>Fig. 2.6</b> Key steps involved in a single cycle of the alternate soaking process (ASP) for the deposition and coating of barium sulfate on the PA TFC membrane surface (Jin et al. 2015). ....	47
<b>Fig. 2.7</b> Typical steps involved in the preparation of a PA TFC membrane with the nanomaterial-incorporated substrate. ....	51
<b>Fig. 2.8</b> Schematic of the co-casting technique used for fabrication of dual-layered GO-incorporated TFC FO membranes (Lim et al. 2017). ....	61
<b>Fig. 2.9</b> View of the atomic structure of INTs. (a) Axial and (b) 3-D side view (adapted from (Pan et al. 2017)). ....	65
<b>Fig. 2.10</b> Typical steps involved in the preparation of a PA TFC membrane incorporated with a nanomaterial interlayer. ....	68
<b>Fig. 2.11</b> Schematic diagram representing the PA development process on porous substrates with and without a nanomaterial interlayer. ....	69
<b>Fig. 2.12</b> Current problems and consequences of nanoparticle (NP) incorporation in the membranes, and some possible solutions to overcome those issues. ....	72
<b>Fig. 3.1</b> Phase inversion technique by immersion precipitation. ....	79

<b>Fig. 3.2</b> HF spinneret assembly used to prepare HF substrates via dry-jet wet PI technique. .....	81
<b>Fig. 3.3</b> Representation of HF membrane substrate development using a conventional dry-jet wet spinneret assembly (Lim et al. 2019).....	81
<b>Fig. 3.4</b> Schematic representation of the modified VAIP technique for the development of OSHF TFC FO membrane (Lim et al. 2019).....	83
<b>Fig. 3.5</b> Schematic of the lab-scale FO experimental setup used for testing membrane performance.....	87
<b>Fig. 4.1</b> ATR-FTIR spectra of the pristine and modified TFC membranes.....	102
<b>Fig. 4.2</b> SEM images revealing the surface morphology of the (a) pristine TFC membrane; and PVA hydrogel coated TFC membranes with different GO loadings: (b) 0, (c) 0.01, (d) 0.02, and (e) 0.04 wt%.....	103
<b>Fig. 4.3</b> AFM images revealing the surface roughness of the (a) pristine TFC membrane; and PVA hydrogel coated TFC membranes with different GO loadings: (b) 0, (c) 0.01, (d) 0.02, and (e) 0.04 wt%. Error bars for membrane surface roughness represent one standard error obtained from at least four membrane samples for each condition. ....	105
<b>Fig. 4.4</b> Water contact angle measurements, and (b) zeta potentials as a function of pH for the pristine and modified TFC membrane surfaces. Error bars for water contact angle measurements represent one standard error obtained from at least seven measurements for each membrane sample.....	107
<b>Fig. 4.5</b> FO performance of the pristine and modified TFC membranes. Operating conditions: FS, DI water; DS, 1 M NaCl; cross-flow velocity, $12.6 \text{ cm}\cdot\text{s}^{-1}$ ; membrane orientation, AL-FS. Error bars represent one standard error obtained from at least three membrane samples for each condition. ....	110
<b>Fig. 4.6</b> Normalised flux of the pristine and modified TFC membranes during the FO (a) baseline test, (b) fouling test and (c) after hydraulic cleaning. Operating conditions: Initial baseline water flux ( $J_{w,0}$ ), $\sim 22 \text{ L}\cdot\text{m}^{-2}\cdot\text{h}^{-1}$ ; DS, 0.5 M to 1 M NaCl; flow rate (baseline and fouling test), $0.5 \text{ L}\cdot\text{min}^{-1}$ ; flow rate (physical cleaning), $0.7 \text{ L}\cdot\text{min}^{-1}$ ; membrane orientation, AL-FS; foulants, 1 mM calcium chloride and 200 ppm SA. ....	113
<b>Fig. 4.7</b> Foulant resistance of pristine and modified TFC membranes during the FO fouling test.....	115
<b>Fig. 4.8</b> Static bacterial adhesion on (a) pristine and modified TFC membranes with different GO loadings: (b) 0, (c) 0.01, (d) 0.02, and (e) 0.04 wt%. ....	116



<b>Fig. 4.9</b> Relative bacterial coverage on the pristine and modified TFC membrane surfaces. The bacterial adhesion on each membrane surface was normalised with respect to the pristine TFC membrane. Error bars represent one standard error obtained from at least three membrane samples for each condition. ....	117
<b>Fig. 5.1</b> AFM images of GO flakes deposited on mica sheets (top) and height profiles of GO flakes (bottom) along the red lines represented on AFM images at different sonication times (A) 0 h, (B) 0.5 h, (C) 4 h, and (D) 8 h. ....	135
<b>Fig. 5.2</b> Average GO flake area at various durations of sonication. The size distributions were obtained from AFM images by measuring the area of nearly 200 GO flakes for each sample using the ImageJ software. Inset plot: Histograms depicting the GO flake size distributions at various durations of tip sonication. ....	136
<b>Fig. 5.3</b> FTIR spectra of TFC and GO-modified TFN membranes. ....	138
<b>Fig. 5.4</b> SEM images of PA surface: (A) TFC, (B) MGO-0, (C) MGO-0.5 (D) MGO-4, and (E) MGO-8 membranes. The GO loading was fixed at 0.01 wt% for all the TFN membranes. The red borders present the smooth patches that form when GO flakes impede the IP reaction. ....	139
<b>Fig. 5.5</b> SEM images of membrane cross-section, (A) TFC, (B) MGO-0, (C) MGO-0.5 (D) MGO-4, and (E) MGO-8 membranes. (F) PA layer height of the TFC and GO-modified TFN membranes. The GO loading was fixed at 0.01 wt% for all the TFN membranes. ....	140
<b>Fig. 5.6</b> AFM images representing PA surface topography of (A) TFC, (B) MGO-0, (C) MGO-0.5 (D) MGO-4, and (E) MGO-8 membranes. (F) Surface roughness parameters of the developed membranes obtained by examining three arbitrarily chosen membrane areas (5 $\mu\text{m} \times 5 \mu\text{m}$ ). ....	142
<b>Fig. 5.7</b> (A) Initial water contact angles and (B) surface charge measurements as a function of pH for fabricated TFC and GO-modified TFN membranes. ....	143
<b>Fig. 5.8</b> FO performance of the developed TFC and GO-modified TFN membranes in AL-FS/AL-DS arrangements: (A) water flux and (B) <i>SRSF</i> . ....	147
<b>Fig. 5.9</b> Normalized flux of the TFC, MGO-0 and MGO-8 membranes throughout the FO fouling test. The normalized flux was attained by dividing the water flux obtained after every 5 minute interval by the initial water flux ( $\sim 25 \text{ L}\cdot\text{m}^{-2}\cdot\text{h}^{-1}\cdot\text{bar}^{-1}$ ). NaCl (0.75 M to 2 M) and synthetic wastewater (200 $\text{mg}\cdot\text{L}^{-1}$ of sodium alginate and colloidal silica) were used as DS and FS, respectively. ....	151

<b>Fig. 5.10</b> Normalized flux of the TFC, MGO-0 and MGO-8 membranes before and after hydraulic cleaning (Hydraulic cleaning conditions: FS and DS, DI water; membrane orientation, AL-FS; cross-flow velocity, $12.6 \text{ cm}\cdot\text{s}^{-1}$ ; physical rinsing duration, 1 h; temperature, $22 \text{ }^\circ\text{C}$ ).....	152
<b>Fig. 6.1</b> FTIR spectra of the pristine and modified TFC membranes.....	168
<b>Fig. 6.2:</b> AFM images representing the PA surface roughness of the prepared TFC and TFN membranes. Error bars represent one standard error obtained from roughness measurements of at least three membrane samples for each condition. ....	169
<b>Fig. 6.3</b> SEM images demonstrating both the surface morphology of the PA layer (top) and cross-section of the prepared membranes (bottom): (a) pristine TFC, (b) TFN0, (c) TFN25, (d) TFN50 and (e) TFN75. ....	170
<b>Fig. 6.4:</b> PA layer height of the prepared pristine TFC and modified TFN membranes. Error bars represent one standard error obtained from at least three measurements for each membrane sample.....	172
<b>Fig. 6.5:</b> (a) Water contact angle and (b) zeta potential measurements of the pristine TFC and modified TFN membrane surfaces. Error bars for water contact angle measurements represent one standard error obtained from at least seven measurements for each membrane sample.....	174
<b>Fig. 6.6:</b> FO performance of the pristine TFC and modified TFN membranes. Operating conditions: membrane orientation, AL-FS; DS, 0.5 M NaCl; FS, DI water; cross-flow velocity, $12.6 \text{ cm}\cdot\text{s}^{-1}$ . Error bars represent one standard error obtained from the performance test results of at least three membrane samples for each condition. ....	176
<b>Fig. 7.1</b> Schematic and simulation model of the water-hexane interface system. a) WH-GQD0, b) WH-GQD1 and c) WH-GQD3; blue: nitrogen atom, grey: carbon atom, white: hydrogen atom, red: oxygen atom and yellow: GQD. ....	193
<b>Fig. 7.2</b> Schematic and simulation model of the water-PA interface system. a) WP-GQD0, b) WP-GQD1, c) WP-GQD3 and d) WP-GQD1S; blue: nitrogen atom, grey: carbon atom, white: hydrogen atom, red: oxygen atom and yellow: GQD. ....	194
<b>Fig. 7.3</b> SEM images of PA layer surface: (a) TFC, (b) TFN2, (c) TFN5 (d) TFN10, (e) TFN25 and (f) TFN50 OSHF membranes. ....	196
<b>Fig. 7.4</b> AFM images signifying PA surface roughness of (a) TFC, (b) TFN10 and (c) TFN50 OSHF membranes. The $R_q$ values of membrane surface roughness were acquired by inspecting four arbitrarily selected membrane areas.....	197
<b>Fig. 7.5</b> FTIR spectra of the TFC and TFN membranes.....	198

<b>Fig. 7.6</b> Water contact angles of the OSHF PA TFC and TFN FO membranes.....	199
<b>Fig. 7.7</b> FO performance of OSHF TFN membranes incorporated with GQD under AL-FS orientation with DI water as FS and 1 M NaCl as DS.....	201
<b>Fig. 7.8</b> Snapshots of water-hexane interface system at 0 ns: (a, d), WH-GQD0, (b, e), WH-GQD1, (c, f), WH-GQD3; and at 4 ns: (g, j), WH-GQD0, (h, k), WH-GQD1, (i, l), WH-GQD3. Blue: nitrogen atom, grey: carbon atom, white: hydrogen atom, red: oxygen atom and yellow: GQD. In (a) to (c) and (g) to (i), water and hexane molecules are omitted to demonstrate GQD behaviour. ....	204
<b>Fig. 7.9</b> Diffusivity of water, hexane, MPD and TMC molecules.....	205
<b>Fig. 7.10</b> (a) Effect of GQD on water molecular density distribution at the water-PA interface and (b) diffusivity of water molecules at the water-PA interface. ....	207

## LIST OF TABLES

<b>Table 2.1</b> Summary of the fabrication conditions and FO performance of porous nanomaterial-incorporated PA TFN membranes. ....	23
<b>Table 2.2</b> Summary of the fabrication conditions and FO performance of non-porous nanomaterial-incorporated PA TFN membranes. ....	24
<b>Table 2.3</b> Summary of the fabrication conditions and FO performance of PA TFC membranes with nanomaterial-modified surfaces. ....	40
<b>Table 2.4</b> Summary of the fabrication conditions and FO performance of PA TFC membranes with porous nanomaterial-incorporated substrates. ....	52
<b>Table 2.5</b> Summary of the fabrication conditions and FO performance of PA TFC membranes with non-porous nanomaterial-incorporated substrates.....	53
<b>Table 3.1</b> Spinning conditions of HF membrane substrates.....	82
<b>Table 3.2</b> A summary of the membrane characterisations and instruments employed in this study. ....	84
<b>Table 4.1</b> Surface modification conditions of PA TFC FO membranes. ....	97
<b>Table 4.2</b> Intrinsic transport parameters of the membranes. ....	110
<b>Table 5.1</b> Separation parameters of the fabricated membranes determined using the algorithm established by Tiraferri et al. (2013). ....	148
<b>Table 5.2</b> FO performance summary of the various GO-modified PA TFN flat-sheet in AL-FS orientation. ....	153
<b>Table 6.1</b> AQN and GO compositions of the pristine TFC and modified TFN membranes. ....	165
<b>Table 6.2</b> Intrinsic transport parameters of the membranes. ....	177
<b>Table 7.1</b> Chemical compositions of OSHF TFC/TFN membranes. ....	190
<b>Table 7.2</b> Intrinsic transport parameters of the pristine TFC and selected GQD-modified TFN membranes.....	202
<b>Table 8.1</b> FO performance summary in AL-FS orientation of the various GO-modified PA TFN flat-sheet membranes prepared in this study. ....	216

## **ABSTRACT**

Polyamide (PA) thin-film composite (TFC) membranes have attained much attention for separation processes like water treatment, wastewater reclamation and desalination due to their superior intrinsic properties, such as high salt rejection and water permeability compared to the first generation of cellulose-based membranes. Nonetheless, several problems like fouling and trade-off between membrane selectivity and water permeability hinder the progress of conventional PA TFC forward osmosis (FO) membranes for real applications. To overcome these issues, nanomaterials have been integrated into the TFC membranes. Nanomaterial-modified membranes have demonstrated significant improvement in their anti-fouling properties and performance. Besides, PA TFC membranes can be designed for targeted applications like heavy metal removal and osmotic membrane bioreactor by using specific nanomaterials to modify their physicochemical properties (porosity, surface charge, hydrophilicity, membrane structure and mechanical strength). However, poor compatibility between nanomaterial and polymer matrix can result in poor membrane stability and selectivity. Hence, it is important to improve the stability of nanocomposite membranes to enable their successful application. Therefore, this doctoral study aims to modify the TFC membranes using graphene oxide (GO) derivatives for FO processes. Different TFC membrane and GO modification techniques have been employed and extensively characterized to understand and possible interaction between GO and TFC membranes to overcome and explain the existing challenges.

Firstly, the PA layer of commercial TFC FO membrane was coated with glutaraldehyde cross-linked polyvinyl alcohol (PVA) hydrogel solution comprising of GO at various loadings to enhance their fouling resistance. Experimental results showed that the

PVA/GO coating improved the smoothness and hydrophilicity of the membrane surface. PVA hydrogel with an optimal GO loading of 0.02 wt% showed a 55% reduction in specific reverse solute flux (*SRSF*), only a marginal reduction in the water flux, and the best anti-fouling property with a 58% higher flux recovery compared to the pristine TFC membrane. The significant improvement in the selectivity of the modified membranes meant that the hydrogel coating could be used to seal PA defects. The addition of GO flakes in PVA hydrogel coating also improved the biofouling resistance of the modified membranes, which can be attributed to the biocidal activity of GO and the superior surface properties and morphology of the modified membranes arising from hydrophilic PVA coating.

Following the surface modification of commercial TFC FO membranes with PVA/GO hydrogel, the effect of GO flake lateral size on the PA layer formation, TFC membrane properties and performance was investigated. GO suspensions with an average flake size ranging from 0.01 to 1.06  $\mu\text{m}^2$  were prepared by varying the sonication duration. It was observed that the large GO flakes obstructed the reaction between m-phenylenediamine (MPD) and trimesoyl chloride (TMC) monomers during the interfacial polymerization (IP) process by creating impervious regions that deteriorated membrane performance by forming defective PA layer formation. Whereas, smaller GO flakes were distributed more uniformly in the PA layer, creating fewer defects and demonstrating better desalination performance and anti-fouling property than the thin-film nanocomposite (TFN) membranes modified with larger GO flakes. The *SRSF* and water flux of the GO-modified TFN membranes improved by over 60% and 50%, respectively, when the average GO flake size was reduced from 1.06 to 0.01  $\mu\text{m}^2$  due to the formation of a thinner and more uniform PA layer. Our findings showed that a smaller GO flake size could be beneficial for minimizing PA layer defects.

After establishing that large GO flakes increase PA defects and deteriorate membrane selectivity, Aquaporin Z (AqpZ) reconstituting nanostructures (AQN) were embedded in the PA layer of GO TFN membranes to enhance their FO separation performance. The effect of increasing GO loading while retaining the AQN at an optimal loading of 0.2 wt% in the PA layer was investigated. Experimental results showed that GO flakes increased membrane water flux but decreased selectivity; whereas, AQN increased membrane selectivity by reducing the PA defects created by the GO flakes. As a consequence of favourable synergies between GO and AQN, the GO/AQN-incorporated TFN membranes demonstrated significantly higher *SRSF* while retaining the water permeability compared to the GO-incorporated TFN membranes. The TFN50 membrane with 0.2 wt% AQN and 0.005 wt% GO loading showed almost 3 folds increase in water flux ( $24.1 \text{ L}\cdot\text{m}^{-2}\cdot\text{h}^{-1}$ ) in comparison to the TFC membrane ( $8.2 \text{ L}\cdot\text{m}^{-2}\cdot\text{h}^{-1}$ ), while retaining membrane selectivity ( $0.37 \text{ g}\cdot\text{L}^{-1}$ ). However, the TFN50 membrane demonstrated a 27% lower *SRSF* and a marginal increase in water flux than the TFNGO50 membrane embedded with 0.005 wt% GO and no AQN. It was concluded that the synergistic effect of GO and aquaporin facilitated enhancement in both the membrane permeability and selectivity.

Finally, graphene oxide quantum dots (GQD) were used for their small size ( $< 5 \text{ nm}$ ) to improve the FO performance of outer-selective hollow fiber (OSHF) TFC membranes fabricated using the vacuum-assisted interfacial polymerization (VAIP) technique. Both experimental and molecular dynamics (MD) simulation proved that the GQD loading could influence both the IP process and the water transport across the PA layer. The TFN5 membrane with an optimal GQD loading of  $5 \text{ mg}\cdot\text{L}^{-1}$  demonstrated a 64% lower *SRSF* ( $0.12 \text{ g}\cdot\text{L}^{-1}$ ) and 68% higher water flux ( $30.9 \text{ L}\cdot\text{m}^{-2}\cdot\text{h}^{-1}$ ) compared to the TFC membrane due to its improved hydrophilicity and creation of more water channels inside the PA

layer after addition of GQDs. MD simulation was also employed at water-hexane and water-PA interface to investigate the effect of GQD loading on the IP reaction and membrane separation performance. The MD simulation results showed that a very high loading of GQDs could result in their aggregation at the water-hexane interface during the IP reaction and form a defective PA layer. It was also found that uniform dispersion of GQDs inside the PA layer can increase the water diffusivity inside the membrane leading to high water permeability, but too high GQD density can reduce the membrane water permeability by GQDs acting as barriers to water transport.

Overall, this study considered various strategies to improve the performance of GO-incorporated PA TFC and TFN membrane by investigating the factors that govern water transport across the membranes. The findings of this study could deliver strategies for future improvements in GO-based PA TFC membranes.



# **CHAPTER 1**

## **INTRODUCTION**

# **1. CHAPTER 1 Introduction**

## **1.1 Research background**

Rapid population growth and climate change have made water shortage a severe global problem. According to WHO, approximately 663 million people will lack access to safe water sources, and half of the world's population is anticipated to reside in water-stressed areas by 2025 (WHO 2015). Water scarcity issues are further worsened due to large quantities of contaminants produced from human activity, such as organic pollutants, being discharged into the water supplies. Consequently, treatment and safe reclamation of industrial and municipal wastewater are necessary as a sustainable solution to meet the growing water demand, improve agricultural productivity and protect human health and the environment from harmful pollutants (Shannon et al. 2008). Stringent water guidelines and the need to treat wastewater with robust, energy-efficient and low-cost methods that require minimal chemicals have made membrane technology popular for wastewater reuse and reclamation (Chen et al. 2014; Kim et al. 2004; Mozia 2010). Pressure-driven membrane processes, such as reverse osmosis (RO) and nanofiltration (NF), have been studied for high-quality clean water production (Kim et al. 2004). Nonetheless, the efficiency of these processes is hampered with high-fouling complex feed types that results in high process energy consumption due to membrane fouling.

Forward osmosis (FO) process, on the other hand, uses the osmotic pressure difference existing between the feed solution (FS) and draw solution (DS), rather than the hydraulic pressure, to transport water molecules from FS to DS across a selective membrane (Akther et al. 2015). The absence of hydraulic pressure in the FO process makes membrane cleaning

much simpler than pressure-driven processes without the absolute requirement for chemical reagents due to the reversible nature of membrane fouling in the FO process (Mi & Elimelech 2010; Xie et al. 2015). Consequently, FO membranes have been extensively researched for application in osmotic membrane bioreactor (OMBR) for wastewater treatment and reuse. Additionally, FO membranes can produce high-quality water by rejecting pathogens, particles and total dissolved solids (TDS); and the FO process is more energy-efficient than RO when DS recovery is not required. For instance, FO can be used for fertigation (Kim et al. 2019), treating wastewater (Tran et al. 2019), dewatering sludge (Zhu et al. 2012) and concentrating juice (Petrotos & Lazarides 2001) without needing DS recovery.

Moreover, FO process can be implemented to treat highly saline feeds that cannot be treated by the RO process (Lutchmiah et al. 2014). Hence, FO is a suitable application for directly pretreating complex feed and wastewaters (Lutchmiah et al. 2014; Ly et al. 2019). Although the fouling in FO process is lower than other membrane processes, it is a major drawback of FO as it can severely impede the flux efficiency, membrane lifespan and operating costs. Furthermore, the absence of an ideal FO membrane with high water flux, low reverse solute flux, minimal fouling tendency, and high mechanical and chemical stability has hindered this technology's industrial use. Therefore, it is essential to develop highly selective FO membranes with excellent anti-fouling properties, which will reduce the use of chemical cleaning reagents and maintenance costs and increase the membrane lifetime and offer consistent membrane performance.

## **1.2 Research motivation**

The fabrication of robust and highly selective osmotic membranes is among the most critical research areas in the field of engineered osmotic processes. Numerous works have been done

on polyamide (PA) based thin-film composite (TFC) membranes compared to other asymmetric membranes, such as cellulose triacetate, as they demonstrate much higher water permeability combined with superior selectivity over a wide pH and temperature range (Yip et al. 2010). However, conventional PA TFC membranes can be highly susceptible to fouling and demonstrate a trade-off relationship between membrane selectivity and water permeability. To overcome these issues, nanomaterials or chemical additives have been integrated into the TFC membranes. Nanomaterial-modified TFC membranes have demonstrated significant improvement in their anti-fouling properties and FO performance. Also, PA TFC membranes can be designed for specific applications like heavy metal removal and osmotic membrane bioreactor by using nanomaterials to modify their physicochemical properties (porosity, surface charge, hydrophilicity, membrane structure and mechanical strength).

Nonetheless, the challenges confronted by nanocomposite PA TFC FO need to be addressed before deeming them suitable for practical application. These challenges include nanomaterial loss and poor compatibility between fillers and polymer matrix that worsen membrane selectivity. It is, therefore, imperative to understand the polymer-nanomaterial interaction to enhance the stability and development of nanocomposite membranes.

Over the last few years, graphene oxide (GO) has drawn researchers' attention because of its distinct structure, hydrophilicity, superior antibacterial properties, high chemical stability and low production cost (Dreyer et al. 2010; Hegab, ElMekawy, Zou, et al. 2016). GO-modified membranes have been reported to demonstrate improved mechanical strength, thermal stability, water permeability, chlorine resistance and anti-fouling properties (Goh et al. 2015; Pang et al. 2019). The numerous studies published on GO-incorporated membranes proved

that membrane modification using GO is a promising approach to augment membrane performance. Moreover, bulk production of GO in recent years has made it affordable, thus, making it potentially feasible for large-scale nanocomposite membrane production. However, very few studies provided an in-depth explanation of the possible interaction between GO and polymer matrix that alter the membrane chemical and physical properties. This research gap is the main motivation for using GO and its derivatives as fillers to modify PA TFC FO membranes to understand the possible interactions between GO and TFC membranes.

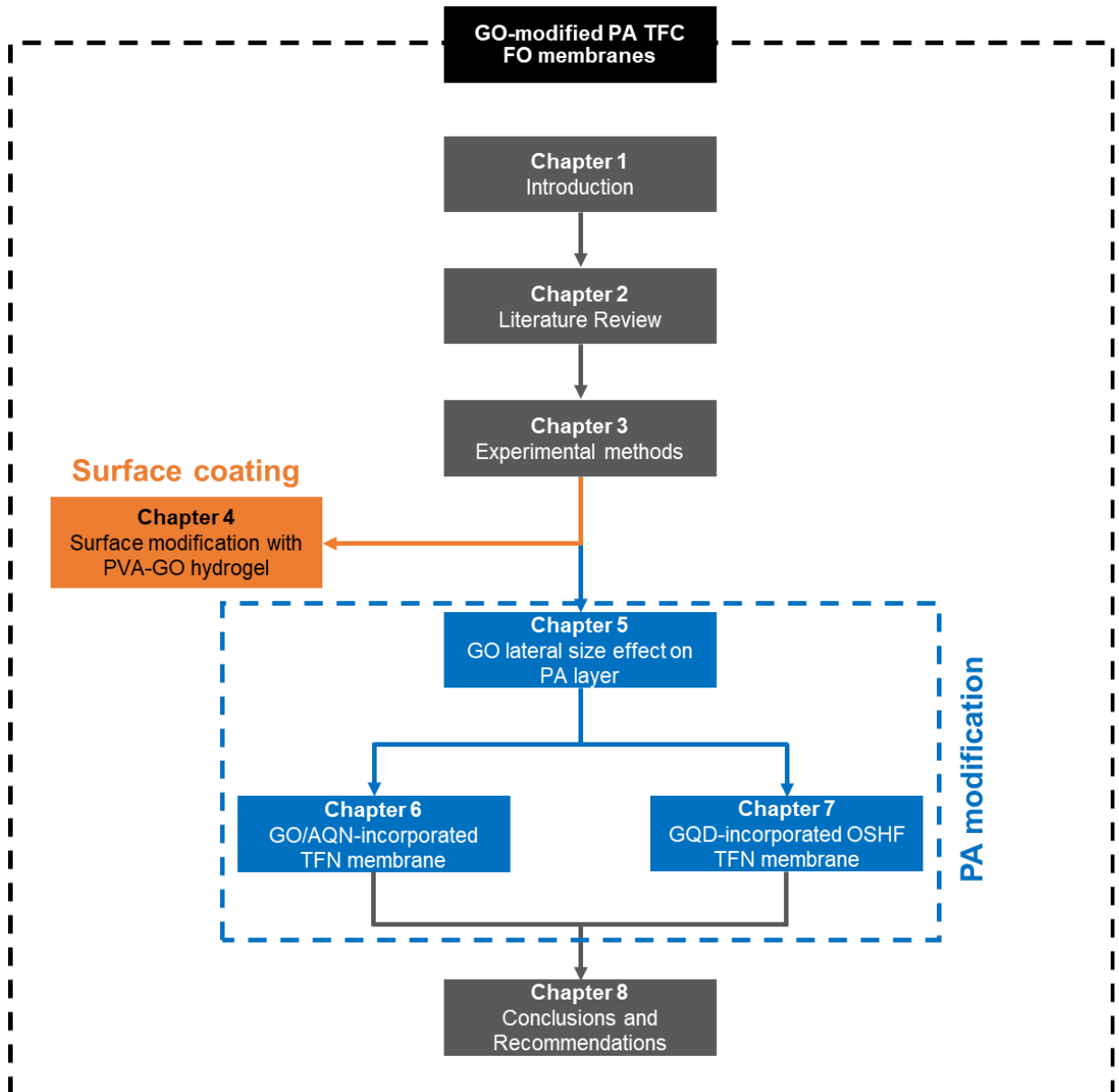
### **1.3 Research aim**

The broad aim of this research is to develop high-performance TFC flat sheet and hollow fiber (HF) membranes modified with GO and its derivatives to help realise the commercial application of the FO technology.

### **1.4 Research objectives and scope**

This study systematically investigated the effect of GO and its derivatives on the properties and performances of TFC flat-sheet and HF membranes. Flat-sheet TFC membranes have a planar configuration, while HF TFC membranes possess a tubular structure with dense PA layers formed on top of micro-thin semi/porous substrates. Two different TFC membrane fabrication and GO modification techniques have been employed and expansively characterized to understand the possible interaction between GO and TFC membranes that govern water transport across the membranes. Specifically, GO was used to modify the surface or PA layer of the TFC membranes to improve their performances. Surface modification of TFC membrane involved coating the GO flakes on the PA layer; whereas, PA layer modification comprised of GO addition inside the PA layer during the interfacial

polymerization (IP) reaction. The effect of physicochemical properties of the prepared pristine and modified membranes on their performances have also been expansively assessed to overcome the existing challenges and deliver strategies for future improvements in GO-based PA TFC membranes. The overall structure of this thesis is illustrated in **Fig. 1.1**.



**Fig. 1.1** Thesis structure on the development of GO-modified PA TFC membranes for FO processes.

The objectives of this study are listed below:

- To modify the surfaces of commercial PA TFC FO membrane with various polyvinyl alcohol (PVA)/GO hydrogels and investigate their effect on the performance and anti-fouling properties of the membranes.
- To study the influence of GO flake lateral size on the PA layer formation and the physicochemical properties and performances of the modified TFC membranes.
- To assess the influence of aquaporin nanostructures (AQN) as fillers on the performance of GO-modified PA TFN FO membranes.
- To explore the influence of graphene oxide quantum dot (GQD) loading on the IP reaction and water transport behaviour across outer-selective hollow fiber (OSHF) TFN membranes from experimental study and molecular dynamics (MD) simulation.
- To provide insights on the role of GO in the polymer matrix and deliver strategies for future improvements in GO-based PA TFC membranes.

## 1.5 Thesis organization

This thesis is written in a “Thesis by compilation” format and comprises 8 chapters, with chapters 4 to 7 presenting the key experimental findings of this study and comprising published articles or unpublished articles submitted to peer-reviewed journals.

The structure of the thesis is summarized, as shown below:

- **Chapter 1** presents the introduction, research background, motivation and highlights the objectives of this Doctoral study.
- **Chapter 2** reviews the recent advances in nanomaterial-modified PA TFC FO membranes and provides a comprehensive summary of the progress of nanocomposite PA TFC membrane since its first development for FO in the year

2012. The various fabrication techniques for nanomaterial-incorporated TFC membranes are provided. Finally, the key challenges still being confronted and the future research directions for nanocomposite PA TFC FO are also discussed. The literature review is published as:

Akther, N., Phuntsho, S., Chen, Y., Ghaffour, N. & Shon, H.K. 2019, 'Recent advances in nanomaterial-modified polyamide thin-film composite membranes for forward osmosis processes', *Journal of Membrane Science*, vol. 584, pp. 20-45.

- **Chapter 3** presents the information on the materials and experimental methods used in this study.
- **Chapter 4** considers the surface modification of commercial PA TFC FO membrane with glutaraldehyde cross-linked PVA hydrogel solution comprising of GO at various loadings. The properties of the modified membranes, such as surface morphology, surface charge and wettability are investigated. The optimal GO concentration in hydrogel solution and its influence on membrane anti-fouling properties is confirmed by FO membrane performance results. This chapter is written and published as a journal article:

Akther, N., Ali, S.M., Phuntsho, S. & Shon, H.K. 2020, 'Surface modification of thin-film composite forward osmosis membranes with polyvinyl alcohol-graphene oxide composite hydrogels for anti-fouling properties', *Desalination*, vol. 491, p. 114591.

- **Chapter 5** explores the effect of varying GO flake lateral sizes on the IP reaction and PA layer properties using extensive characterisation techniques to get an insight into the interaction between GO and PA. The influence of GO flake size on the FO performance and anti-fouling properties of the modified membranes is also studied



and correlated to the physicochemical properties of the membranes. This chapter is written and published as a journal article:

Akther, N., Yuan, Z., Chen, Y., Lim, S., Phuntsho, S., Ghaffour, N., Matsuyama, H. & Shon, H.K. 2020, 'Influence of graphene oxide lateral size on the properties and performances of forward osmosis membrane', *Desalination*, vol. 484, p. 114421.

- **Chapter 6** proposes incorporating AQN as fillers to further improve the performance of GO-modified PA TFN FO membranes developed in Chapter 5. AQNs are used at their optimal loading, while the concentration of GO flakes is varied during the IP process. The surface properties and performance of the AQN/GO-modified membrane is compared with pristine and GO-modified membranes to evaluate the obtained experimental results. This chapter is written and published as a journal article:

Akther, N., Sanahuja-Embuena, V., Górecki, R., Phuntsho, S., Helix-Nielsen, C. & Shon, H.K. 2021, 'Employing the synergistic effect between aquaporin nanostructures and graphene oxide for enhanced separation performance of thin-film nanocomposite forward osmosis membranes', *Desalination*, vol. 498, p. 114795.

- **Chapter 7** investigates the effect of GQD loading on the IP reaction and transport behaviour of water molecules in OSHF PA TFN membrane using both experimental data and MD simulation. This chapter is written and published as a journal article:  
Akther, N., Kawabata, Y., Lim, S., Yoshioka, T., Phuntsho, S., Matsuyama, H. & Shon, H.K. 2021, 'Effect of graphene oxide quantum dots on the interfacial polymerization of a thin-film nanocomposite forward osmosis membrane: An

experimental and molecular dynamics study', *Journal of Membrane Science*, vol. 630, p. 119309.

- **Chapter 8** summarizes the key findings of this study and provides recommendations for future works.

# **CHAPTER 2**

## **LITERATURE REVIEW**

## STATEMENT OF CONTRIBUTION OF AUTHORS

Title of Paper	Recent advances in nanomaterial-modified polyamide thin-film composite membranes for forward osmosis processes		
Publication Status	<input checked="" type="checkbox"/> Published <input type="checkbox"/> Accepted for Publication <input type="checkbox"/> Submitted for Publication <input type="checkbox"/> Unpublished and Unsubmitted work written in manuscript style		
Publication Details	Akther, N., Phuntsho, S., Chen, Y., Ghaffour, N. & Shon, H.K. 2019, 'Recent advances in nanomaterial-modified polyamide thin-film composite membranes for forward osmosis processes', <i>Journal of Membrane Science</i> , vol. 584, pp. 20-45.		
<b>PRINCIPAL AUTHOR</b>			
Name of Principal Author (Candidate)	Nawshad Akther		
Contribution to the paper	Literature review, Data curation, Critical analysis, Writing - original draft		
Certification	This paper reports on original research I conducted during the period of my Higher Degree by Research candidature and is not subject to any obligations or contractual agreements with a third party that would constrain its inclusion in this thesis. I am the primary author of this paper.		
Signature	Production Note: Signature removed prior to publication.	Date	04/09/2020
<b>CO-AUTHOR CONTRIBUTIONS</b>			
By signing the Statement of Contribution of Authors, each author certifies that:			
i. the candidate's stated contribution to the publication is accurate (as detailed above); and ii. permission is granted for the publication to be included in the candidate's thesis.			
Name of Co-Author 1	Dr. Sherub Phuntsho		
Contribution to the paper	Writing - review & editing.		
Signature	Production Note: Signature removed prior to publication.	Date	04/09/2020
Name of Co-Author 2	Prof. Yuan Chen		
Contribution to the paper	Writing - review & editing.		
Signature	Production Note: Signature removed prior to publication.	Date	04/09/2020
Name of Co-Author 3	Prof. Noreddine Ghaffour		
Contribution to the paper	Writing - review & editing.		
Signature	Production Note: Signature removed prior to publication.	Date	04/09/2020
Name of Co-Author 4	Prof. Ho Kyong Shon		
Contribution to the paper	Supervision, Writing - review & editing.		
Signature	Production Note: Signature removed prior to publication.	Date	04/09/2020

## 2. CHAPTER 2 Literature review

### **Abstract**

Polyamide thin-film composite (PA TFC) membranes have attained much attention for forward osmosis (FO) applications in separation processes, water and wastewater treatment due to their superior intrinsic properties, such as high salt rejection and water permeability compared to the first generation of cellulose-based FO membranes. Nonetheless, several problems like fouling and trade-off between membrane selectivity and water permeability hinder the progress of conventional PA TFC FO membranes for real applications. To overcome these issues, nanomaterials or chemical additives have been integrated into the TFC membranes. Nanomaterial-modified membranes have demonstrated significant improvement in their anti-fouling properties and FO performance. In addition, PA TFC membranes can be designed for specific applications like heavy metal removal and osmotic membrane bioreactor by using nanomaterials to modify their physicochemical properties (porosity, surface charge, hydrophilicity, membrane structure and mechanical strength). This review provides a comprehensive summary of the progress of nanocomposite PA TFC membrane since its first development for FO in the year 2012. The nanomaterial-incorporated TFC membranes are classified into four categories based on nanomaterial location in/on the membranes: embedded inside the PA active layer, incorporated within the substrate, coated on the PA layer surface, or deposited as an interlayer between the substrate and the PA active layer. The key challenges still being confronted and the future research directions for nanocomposite PA TFC FO are also discussed.

**Keywords:** Forward osmosis membrane, thin-film composite (TFC), thin-film nanocomposite (TFN), nanoparticles, interfacial polymerization

## 2.1 Introduction

Membrane technologies like reverse osmosis (RO) and forward osmosis (FO) have attracted enormous research interest as more energy-efficient and sustainable methods for desalination, wastewater treatment and separation processes over the past decades (Ali, Tufa, et al. 2018; Buonomenna & Bae 2015; Subramani & Jacangelo 2015). They are simple to install and operate, highly scalable, consume relatively low energy, and their performance mechanism is well-understood (Attarde et al. 2017; Le & Nunes 2016; Quist-Jensen, Macedonio & Drioli 2015). RO is the most commonly used membrane technology as it produces the best water quality compared to other commercial membrane-based technologies like ultrafiltration (UF) and nanofiltration (NF) (Lee, Arnot & Mattia 2011). However, RO is a very energy-intensive process, where membrane replacement can be costly and membrane scaling and fouling can be a significant challenge (Liyanaarachchi et al. 2014; Motsa et al. 2014).

On the other hand, FO has turned out to be an active research area as a prospective low-energy membrane-separation technology, mainly for application in wastewater treatment, RO pre-treatment and brine dilution (Akther et al. 2015; Cath, Childress & Elimelech 2006). Unlike RO, which operates at a very high hydraulic pressure, FO processes are driven naturally by the osmotic pressure difference existing between the draw and feed solution with the existence of little or zero transmembrane pressure (Chung, Zhang, et al. 2012). In a FO process, water moves from a low concentrated feed to a highly concentrated draw solution through a semi-permeable membrane while rejecting solutes on both sides of the membrane. Pure water is then separated from the diluted draw solution using a suitable separation technique (Akther, Daer, et al. 2019; Zhao et al. 2012). However, the draw solute

regeneration step in the FO process is significantly energy-intensive, making direct desalination with RO more energy-efficient than FO (McGovern & Lienhard V 2014). Nonetheless, FO may be more energetically favourable than RO for high salinity and high fouling potential applications that do not require draw solution regeneration, such as food concentration and brine dilution (Akther, Daer & Hasan 2018; Shaffer et al. 2015).

Besides, FO processes can remove an extensive range of pollutants present in the feed solution (Zhang et al. 2010) and function at much greater feed recovery rates than the RO processes (Martinetti, Childress & Cath 2009). FO membranes have higher fouling reversibility than the pressure-driven RO process, and most FO foulants can generally be removed by physical cleaning requiring only limited chemical cleaning frequency (Ali, Kim, et al. 2018; Siddiqui et al. 2018; Tran et al. 2019). However, membrane characteristics play a significant role in the process performance and the economics of the FO technology in addition to the other factors, such as draw solution type and regeneration method (Akther et al. 2015).

The development of FO membranes started around the year 2000. Prior to that, FO studies were primarily conducted using RO membranes, which are unsuitable for FO applications due to their thick support layers. For a FO process to work efficiently, the membranes should exhibit high water flux, low reverse solute flux, excellent mechanical stability, chemical resistance and anti-fouling property (Cath, Childress & Elimelech 2006). McCutcheon and Elimelech concluded, based on the results from their asymmetric membrane flux modelling, that FO membranes should have smaller solute resistance to diffusion ( $K$ ) values to diminish the internal concentration polarization (ICP) effect and achieve high water flux during the FO operation (McCutcheon & Elimelech 2006, 2007; McCutcheon, McGinnis & Elimelech

2005). The K values could be improved by increasing the membrane porosity and reducing membrane thickness. The first generation FO membrane commercialized by Hydration Technologies, Inc. (HTI) comprised of cellulose triacetate (CTA) supported on a thin woven polyester mesh (Herron 2008). Although the commercial CTA FO membranes were able to reduce the ICP effects, the water permeability and selectivity of the CTA membranes were not impressive (Yip et al. 2010). HTI later developed a thin-film composite (TFC) FO membrane that included a thin polyamide (PA) selective layer on top of a porous substrate layer supported by a polyester (PET) mesh. The HTI TFC membrane demonstrated a much higher solute rejection and a water flux nearly double that achieved using CTA FO membrane (Ren & McCutcheon 2014). Unlike the CTA membranes, which can operate under a limited pH range of 4 to 8 (Vos, Burris & Riley 1966), the TFC membranes can tolerate a wide pH range of 2 to 12 and have better chemical stability (Yip et al. 2010). The high biodegradability of the CTA membrane reduces its membrane lifespan; thereby, limiting its application (Cath, Childress & Elimelech 2006). As a result, most recent studies on FO membranes are aimed towards TFC membrane fabrication and their modification.

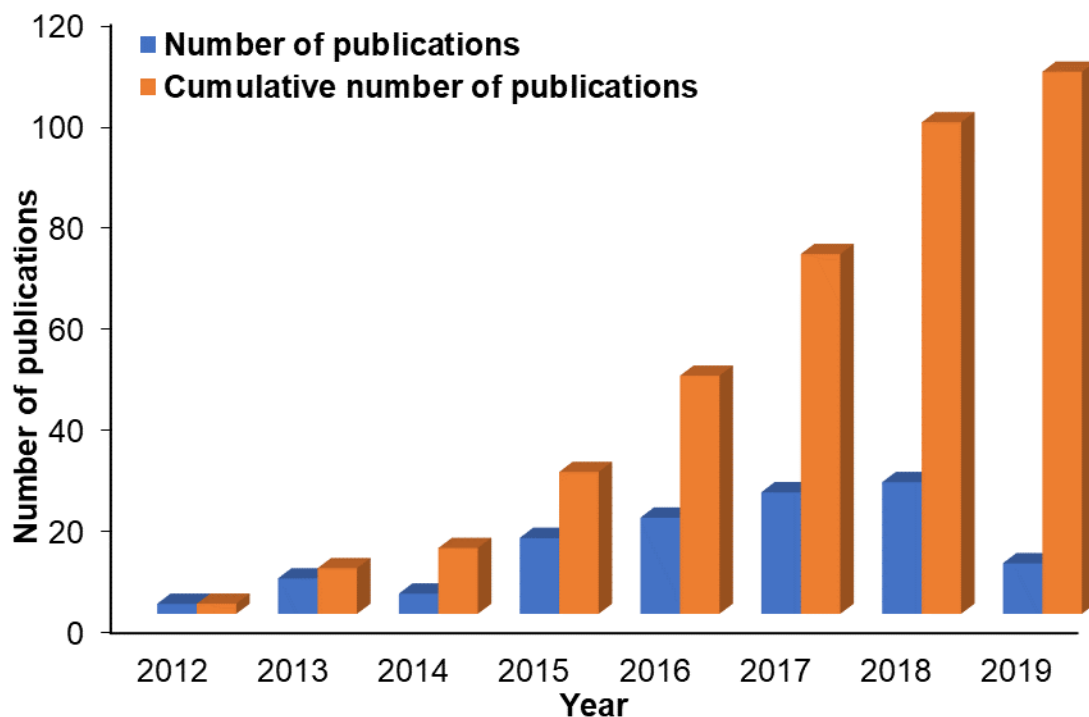
Polymeric TFC membranes have been previously used for NF and RO applications, and they usually involve the development of a thin dense active layer on top of a porous substrate (Ismail et al. 2015; Lau, Gray, et al. 2015). The thin selective or active layer is usually formed by interfacial polymerization (IP) reaction of monomers, and its thin-film formation is significantly governed by the structure and properties of the membrane substrate (Han et al. 2012; Wei et al. 2011; Widjojo et al. 2011). The substrate structure and morphology significantly influence the degree of ICP within the porous layer (Liu et al. 2016); whereas, the active layer controls the extent of solute and water fluxes across the membrane (Klaysom,



Hermans, et al. 2013). Additionally, membrane fouling lowers water flux by increasing membrane resistance, which further reduces the mass transfer coefficient and enhances external concentration polarization (ECP) on the membrane surface (Bell et al. 2017; Chun et al. 2017; Li, Yangali-Quintanilla, et al. 2012; Wang et al. 2016). Although PA-based TFC FO membranes have better performance compared to the cellulose-based membranes, the overall FO performance in terms of ICP, fouling resistance and chlorine tolerance is still an issue (Akther et al. 2015).

Inspired by nanocomposite membranes developed in the 1990s for gas separation (Robeson 1991), several studies have incorporated nanomaterials in RO and FO membranes to improve the overall membrane performance as reviewed by Li, Yan & Wang (2016). Xiao et al. developed a general multiscale modelling and simulation framework to predict the properties of polymer nanocomposites like mechanical strength and permeability for gas separation (Xiao, Huang & Manke 2010). The framework could be used to investigate the molecular-level interactions between thermoset polymer and various types of nanoparticles that affect the performance of polymer nanocomposites. Nanomaterial incorporation has shown to enhance not only the water permeability, antimicrobial properties, fouling and chlorine resistance of the membranes, but also their thermal stability and mechanical strength. Silver nanoparticles have been extensively used as an antimicrobial agent in nanocomposite membranes to improve their antimicrobial properties (Soroush et al. 2015). Whereas, the addition of porous nanoparticles like zeolites were found to increase the water permeability of the nanocomposite membranes by creating channels for water transport (Ma et al. 2012). The changes in properties of nanocomposite membranes are strongly influenced by the chemical properties, type, size and concentration of the nanomaterial used. As such, the

nanocomposite membrane properties can be tailored depending on the type of nanomaterial chosen. Tang's group developed the first nanocomposite FO membrane with improved water permeability in 2012 (Ma et al. 2012), which was inspired by the study on zeolite-incorporated TFC RO membrane (Jeong et al. 2007a). The increasing interest in the development of nanomaterial-based PA TFC FO membranes is evident from the increasing number of studies published as presented in **Fig. 2.1**.



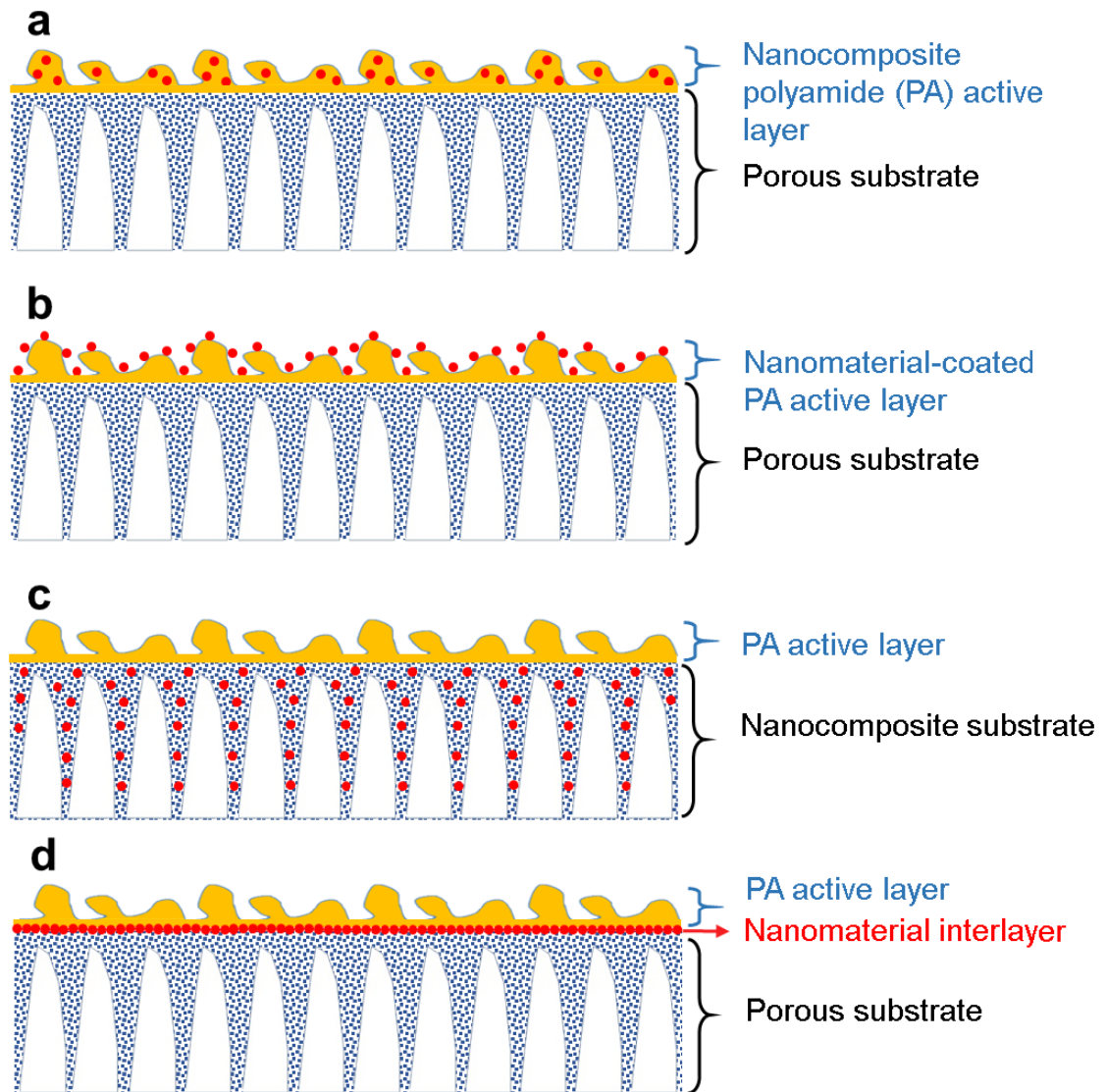
**Fig. 2.1** Number of publications related to nanomaterial-modified PA TFC FO membranes (Retrieved from Web of Science on 14<sup>th</sup> March 2019).

Nanomaterials can be added either into the active layer or into the substrate of the membrane to enhance active layer's transport properties, substrate's structural characteristics, and membrane's overall mechanical stability and chemical resistance (Li, Yan & Wang 2016). Some studies have also coated or covalently bonded nanomaterials on the membrane surface

to improve membrane hydrophilicity, surface charge density and anti-fouling property (Hegab, ElMekawy, Barclay, et al. 2016; Tiraferri, Vecitis & Elimelech 2011). Whereas, others have deposited nanomaterial interlayer on porous substrates for the formation of defect-free PA active layer (Karan, Jiang & Livingston 2015; Xu et al. 2017). Based on the approach of nanomaterial integration, TFC membranes can be classified as follows: (a) thin-film nanocomposite (TFN) membrane, (b) TFC membrane with a nanomaterial-coated PA layer surface, (c) TFC membrane with a nanocomposite substrate, and (d) TFC membrane with a nanomaterial interlayer (**Fig. 2.2**). Some of the inorganic nanomaterials that have been most widely used for FO membrane modification include zeolite (Ma et al. 2012; Ma, Wei, et al. 2013), graphene oxide (GO) (Jin et al. 2018a; Park et al. 2015; Salehi, Rastgar & Shakeri 2017), carbon nanotubes (CNTs) (Dumée et al. 2013; Fan, Liu & Quan 2018; Goh et al. 2013; Wang, Song, et al. 2015), silica (Lee et al. 2014; Lee, Wang, et al. 2015) and titanium oxide (Amini, Rahimpour & Jahanshahi 2016; Huang et al. 2015b; Zhang, Huang, et al. 2017).

The review articles on FO membranes that have been published to date have considered draw solutes (Alejo et al. 2017; Luo et al. 2014; Zhao et al. 2016), membrane fouling (Bogler, Lin & Bar-Zeev 2017; Chun et al. 2017; Xie et al. 2017), various FO applications (Ansari et al. 2017; Chekli et al. 2016; Chung, Li, et al. 2012; Chung et al. 2015), FO membrane materials, fabrication methods and their chemical modifications (Alsvik & Hägg 2013; Lu, Gao, et al. 2015; Xu, Chen & Ge 2017). However, a specialized review providing ample information on the advancement of nanomaterial-incorporated PA TFC membranes for FO applications is currently lacking. The development of high-performing FO membranes, especially those incorporated with nanoparticles, has gained significant research interests recently as they have the potential to enhance FO performance. Hence, for the first time, we set out to provide

a comprehensive review on the progress and developments of incorporating various kinds of nanomaterials into the active layer, substrate and surface of PA TFC FO membranes. The major challenges, future research directions and prospects in the development of nanomaterial-incorporated PA TFC membrane are also critically discussed.

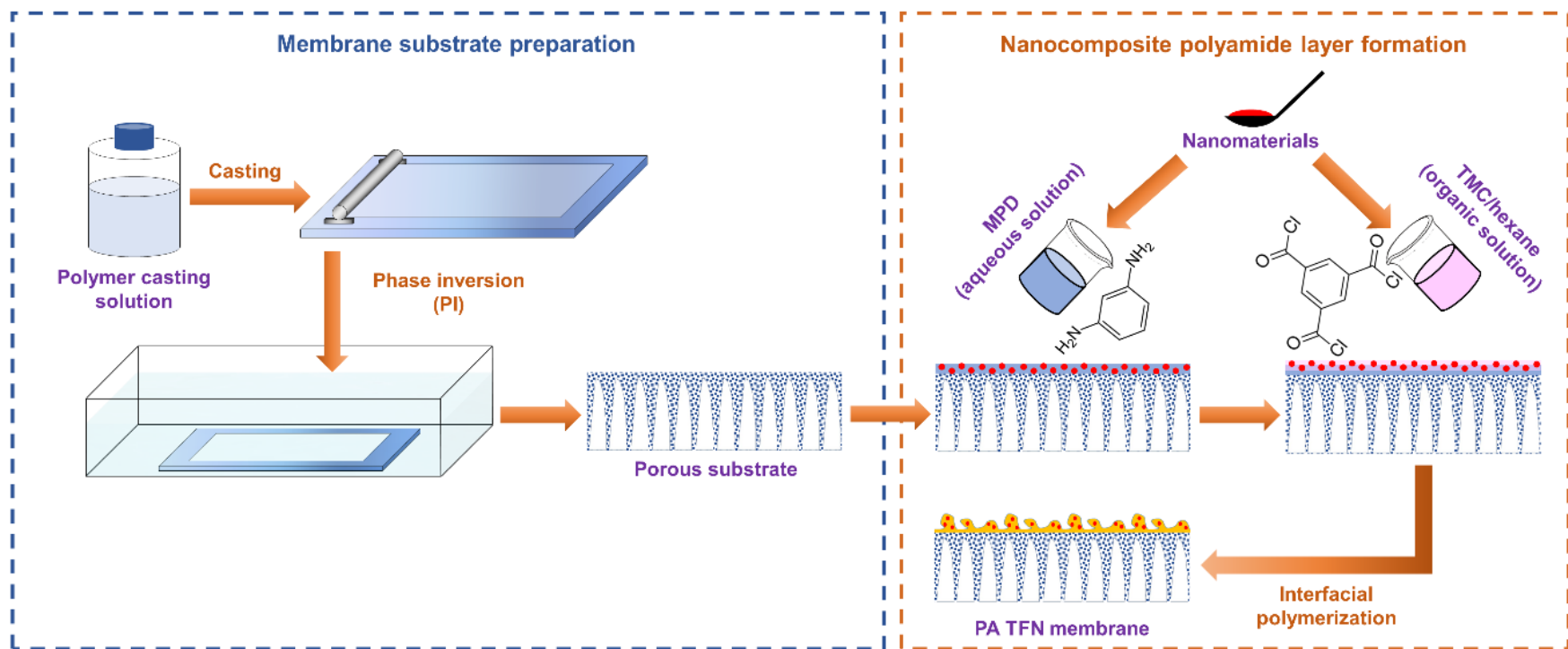


**Fig. 2.2** Schematic illustrations demonstrating typical structures of nanomaterial-incorporated PA TFC membranes: a) TFN membrane, b) TFC membrane with nanomaterial-coated PA layer surface, c) TFC membrane with nanocomposite substrate and d) TFC membrane with nanomaterial interlayer.

The aquaporin-based biomimetic FO membranes have not been included in this review due to the difference in their fabrication technique and behaviour from that of the nanocomposite PA TFC membranes. Habel et al. provided an extensive review of the different fabrication and characterisation approaches for aquaporin-based biomimetic membranes (Habel et al. 2015). This review is expected to inspire more studies to address the existing challenges in membrane development and realize the practical applications of membranes for enhancing FO performance.

## **2.2 Nanomaterial-modified PA active layers**

Since 2012, several studies have dispersed inorganic nanomaterials into the thin PA active layer of the TFC FO membranes to improve their separation performance. The PA layer is made via IP reaction between trimesoyl chloride (TMC) organic solution and m-phenylenediamine (MPD) aqueous solution. Depending on the hydrophilic/hydrophobic nature of the nanofillers, they can be distributed in either an aqueous MPD or organic TMC phase. **Fig. 2.3** illustrates the typical steps involved in the TFN membrane fabrication process. Nanomaterials like zeolites, silica, GO, CNTs that have been previously used for RO nanocomposite membranes have also been studied for the preparation of TFN FO membranes (Giwa et al. 2016; Li, Yan & Wang 2016). **Table 2.1** and **Table 2.2** list the research articles based on the development of PA TFN membranes.



**Fig. 2.3** Typical steps involved in the fabrication of a TFN membrane through the IP process. Nanomaterials are uniformly-dispersed either in the MPD aqueous or TMC organic solution for the formation of nanocomposite PA layer.

**Table 2.1** Summary of the fabrication conditions and FO performance of porous nanomaterial-incorporated PA TFN membranes.

TFN membrane		Optimal particle loading	Intrinsic properties	Substrate fabrication method & conditions	FO performance (AL-FS)				References
Fillers embedded in PA layer (Particle size)	Substrate (PA layer monomers)				DS (FS)	CFV	$J_w$ (LMH)	$J_s$ (gMH)	
Zeolite; NaY (40-150 nm)	PSf (MPD, TMC)	0.1 wt/v% in TMC/n-hexane	$A = 2.59 \text{ LMH}\cdot\text{bar}^{-1}$ $B = 1.57 \text{ LMH}$ $S = 782 \mu\text{m}$	PI; Casting/overall thickness = 150/70 $\mu\text{m}$	1 M NaCl (10 mM NaCl)	$20 \text{ cm}\cdot\text{s}^{-1}$	14.6	3.5	(Ma et al. 2012)
Amine functionalized CNTs (OD: 5 nm, ID: 1.3-2 nm, L: 50 $\mu\text{m}$ )	PSf (MPD, TMC)	0.05 wt/v% in MPD solution	$A = 3.56 \text{ LMH}\cdot\text{bar}^{-1}$ $B = 0.10 \text{ LMH}$ $S = 380 \mu\text{m}$	PI; Casting/overall thickness = n/a	2 M NaCl (10 mM NaCl)	$7.2 \text{ cm}\cdot\text{s}^{-1}$	30.0	2.4	(Amini, Jahanshahi & Rahimpour 2013a)
CNTs (D: 20 nm, L: 0.5-2 $\mu\text{m}$ )	PSf (DA Tris buffer solution, TMC)	0.05 wt/v% in DA solution	-	PI; Casting/overall thickness = n/a	2 M MgCl <sub>2</sub> (DI water)	$1.6 \text{ cm}\cdot\text{s}^{-1}$	8.6	2.1	(Song et al. 2015)
Amine functionalized TNTs (ID: 5-25 nm)	PSf (MPD, TMC)	0.05 wt/v% in TMC/cyclohexane solution	$A = 2.38 \text{ LMH}\cdot\text{bar}^{-1}$ $B = 0.37 \text{ LMH}$ $S = 368 \mu\text{m}$	PI; Casting/overall thickness = n/a	1 M NaCl (10 mM NaCl)	$32.7 \text{ cm}\cdot\text{s}^{-1}$	20.8	4.3	(Emadzadeh et al. 2015)
HNTs (ID: 10-15 nm)	PSf (MPD, TMC)	0.05 wt/v% in TMC/cyclohexane solution	$A = 1.87 \text{ LMH}\cdot\text{bar}^{-1}$ $B = 0.63 \text{ LMH}$	PI; Casting/overall thickness = n/a	2 M NaCl (10 mM NaCl)	$350 \text{ mL}\cdot\text{min}^{-1}$	20.1	5.8	(Ghanbari, Emadzadeh, Lau, Lai, et al. 2015)
TiO <sub>2</sub> /HNT nanocomposites (ID: 5-15 nm)	PSf (MPD, TMC)	0.05 wt/v% in TMC/cyclohexane solution	$A = 2.45 \text{ LMH}\cdot\text{bar}^{-1}$ $B = 0.60 \text{ LMH}$	PI; Casting/overall thickness = 120/70-90 $\mu\text{m}$	2 M NaCl (10 mM NaCl)	$350 \text{ mL}\cdot\text{min}^{-1}$	25.5	4.9	(Ghanbari, Emadzadeh, Lau, Matsuura, Davoody, et al. 2015)
CNTs (D: 20 nm, L: 0.5-2 $\mu\text{m}$ )	PSf (DA Tris buffer solution, MPD, TMC)	0.05 wt/v% in DA solution	$A = 6.7 \text{ LMH}\cdot\text{bar}^{-1}$ $B = 8.3 \text{ LMH}$ $S = 1637 \mu\text{m}$	PI; Casting thickness = 80 $\mu\text{m}$	2 M MgCl <sub>2</sub> (DI water)	$7.8 \text{ cm}\cdot\text{s}^{-1}$	14.5	7.5	(Song, Wang, et al. 2016)
Al <sub>2</sub> O <sub>3</sub> (<50 nm)	PSf, 0.5 wt% Al <sub>2</sub> O <sub>3</sub> (MPD, TMC)	0.05 wt/v% in TMC/n-hexane solution	$A = 8.43 \text{ LMH}\cdot\text{bar}^{-1}$ $B = 1.66 \text{ LMH}$ $S = 1028 \mu\text{m}$	PI; Casting thickness = 90 $\mu\text{m}$	1 M NaCl (DI water)	$18.5 \text{ cm}\cdot\text{s}^{-1}$	27.6	7.1	(Ding et al. 2017)
MOF: UiO-66 (n/a)	PSf (MPD, TMC)	0.1 wt/v% in TMC/n-hexane solution	$A = 3.3 \text{ LMH}\cdot\text{bar}^{-1}$ $B = 0.3 \text{ LMH}$ $S = 1637 \mu\text{m}$	PI; Casting/overall thickness = 150/62 $\mu\text{m}$	2 M NaCl (DI water)	$1.1 \text{ cm}\cdot\text{s}^{-1}$	27.0	6.1	(Ma, Peh, et al. 2017)
MOF (D: 30 nm)	PES (MPD, TMC)	0.04 wt/v% in TMC/n-hexane solution	$A = 4.7 \text{ LMH}\cdot\text{bar}^{-1}$ $B = 0.6 \text{ LMH}$ $S = 238 \mu\text{m}$	PI; Casting thickness = 100 $\mu\text{m}$	2 M NaCl (DI water)	$21 \text{ cm}\cdot\text{s}^{-1}$	46.0	102.3	(Zirehpour, Rahimpour & Ulbricht 2017)
Zwitterion (AEPPS) (n/a)	PSf (MPD, TMC)	30 wt/v% in MPD solution	$A = 4.81 \text{ LMH}\cdot\text{bar}^{-1}$ $B = 0.19 \text{ LMH}$ $S = 747 \mu\text{m}$	PI; Casting/overall thickness = n/a	2 M NaCl (n/a)	n/a	22.5	12.5	(Chiao et al. 2018)
COF; SNW-1 (D: ~30 nm)	PSf (MPD, TMC)	0.005 wt/v% in MPD solution	$A = 1.77 \text{ LMH}\cdot\text{bar}^{-1}$ $B = 0.46 \text{ LMH}$	PI; Casting/overall thickness = 120/58 $\mu\text{m}$	1 M NaCl (DI water)	$12.6 \text{ cm}\cdot\text{s}^{-1}$	15.6	4.8	(Akther, Lim, et al. 2019)
COF; SNW-1 (D: ~30 nm)	PES (MPD, TMC)	0.001 wt/v% in MPD solution	$A = 2.37 \text{ LMH}\cdot\text{bar}^{-1}$ $B = 0.41 \text{ LMH}$	HF, PI; Overall thickness = 66 $\mu\text{m}$	1 M NaCl (DI water)	FS = $20.9 \text{ cm}\cdot\text{s}^{-1}$ DS = $10.4 \text{ cm}\cdot\text{s}^{-1}$	31.5	5.7	(Lim, Akther, et al. 2020)

A: water permeability coefficient; Al<sub>2</sub>O<sub>3</sub>: aluminium oxide; B: solute permeability coefficient; CFV: cross-flow velocity; CNT: carbon nanotube; COF: covalent-organic framework; DA: dopamine; DS: draw solution; FS: feed solution; Js: solute flux; Jw: water flux; HF: hollow fiber; HNT: halloysite nanotube; MOF: metal-organic framework; MPD: m-phenylenediamine; PES: poly(ethersulfone); PI: phase inversion; PSf: polysulfone; S: structural parameter; SNW-1: Schiff base network-1; TMC: trimesoyl chloride; TNT: titanate nanotubes

**Table 2.2** Summary of the fabrication conditions and FO performance of non-porous nanomaterial-incorporated PA TFN membranes.

TFN membrane		Optimal particle loading	Intrinsic properties	Substrate fabrication methods and conditions	FO performance (AL-FS)				References
Fillers embedded in PA layer (Particle size)	Substrate (PA layer monomers)				DS (FS)	CFV	$J_w$ (LMH)	$J_s$ (gMH)	
SiO <sub>2</sub> (15-20 nm)	PSf (MPD, TMC)	0.05 wt% in MPD solution	$A = 3.43$ LMH.bar <sup>-1</sup> $B = 1.02$ LMH $S = 368$ μm	PI; Casting thickness = 100 μm	2 M NaCl (10 mM NaCl)	800 mL·min <sup>-1</sup>	15.0	1.6	(Niksefat, Jahanshahi & Rahimpour 2014)
GO (Lateral size: 35-90 nm, T: 0.75-1.25 nm)	PAN (MPD, TMC)	0.06 wt% in MPD solution	$A = 2.0$ LMH.bar <sup>-1</sup> $B = 0.8$ LMH $S = 85$ μm	PI; Casting thickness = 100 μm	1 M NaCl (DI water)	300 mL·min <sup>-1</sup>	23.6	4.4	(Shen, Xiong & Wang 2016)
TiO <sub>2</sub> (20 nm)	PSf (MPD, TMC)	0.05 wt/v% in MPD solution	$A = 3.89$ LMH.bar <sup>-1</sup> $B = 1.33$ LMH $S = 650 \pm 70$ μm	PI; Casting thickness = 100 μm	2 M NaCl (10 mM NaCl)	800 mL·min <sup>-1</sup>	20.8	8.8	(Amini, Rahimpour & Jahanshahi 2016)
TiO <sub>2</sub> (n/a)	PSf (MPD, TMC)	0.05 wt/v% in TMC/n-hexane solution	n/a	n/a	2 M NaCl (10 mM NaCl)	300 mL·min <sup>-1</sup>	26.0	4.98	(Emadzadeh et al. 2016)
PVP modified GO (T: 0.55-1.2 nm)	PSf (MPD, TMC)	0.0175 wt% in MPD solution	-	PI; Casting thickness = 175 μm	2 M NaCl (10 mM NaCl)	333 mL·min <sup>-1</sup>	14.6	14.6	(Wu et al. 2017)
Polyrhodanine (50 nm)	PES (MPD, TMC)	0.01 wt/v% in TMC/n-hexane solution	$A = 1.60$ LMH.bar <sup>-1</sup> $B = 0.22$ LMH $S = 128$ μm	PI; Casting/overall thickness = n/a	1.5 M NaCl (DI water)	20 cm·s <sup>-1</sup>	41.0	6.7	(Rahimpour et al. 2018)
Fe <sub>3</sub> O <sub>4</sub> /ZnO (n/a)	PSf, 0.2 wt% Fe <sub>3</sub> O <sub>4</sub> /ZnO (MPD, TMC)	0.02 wt/v% in MPD solution	$A = 2.97$ LMH.bar <sup>-1</sup> $B = 0.28$ LMH $S = 400$ μm	PI; Casting/overall thickness = 100/131 μm	2 M NaCl (10 mM NaCl)	721 cm·s <sup>-1</sup>	29.3	5.6	(Ramezani Darabi, Jahanshahi & Peyravi 2018)
GO (Flake size: 57.3 nm)	PSf (MPD, TMC)	0.1 wt% in MPD, TEA and SDS solution	$A = 2.35$ LMH.bar <sup>-1</sup> $B = 0.67$ LMH $S = 570$ μm	PI; Casting thickness = 100 μm	1 M NaCl (DI water)	25 L·min <sup>-1</sup>	14.5	2.6	(Eslah et al. 2018)
GO/Fe <sub>3</sub> O <sub>4</sub> nanohybrid (n/a)	PES (MPD, TMC)	0.02 wt/v% in MPD solution	$A = 2.51$ LMH.bar <sup>-1</sup> $B = 0.27$ LMH	PI; Casting/overall thickness = 80/65 μm	1 M NaCl (DI water)	8 cm·s <sup>-1</sup>	27.5	3.0	(Rastgar et al. 2018)
Fullerenol (D: ~1 nm)	PSf (MPD, TMC)	0.04 wt/v% in MPD solution	$A = 3.87$ LMH.bar <sup>-1</sup> $B = 0.59$ LMH	PI; Casting/overall thickness = n/a	1 M NaCl (DI water)	6.4 cm·s <sup>-1</sup>	26.1	4.7	(Perera et al. 2018)
Graphitic carbon nitride (g-C <sub>3</sub> N <sub>4</sub> ) (n/a)	PSf, 0.5 wt% HNTs (MPD, TMC)	0.05 wt/v% in MPD solution	$A = 2.17$ LMH.bar <sup>-1</sup> $B = 0.38$ LMH $S = 370$ μm	PI; Casting thickness = 140 μm	2 M NaCl (DI water)	21.4 cm·s <sup>-1</sup>	18.9	2.74	(Rezaei-DashtArzhandi et al. 2018)
GQDs (3.4-8.8 nm)	PES (MPD, TMC)	0.1 wt% in MPD, TEA and CSA solution	$A = 3.35$ LMH.bar <sup>-1</sup> $B = 0.26$ LMH $S = 189$ μm	PI; Casting/overall thickness = n/a	1 M NaCl (DI water)	8.5 cm·s <sup>-1</sup>	28	5.84	(Seyedpour et al. 2018)
C60@PAF900 (n/a)	PSf (MPD, TMC)	0.015 wt/v% in TMC/n-hexane solution	$A = 3.19$ LMH.bar <sup>-1</sup> $B = 0.66$ LMH	PI; Casting thickness = 175 μm	2 M NaCl (10 mM NaCl)	n/a	12.4	10.4	(Wu et al. 2018)
GO (Lateral area: 0.01 μm <sup>2</sup> , T: ~1 nm)	PSf (MPD, TMC)	0.01 wt% in MPD solution	$A = 3.71$ LMH.bar <sup>-1</sup> $B = 0.89$ LMH	PI; Casting thickness = 120 μm	0.5 M NaCl (DI water)	12.6 cm·s <sup>-1</sup>	24.7	5.19	(Akther, Yuan, et al. 2020)
GO (Lateral area: 0.65 μm <sup>2</sup> )	PES (MPD, TMC)	0.0005 wt% in MPD solution	$A = 5.79$ LMH.bar <sup>-1</sup> $B = 0.81$ LMH	HF, PI; Overall thickness = 66 μm	1 M NaCl (DI water)	FS = 39.0 cm·s <sup>-1</sup> DS = 0.16 cm·s <sup>-1</sup>	31.5	5.67	(Lim, Park, et al. 2020a)
GO/aquaporin (GO lateral size: <10 μm <sup>2</sup> )	PSf (MPD, TMC)	0.005 wt% GO and 0.2 wt% aquaporin in MPD solution	$A = 2.78$ LMH.bar <sup>-1</sup> $B = 1.21$ LMH	PI; Casting thickness = 120 μm	0.5 M NaCl (DI water)	12.6 cm·s <sup>-1</sup>	24.1	8.92	(Akther, Sanahuja-Embuen, et al. 2021)
GQDs (<5 nm)	PES (MPD, TMC)	0.0005 wt% in MPD solution	$A = 2.24$ LMH.bar <sup>-1</sup> $B = 0.30$ LMH	HF, PI; Overall thickness = 66 μm	1 M NaCl (DI water)	FS = 39.0 cm·s <sup>-1</sup> DS = 0.16 cm·s <sup>-1</sup>	30.9	3.71	(Akther, Kawabata, et al. 2021)

A: water permeability coefficient; B: solute permeability coefficient; C60@PAF900: fullerene impregnated porous aromatic framework; CFV: cross-flow velocity; CNT: carbon nanotube; CSA: camphorsulfonic acid; DS: draw solution; Fe<sub>3</sub>O<sub>4</sub>: iron (III) oxide, FS: feed solution; GO: graphene oxide; GQDs: graphene quantum dots; Js: solute flux; Jw: water flux; MPD: m-phenylenediamine; PAN: polyacrylonitrile; PES: poly(ethersulfone); PI: phase inversion; PSf: polysulfone; S: structural parameter; SDS: sodium dodecyl sulfate; SiO<sub>2</sub>: silica; TEA: triethylamine; TiO<sub>2</sub>: titanium oxide; TMC: trimesoyl chloride



### 2.2.1 Zeolites and silica

Zeolites are microporous aluminosilicate materials with a porous crystalline structure that act as molecular sieves. The uniform and well-defined pore system of zeolites can be customized to facilitate the size or shape selective separation of molecules. Additionally, zeolites are both chemically and thermally stable; hence, zeolites have been utilized extensively for membrane development in applications like pervaporation, membrane reactors, reverse osmosis and gas separation (McLeary, Jansen & Kapteijn 2006).

Motivated by the zeolite-incorporated TFN RO membrane, Tang's group was the first to develop TFN membrane for FO application by loading zeolite NaY nanoparticles in the range of 0.02-0.4 wt/v% into TMC/n-hexane organic solution (Ma et al. 2012). The membrane water flux improved with increasing zeolite loading between 0.02 to 0.1 wt/v% but decreased when zeolite loading exceeded 0.1 wt/v%. The membrane, with a zeolite loading of 0.1 wt/v% (TFN0.1), was found to be optimal. TFN0.1 exhibited a water flux of around 15 LMH (32 LMH) in AL-FS (AL-DS) orientation; whereas, a water flux of about 10 LMH (22 LMH) was obtained using TFC membrane when 1 M and 10 mM NaCl were used as the draw and feed solution, respectively. The authors attributed the improvement in membrane water permeability within the range of 0.02–0.1 wt/v% zeolite loading to the porous structure of the zeolite. However, increasing the zeolite loading beyond 0.1 wt/v% resulted in thicker PA layer formation causing the water permeability to decrease. Nonetheless, the authors did not comment on the homogeneity of zeolite dispersion within the PA layer, which may impact FO performance.

Similar to zeolites, silica incorporated membranes have been applied in many areas like gas separation, RO, NF and FO owing to its distinctive properties like high specific surface area, good surface hydrophilicity from the presence of silicon hydroxyl groups, and uniform nanostructures that can be controlled for size selectivity (Kresge et al. 1992).

In addition, silica particles have a spherical morphology, allowing them to disperse more effectively than zeolites. Niksefat et al. (Niksefat, Jahanshahi & Rahimpour 2014) explored the influence of silica nanoparticles on the characteristics and FO performance of TFN membranes. It was reported that increasing silica concentration (0.01, 0.05 and 0.1 wt/v%) in MPD solution also increased the membrane surface roughness, hydrophilicity and water permeability. The membrane with 0.05 wt/v% silica in MPD solution showed the highest NaCl rejection (89%) with a higher water flux (15 LMH) than that of the unmodified membrane (72% and 10.3 LMH) in AL-FS orientation. The improvement in salt rejection at higher silica loadings was associated with the pore blockage of membranes by silica nanoparticles, which is supposed to reduce the water flux. On the contrary, the integration of silica in PA active layer unexpectedly enhanced water flux. Additionally, the authors attributed the decrease in NaCl rejection (increase in salt flux) observed at the highest silica loading of 0.1% wt/v% (TFN0.1) to the formation of a defective PA layer. A defective selective layer is supposed to increase the salt flux across the membrane, as suggested by the authors. However, the FO test results showed that the TFN0.1 demonstrated the lowest salt flux than other TFN membranes, which contradicts the results obtained for NaCl rejection in the RO test.

### **2.2.2 Carbon nanotubes and graphene oxide**

CNT-modified membranes have been researched extensively for desalination and water purification due to their low biofouling potential, good chlorine resistance, self-cleaning properties, superior separation and mechanical properties (Das, Abd Hamid, et al. 2014; Goh et al. 2016; Goh, Ismail & Ng 2013; Mattia, Lee & Calabrò 2014). The hollow tubular structures of CNTs act as pores in membranes and facilitates frictionless transport of water molecules to produce high water flux (Das, Ali, et al. 2014). Besides, the specific pore diameter of CNTs improves the membrane selectivity by rejecting salt ions and

permitting the transport of water molecules (Corry 2008). Owing to the hydrophobicity of CNTs and their inadequate dispersibility in organic/aqueous monomer solution or polymer matrix, it is required to functionalize CNTs with carboxylic or amine functional groups by treating them with acids or amines. The dispersion of CNTs in polymer dope or monomer solutions for IP reaction can be extensively influenced by the functionalization reaction conditions of CNTs like acid concentration, reaction temperature and time (Kim et al. 2014).

Rahimpour and co-workers amine-functionalized multi-walled carbon nanotubes (f-MWCNTs) using 1,3-phenylenediamine (mPDA) to augment the hydrophilicity of PA TFC membranes (Amini, Jahanshahi & Rahimpour 2013a; Rahimpour et al. 2012). The CNTs were first carboxylated by treating in a H<sub>2</sub>SO<sub>4</sub>: HNO<sub>3</sub> mixed acid solution with a volume ratio of 3:1 at 90°C for 1 h. The carboxylated CNTs were then added to mPDA dissolved in dimethylformamide at 70°C for 96 h. The most permeable membrane, with a loading of 0.1 wt% f-MWCNTs (TFN0.1) in MPD aqueous solution, achieved a water flux of 95.7 LMH in AL-DS orientation, which is roughly 160% more than that of TFC membrane (Amini, Jahanshahi & Rahimpour 2013a). The NaCl rejection for TFN0.1 and the control membrane was observed to be similar (70-73%) and was evaluated using a cross-flow RO setup with 20 mM NaCl feed and a pressure of 2.4 bar. The authors deduced that the enhanced water flux in TFN membranes could have resulted from the capillary force within the f-MWCNTs nanochannels or the formation of external nanochannels (voids) between the polymer and f-MWCNTs at the PA layer interface. The increased surface hydrophilicity of TFN membranes could have also increased the water permeation through the membrane. The TFN membranes exhibited a lower solute flux than that of the control membrane; however, the authors did not discuss the possible reasons that enhanced membrane selectivity. Kim et al. later reported that the decline in

solute flux might be ascribed to the formation of narrower nanochannels due to PA partially covering CNTs, which hindered the transport of hydrated solute ions (Kim et al. 2014).

Wang and his group were the first to prepare double-skinned TFN membranes using unmodified CNTs (Song et al. 2015). They also explored the impact on membrane performance and characteristics by changing the location of CNTs inside the membrane (Song, Wang, et al. 2016). In both studies, the membranes were prepared via IP of polydopamine (pDA)/CNTs and TMC on PSf substrates; and the contact angles of TFC and TFN membranes at all conditions were observed to be similar ( $67.0^{\circ}$ - $67.5^{\circ}$ ). This is because the unmodified CNTs did not improve membrane hydrophilicity, unlike the amine-functionalized CNTs prepared by Rahimpour's group ( $47.4^{\circ}$  with 0.05 wt% CNTs in the PA layer) (Amini, Jahanshahi & Rahimpour 2013a). The double-skinned membranes, both TFC and TFN, exhibited outstanding solute rejection compared to single-skinned membranes without sacrificing water flux. The antifouling capacity of the double-skinned membranes to humic acid (HA) was much higher than that of single-skinned membranes. The TFN double-skinned membrane with 0.05 wt% CNTs (TFN0.05) had the highest antifouling capacity because CNTs in the active layer weakened the adhesion between CNTs and HA. The normalized flux recovery for double-skinned TFN0.05 was 81.4% after the third cycle of fouling and cleaning process, which was much higher than the double-skinned TFC membrane (60.8%). Moreover, water flux through the TFN0.05 double-skinned membrane was 54% higher than the control double-skinned membrane in AL-FS orientation. In addition, incorporation of CNTs into both the PA active layer and substrate of single-skinned TFC membrane (nTFN) improved membrane porosity, which led to a reduction in the structural parameter. Similar to the double-skinned TFN membranes, nTFN membranes demonstrated enhanced antifouling

property to HA. The normalized flux recovery for the nTFN membrane was 87.8% after the third cycle of fouling and cleaning, compared to 70.7% flux recovery achieved by the TFC membrane. Although the nTFN membranes demonstrated higher water flux, the CNT-polymer incompatibility resulted in poor salt rejection due to the formation of macrovoids within the polymer matrix.

GO is a chemical derivative of graphene with abundant surface functional groups and a high area-to-thickness ratio (Chen et al. 2009). GO is amphiphilic and can improve water flux by creating water channels between the GO interlayers, where water molecules are initially adsorbed by the hydrophilic hydroxyl groups and then diffused rapidly between the hydrophobic carbon core (Hung et al. 2014). The hydrophilic nature of GO promotes better GO dispersion in water and assists in developing nano-sized laminates involving GO layers in forming a mesh-like structure (Hegab & Zou 2015b), which is beneficial for water filtration membranes. GO has been studied only recently to prepare high-performance polymeric membranes for water treatment applications (Chong, Wang & Li 2016; Hegab & Zou 2015b; Hu & Mi 2014; Mahmoud et al. 2015). GO-modified membranes were reported to have better water permeability, salt rejection, mechanical strength, chlorine resistance, surface charge and antimicrobial properties than pristine membranes in various applications like UF, RO and FO (Ganesh, Isloor & Ismail 2013; Kim et al. 2013; Lim, Park, et al. 2020a; Yu et al. 2013; Zhang, Xu, et al. 2013; Zhao, Wu, et al. 2013). GO membranes have also been studied for solvent pervaporation and NF as the membranes are chemically inert (Salehian & Chung 2017; Wang et al. 2014; Wang et al. 2012; Yuan et al. 2017). Several reviews have been published recently that discuss the application of GO-based membranes in various areas (Hegab & Zou 2015a; Huang, Ying & Peng 2014; Liu, Jin & Xu 2015).

The GO-incorporated PA TFN membrane not only demonstrated enhanced hydrophilicity and surface smoothness but also had a thinner PA layer compared to the control TFC membrane (Shen, Xiong & Wang 2016). As a result, water permeability increased upon GO incorporation in the PA layer. The optimal GO loading in the PA layer was reported to be about 400-600 ppm, beyond which the performance of TFN membranes aggravated due to GO agglomeration. The water flux achieved in AL-FS orientation with 600 ppm GO-incorporated TFN membrane was ~48% higher compared to that of the unmodified membrane with a comparable solute flux. The smooth, hydrophilic and negatively-charged surface of the GO-modified membrane was also able to efficiently suppress sodium alginate (SA) fouling by electrostatic repulsion and providing fewer adhesion sites on the membrane surface. The flux recovery ratio (FRR) value of TFC membranes was only ~60% after cleaning; whereas, the FRR value of all GO-modified membranes was higher than 90% (Shen, Xiong & Wang 2016).

GO was also chemically modified to improve its dispersibility in MPD aqueous solution and minimize its aggregation in the polymer matrix. Polyvinylpyrrolidone (PVP) coated GO (PVP-GO) was synthesized by Wu et al. as a nanofiller to prepare TFN membrane for desalination (Wu et al. 2017). It was found that PVP-GO had better dispersion than unmodified GO in MPD aqueous solution, which helped to reduce GO aggregation in the PA layer. Moreover, the membrane hydrophilicity, salt rejection and water flux of PVP-GO modified membranes were much higher than pristine TFC and unmodified-GO-incorporated TFN membranes. The optimal TFN membrane with a PVP-GO loading of 0.0175 wt% demonstrated a water flux of 33.2 LMH in AL-DS orientation, which is approximately 3.3 times greater than that of pristine TFC membrane when 10 mM and 2 M NaCl feed and draw solution, respectively.

### 2.2.3 Other carbon-based nanomaterials

Graphene quantum dots (GQDs), graphene oxide quantum dots or carbon quantum dots have been recently studied as biocidal agents in TFC FO membranes by Seyedpour et al. (Seyedpour et al. 2018). The oxygen-containing functional groups on the surfaces of GQDs allows them to demonstrate excellent water solubility and polymeric compatibility. The biocidal property of GQDs occurs from their electron transport property, which improves their peroxidase activity. Incorporation of 0.5 wt% GQD in the MPD solution during IP reaction not only improved the TFN FO membrane's anti-bacterial property (>90% and 95% inactivation for *E. coli* and *S. aureus*, respectively, during 1h incubation) but also enhanced FO performance by increasing membrane surface hydrophilicity. Additionally, the strong covalent bonding between the GQDs and PA layer ensured long-term membrane stability during the FO test. The authors attributed the exceptional anti-bacterial property of the GQD-modified TFC FO membrane to the uniform dispersion of GQDs that enabled more of their active edges to disrupt bacterial cells on the membrane surface via contact mechanism. Nonetheless, the contact mechanism for cell disruption is unlikely to be effective when GQDs are embedded in the polymer matrix, as suggested by Faria et al. (Faria et al. 2017). This is because most of the nanoparticles are washed off with the excess monomer solution during the IP process, and the remaining nanoparticles on the substrate surface get embedded in the PA layer. However, other studies reported that graphene derivatives could kill bacteria by contact mechanism even when embedded in the PA layer (Inurria et al. 2018; Perreault et al. 2016). Hence, the exact mechanism behind the antimicrobial property of graphene derivatives when embedded in a polymer matrix is still dubious and should be further investigated.

Fullerenols are carbon-containing spherical molecules ( $C_{60}(OH)_n$ ) with abundant hydroxyl groups, which have also been used to modify the PA layer to augment the

hydrophilicity and antifouling properties of the TFC FO membranes. Recently, Perera et al. developed fullereneol-modified TFC membrane, and a 400 ppm fullereneol loading (FTFC-4) demonstrated an 83% increase (26.1 LMH) and 78% decrease ( $0.18 \text{ g}\cdot\text{L}^{-1}$ ) in the water flux and specific reverse solute flux (*SRSF*), respectively, compared to those of the TFC membrane when tested in AL-FS orientation using DI water as feed solution against 1 M NaCl as draw solution (Perera et al. 2018). Although this study attributed the improvement in water flux of the fullereneol-modified TFC membranes to the increased membrane surface hydrophilicity, no in-depth explanation has been provided for their improved selectivity. Moreover, the authors stated that incorporation of fullereneol creates interfacial voids between the fullereneol and the PA matrix that facilitate quick transport of water molecules. In that case, the solute flux is also expected to increase at higher fullereneol loadings as interfacial voids are mostly non-selective and allow draw solutes to diffuse across the membrane easily. However, the salt flux was observed to decrease up to a fullereneol loading of 400 ppm. A change in surface charge of the nanocomposite membranes could have increased salt rejection, but no such data was provided by the authors for further validation. Besides good membrane performance, FTFC-4 demonstrated good antifouling propensity by acquiring a FRR value of 87.2%, which is significantly higher than the FRR value of the TFC membrane (53.4%). The hydrophilic surface of the fullereneol-modified TFC membrane created a hydration layer that hindered the progress of foulant adsorption on the membrane surface and created a loose cake layer that could be easily eradicated by physical cleaning (Perera et al. 2018).

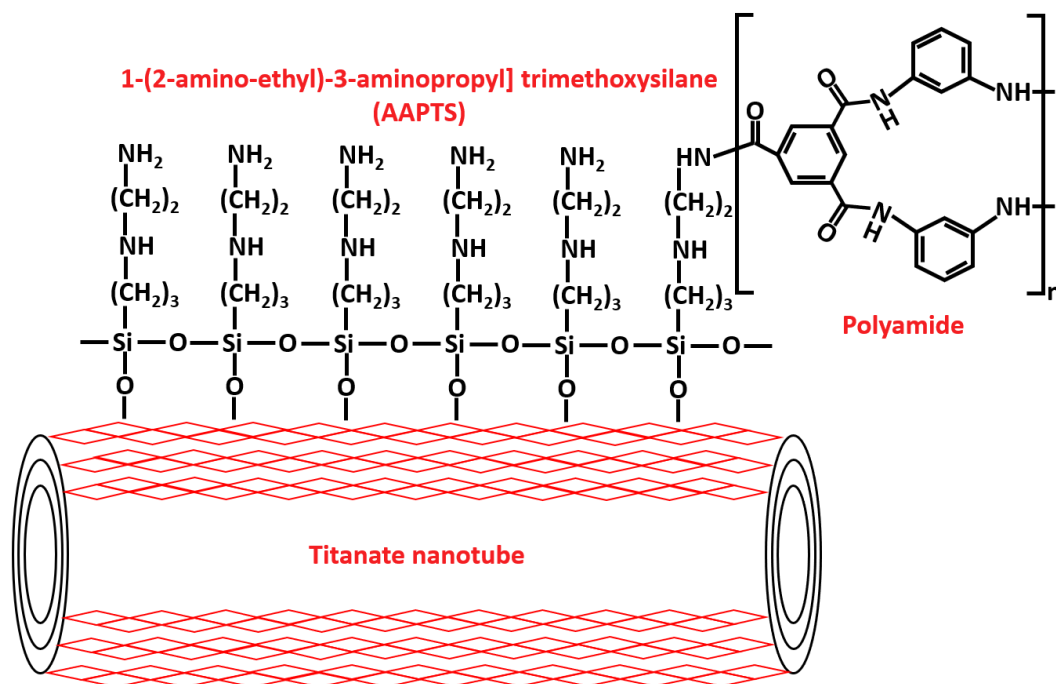
#### **2.2.4 Titanate and halloysite nanotubes**

Besides CNTs, titanate nanotubes (TNTs) and halloysite nanotubes (HNTs) have also been explored as nanofillers for fabricating TFN FO membranes because their tubular form provides additional channels for water transport across the membranes. Both TNTs



and HNTs have hydrophilic properties, good stability, and large pore volumes and specific surface area (Chen & Peng 2007; Wang et al. 2011). Although TNTs, HNTs and CNTs have similar tubular and hydrophilic characteristics, the production cost for HNTs and TNTs is significantly lower than that of CNTs (Ghanbari, Emadzadeh, Lau, Matsuura & Ismail 2015; Zhang et al. 2012).

To date, only a few scientific articles have been published on TNTs and HNTs-modified FO membranes; most of which have been produced by Ismail's group (Emadzadeh et al. 2015; Ghanbari, Emadzadeh, Lau, Lai, et al. 2015; Ghanbari, Emadzadeh, Lau, Matsuura, Davoody, et al. 2015; Ghanbari et al. 2016; Kumar et al. 2017). The first and only study exploring the possibility of self-synthesized amine-functionalized TNTs as nanofillers for TFN FO membrane was reported by Emadzadeh et al. in 2015 (Emadzadeh et al. 2015). The surface of calcinated hydrophilic TNTs was amine-functionalized using 1-(2-aminoethyl)-3-aminopropyl] trimethoxysilane (AAPTS) to prevent agglomeration OF TNTs in the PA active layer during the IP reaction. The amine-functionalized TNTs (f-TNTs) dispersed in the TMC/cyclohexane solution were covalently bonded to the PA layer by forming amide linkages during the IP reaction, as shown in **Fig. 2.4**. The f-TNT modified membranes had higher surface roughness and hydrophilicity compared to the control TFC membrane. As a result, the water flux of the TFN membrane with 0.05 wt% f-TNT loading was 2 times more than that of the control membrane in both membrane orientations. Additionally, the nanochannels of f-TNTs and voids between f-TNTs and PA matrix may have also contributed to the increased flux of the TFN membranes. The authors believe that f-TNTs assisted in a higher degree of PA cross-linking by facilitating quick MPD diffusion to the surface of hydrophilic f-TNTs. The high PA cross-linking degree in TFN membrane resulted in lower reverse solute flux for TFN membranes in both orientations than the control membrane.



**Fig. 2.4** Schematic illustration of the interaction between amine-functionalized titanate nanotube and polyamide (adapted from (Emadzadeh et al. 2015)).

Besides incorporating only one type of nanofiller in the PA layer, two or more nanofillers have occasionally been embedded in the TFN membrane to improve FO membrane performance. For instance, Ghanbari et al. investigated the effect of adding HNTs (Ghanbari, Emadzadeh, Lau, Lai, et al. 2015) and TiO<sub>2</sub>-coated HNTs (TiO<sub>2</sub>/HNT) (Ghanbari, Emadzadeh, Lau, Matsuura, Davoody, et al. 2015) in the PA layer on the performance and antifouling property of the membranes. The experimental results showed that compared to HNTs, the degree of TiO<sub>2</sub>/HNTs aggregation in the active layer was negligible due to their good compatibility with PA structure. Moreover, integration of TiO<sub>2</sub>/HNTs into the PA active layer enhanced membrane hydrophilicity, resulting in better separation performance than pristine TFC and HNTs-incorporated TFN membranes. The 0.05 wt% TiO<sub>2</sub>/HNT incorporated TFN membrane demonstrated a water and solute flux of 40.8 LMH and 7.3 gMH, respectively, with 2 M NaCl as draw solution and 10 mM NaCl as feed solution in AL-DS mode. Whereas, the TFN membrane with

0.05 wt% HNTs (TFC membrane) attained a water flux of 33.6 LMH (24 LMH) and a solute flux of 9.2 gMH (6.4 gMH ). The tubular structure of HNTs provided additional passages for water molecule transport across the membranes. The TiO<sub>2</sub>/HNTs nanoparticles also significantly enhanced the antifouling property of the TFN membranes to bovine serum albumin (BSA). The normalized flux of TFC membrane decreased to 0.71 after 10 hours of fouling test; while, the normalized flux decreased to ~0.88 and 0.85 for TiO<sub>2</sub>/HNTs and HNTs TFN membrane, respectively. The BSA fouling in TiO<sub>2</sub>/HNTs and HNTs-modified TFN membranes was almost entirely reversible with a water recovery of 100% and 96.5%, respectively, compared to a recovery of ~83% with TFC membrane. The improved hydrophilicity of the TFN membranes enhanced their antifouling property by weakening the interactions between the BSA foulant and PA layer.

### **2.2.5 Porous coordination polymers**

In recent years, porous coordination polymer (PCP), a new kind of nanomaterial, has been used to develop nanocomposite membranes for various applications like gas separation, liquid separation and catalysis (Car, Stropnik & Peinemann 2006; Ding et al. 2011; Kasik & Lin 2014; Li, Li, et al. 2019; Liu et al. 2011; Sorribas et al. 2013; Tiscornia et al. 2010). Metal-organic frameworks (MOFs) and covalent-organic frameworks (COFs) are two or three-dimensional PCPs, which have been used to improve the structure and performance of FO nanocomposite membranes (Akther, Lim, et al. 2019; Lee, She, et al. 2015; Ma, Peh, et al. 2017; Zirehpour et al. 2016; Zirehpour, Rahimpour & Ulbricht 2017). MOFs are porous inorganic/organic hybrid nanostructured material comprising of metal ions coordinated to organic ligands as linkers (Cui et al. 2012; Furukawa et al. 2013); whereas, COFs are organic nanoporous solids with extended structures of light elements

comprising functional groups that are linked by strong covalent bonds (Feng, Ding & Jiang 2012).

MOFs and COFs are promising for membrane application as their pore structure can be customized, and they have an exceptionally high surface area, porosity and thermal stability. Moreover, organic linkers in MOF and COF assembly improve their compatibility with the polymer matrix compared to inorganic nanofillers, which minimizes the development of non-selective cavities between the MOFs/COFs and the polymer matrix. The formation of covalent or non-covalent bonds between MOFs/COFs and polymer could attribute to their good compatibility in the polymer matrix, which can be beneficial for enhancing the properties of the PA layer without compromising on the membrane selectivity (Akther, Lim, et al. 2019; Li, Sculley & Zhou 2012; Lim, Akther, et al. 2020).

Ma et al. modified the PA layer using self-synthesized zirconium (IV) carboxylate MOFs (UiO-66) to produce highly selective TFN FO membranes (Ma, Peh, et al. 2017). The hydrophilicity and molecular-sieving effect of UiO-66 increased the water permeability of the TFN membrane by 52% (0.1 wt% UiO-66 loading) compared to the control TFC membrane. As a consequence of the hydrophilic nature of UiO-66, increasing its concentration in the organic phase also increased the PA layer thickness. Increasing the UiO-66 loading beyond 0.1 wt% formed a very thick PA layer, which decreased water flux by increasing the transport resistance of the water molecules in the active layer. The TFN membrane with 0.1 wt% UiO-66 loading showed a 40% (AL-DS) and 25% (AL-FS) increase in water flux than the control TFC membrane without significantly affecting the membrane selectivity.

Similarly, Zirehpour et al. found that dispersing MOFs, consisting of silver (I) and 1,3,5-benzene tricarboxylic acid (3HBTC), in the PA layer of FO membranes improved both the membrane hydrophilicity and transport properties without negatively altering the membrane selectivity for seawater desalination (Zirehpour, Rahimpour & Ulbricht 2017). With an optimal MOF loading of 0.04 wt/v%, the water flux of TFN0.04 increased by 27% compared to the TFC membrane without deteriorating membrane selectivity. However, the integrity of the PA layer was lost when MOF loading was increased beyond 0.04 wt/v%, which hampered membrane selectivity.

The first study investigating the effect of COF nanofillers, Schiff base network-1 (SNW-1), on the performance of PA TFN membrane for FO process was conducted by Akther et al. (Akther, Lim, et al. 2019). The hydrophilic SNW-1 nanoparticles reacted with the acyl chloride groups of TMC during the IP reaction to form strong tertiary amide bonds, which aided the stability of SNW-1 nanoparticles in the PA layer. The addition of SNW-1 nanoparticles formed a thinner PA layer by hindering the reaction between MPD and TMC during the IP reaction. The thin PA active layer reduced the transport resistance, and the porous SNW-1 structure provided extra channels for water molecule transport. As a result, the TFN membranes demonstrated higher water flux than the pristine TFC membrane. The optimal SNW-1 loading was found to be 0.005 wt% (TFN0.005), which increased the water flux by 29% from that of the control membrane when tested in AL-FS orientation with deionized water and 0.5 M NaCl as feed and draw solution, respectively.

### **2.2.6 Issues and challenges of nanomaterial-modified PA layers**

The selectivity of TFC membranes depends on the integrity of their dense PA layer, which will be affected by nanomaterial addition. Nanoparticle incorporation in the PA active layer mostly improves water permeability but at the expense of membrane selectivity.

The performance of TFN membranes that can overcome the trade-off relationship is only marginally better than those of pristine TFC membranes. Any further increase in nanoparticle loading can cause particle agglomeration and hinder the reaction between monomers during the IP process. As a result, a defective PA layer will form that will reduce membrane selectivity. Moreover, the effective nanoparticle loading in the PA layer is much lower than that in the monomer solution as most of the nanoparticles are washed out when extra monomer solutions are discarded during the IP process. Consequently, a significant quantity of nanomaterial is lost, making the commercial development of TFN membrane costly. One possible strategy to reduce nanomaterial loss during the fabrication process is to use a vacuum-assisted IP process (Lai et al. 2019; Sun & Chung 2013). Additionally, nanoparticles may be lost during FO operation if they are incompatible with the PA matrix. Therefore, fabrication techniques should be improved, and polymer-compatible nanoparticles should be developed to achieve cost-effective development of TFN membranes. This may include exploring new nanomaterials or modifying the existing commercially available nanomaterials through functionalization to enhance their stability within the PA matrix.

### **2.3 Nanomaterial-coated PA layer surfaces**

Surface modification is an attractive technique as it allows alteration of membrane performance without significantly changing the intrinsic structures of the membrane. The surface modification allows nanomaterials to be directly coated, grafted, assembled by a layer-by-layer (LbL) method or covalently bonded to the TFC membrane surface. Modification of membrane surface using nanoparticles is often adopted to improve membrane hydrophilicity, tune the charge density and surface roughness to reduce membrane fouling, impart biocidal properties, enhance chlorine resistance, and eliminate the trade-off between membrane selectivity and water permeability. For instance, Yang

et al. stacked GO nanosheets on membrane supports to enhance selectivity and antifouling property of the membranes (Yang, Alayande, et al. 2018; Yang, Ham, et al. 2018). **Table 2.3** presents the studies on surface-modified TFC FO membranes.

### **2.3.1 Carbon nanotubes and graphene oxide**

Tiraferrri et al. developed membranes with biocidal properties by covalently binding antimicrobial functionalized single-walled CNTs to the TFC membrane surface using amide bonds. Based on characterisation results, it was observed that the CNTs were firmly bonded to the surface of the membrane and provided a homogenous surface coverage. The modified membrane was able to inactivate up to 60% of the bacteria adhered to membrane surface within an hour of contact time; thus, indicating its potential to delay initiation of membrane fouling during the FO process (Tiraferrri, Vecitis & Elimelech 2011). The same research group also altered the surface chemistry of the TFC membrane using modified silica nanoparticles to achieve lower foulant-membrane adhesion for fouling mitigation. The surface of the silica nanoparticles was altered via super hydrophilic ligands coating that made the silica nanoparticles more stable and bind irreversibly to the carboxylic groups of the PA layer using the dip-coating technique. Although the surface chemistry of the TFC membrane changed due to nanoparticle coating, the morphology and salt/water permeability of the membrane remained the same as that of the pristine membrane. The uniform coating of nanoparticles on the membrane surface increased the surface hydrophilicity, which formed a tightly bound hydration layer on the membrane surface. The hydration layer acted as a barrier between the membrane and the organic foulants. The neutralization of membrane carboxyl groups also contributed to the membrane's antifouling property (Tiraferrri et al. 2012a, 2012b).

**Table 2.3** Summary of the fabrication conditions and FO performance of PA TFC membranes with nanomaterial-modified surfaces.

TFC membrane surface modification using nanomaterials		Modification method	Modification benefits	FO performance (AL-FS)				References
Nanomaterial or nanocomposite (Particle size)	Substrate (PA layer monomers)			DS (FS)	CFV	$J_w$ (LMH)	$J_s$ (gMH)	
<i>f</i> -SWNTs (n/a)	PSf (MPD, TMC)	EDC/NHS facilitated GO binding	Improved hydrophilicity, biofouling control	-	-	-	-	(Tiraferrri, Vecitis & Elimelech 2011)
Superhydrophilic ligand-coated SiO <sub>2</sub> nanoparticles (D: ~8 nm)	PSf (MPD, TMC)	Dip-coating	Reduced surface roughness, improved hydrophilicity, lower fouling propensity: hydration layer barrier	-	-	-	-	(Tiraferrri et al. 2012a, 2012b)
Ag-PEGylated dendrimer (n/a)	PES (MPD, TMC)	In situ synthesis of AgNPs via photolysis of AgNO <sub>3</sub> within the PEGylated dendrimer matrix	Antiadhesive and antibacterial properties, anti-protein fouling property	1 M NaCl (DI water)	3.3 cm <sup>2</sup> s <sup>-1</sup>	25.0	5.0	(Zhang, Qiu, et al. 2013)
GO/PLL (n/a)	PSf (MPD, TMC)	EDC/NHS facilitated GO/PLL grafting	Improved hydrophilicity and selectivity, anti-biofouling and biocidal property	2 M NaCl (DI water)	500 mL·min <sup>-1</sup>	11.0	15.0	(Hegab et al. 2015)
GO-Ag (n/a)	PSf (MPD, TMC)	In situ synthesis of AgNPs on GO surface by chemically reducing AgNO <sub>3</sub> . GO-Ag nanocomposites grafted onto the membrane surface via amide forming condensation reaction	Improved hydrophilicity, antibacterial properties	1 M NaCl (DI water)	200 mL·min <sup>-1</sup>	5.4	35.1	(Soroush et al. 2015)
BaSO <sub>4</sub> (n/a)	PSf (MPD, TMC)	Deposition of BaSO <sub>4</sub> via surface mineralization of TFC membrane with BaCl <sub>2</sub> and Na <sub>2</sub> SO <sub>4</sub> aqueous solutions using ASP technique	Improved surface hydrophilicity, better FO performance	1 M NaCl (DI water)	250 mL·min <sup>-1</sup>	10.7	3.99	(Jin et al. 2015)
GO (T: ~1.4 nm, A: 0.19 μm <sup>2</sup> )	PSf (MPD, TMC)	EDC/NHS facilitated GO binding	Improved hydrophilicity, antiadhesive and antimicrobial properties, biofouling resistance	-	-	-	-	(Perreault, Tousley & Elimelech 2014) (Perreault et al. 2016)
GO-pDA (T: 1.5-2.5 nm, Lateral size: 0.2-1 μm)	PSf (MPD, TMC)	Coating	Smoother membrane surface, improved hydrophilicity, biofouling resistance	2 M NaCl (DI water)	500 mL·min <sup>-1</sup>	13.0	8.75	(Hegab, ElMekawy, Barclay, et al. 2016)
Ag (n/a)	PSf (MPD, TMC)	In situ production of AgNPs on GO-modified membrane surface via wet chemical reduction of AgNO <sub>3</sub> by NaBH <sub>4</sub>	Improved antibacterial property, 98% bacterial inactivation with E. Coli	-	-	-	-	(Soroush et al. 2016)
AgCl (n/a)	PSf (MPD, TMC)	Deposition of AgCl via surface mineralization of TFC membrane with AgNO <sub>3</sub> and NaCl aqueous solutions using ASP technique	Improved surface hydrophilicity, Better FO performance, fouling resistance, better phenol removal efficiency	1 M NaCl (DI water)	315 mL·min <sup>-1</sup>	24.0	2.8	(Jin et al. 2017) (Huang et al. 2018)
Ag (28.1 nm)	PSf (MPD, TMC)	In situ synthesis of AgNPs on pDA-coated TFC membranes by incubation in AgNO <sub>3</sub> aqueous solution at room temperature for 2 h	Improved anti-adhesive and anti-bacterial property, 94% reduction in cell viability with P. Aeruginosa	-	-	-	-	(Qi, Hu, et al. 2018)
Zwitterion-Ag (n/a)	PES (MPD, TMC)	In situ formation of AgNPs via reduction of Ag <sup>+</sup> using 0.01M NaBH <sub>4</sub>	Antiadhesive and antibacterial properties, >96% antimicrobial efficiency with E. Coli	1 M NaCl (DI water)	8.5 cm <sup>2</sup> s <sup>-1</sup>	15.2	7.7	(Qiu & He 2018)
GO (Lateral size: <10 μm)	PSf (MPD, TMC)	Dip-coating	Reduced surface roughness, improved hydrophilicity, reduced SRSF, lower fouling propensity, biofouling control	1 M NaCl (DI water)	12.6 cm <sup>2</sup> s <sup>-1</sup>	24.7	5.2	(Akther, Ali, et al. 2020)
SiO <sub>2</sub> (n/a)	PSf (MPD, TMC)	In situ synthesis of SiO <sub>2</sub> NPs on TFC membranes using APTES as the silane coupling agent and TEOS as the silica precursor	Improved hydrophilicity, water layer barrier lower fouling propensity, higher water flux, higher FRR	1 M NaCl (DI water)	12 cm <sup>2</sup> s <sup>-1</sup>	25.9	6.9	(Akther, Lin, et al. 2020)

AgCl: silver chloride; AgNO<sub>3</sub>: silver nitrate; AgNP: silver nanoparticle; APTES: 3-aminopropyltriethoxysilane; ASP: alternate soaking process; BaCl: barium chloride; BaSO<sub>4</sub>: barium sulfate; CFV: cross-flow velocity; DS: draw solution; EDC: *n*-(3-Dimethylaminopropyl)-*n*'-ethylcarbodiimide hydrochloride; FRR: flux recovery ratio; FS: feed solution; *f*-SWNTs: functionalized single-walled carbon nanotubes; GO: graphene oxide;  $J_s$ : solute flux;  $J_w$ : water flux; MPD: *m*-phenylenediamine; NaBH<sub>4</sub>: sodium borohydride; NaCl: sodium chloride; Na<sub>2</sub>SO<sub>4</sub>: sodium sulfate; NHS: *n*-hydroxysuccinimide; NPs: nanoparticles; pDA: polydopamine; PEG: polyethylene glycol; PES: poly(ethersulfone); PLL: poly-L-lysine; PSf: polysulfone; SiO<sub>2</sub>: silica; TEOS: tetraethoxysilane; TMC: trimesoyl chloride



Surface coating of the membrane using biocidal GO nanosheets is often challenging. To overcome this issue, Hegab et al. utilized bioadhesive pDA to incorporate GO nanosheets on the TFC membrane surface. Deposition of pDA occurs via oxidative polymerization and self-assembly, both of which reduce and immobilize GO on the membrane surface. The best performing GO-pDA membrane was fabricated using a GO concentration of  $80 \mu\text{g}\cdot\text{mL}^{-1}$  and a pDA deposition time of 30 min. At the optimal GO loading, the GO nanosheets did not aggregate and bound firmly to the membrane surface. The optimal GO-pDA modified membrane demonstrated 21.5% and 80% higher water flux and selectivity, respectively, compared to the pristine membrane because of improved membrane hydrophilicity and morphology. Moreover, the modified membrane was able to significantly extend the biofouling onset because of its outstanding anti-bacterial properties (Hegab, ElMekawy, Barclay, et al. 2016).

Perreault et al. investigated the anti-biofouling property of GO by covalently bonding GO nanosheets on commercial TFC FO membranes using an amide coupling reaction. In addition to possessing improved antimicrobial property, the GO functionalized TFC membrane demonstrated enhanced surface hydrophilicity without significantly affecting its transport properties. During the treatment of synthetic secondary wastewater accompanied with *P. aeruginosa* cells, the GO functionalized membranes showed a flux decline of 20% after 24 h of operation due to biofouling; whereas, a 40% flux decline was observed with the unmodified membrane. The improved anti-bacterial property of the GO modified membrane can be ascribed to the reduction of microbial biomass build-up on the membrane surface owing to the biocidal property of GO nanosheets (Perreault et al. 2016).

Hegab et al. used two unique techniques, layer-by-layer (LbL) and hybrid (H) grafting, to covalently attach GO nanosheets on the PA TFC membrane surface through a poly L-

Lysine (PLL) intermediary. The GO nanosheets were firmly bound to the membrane surface and each other when hybrid grafting technique was used, which resulted in better membrane hydrophilicity, morphology, smoother surface and antibacterial property. The GO/PLL-H membrane demonstrated higher selectivity compared to the pristine and GO/PLL-LbL membranes due to the formation of a tight active layer. The GO/PLL-H and GO/PLL-LbL membranes reduced the bacteria by 99% and 48.5%, respectively, compared to the pristine membrane. GO nanosheets enhanced the anti-bacterial properties of the membranes by penetrating and damaging the bacterial cell membranes with their sharp edges. Additionally, when PLL bonded GO nanosheets pierced the bacterial cell membranes, they inhibited several cellular enzymatic systems that killed the bacteria and impeded bacterial growth. The reverse solute flux demonstrated by GO/PLL-LbL membrane was 78% higher than the pristine membrane because of substantial swelling that occurred as a result of the membrane coming in contact with high salt concentration and forming loose structures that increased both ICP and draw solute diffusion (Hegab et al. 2015).

Besides modifying membranes for use in water treatment processes, the surface of the PA layer was impregnated with nanomaterials for rejection or adsorption of trace pharmaceuticals (Huang et al. 2015a) and shale gas wastewater treatment (Qin et al. 2015). The modified TFC membrane demonstrated less fouling tendency and higher rejection capacity for pharmaceuticals than the pristine membrane. In shale gas water treatment, a membrane comprising of a GO-incorporated PES substrate and a salt-rejecting and oil-repelling hydrogel selective layer was used. The modified membrane exhibited excellent fouling resistance under several oil/water emulsions due to the robust underwater oleophobicity of the hydrogel selective layer. The structural parameter of the GO-incorporated support was 20% lower than the virgin membrane. The membrane also

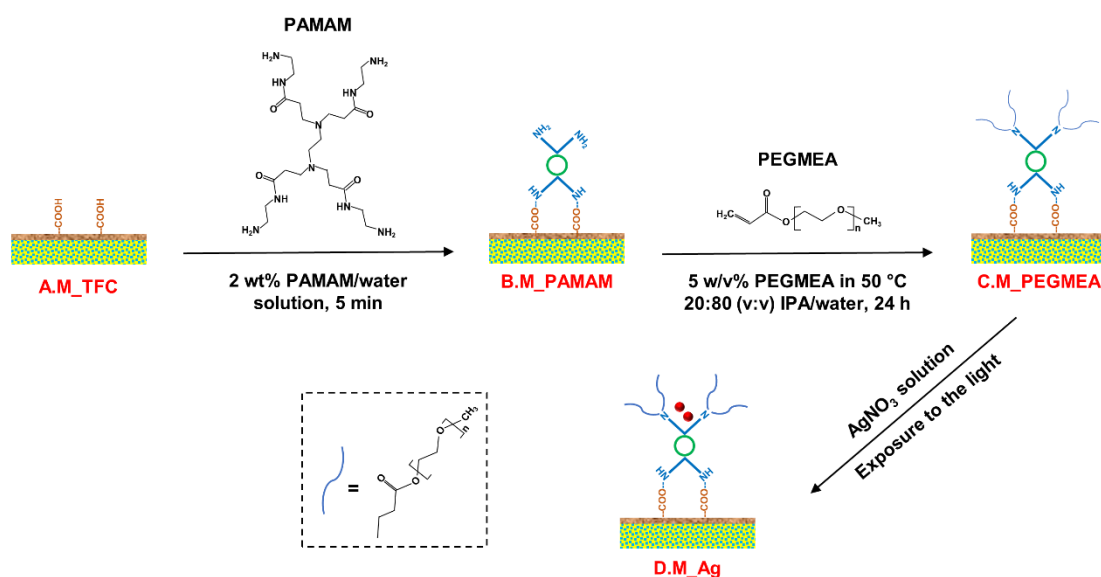
demonstrated 3 times higher water flux than the commercial FO membrane and removal percentage higher than 99.7% and 99.9% for multivalent ions and oil, respectively.

### **2.3.2 Silver nanoparticles and nanocomposites**

Chung and co-workers coated TFC membrane surface with silver–polyethylene glycol PEGylated dendrimer nanocomposite to diminish both protein and bacterial fouling during water treatment processes. They compared the antifouling property of four types of functional groups (carboxylic acid, amine, PEG or silver nanoparticles) that were imparted on the TFC membrane surface during the modification process (**Fig. 2.5**). All modified membranes obtained desired electrochemical characteristics and demonstrated enhanced hydrophilicity and antifouling property compared to the pristine membrane. However, the silver–PEGylated dendrimer modified membrane was the most effective in fouling mitigation and decreased fouling by 99.8%. The silver nanoparticle and PEG-modified membranes weakened the electrostatic interactions between the membrane surface and the foulants to lower the protein fouling propensity. Whereas, the solid electrostatic interactions between the amine-modified membranes and the proteins resulted in quick initial protein deposition on the membrane surface (Zhang, Qiu, et al. 2013).

Qiu and He developed a zwitterion-Ag nanocomposite to increase the biofouling resistance and water flux of the TFC FO membrane without significantly deteriorating the membrane selectivity (Qiu & He 2018). The nanocomposites were assembled on the membrane surface using a second IP of zwitterion followed by in situ preparation of silver nanoparticles (AgNPs). The carboxylic acid functional groups of zwitterions acted as binders to Ag ions and reduced them to AgNPs. The hydrophilic and functional surface of the modified membrane resulted in better water flux and selectivity compared to the unmodified TFC membrane. The zwitterion-Ag nanocomposite improved the membrane

biofouling resistance by improving the anti-adhesion and anti-bacterial property of the membranes. The modified membranes also demonstrated long-term biofouling resistance with an antimicrobial efficiency >96%. A flux decline of only 8% was observed with the modified membrane after 10 hours of fouling test; whereas, a 50% flux decline occurred with the unmodified membrane. Additionally, it was possible to regenerate the AgNPs on the membrane surface once used (Qiu & He 2018).



**Fig. 2.5** Illustration of the steps involved in the modification of PA TFC membrane surface with silver-PEGylated dendrimer nanocomposite structure (Zhang, Qiu, et al. 2013).

Silver nanoparticles (AgNPs) have also been studied as a biocidal agent by Soroush et al. where silver nitrate was reduced to AgNPs via wet chemical reduction on the surface of GO nanosheets to form silver-coated GO (GO/Ag) nanocomposites (Soroush et al. 2015). GO was chosen as a substrate to reduce the agglomeration of AgNPs. Moreover, GO offered a larger active surface area to AgNPs by dictating spherical morphology, which resulted in higher antimicrobial activity. The GO/Ag nanocomposites were bonded covalently to the surface of the PA layer via amide forming condensation reaction using cysteamine via dip-coating technique. Surface modification improved the hydrophilicity

of membranes and inactivated bacteria (*E. coli*) by more than 95% without significantly changing the membrane transport properties. The antibacterial property of the membranes modified with GO/Ag nanocomposites was much more effective than using GO (40%) or silver nanoparticles (60%) individually due to the synergistic capture-killing mechanism exhibited by the GO/Ag nanocomposites. GO/Ag nanocomposites inactivate bacteria by (1) penetrating silver ions into the bacterial cells, (2) capturing bacteria onto the GO surface, (3) and breaking the bacterial membrane through the sharp edges of GO nanosheets.

In addition to exploring the biocidal properties of GO/Ag nanocomposites, Soroush et al. modified commercial HTI TFC FO membranes via in situ development of AgNPs on both the control and GO-modified TFC membrane surfaces. The GO-incorporated membrane surface resulted in a more uniform AgNPs distribution and production of smaller sized AgNPs due to the presence of oxygen-containing functional groups on the GO surface. The functional groups on the GO surface also provided better anchoring to silver ions that facilitated improved stability, higher Ag loading and greater control on Ag ion release. In terms of biocidal properties, GO/Ag modified FO membranes demonstrated higher bacterial inactivation (98%) than the Ag-only modified (80%) or GO-only modified membranes (50%). Regeneration of AgNPs on the GO/Ag modified membrane surface after 7 days of Ag leaching resulted in the retrieval of 70% of the initial silver loading and almost complete restoration of its antibacterial properties (95%) (Soroush et al. 2016).

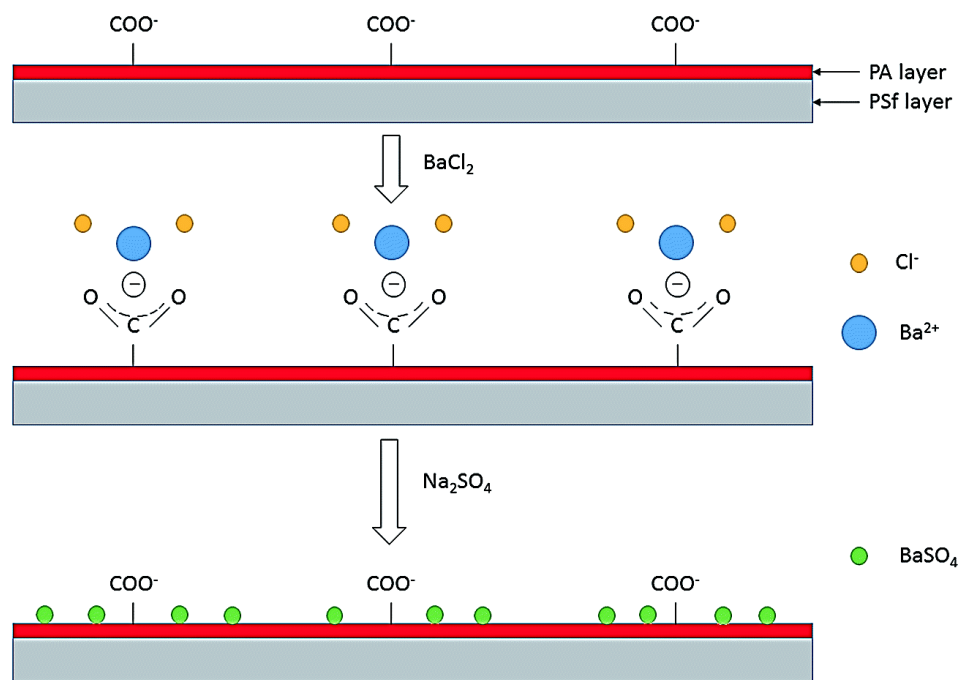
The antibacterial property of AgNPs was further investigated by combining pDA and AgNPs to simultaneously achieve both passive and active antibacterial properties (Qi, Hu, et al. 2018). Under static conditions, the pDA coating demonstrated both antibacterial and anti-adhesive properties by deactivating 30% *Pseudomonas aeruginosa* cells and decreasing the number of adhered cells by 85% compared to the control TFC

membrane. The pDA coating demonstrated good anti-adhesive property due to the hydration layer formation that helped to minimize the adsorption of foulants. The anti-bacterial property of pDA coating was ascribed to the protonation of pDA amine groups that assisted in bacteria lysis via contact with the bacterial cell walls. However, the pDA coating failed to prevent the growth of attached cells in dynamic conditions as the experimental conditions increased foulant interaction that covered the membrane surface entirely with biofilm. On the other hand, the AgNPs minimized microbial biomass and inhibited biofilm growth via inactivation of the attached bacterial cells. Moreover, the AgNPs on the TFC FO membrane surface showed good activity and stability during the 24 h cross-flow FO operation with a permeate flux decline of only 0.5%. Overall, the authors concluded that the hydrophilic pDA coating would be ineffective in mitigating biofilm growth and biofouling, but its anti-adhesion properties may facilitate easy biofilm removal using physical backwash (Qi, Hu, et al. 2018). Despite several studies proving the regeneration possibility of AgNPs on the membrane surface and its excellent biocidal property, the concern for AgNPs leaching and its effect on the environment cannot be overlooked. Moreover, in situ regeneration of AgNPs on membrane surface requires more chemicals, which is associated with additional costs and negative impacts on the environment.

### **2.3.3 Membrane surface mineralization**

Besides surface coating and covalent binding, Yu's group adopted a new technique called surface mineralization to chemically-modify membrane surface. Barium sulfate was deposited on PA TFC membrane surface using alternate soaking process (ASP), where the membrane was soaked separately into barium chloride and sodium sulfate aqueous solutions (**Fig. 2.6**). The number of ASP cycles was varied to prepare membranes with various degrees of mineralization. The characterisation results showed that the barium

sulfate particles were dispersed uniformly on the membrane surface. The mineral coating did not increase the TFC membrane active layer thickness, but it made the membrane surface smoother and denser. Increasing the mineralization degree made the membrane more negatively charged and hydrophilic. The salt rejection and water flux of mineralized TFC membrane were found to be better than those of the unmodified TFC membrane and commercial CTA FO membrane. The FO water flux of mineralized membrane improved with an increasing number of ASP cycles because the enhanced surface hydrophilicity at higher mineralization degree counterweighed the decrease in water permeability caused by the additional barium sulfate coating layer. Increasing the number of ASP cycles also decreased the reverse solute flux as the membrane surface acquired more negative charge, which increased the repulsion force between the membrane surface and anions (chloride ions) in the draw solution; thus, hindering the permeation of anions across the mineralized membrane (Jin et al. 2015).



**Fig. 2.6** Key steps involved in a single cycle of the alternate soaking process (ASP) for the deposition and coating of barium sulfate on the PA TFC membrane surface (Jin et al. 2015).

Yu and co-workers also deposited silver chloride on PA TFC membrane surface by separately soaking the membrane in 0.1 M sodium chloride and 0.1 M silver nitrate aqueous solutions using the ASP technique (Jin et al. 2017). The membrane fabricated with four ASP cycles (M4) was found to be optimal with a 67.8% higher water flux and 64.5% lower reverse solute flux than the control TFC membrane. The water flux decreased for membranes beyond four ASP cycles (M5 and M6) due to the increased resistance from the large quantity of deposited silver chloride coating. However, all the mineralized membranes demonstrated a higher water flux and lower reverse solute flux than the pristine membrane due to the negatively-charged surface of the mineralized membrane that repelled chloride ions. Additionally, the enhanced surface hydrophilicity of mineralized membranes contributed to lower solute flux by preferentially allowing water molecules to diffuse through the membrane instead of salt ions. The negative surface charge, reduced surface roughness and improved hydrophilicity of the mineralized membranes enhanced their water flux recovery and fouling resistance to BSA (Jin et al. 2017). Due to the high selectivity and improved fouling resistance, the optimal mineralized membrane with 4 ASP cycles was used for separating phenol from water using the FO process. FO performance tests showed higher flux and phenol rejection with mineralized membranes compared to TFC membranes. Moreover, increasing both the feed solution pH and draw solution concentration resulted in better phenol rejection. Maximum phenol rejection of 98.8% was achieved when the feed solution pH was changed to 11. This is because of the electrostatic repulsion existing between the membrane surface and phenolate ion when the feed solution pH is maintained above 9.96, which is the  $pK_a$  of phenol. In addition, the phenol adsorption behaviour on the membrane surface was found to be significantly influenced by operating parameters and the reverse salt flux, electrostatic interaction and solute hydrophobic character. It was observed from



the fouling tests that the phenol fouling for the mineralized membrane was reversible (90% flux recovery of the initial flux) and could be simply eliminated using physical cleaning (Huang et al. 2018).

Although several studies have considered surface modification of PA TFC membranes, none of them reported the effect of long-term FO operation and nanomaterials leaching on the FO performance. Therefore, investigating the stability of nanomaterials in water and the PA layer is essential to retain a stable FO performance for an extended period. In general, the continuing research on surface modifications of the membrane using nanoparticles can develop high-performance PA TFC FO membranes with good antifouling properties and chlorine resistance.

#### **2.3.4 Issues and challenges of nanomaterial-coated PA layer surfaces**

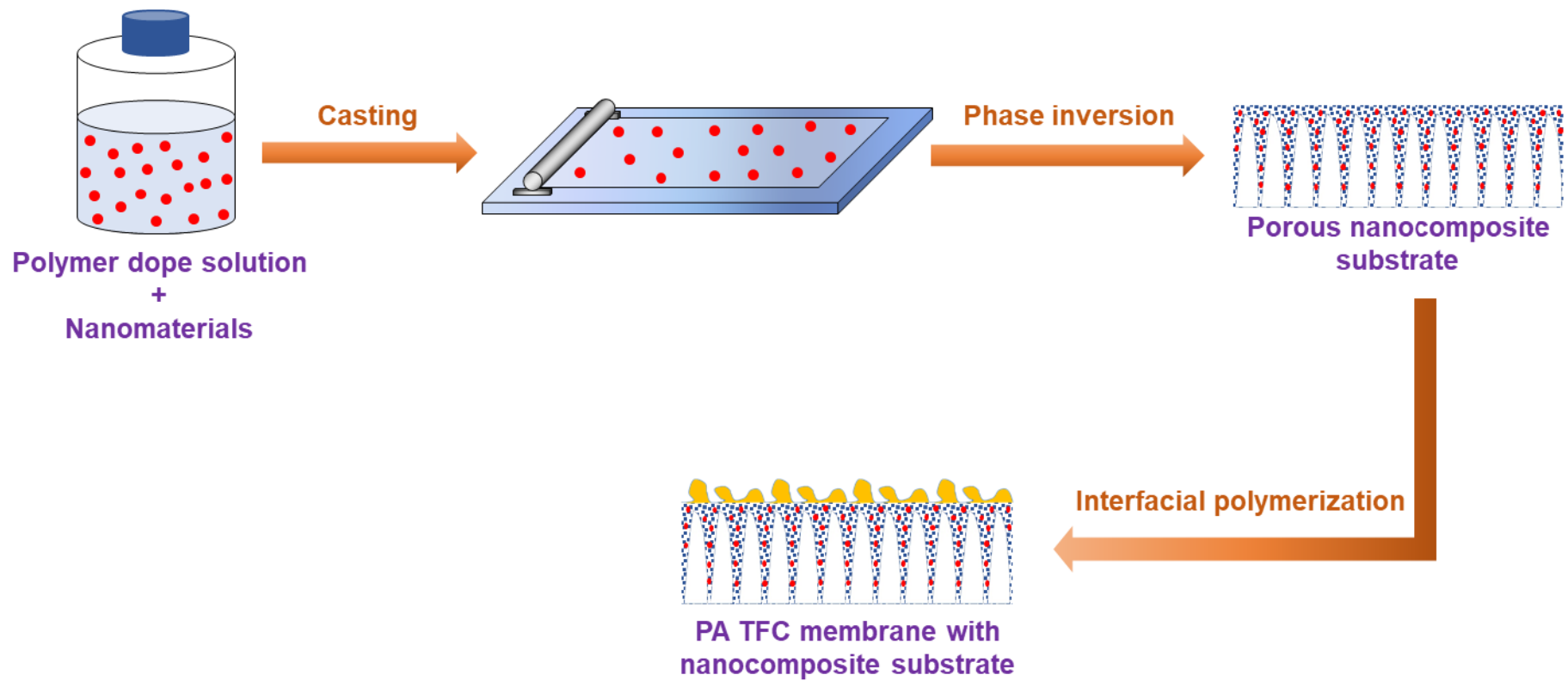
Surface modifications with nanomaterials have proven to be successful in imparting chemical functionality and improving the fouling and chlorine resistance of the membranes (Lu et al. 2017). However, nanoparticle deposition on membrane surface increases mass transfer resistance and may block pores on the selective layer, which ultimately increases CP and reduces water flux. Therefore, coating layers should be ultrathin to reduce water transport resistance. Advanced surface modification techniques like layer-by-layer (LbL) assembly and chemical vapour deposition (CVD) can be employed as they provide control over coating layer thickness at the nanoscale level. Moreover, the coating layers prepared by the LbL and CVD methods are thinner and more stable than those developed using other techniques (Zaidi, Mauritz & Hassan 2018).

Nanomaterial detachment from the membrane surface is another major issue that occurs with the implementation of physical surface coating methods. Nanomaterial loss will not only reduce membrane functionality but will also cause secondary environmental

pollution. For instance, *in situ* formation of silver nanoparticles allows the release of silver ions, which are toxic to bacterial and human cells (Soroush et al. 2016). Hence, good mechanical and chemical stability of coating layers is imperative for long term operations, which may be achieved by chemical grafting. Future studies on surface modifications should validate long-term efficiency and stability of the coating layer on the membrane surface under practical conditions.

## **2.4 Nanomaterial-modified substrates**

A desired PA TFC membrane is anticipated to have not only a dense active layer with high selectivity and water permeability but also a hydrophilic substrate/support with a low structural parameter to minimize ICP and allow a high mass transfer. One possible strategy to achieve high-performance membrane substrates with good mechanical strength, chemical stability and antifouling resistance is to blend nanomaterials in the polymer dope solution. Until now, HF and flat-sheet substrates for PA TFC FO membranes have been produced mostly by phase inversion method as illustrated in **Fig. 2.7**, and most recently by electrospinning (nanofiber mat). **Table 2.4** and **Table 2.5** summarise the studies on nanomaterial-incorporated TFC FO membrane substrates along with their FO performance.



**Fig. 2.7** Typical steps involved in the preparation of a PA TFC membrane with the nanomaterial-incorporated substrate.

**Table 2.4** Summary of the fabrication conditions and FO performance of PA TFC membranes with porous nanomaterial-incorporated substrates.

TFC membrane with nanocomposite substrate		Optimal particle loading	Intrinsic properties	Substrate fabrication method & conditions	FO performance (AL-FS)				References
Filler embedded in substrate (Particle size)	Substrate (PA layer monomers)				DS (FS)	CFV	$J_w$ (LMH)	$J_s$ (gMH)	
Zeolite: NaY (40-150 nm)	PSf (MPD, TMC)	0.5 wt% in dope solution	$A = 3.3 \text{ LMH}\cdot\text{bar}^{-1}$ $R = 91.0\%$ $S = 340 \mu\text{m}$	PI; Casting/overall thickness = 150/66.3 $\mu\text{m}$	2 M NaCl (10 mM NaCl)	500 $\text{mL}\cdot\text{min}^{-1}$	40.0	29.1	(Ma, Wei, et al. 2013)
Carboxylated CNTs (OD: 10-20 nm, L: 1-5 $\mu\text{m}$ )	PES (MPD, TMC)	2 wt% in dope solution	$A = 2.3 \text{ LMH}\cdot\text{bar}^{-1}$ $B = 0.08 \text{ LMH}$ $S = 2042 \mu\text{m}$	PI; Overall thickness = 90.1 $\mu\text{m}$	2 M glucose (10 mM NaCl)	2.0 $\text{cm}\cdot\text{s}^{-1}$	12.0	-	(Wang et al. 2013b)
Acid functionalized CNTs (D: ~11 nm, L: ~10 $\mu\text{m}$ )	PEI (MPD, TMC)	0.3 wt% (weight ratio to PEI) in dope solution	$A = 2.5 \text{ LMH}\cdot\text{bar}^{-1}$ $B = 0.7 \text{ LMH}$ $S = 310 \mu\text{m}$	Electrospinning; Flow rate = 30 $\mu\text{L}/\text{min}$ , Voltage = 30 kV, Working distance = 12 cm, Humidity = 60%	1 M NaCl (DI water)	9.0 $\text{cm}\cdot\text{s}^{-1}$	33.0	3.7	(Tian, Wang & Wang 2015)
Acid functionalized CNT/TiO <sub>2</sub> composites (OD: 9.5 nm, L: 1.5 $\mu\text{m}$ )	PSf (MPD, TMC)	0.5 wt% in dope solution	-	PI; Spin-coating at 3000 rpm for 1 s	1 M NaCl (DI water)	0.09 $\text{cm}\cdot\text{s}^{-1}$	12.7	5.8	(Morales-Torres et al. 2016)
CNTs (D: 20 nm, L: 0.5-2 $\mu\text{m}$ )	PSf (2 $\text{mg}\cdot\text{mL}^{-1}$ DA Tris buffer solution, MPD, TMC)	0.15 wt% in dope solution	$A = 6.5 \text{ LMH}\cdot\text{bar}^{-1}$ $B = 7 \text{ LMH}$ $S = 1669 \mu\text{m}$	PI; Casting thickness = 80 $\mu\text{m}$	2 M MgCl <sub>2</sub> (DI water)	7.8 $\text{cm}\cdot\text{s}^{-1}$	14.5	6.6	(Song, Wang, et al. 2016)
HNT (ID: 5-15 nm)	PVDF (MPD, TMC)	0.5 wt% in dope solution	$A = 2.02 \text{ LMH}\cdot\text{bar}^{-1}$ $B = 0.33 \text{ LMH}$ $S = 370 \mu\text{m}$	PI; Casting/overall thickness = 150/70-90 $\mu\text{m}$	2 M NaCl (10 mM NaCl)	350 $\text{mL}\cdot\text{min}^{-1}$	27.7	14.6	(Ghanbari et al. 2016)
Acid functionalized CNTs (n/a)	PES (MPD, TMC)	0.5 wt% in dope solution	$A = 1.8 \text{ LMH}\cdot\text{bar}^{-1}$ $B = 1.89 \text{ LMH}$ $S = 387 \mu\text{m}$	PI; Casting thickness = 100 $\mu\text{m}$	0.6 M NaCl (DI water)	FS: 200 $\text{mL}\cdot\text{min}^{-1}$ DS: 400 $\text{mL}\cdot\text{min}^{-1}$	11.98	7.7	(Choi, Son & Choi 2017)
INTs (OD: 2 nm, ID: 1 nm, L: 100 -200 nm)	PSf (MPD, TMC)	0.66 wt% (weight ratio to PSf) in dope solution	$A = 3.0 \text{ LMH}\cdot\text{bar}^{-1}$ $B = 2.9 \text{ LMH}$ $S = 2090 \mu\text{m}$	PI; Casting/overall thickness = 100/64.2 $\mu\text{m}$	1 M NaCl (DI water)	333.3 $\text{mL}\cdot\text{min}^{-1}$	7.5	11.6	(Pan et al. 2017)
MOF: UiO-66 (507 nm)	PSf (MPD, TMC)	6.5 wt% (weight ratio to PSf) in dope solution	$A = 3.31 \text{ LMH}\cdot\text{bar}^{-1}$ $B = 0.53 \text{ LMH}$ $S = 351 \mu\text{m}$	PI; Casting/overall thickness = 150/61 $\mu\text{m}$	1 M NaCl (DI water)	1.1 $\text{cm}\cdot\text{s}^{-1}$	24.5	4.4	(Ma, Han, et al. 2017)
SiO <sub>2</sub> /MWCNTs nano-rod (n/a)	PVDF (MPD, TMC)	0.75 wt% in dope solution	$A = 1.21 \text{ LMH}\cdot\text{bar}^{-1}$ $B = 0.12 \text{ LMH}$ $S = 240 \mu\text{m}$	PI; Casting thickness = 150 $\mu\text{m}$	1 M NaCl (DI water)	300 $\text{mL}\cdot\text{min}^{-1}$	22.1	4.1	(Zhang et al. 2018)
Zwitterion (PMAFS) (n/a)	PES (MPD, TMC)	1.0 wt% in MPD solution	$A = 0.69 \text{ LMH}\cdot\text{bar}^{-1}$ $B = 0.56 \text{ LMH}$	PI Casting/overall thickness = n/a	2 M NaCl (1,000 ppm oily WW)	32.7 $\text{cm}\cdot\text{s}^{-1}$	15.8 (AL-DS)	4.2 (AL-DS)	(Lee et al. 2018)

A: water permeability coefficient; B: solute permeability coefficient; CFV: cross-flow velocity; CNT: carbon nanotube; DS: draw solution; FS: feed solution; HNT: halloysite nanotube; INT: imogolite nanotube; Js: solute flux; Jw: water flux; MF: microfiltration; MPD: m-phenylenediamine; MWCNT: multi-walled carbon nanotube; pDA: polydopamine; PEI: polyethylenimine; PES: poly(ethersulfone); PI: phase inversion; PSf: polysulfone; PVDF: polyvinylidene fluoride; S: structural parameter; TMC: trimesoyl chloride; TNT: titanate nanotube; WW: wastewater

**Table 2.5** Summary of the fabrication conditions and FO performance of PA TFC membranes with non-porous nanomaterial-incorporated substrates.

TFC membrane with nanocomposite substrate					FO performance (AL-FS)				References
Filler embedded in substrate (Particle size)	Substrate (PA layer monomers)	Optimal particle loading	Intrinsic properties	Substrate fabrication method & conditions	DS (FS)	CFV	$J_w$ (LMH)	$J_s$ (gMH)	
TiO <sub>2</sub> (~21 nm)	PSf (MPD, TMC)	0.5 wt% in dope solution	$A = 1.98 \text{ LMH}\cdot\text{bar}^{-1}$ $B = 0.39 \text{ LMH}$ $S = 420 \mu\text{m}$	PI; Casting/overall thickness = 150/76 $\mu\text{m}$	2 M NaCl (10 mM NaCl)	32.72 $\text{cm}\cdot\text{s}^{-1}$	29.7	7.4	(Emadzadeh, Lau & Ismail 2013) (Emadzadeh, Lau, Matsuura, Hilal, et al. 2014)
TiO <sub>2</sub> (~21 nm)	PSf (MPD, TMC)	0.6 wt% in dope solution	$A = 2.63 \text{ LMH}\cdot\text{bar}^{-1}$ $B = 0.45 \text{ LMH}$ $S = 390 \mu\text{m}$	PI; Casting/overall thickness = 140/60-70 $\mu\text{m}$	2 M NaCl (DI water)	350 $\text{mL}\cdot\text{min}^{-1}$	33	15.7	(Emadzadeh, Lau, Matsuura, Ismail, et al. 2014)
SiO <sub>2</sub> (160-240 nm)	Bottom layer: 10 wt% PSf Top layer: 7 wt% PSf (MPD, TMC)	3 wt% in bottom layer and 0 wt% in top layer dope solution	$A = 1.64 \text{ LMH}\cdot\text{bar}^{-1}$ $B = 0.29 \text{ LMH}$ $S = 169 \mu\text{m}$	PI; Casting thickness of bottom/top layer = 0/80 $\mu\text{m}$ on top of PET mesh, Overall thickness = 97.2 $\mu\text{m}$	1 M NaCl (DI water)	25 $\text{cm}\cdot\text{s}^{-1}$	31	7.4	(Liu & Ng 2015)
GO (T: 1-2 nm)	PSf (MPD, TMC)	0.25 wt% (weight ratio to PSf) in dope solution	$A = 1.76 \text{ LMH}\cdot\text{bar}^{-1}$ $B = 0.19 \text{ LMH}$ $S = 191 \mu\text{m}$	PI; Casting/overall thickness = 150/50 $\mu\text{m}$	1 M NaCl (DI water)	25.0 $\text{cm}\cdot\text{s}^{-1}$	29.5	5.5	(Park et al. 2015)
CN/rGO (n/a)	PES (MPD, TMC)	0.5 wt% (weight ratio to PES) in dope solution	$A = 1.6 \text{ LMH}\cdot\text{bar}^{-1}$ $B = 0.3 \text{ LMH}$ $S = 163 \mu\text{m}$	PI; Casting/overall thickness = 100/51 $\mu\text{m}$	2 M NaCl (DI water)	-	41.1	9.6	(Wang, Ou, et al. 2015)
Zn <sub>2</sub> GeO <sub>4</sub> nanowires (D: 20-50 nm, L: 200-300 nm)	PES (MPD, TMC)	0.05 wt% in dope solution	$A = 2.47 \text{ LMH}\cdot\text{bar}^{-1}$ $B = 8.4 \text{ LMH}$ $S = 540 \mu\text{m}$	PI; Casting/overall thickness = 150/64 $\mu\text{m}$	2 M NaCl (DI water)	500 $\text{mL}\cdot\text{min}^{-1}$	21.6	4	(Low et al. 2015)
LDH/GO (T: 100-150 nm)	PSf (MPD, TMC)	2 wt% in dope solution	$A = 0.53 \text{ LMH}\cdot\text{bar}^{-1}$ $B = 0.15 \text{ LMH}$ $S = 138 \mu\text{m}$	PI; Casting/overall thickness = 150/58.6 $\mu\text{m}$	1 M NaCl (DI water)	2.6 $\text{cm}\cdot\text{s}^{-1}$	13.4	6.2	(Lu, Liang, Zhou, et al. 2016)
SiO <sub>2</sub> (200 nm)	PAN (MPD, TMC)	15 wt% (weight ratio to PAN) in dope solution	$A = 2.5 \text{ LMH}\cdot\text{bar}^{-1}$ $B = 1.7 \text{ LMH}$ $S = 65 \mu\text{m}$	Electrospinning; Flow rate = 1 $\text{mL}\cdot\text{h}^{-1}$ , Voltage = 28.5 kV, Working distance = 16 cm, Humidity = 50%	1 M NaCl (DI water)	15.8 $\text{cm}\cdot\text{s}^{-1}$	56.2	8.2	(Bui & McCutcheon 2016)
SiO <sub>2</sub> (n/a)	PAN (MPD, TMC)	15 wt% (weight ratio to PAN) in dope solution	$A = 1.36 \text{ LMH}\cdot\text{bar}^{-1}$ $B = 0.88 \text{ LMH}$ $S = 29.7 \mu\text{m}$	Electrospinning; Flow rate = n/a, Voltage = 20 kV, Working distance = 15 cm, Humidity = 47%	1 M NaCl (DI water)	7.5 $\text{mL}\cdot\text{min}^{-1}$	52	34.8	(Obaid et al. 2016)
GO (n/a)	PSf (MPD, TMC)	0.1 wt% in dope solution	-	PI; Spin-coating at 3000 rpm for 1 s	0.6 M NaCl (DI water)	0.09 $\text{cm}\cdot\text{s}^{-1}$	3.6	1.7	(Morales-Torres et al. 2016)
LDH nanoparticles (20-30 nm)	PSf (MPD, TMC)	2 wt% in dope solution	$A = 0.61 \text{ LMH}\cdot\text{bar}^{-1}$ $B = 0.27 \text{ LMH}$ $S = 148 \mu\text{m}$	PI; Casting/overall thickness = 150/57.4 $\mu\text{m}$	1 M NaCl (DI water)	2.6 $\text{cm}\cdot\text{s}^{-1}$	18.1	8.1	(Lu, Liang, Qiu, et al. 2016)
CaCO <sub>3</sub> (40– 80 nm)	PSf (MPD, TMC)	7.5 wt% in dope solution	$A = 1.86 \text{ LMH}\cdot\text{bar}^{-1}$ $B = 0.77 \text{ LMH}$ $S = 796 \mu\text{m}$	PI; Casting thickness = 150 $\mu\text{m}$	2 M NaCl (DI water)	166.7 $\text{mL}\cdot\text{min}^{-1}$	17	44.3	(Kuang et al. 2016)
GO (T: 1-2 nm)	Bottom layer: 7 wt% PSf Top layer: 15 wt% PSf (MPD, TMC)	0.25 wt% in both top layer and bottom layers	$A = 1.46 \text{ LMH}\cdot\text{bar}^{-1}$ $B = 0.25 \text{ LMH}$ $S = 130 \mu\text{m}$	PI; Casting thickness of bottom/top layer = 100/150 $\mu\text{m}$ , Overall thickness = 61 $\mu\text{m}$	1 M NaCl (DI water)	16.7 $\text{cm}\cdot\text{s}^{-1}$	33.8	6.9	(Lim et al. 2017)

GO (n/a)	PSf (MPD, TMC)	0.5 wt% in dope solution	$A = 0.54 \text{ LMH}\cdot\text{bar}^{-1}$ $B = 0.07 \text{ LMH}$ $S = 420 \text{ }\mu\text{m}$	PI; Overall thickness = 70-90 $\mu\text{m}$	2 M NaCl (DI water)	$2.5 \text{ cm}\cdot\text{s}^{-1}$	11.7	3.5	(Sirinupong et al. 2017)
TiO <sub>2</sub> /GO (< 21 nm)	PSf (MPD, TMC)	0.5 wt% in dope solution	$A = 0.58 \text{ LMH}\cdot\text{bar}^{-1}$ $B = 0.05 \text{ m/s}$ $S = 0.2 \text{ }\mu\text{m}$	PI; Overall thickness = 70-90 $\mu\text{m}$	2 M NaCl (DI water)	$2.5 \text{ cm}\cdot\text{s}^{-1}$	23.9	2.7	(Sirinupong et al. 2017)
Fe <sub>3</sub> O <sub>4</sub> (20-30 nm)	PES (MPD, TMC)	0.2 wt% in dope solution	$A = 3.06 \text{ LMH}\cdot\text{bar}^{-1}$ $B = 0.56 \text{ m/s}$ $S = 420 \text{ }\mu\text{m}$	PI; Casting thickness = 100 $\mu\text{m}$ on top of PE mesh, Overall thickness = 99.47 $\mu\text{m}$	2 M NaCl (10 mM NaCl)	$800 \text{ mL}\cdot\text{min}^{-1}$	28.8	14.7	(Darabi et al. 2017)
ZnO-SiO <sub>2</sub> core-shell (30 nm)	PES (MPD, TMC)	1.0 wt% (weight ratio to PES) in dope solution	$A = 3.5 \text{ LMH}\cdot\text{bar}^{-1}$ $B = 4.0 \text{ LMH}$ $S = 297 \text{ }\mu\text{m}$	PI; Casting/overall thickness = 100/59.8 $\mu\text{m}$	1 M NaCl (DI water)	$8.3 \text{ cm}\cdot\text{s}^{-1}$	33.5	11.5	(Rastgar et al. 2017)
SiO <sub>2</sub> (5-15 nm)	PEI (MPD, TMC)	1.6 wt% in dope solution	$A = 2.99 \text{ LMH}\cdot\text{bar}^{-1}$ $B = 0.4 \text{ LMH}$ $S = 174 \text{ }\mu\text{m}$	Electrospinning; Flow rate = 15 $\mu\text{L}\cdot\text{min}^{-1}$ , Voltage = 30 kV, Working distance = 12 cm, Humidity = 50%, $l = 93.7 \text{ }\mu\text{m}$ , $D = 249 \text{ nm}$ , $d_a = 1.28 \text{ }\mu\text{m}$	1 M NaCl (DI water)	$9.0 \text{ cm}\cdot\text{s}^{-1}$	42.0	5.1	(Tian et al. 2017)
TiO <sub>2</sub> (<25 nm)	PSf (MPD, TMC)	0.25 wt% in dope solution	n/a	Electrospinning; Flow rate = 16.66 $\mu\text{L}\cdot\text{min}^{-1}$ , Voltage = 35 kV, Working distance = 15 cm, Humidity = 25%	1 M NaCl (DI water)	$10.0 \text{ cm}\cdot\text{s}^{-1}$	51.5	12	(Zhang, Huang, et al. 2017)
ZnO (50 nm)	PES (MPD, TMC)	1.0 wt% (weight ratio to PES) in dope solution	$A = 3.1 \text{ LMH}\cdot\text{bar}^{-1}$ $B = 3.7 \text{ LMH}$ $S = 300 \text{ }\mu\text{m}$	PI; Overall thickness = 70-90 $\mu\text{m}$	1 M NaCl (DI water)	$8.3 \text{ cm}\cdot\text{s}^{-1}$	31.2	12.6	(Rastgar et al. 2017)
TiO <sub>2</sub> (< 21 nm)	PSf (MPD, TMC)	0.5 wt% in dope solution	$A = 1.5 \times 10^{-12} \text{ m/s Pa}$ $B = 0.03 \text{ LMH}$ $S = 310 \text{ }\mu\text{m}$	PI; Overall thickness = 70-90 $\mu\text{m}$	2 M NaCl (DI water)	$2.5 \text{ cm}\cdot\text{s}^{-1}$	18.9	1.7	(Sirinupong et al. 2017)

A: water permeability coefficient; B: solute permeability coefficient; CaCO<sub>3</sub>: calcium carbonate; CFV: cross-flow velocity; DS: draw solution; Fe<sub>3</sub>O<sub>4</sub>: iron (III) oxide, FS: feed solution; GO: graphene oxide; Js: solute flux; Jw: water flux; LDH: layered double hydroxide; MPD: m-phenylenediamine; pDA: polydopamine; PAN: polyacrylonitrile; PEI: polyethylenimine; PES: poly(ethersulfone); PI: phase inversion; PSf: polysulfone; rGO: reduced graphene oxide; S: structural parameter; SiO<sub>2</sub>: silica; TiO<sub>2</sub>: titanium oxide; TMC: trimesoyl chloride; Zn<sub>2</sub>GeO<sub>4</sub>: zinc germinate; ZnO: zinc oxide

#### 2.4.1 Zeolites, silica and zinc oxide

Several works have been published on zeolite-incorporated TFC membrane for RO applications because the unique pore structure of super-hydrophilic zeolite molecular sieves allows greater shape and size selectivity (Fathizadeh, Aroujalian & Raisi 2011; Huang et al. 2013; Lind et al. 2009; Pendergast, Ghosh & Hoek 2013). However, only two studies reported zeolite-modified PA TFC FO membrane, both studied by Tang's group (Ma et al. 2012; Ma, Wei, et al. 2013). Ma et al. were the first to prepare a nanocomposite substrate for the TFC membrane to control ICP in the FO process (Ma, Wei, et al. 2013). The PA TFC membrane with an optimal porous zeolite loading of 0.5 wt% in the PSf substrate (PSfN0.5-TFC) demonstrated a water flux that was more than 2 times higher than that of the conventional TFC membrane. The structural parameter of the PSfN0.5-TFC (control TFC) membrane was found to be 340  $\mu\text{m}$  (960  $\mu\text{m}$ ). The zeolite-loaded TFC membranes showed improvement in hydrophilicity, surface porosity and water permeability. However, the nanocomposite membrane was not highly selective, with a NaCl rejection of only ~91% attained using PSfN0.5-TFC membrane at 5 bar using a 10 mM NaCl feedwater (Ma, Wei, et al. 2013).

Silica-modified PSf flat-sheet substrates have also been developed for PA TFC FO membranes. A dual-layered flat-sheet membrane was made via the phase-inversion technique using silica-incorporated PSf solution for the bottom layer and pristine PSf solution for the top layer (Liu & Ng 2015). The dual-layered TFC membranes had a much higher NaCl rejection (~98%) than the single-layered TFC membranes (~15-97%) at all silica loadings (1-4 wt%). However, only minor enhancement in water flux was attained in comparison to control membrane in AL-FS orientation for both single and dual-layered silica-modified TFC membranes. In contrast, water flux improved significantly in AL-DS orientation for nanocomposite TFC membranes compared to the pristine TFC membrane.

The selectivity of single-layered silica-modified TFC membranes deteriorated with increasing silica concentration but remained nearly constant with dual-layered silica-incorporated membranes (Huang et al. 2016). The better selectivity of the dual-layered substrate could be attributed to its desirable surface morphology for the formation of a high salt rejecting and dense PA layer. Additionally, the porous and hydrophilic structure of the dual-layered substrate helped to reduce ICP.

More recently, electrospun silica-embedded nanofiber mats were prepared as porous substrates for PA TFC membranes (Bui & McCutcheon 2016; Tian et al. 2017). The low tortuosity and high porosity of the nanofiber mats substantially reduced ICP by reducing the structural parameter of the nanofiber supported membranes ( $<175 \mu\text{m}$  with the optimal silica loading). The high porosity of silica-nanofibrous substrate enhanced mass transfer within the support layer, which increased the osmotic water flux of FO membranes. The water and salt permeability of the best performing FO membrane increased by more than 7 and 3.5 times, respectively, compared to the commercial HTI-CTA FO membrane. The surface roughness of the silica-embedded nanofibers has not been reported in both works; however, the high surface roughness is more likely to impair PA layer formation on nanofiber support (Li, Wang, et al. 2012).

Rastgar et al. dispersed ZnO and ZnO-SiO<sub>2</sub> core-shell nanoparticles (ZSCSNPs) in the poly(ethersulfone) (PES) substrate to explore the effect of different nanoparticle surface characteristics on the pore structure and performance of PA TFC FO membranes (Rastgar et al. 2017). The cross-sectional SEM images exhibited a dense sponge-like porous structure for pristine PES substrates and loose and long finger-like porous structures for ZnO and ZSCSNPs-incorporated substrates. The hydrophilicity and large surface area of ZnO and ZSCSNPs could have augmented the exchange rate of solvent/non-solvent phases during the phase-inversion process that resulted in the development of finger-like pore structures. The



finger-like pore structures reduced ICP by decreasing membrane tortuosity and structural parameter. The water fluxes of ZnO and ZNCSNPs-incorporated TFC membranes were more than twofold higher than that of the pristine TFC membrane. The TFC membrane with 1.0 wt% ZNCSNPs loading had higher hydrophilicity, permeability, pore density, and bigger surface pore size compared to the 1.0 wt% ZnO loaded TFC membrane. Although the ZnO nanoparticles had 10 times higher surface area than the ZNCSNPs, the water fluxes obtained using ZNCSNPs-modified TFC membranes were higher with comparable solute flux. Hence, the impact of nanoparticle hydrophilicity on the FO performance was found to dominate the effect of surface area.

#### **2.4.2 Carbon nanotubes and graphene oxide**

Unlike conventional PA TFC membranes supported on polymeric substrates (PSf/ PES), novel membranes with PA layer supported on robust and highly stable self-supporting Bucky-papers (BPs) were fabricated for potential application in FO/RO processes by Dumée et al. (Dumée et al. 2013). The BPs were solely comprised of hydroxyl-functionalized entangled CNTs that demonstrated enhanced wettability (contact angle  $< 20^\circ$ ) after plasma treatment. The high porosity of BPs allowed good water permeation (water uptake capacity of 17%), and the comparable pore size of BPs and PSf support meant that the PA layer could effectively form on BP without damage. The BP supported PA TFC membranes also had a smoother surface (29.2 nm) than the PSf-supported (56 nm) and commercial TFC membranes (49.7 nm). The low structural parameter (620  $\mu\text{m}$ ) for BPs could potentially reduce ICP. Additionally, the water and salt permeability of BPs could be adjusted by preparing thin sheets and fine-tuning their chemistry. Nonetheless, no data on water flux and salt rejection have been provided for FO performance tests, possibly due to the membrane's fragility.

It is essential to functionalize CNTs to improve their hydrophilicity before blending them in the polymer dope solution in order to improve the performance of CNT-incorporated FO membranes. Pristine CNTs are hydrophobic and form low porosity substrates with macrovoids that increase draw solute leakage and reduce water flux. Moreover, pristine CNTs can readily agglomerate in organic and/or polymer solutions (Morales-Torres et al. 2016). Wang et al. produced a high-performance PA TFC membrane for desalination using carboxylated MWCNTs-blended PES substrates (Wang et al. 2013a). The nanomaterial-incorporated substrates were observed to have finger-like macrovoid structures that resulted in better water permeability, higher salt rejection (>90%), and smaller structural parameter than the neat PES and CTA commercial membrane. The open porous structure of the substrate significantly reduced ICP and improved water flux. The nanomaterial-incorporated PES substrate also demonstrated higher tensile strength; thus, creating the possibility of producing substrates without fabric supports.

Similarly, Choi et al. used carboxylated MWCNTs (f-MWCNTs) incorporated PA TFC membrane for application in combined seawater desalination and wastewater recovery FO process (Choi, Son & Choi 2017). The increased porosity and hydrophilicity of the nanocomposite membrane resulted in a 72% higher water flux than the baseline TFC membrane. The *SRSF* of the nanocomposite membrane was 15% lower than the TFC membrane. The nanocomposite membrane also exhibited a 19% less decline in normalized flux under the alginate fouling test compared to the TFC membrane because of the negatively-charged membrane surface, which improved repulsive foulant–membrane interaction. The smoother surface and electrostatic repulsive force of the nanocomposite membrane improved fouling reversibility, and the recovered normalized flux of nanomaterial-incorporated TFC membrane was observed to be 6% higher than the TFC membrane after physical cleaning.

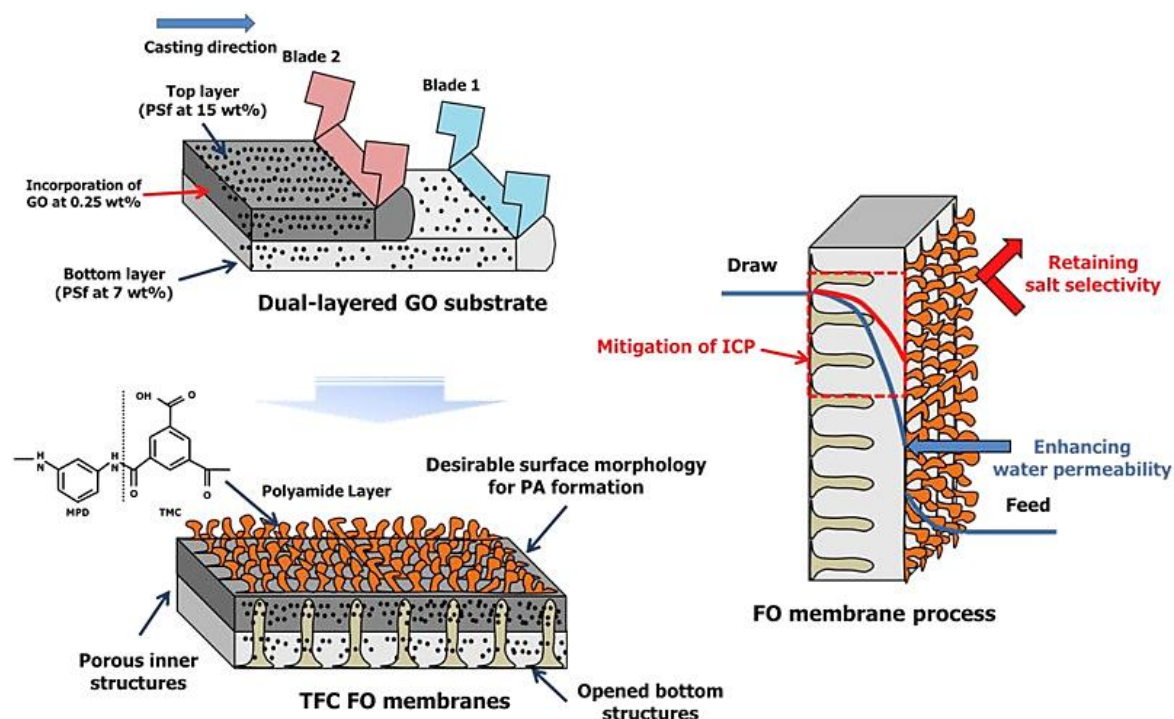
Polyetherimide (PEI) nanofibers embedded with f-MWCNTs were also explored as potential substrates for PA TFC membranes (Tian, Wang & Wang 2015). The f-MWCNTs were well-distributed in the nanofibers, which improved the average substrate porosity and tensile strength by 18% and 53% respectively and decreased the structural parameter by 30% compared to neat PEI nanofibers. The dispersed f-MWCNTs retained the porous structure by providing better compaction resistance to nanofibers during heat-press treatment. The nano-sized water channels of f-MWCNTs could have also contributed to the higher substrate porosity and improved pure water permeability. The high mechanical strength of f-MWCNTs-incorporated nanofibers assisted in ICP mitigation by allowing a further increase in substrate porosity and pore size and forming large interconnected pores. As a result, the water flux of nanomaterial-incorporated TFC membranes was much higher than neat TFC membranes. The nanomaterial-incorporated TFC membranes also demonstrated a lower *SRSF* than the control TFC membrane.

In addition to CNTs, graphene derivatives like graphene oxide (GO) and reduced GO (rGO) have been explored as potential nanofillers for TFC FO membrane substrate due to their smooth structure, high mechanical strength, good chemical stability, low thickness (1-2 nm), favourable surface chemistry and high surface area-to-volume ratios that assist in better interaction with the polymer matrix (Hu & Mi 2013; Lai, Lau, Goh, et al. 2016; Lai, Lau, Gray, et al. 2016; Stankovich et al. 2006). GO's surface contains hydrophilic oxygen-containing functional groups like epoxide, carbonyl, hydroxyl and carboxyl groups, which can improve the hydrophilicity and antifouling properties of the nanocomposite membranes (Zinadini et al. 2014).

Recent studies have reported that GO incorporation into TFC substrate enhanced the membrane pore diameter, porosity, and hydrophilicity, which markedly increased water permeability and allowed the efficient formation of the PA layer (Morales-Torres et al. 2016;

Park et al. 2015; Sirinupong et al. 2017). Moreover, the addition of GO/TiO<sub>2</sub> composite and/or mixture to membrane substrate further improved the water flux, compared to pristine and GO-modified TFC membrane, without significantly sacrificing the reverse solute flux due to the establishment of straight finger-like elongated pores and increased the support layer porosity (Morales-Torres et al. 2016; Sirinupong et al. 2017). A similar observation was made using rGO modified graphitic carbon nitride (CN/rGO) as PES substrate filler, which reduced membrane structural parameter by changing the PES substrate structure (Wang, Ou, et al. 2015).

Lim et al. developed a TFC FO membrane with a dual-layered nanocomposite substrate (Lim et al. 2017), as shown in **Fig. 2.8**. The substrate layers were made using 15 wt% and 7 wt% PSf solution for the top and bottom layers, respectively. The lower PSf concentration of the bottom layer resulted in creating highly porous finger-like structures, which helped diminish ICP effects. Whereas, the higher concentration of PSf in the top layer formed a smooth, thin skin layer with desirable pore size for adequate development of the dense PA layer. The pure water permeability and porosity of the dual-layered membrane substrate were suggestively higher than the single-layered substrate. Dual-layered TFC membrane incorporated with 0.25 wt% hydrophilic GO nanosheets demonstrated a lower structural parameter, higher water permeability and ion selectivity compared to the GO-free membrane. The water flux of GO-modified dual-layered TFC membrane was 69% higher than the single-layered TFC membrane under AL-FS mode using 1 M NaCl and DI water as a draw and feed solution, respectively. Moreover, the reverse solute flux of GO-modified dual-layered TFC membrane was less than that of single-layered TFC membrane under the same operating conditions, suggesting that water permeability improvement was achieved without comprising on membrane selectivity. The dual-layered PSf substrates were also able to mitigate the ICP effects at higher draw solution concentrations effectively.



**Fig. 2.8** Schematic of the co-casting technique used for fabrication of dual-layered GO-incorporated TFC FO membranes (Lim et al. 2017).

### 2.4.3 Titanium oxide

TiO<sub>2</sub> nanoparticles have been extensively used to enhance characteristics of RO, NF, UF, membrane distillation (MD), pervaporation, and FO membranes due to their outstanding hydrophilicity, good antifouling properties, high chemical stability and adequate photochemical reactivity (Lee et al. 2016; Razmjou et al. 2012; Safarpour, Khataee & Vatanpour 2015; Yang et al. 2009; Yang et al. 2011). Ismail's group was the first to incorporate TiO<sub>2</sub> nanoparticles in the PSf substrate of PA TFC membrane using direct blending to control ICP in the substrate during FO operation (Emadzadeh, Lau & Ismail 2013; Emadzadeh, Lau, Matsuura, Ismail, et al. 2014). Like MWCNTs and GO, incorporating TiO<sub>2</sub> in the membrane substrate formed long finger-like pores, improved hydrophilicity and porosity (Emadzadeh, Lau, Matsuura, Ismail, et al. 2014). The structural parameter of the 0.5 wt% TiO<sub>2</sub> embedded membrane was 420 μm, which was much smaller than that of the TFC membrane (980 μm). The water flux of nanocomposite membrane

embedded with 0.5 wt% TiO<sub>2</sub> was approximately 87% higher than the TFC membrane in AL-FS mode when tested using 10 mM and 0.5 M NaCl as feed and draw solution, respectively. In addition, the TFN membrane demonstrated good water flux stability under long-term FO test due to the diminished effect of ICP in the support layer (Emadzadeh, Lau & Ismail 2013). Increasing the TiO<sub>2</sub> loading beyond 0.5 wt% caused in particle agglomeration at the surface of the substrate, causing a lower degree of cross-linking in the PA layer. Consequently, water flux increased but at the expense of deteriorating membrane selectivity (Emadzadeh, Lau, Matsuura, Rahbari-Sisakht, et al. 2014).

Additionally, the TiO<sub>2</sub>-embedded TFC membrane was tested for organic fouling in AL-DS mode using BSA in the presence of Ca<sup>2+</sup>. The hydrophilic nature of the nanocomposite membrane significantly diminished the hydrophobic BSA adsorption on the membrane surface. The fouling in nanocomposite membrane was highly reversible with a pure water flux recovery of 92% after rinsing with water for 30 minutes without any chemical cleaning reagents; while the control TFC membrane achieved a water flux recovery of 79% (Emadzadeh, Lau, Matsuura, Hilal, et al. 2014).

#### **2.4.4 Other nanomaterials**

A Zn<sub>2</sub>GeO<sub>4</sub> nanowire embedded PSf UF membrane with high surface porosity was employed as a substrate for PA TFC FO membrane preparation. The surface characteristics of the substrate improved the cross-linking degree of the PA layer that improved membrane selectivity. However, the Zn<sub>2</sub>GeO<sub>4</sub> nanowire-modified substrate demonstrated a lower FO water flux despite achieving a water permeability that was ~42% higher than that of the control PES membrane in RO mode. The contradicting results may have occurred as the Zn<sub>2</sub>GeO<sub>4</sub> incorporated substrate failed to efficiently mitigate ICP due to the increased membrane tortuosity resulting from the formation of thick pore walls near the bottom matrix

of the membrane. The modified membrane also had a higher structural parameter (540 vs 352  $\mu\text{m}$ ) than the pristine PES membrane (Low et al. 2015).

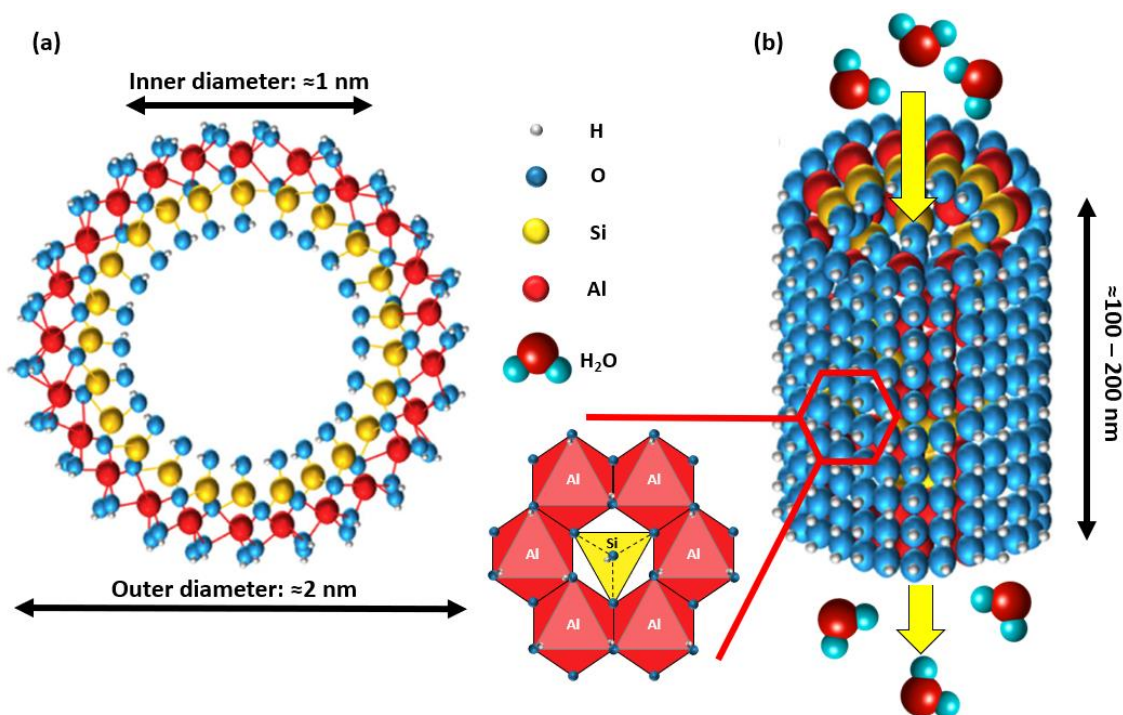
In another study, hydrophilic HNTs were embedded into a PSf substrate with an optimal loading of 0.5 wt%. Increasing the HNTs loading beyond 0.5 wt% resulted in poor salt rejection due to a lower degree of cross-linking in the PA layer. The structural parameter of 0.5 wt% HNT-incorporated membrane (370  $\mu\text{m}$ ) was lower than that of the control TFC membrane (950  $\mu\text{m}$ ) due to higher porosity, enhanced hydrophilicity and extra water pathway formation in the substrate. The HNT-modified membrane also exhibited high water permeability without significantly sacrificing membrane selectivity. The water flux of the nanocomposite membrane was much higher than that of the control TFC membrane in both AL-FS (27.7 vs 13.3  $\text{L}\cdot\text{m}^{-2}\cdot\text{h}^{-1}$ ) and AL-DS (42.3 vs 26.0  $\text{L}\cdot\text{m}^{-2}\cdot\text{h}^{-1}$ ) orientations when 10 mM and 2 M NaCl were used as feed and draw solution, respectively (Ghanbari et al. 2016).

Wang and co-workers developed functional layered double hydroxide (LDH) nanoparticles blended PSf UF substrates for TFC FO membranes (Lu, Liang, Qiu, et al. 2016). The addition of LDH changed the substrate morphology, which significantly enhanced the surface pore diameter, surface hydrophilicity, porosity, thermal stability and mechanical strength of the membrane. The water permeability of nanocomposite membranes was higher than the pristine TFC membrane at all LDH loadings (0 – 4 wt%). The water flux of the optimal LDH-modified membrane (2 wt% LDH loading) was 42.5% more than that of pristine TFC membrane when tested in AL-FS orientation with DI water and 1 M NaCl as feed and draw solution, respectively. The structural parameter of the 2 wt% LDH loaded membrane, and the pristine membrane was evaluated as 148  $\mu\text{m}$  and 287  $\mu\text{m}$ , respectively. Integration of LDH in the membrane substrate reduced the substrate tortuosity and ICP effects (Lu, Liang, Qiu, et al. 2016). The group also synthesized LDH/GO hybrid as a nanofiller for PSf substrate and obtained similar results as the LDH-modified substrate.

However, the LDH/GO-modified membrane exhibited a lower structural parameter (138  $\mu\text{m}$ ) and reverse solute flux compared to the LDH-modified and pristine TFC membranes (Lu, Liang, Zhou, et al. 2016).

Imogolite nanotubes (INTs) are hydrous aluminosilicate single-walled nanotube materials that have evolved as a promising competitor of CNTs (Farmer, Fraser & Tait 1977). Unlike CNTs, INTs are exceptionally hydrophilic due to the existence of ample hydroxyl groups both on their outer and inner walls (**Fig. 2.9**). In addition to their superior hydrophilicity, INTs have a high aspect ratio and surface area that make them potential nanofillers for developing desalination membranes (Baroña, Choi & Jung 2012; Baroña et al. 2013). Pan et al. prepared hydrophilic TFC FO membranes for desalination using INTs blended PSf substrates (Pan et al. 2017). It was found that the TFC membrane with 0.66 wt% INTs blended PSf substrate demonstrated the best FO performance regarding water flux and salt rejection. Moreover, the incorporation of INTs in the substrate enhanced the intrinsic transport properties of the nanocomposite membrane. The INTs blended substrates provided three types of passages for salt and water transport. The first type included the widest channels that are formed during the phase inversion process and comprised of the finger-like pores, top surface spongy pores, and bottom surface macro-voids. The second kind involved the interfacial gaps between the INTs and the polymer matrix; whereas, the third type comprised the INTs nanochannels. The interfacial gaps and INTs nanochannels helped to connect the wide channels or pores in the substrate polymer matrix to assist in water and salt transport. Incorporation of INTs alleviated ICP as the optimal nanocomposite membrane had a much lower structural parameter (2.09 mm) than the TFC membrane (13.34 mm) (Pan et al. 2017).





**Fig. 2.9** View of the atomic structure of INTs. (a) Axial and (b) 3-D side view (adapted from (Pan et al. 2017)).

The work of Deng et al. (Deng et al. 2013) on the development of ultrahigh permeable nanoporous membranes using copper hydroxide nanostrands as sacrificial additives inspired Kuang et al. to develop porous PSf substrates using calcium carbonate nanoparticles ( $\text{CaCO}_3$ -NPs) as sacrificial additives (Kuang et al. 2016). The  $\text{CaCO}_3$ -NPs distributed in the PSf matrix were removed after the phase inversion process by etching with hydrochloric acid to enhance the substrate porosity. Chemical etching of the substrate reduced the membrane structural parameter. Increasing the  $\text{CaCO}_3$ -NPs loading made the substrate more porous and reduced the structural parameter further. The optimal membrane with a 7.5 wt%  $\text{CaCO}_3$ -NPs loading demonstrated a water flux of  $17 \text{ L}\cdot\text{m}^{-2}\cdot\text{h}^{-1}$  ( $27.6 \text{ L}\cdot\text{m}^{-2}\cdot\text{h}^{-1}$ ) in AL-FS (AL-DS) mode compared to a much smaller water flux of  $3.6 \text{ L}\cdot\text{m}^{-2}\cdot\text{h}^{-1}$  ( $5.5 \text{ L}\cdot\text{m}^{-2}\cdot\text{h}^{-1}$ ) obtained using the control TFC membrane under same testing conditions. Although the sacrificial additive helped to increase the membrane porosity and water flux, it hampered membrane selectivity. The salt permeability of the modified membranes was much higher than the control

membrane, and the *SRSF* values were reported between 3 g·L<sup>-1</sup> and 2.3 g·L<sup>-1</sup> at different CaCO<sub>3</sub>-NPs loading in AL-FS mode, which is much higher than those reported in other FO nanocomposite membrane studies (Kuang et al. 2016).

Ferrous-ferric oxide (Fe<sub>3</sub>O<sub>4</sub>) has also be used as a nanofiller in PA TFC membrane substrate due to its numerous desirable properties like high surface area, low toxicity, chemical stability, good biocompatibility and magnetic properties. Darabi et al. added Fe<sub>3</sub>O<sub>4</sub> nanoparticles (0.06-0.5 wt%) in the PES substrate matrix to alleviate ICP. The water and salt permeability increased as the Fe<sub>3</sub>O<sub>4</sub> loading was increased from 0-0.2 wt% due to higher overall porosity and formation of additional water pathways that considerably reduced the membrane structural parameters from 780 to 420 μm. The lowest NaCl rejection (93.2%) was observed at 0.2 wt% Fe<sub>3</sub>O<sub>4</sub> loading due to particle agglomeration that reduced the degree of PA cross-linking. Increasing the Fe<sub>3</sub>O<sub>4</sub> loading beyond 0.2 wt% increased the structural parameter from 420 to 850 μm, decreased water permeability and improved salt rejection, possibly due to pore blockage and reduced overall membrane porosity. The nanocomposite membrane with 0.2 wt% Fe<sub>3</sub>O<sub>4</sub> loading demonstrated the highest water flux and lowest *SRSF* compared to other membranes. (Darabi et al. 2017).

#### **2.4.5 Issues and challenges of nanomaterial-modified substrates**

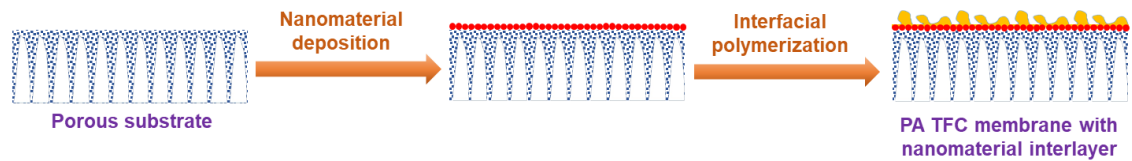
One of the major drawbacks of nanocomposite substrates is that a comparatively higher nanomaterial loading is required compared to the TFN membranes to observe any improvement in membrane performance. The relatively high cost of fabricating TFC membranes with nanocomposite substrates may limit their wide applications. Besides, nanoparticles may agglomerate easily in polymer dope solution due to the solution viscosity and the polymer-nanoparticle incompatibility. Therefore, interfacial voids are formed between the nanomaterial and the polymer, which can cause nanoparticle loss and reduce membrane selectivity. In addition, some nanomaterials can change substrate morphology

and increase surface pore size, which will result in the formation of a defective PA layer during the IP process. Hence, it is preferable to use organic pore formers like PVP and polyethylene glycol (PEG) to prepare a substrate with a porous bottom surface and a tight top surface to form a defect-free PA layer (Ong et al. 2015; Sukitpaneenit & Chung 2012). Moreover, cost-effective nanoparticles can be developed that are hydrophilic and compatible with polymer-phase to reduce ICP and minimize material loss.

## **2.5 Nanomaterial interlayer**

Although commercial TFC FO membranes have demonstrated exceptional separation performance, their practical application is still challenging due to their intrinsic trade-off effect between water flux and salt flux. Further improvement in water permeability without reducing selectivity is difficult by only embedding nanomaterials in the membrane active layer or substrate. Besides nanomaterial modification of TFC membranes, several studies have focused on developing the PA layer structure performance enhancement of TFC membranes by optimizing the IP process conditions. It was found that parameters like the monomer concentration, reaction time and temperature considerably affect the PA layer formation because IP is a diffusion-controlled process, where the amines in the aqueous phase diffuse to the organic phase and react with the acyl chloride at the interface between aqueous and organic solutions (Gorgojo et al. 2014; Khorshidi et al. 2015; Klaysom, Hermans, et al. 2013). In addition, the surface property and pore structure of the substrate surface facing the active layer directly influences the PA layer structure because it serves as a platform for holding the aqueous amine solution during the IP reaction. For example, large pores on the substrate surface can cause the PA to develop inside the porous substrates and form a defective selective layer. Therefore, efforts have been made to fine-tune the surface properties of substrates using nanomaterial-based interlayer between the porous substrate and dense PA layer to form a defect-free PA active layer through controlled IP reaction. **Fig.**

2.10 illustrates the typical steps involved in the fabrication process of PA TFC membranes incorporated with a nanomaterial interlayer.



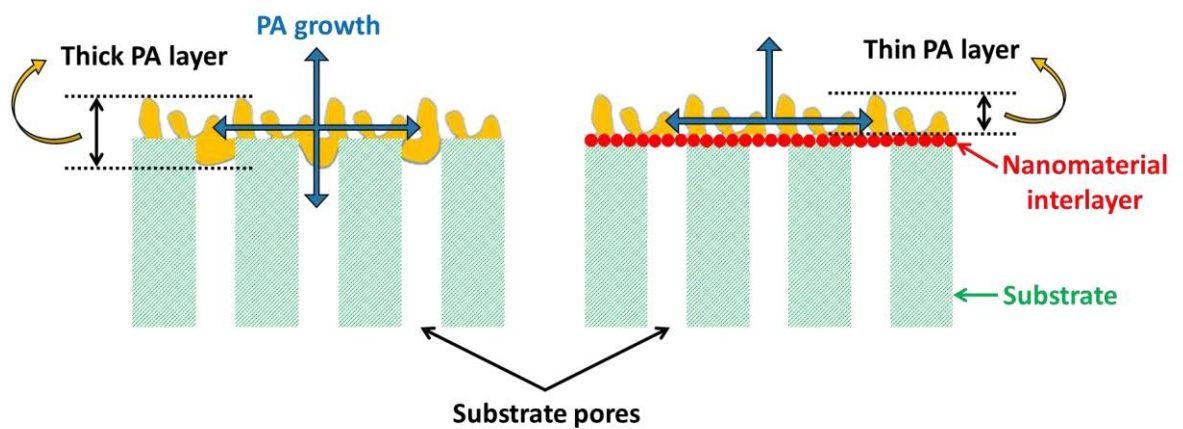
**Fig. 2.10** Typical steps involved in the preparation of a PA TFC membrane incorporated with a nanomaterial interlayer.

### 2.5.1 Carbon nanotubes and graphene oxide

Livingston's group recently developed a free-standing PA layer, <10 nm thick, via controlled IP reaction on top of a porous cadmium hydroxide nanostrand layer coated on a porous substrate (Karan, Jiang & Livingston 2015). The nanostrand interlayer allowed the development of an ultrathin, uniform and defect-free PA active layer through controlled release of MPD solution at the water-hexane interface, which exhibited excellent permeability. Inspired by this study, Zhao et al. developed a TFC membrane using a CNT interlayer between the polyvinylidene fluoride (PVDF) support layer and PA layer (Zhao, Li & Liu 2017). The CNT interlayer improved the effective contact area of the PA layer area by providing a porous three-dimensional free space below the PA skin. The structural parameter of the modified membrane (392  $\mu\text{m}$ ) was significantly lower than the control membrane (1562  $\mu\text{m}$ ) because the CNT interlayer free-space acted as a buffering zone to enhance the feed and draw solution exchange near the PA active layer and maintain the osmotic pressure; thus, diminishing the ICP effect in the FO process (Zhao, Li & Liu 2017).

Meanwhile, Zhang and co-workers deposited GO/MWCNT composite as an intermediate layer on MF support using vacuum filtration to facilitate the successful growth of defect-free PA layer on substrates with large pores (Zhao et al. 2018). The GO/MWCNT layer controlled MPD diffusion by forming hydrogen and/or covalent bonds with the MPD monomers that

contributed to the formation of a thinner PA layer. Moreover, the GO/MWCNT layer prevented the diffusion of TMC inside the substrate pores that restricted the PA growth along the GO/MWCNT layer but not within the substrate pores (**Fig. 2.11**). Consequently, the FO membranes with the interlayer demonstrated higher water flux and better selectivity than the control membranes. The nanochannels in the MWCNT/GO interlayer also contributed towards enhanced water flux of the modified membranes.



**Fig. 2.11** Schematic diagram representing the PA development process on porous substrates with and without a nanomaterial interlayer.

A similar mechanism was reported by Zhou et al. who spray-coated an ultrathin CNT interlayer onto a commercial porous PES MF membrane using an airbrush to develop a high-performance TFC FO membrane (Zhou et al. 2018). The CNT interlayer not only prevented the PA formation into the substrate pores but also enhanced the effective PA surface area, which reduced the water transport resistance. The cross-linking degree of the PA layer formed on the CNT interlayer was found to be higher than that on the PES substrate. The resulting TFC membrane with the CNT interlayer exhibited 7 times higher water flux and 7 times lower *SRSF* than that of the control TFC membrane in AL-DS mode with DI water and 1 M NaCl as feed and draw solution, respectively.

Subsequently, Choi et al. formed a hydrophilic pDA/GO interlayer on the PSf support (Choi et al. 2019). They found that increasing the pDA coating time and GO loading beyond 1 h and  $0.5 \text{ g}\cdot\text{L}^{-1}$ , respectively, resulted in reduced water permeability due to blockage of surface pores by pDA and GO. The TFC membranes with pDA.GO<sup>-1</sup> interlayer demonstrated improved water flux without affecting the selectivity when GO loading was maintained between  $0.25 \text{ g}\cdot\text{L}^{-1}$  and  $0.5 \text{ g}\cdot\text{L}^{-1}$  with a pDA coating duration of 1 h.

### **2.5.2 Porous coordination polymers**

More recently, Wang et al. suggested the construction of an interlayer on PSf substrate using MOF UiO-66 nanoparticles for preparing TFC FO membranes (Wang et al. 2019). The optimal TFC membrane with UiO-66 interlayer showed better water flux, selectivity and lower transport resistance than the pristine and UiO-66 modified TFN membranes. The channels of UiO-66 nanoparticles allow water molecules to pass through while rejecting the hydrated draw solute ions. Future studies can focus on tuning the properties and structure of the PA layer by modifying the properties of the interlayer, such as its surface pore size, roughness and thickness, to achieve high membrane performance.

### **2.5.3 Issues and challenges of nanomaterial interlayer**

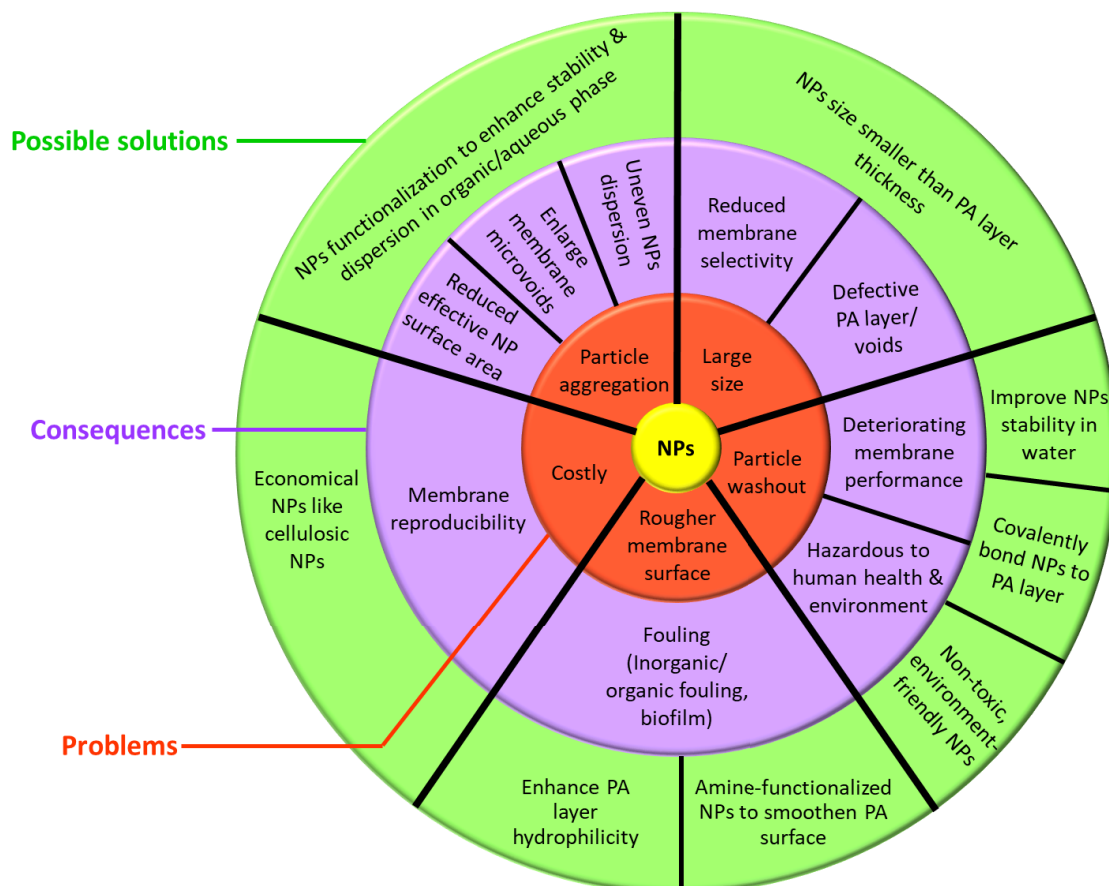
The scalability of nanomaterial interlayer development on porous substrates may be very challenging. Vacuum filtration is the most widely used technique used to deposit nanomaterial interlayer, but its implementation for large-scale membrane production may be unviable. A more feasible strategy may be to use a controlled spray coating, which can be easily installed in the commercial membrane fabrication unit. Besides scalability, the material should be carefully selected for interlayer formation such that they provide a desirable platform of defect-free PA layer formation without causing pore blockage.

## 2.6 Implications and future perspectives

**Fig. 2.12** summarises the critical issues in the fabrication of nanomaterial-incorporated PA TFC membranes that need addressing to achieve further enhancement in membrane performance and scalability. Particle aggregation is one of the major issues encountered during nanocomposite membrane fabrication, and it mainly results from the high surface energy of nanomaterials and high inter-particle interactions. This results in poor dispersion of nanofillers in the monomer solution used for PA layer formation or in the polymer dope solution used for membrane substrate. Agglomeration of nanoparticles decreases the effective nanoparticle surface area and results in a defective PA layer with voids and uneven nanomaterial distribution. Several studies have explored surface functionalization of nanomaterials like amine-functionalized or carboxylated CNTs and HNTs to minimize particle aggregation in the non-polar solvent or polymer matrix and produce a dense defect-free active layer. Besides surface functionalization of nanofillers, new nanomaterials like MOFs and COFs can be designed with customized pore structure and surface charge to facilitate the homogenous distribution of nanofillers in the polymer matrices. In addition, more surface modification methods can be explored to overcome the trade-off relationship between water and solute flux and improve the antifouling property and chlorine resistance of the PA TFC membranes.

Non-uniform nanomaterial dispersion in the solvent or polymer dope solution can hinder membrane reproducibility and cause a significant variation in the FO performance, mainly when a small FO membrane coupon is used for performance tests. For instance, if coupons are tested from a membrane sample with a non-uniform nanoparticle dispersion, then coupons cut from the membrane region with a denser nanoparticle loading will demonstrate higher water flux comparatively. Hence, it is crucial that all lab-scale membrane performance studies are conducted using larger membrane samples instead of small

membrane coupons like 2 cm<sup>2</sup> so that the performance results are comparable and representative of the whole composite membrane.



**Fig. 2.12** Current problems and consequences of nanoparticle (NP) incorporation in the membranes, and some possible solutions to overcome those issues.

The nanoparticle size affects the substrate morphology and influences the development of PA active layer. Consequently, it is vital to ensure that particles smaller than the PA layer thickness (150-300 nm) are used so that they can be effectively incorporated into the PA layer. Nanofillers larger than the PA layer thickness, such as CNTs and HNTs, can damage the active layer and undermine membrane selectivity (Cho et al. 2013; Kong et al. 2011). The loss of nanomaterials during membrane fabrication and FO operation is an additional problem. For example, a large amount of hydrophilic nanomaterial dispersed in the aqueous amine solution for the IP reaction can be lost from the substrate surface when the surplus



amine solution is removed using a rubber roller. As a result, only a small quantity of the nanomaterials would remain inside the substrate pores.

Many works that have used hydrophilic nanotubes (functionalized CNTs and HNTs) as membrane fillers have stated that incorporation of nanotubes into the membrane substrate or PA layer can improve water permeability without significantly affecting salt rejection by providing extra passages for the transport of water molecules (Ghanbari, Emadzadeh, Lau, Lai, et al. 2015; Jia et al. 2010). However, the concept of the preferential pathway for water molecules requires further verification since it is only possible if the nanochannels are aligned towards the water flux direction and not blocked by the polymer matrix inside which they are embedded. So far, most studies on liquid separation reported the membrane performance results with only randomly arranged nanotubes (Song, Wang, et al. 2016; Song et al. 2015; Zhao, Li & Liu 2017). Sharma et al. used an electric field to align CNTs in the polymer membranes for hydrogen separation (Sharma et al. 2009). Thus, it may be possible to use an electric or magnetic field to consider the effect of uniform nanotube alignment on the membrane performance for liquid separation.

Although the FO process is associated with an intrinsic low fouling potential, FO process performance can be significantly affected by the reduced mass transfer resulting from the fouling layer resistance and increased concentration polarization (Bogler, Lin & Bar-Zeev 2017; Li et al. 2017). The addition of hydrophilic nanomaterials in the PA selective layer can significantly improve the membrane hydrophilicity and increase the surface roughness, which can promote fouling and exacerbate biofilm formation (Xu, Wang & Li 2013).

While many studies have developed and tested nanocomposite PA TFC membranes at a lab-scale level, nanomaterial-incorporated TFC membranes are not yet reported on a commercial scale, which raises concerns about the economic competitiveness of the nanocomposite

membranes. Although reproducibility and cost-effectiveness of the nanocomposite membrane are important, it is also crucial that the long-term performance of the nanocomposite membranes under real feed conditions are well understood to determine membrane robustness. Long-term performance tests and thorough assessment of the nanocomposite membrane stability are critical, especially for the surface-modified nanocomposite membranes, to control the leaching of nanomaterials. Leaching of nanomaterial may deteriorate membrane performance and durability. For example, depletion of biocidal agents like AgNPs located on the membrane surface can result in loss of membrane antimicrobial activity with time. Thus, it is worth exploring and developing surface coating materials that firmly adhere to membrane surface that are stable in water, can resist fouling and chlorine attack.

Additionally, it is essential to develop reliable and standard protocols for characterizing FO membranes to facilitate the standardization of the results obtained from different research groups and enable data exchange and analysis. Kim et al. comprehensively reviewed the various approaches available to determine the characteristics of FO membranes (Kim, Gwak & Hong 2017). The RO-FO tests are the most widely used methods to estimate the intrinsic membrane transport and structural parameters. However, the intrinsic parameters obtained for FO membranes using the RO-FO tests are unreliable due to the different driving forces used in the RO and FO process. Moreover, testing the FO membranes at high hydraulic pressures can damage the thin active and support layer of the membrane, which will result in an unreliable estimation of membrane transport and structural parameters (Cath et al. 2013). To address these issues, Tiraferri et al. proposed a non-pressurized method comprising of a four-step FO protocol, where a different draw solution concentration is used in each step (Tiraferri et al. 2013). Non-linear least-squares regression is then performed using the experimental water and reverse salt flux data obtained in each step to estimate the

intrinsic membrane transport and structural parameters. Nonetheless, the four-step FO protocol is unsuitable for predicting the performance parameters of pressure-applied FO processes. Kim et al. have extensively discussed in their review the limitations of the existing protocols and other possible methods to determine FO membrane characteristics (Kim, Gwak & Hong 2017). Furthermore, a standard protocol for FO operating conditions is also required to compare different membranes in terms of FO performance. For instance, a predetermined cross-flow velocity should be used for all studies as it has a significant impact on the mass transfer and mixing of feed and draw solution in the flow channels, which will ultimately affect the water flux, solute flux and membrane fouling.

## **2.7 Conclusions**

In this paper, we reviewed the development of nanomaterial-incorporated PA TFC membranes for FO processes. We focused on different nanofillers and the methods used to fabricate nanocomposite membranes. In addition, we discussed the influence of various nanoparticles on the performance and antifouling property of the membranes. Most studies observed that incorporation of nanofillers into the TFC membranes changed membrane physicochemical properties resulting in a more durable and high-performing TFC membrane with good antifouling property. Several studies also reported that the nanomaterial-incorporated PA TFC membranes can overcome the trade-off between membrane permeability and selectivity that occurs in the conventional TFC membranes; although, their fundamental mechanisms are yet to be fully understood.

The fabrication of nanocomposite membrane, however, faces several challenges. Hence, the commercialization of nanocomposite membranes for industrial-scale application will not be possible unless those challenges are addressed. Some of the major challenges include the high nanomaterial cost, toxicity, and the additional nanomaterial modification steps required to fabricate nanocomposite membranes. Besides, the nanoparticle used should be highly

dispersible in the solvent or polymer dope solution and have high polymer-nanoparticle compatibility to prevent the non-uniform distribution of nanomaterials within the membrane material. Most of the approaches adopted for the lab-scale fabrication of nanocomposite membrane may not be scalable; hence, such methods could need significant modifications.

The robustness and stability of surface-modified nanocomposite membranes to the long-term operation is another significant concern that needs to be addressed through long-term studies. Most of the published works have not reported the robustness of the nanocomposite membranes, including their ability to meet the stringent health and safety for drinking water standards. The loss of nanomaterials during fabrication not only adds to the membrane cost but could be a significant health issue if leached during the FO operation.

Overall, this review shows that the nanocomposite membranes can potentially improve membrane performance compared to the conventional TFC FO membranes. However, more research is required to improve our understanding of the nanoparticle-polymer interactions, its effect on water/solute transport mechanism and membrane fouling so that the membrane design and performance can be improved for specific applications.

# **CHAPTER 3**

## **GENERAL EXPERIMENTAL METHODS**

## **3. CHAPTER 3 General experimental methods**

### **3.1 Introduction**

This chapter presents a detailed description of the general fabrication, surface modification, characterisation and lab-scale performance evaluation methods of various flat-sheet and hollow fiber (HF) substrates prepared in this study. A general description of developing flat-sheet and outer-selective hollow fiber (OSHF) PA TFC and TFN membranes is also provided. More information on materials and experimental methods used in specific studies can be found in the respective chapters.

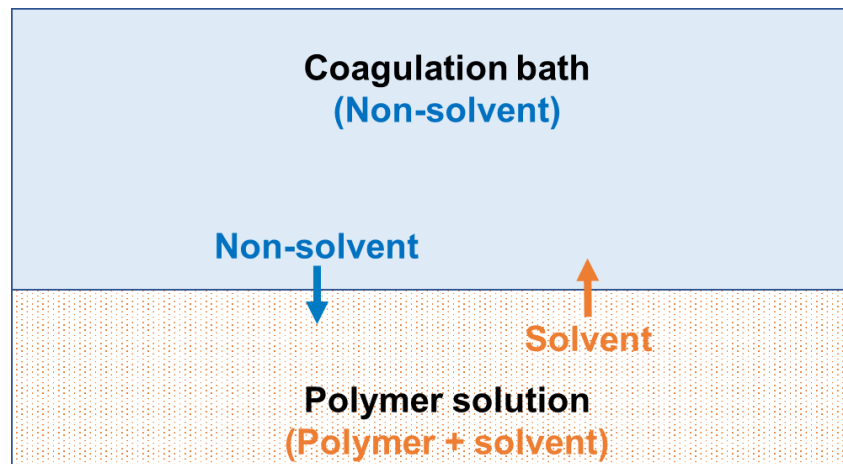
### **3.2 PA TFC FO membrane fabrication**

#### **3.2.1 TFC FO flat-sheet membranes preparation**

##### *3.2.1.1 Flat-sheet membrane substrate*

A typical non-solvent induced phase separation (NIPS) or phase inversion (PI) process is used to prepare flat-sheet membrane substrates for TFC and TFN FO membranes. In this study, polysulfone was used as the polymer to prepare the flat-sheet membrane substrates. At first, a homogenous polymer dope solution was prepared by dissolving a desired concentration of PSf in 1-methyl-2 pyrrolidone (NMP) organic solvent by continuously mixing for 24 h at 60 °C rpm using a magnetic stirrer at 500 rpm. The prepared polymer dope solution was then filtered using a PET mesh with 85 µm opening to remove any impurities and degassed overnight at 34 °C. A casting knife (Elcometer 3530) with the gate height set to 120 µm, and an automatic film applicator (Elcometer 4340) were then used to spread the polymer solution on a glass sheet under ambient conditions. Next, the cast polymer solution film was immediately dipped into a non-solvent coagulation bath, in this case water, to initiate the solvent (NMP) and non-solvent (water) exchange or PI process under ambient conditions. As illustrated in **Fig. 3.1**, the solvent moves from the dope solution

to the non-solvent coagulation bath, while the non-solvent migrates to the dope solution during the NIPS process, resulting in the formation of a membrane substrate. Finally, the PSf substrate was rinsed thoroughly with deionized (DI) water and then stored in DI water at 4 °C for at least 24 h to eradicate the residual solvents before conducting the IP process.



**Fig. 3.1** Phase inversion technique by immersion precipitation.

The structure and characteristics of membrane substrates can be influenced by varying the polymer solution composition, room temperature and humidity, casting thickness and speed, non-solvent coagulation bath temperature and composition, and the solvent/non-solvent exposure time.

#### 3.2.1.2 PA selective layer

A dense PA selective layer was formed on the porous flat-sheet membrane substrate through the IP reaction between amine MPD and acyl chloride TMC monomers. The prepared membrane substrate was first wetted with DI water and fixed on a rectangular acrylic frame (18.5 cm long  $\times$  11.5 cm wide  $\times$  1.5 cm deep). The remaining water droplets on the substrate surface were eliminated with an air knife or filter paper. Next, one side of the substrate was exposed to 50 mL of MPD aqueous solution of a specific concentration (2 or 4 wt%) for 2.5 min. The surplus MPD solution was then removed from the substrate using a nitrogen knife or filter paper. The amine saturated substrate was next contacted with 50 mL of 0.1 wt%

TMC/n-hexane organic solution for 1 min to initiate the IP reaction. The excess TMC/n-hexane was then removed and cured at room temperature for 1 min and at 60 °C for 5 min to improve the PA cross-linking degree. Finally, the TFC FO membrane was gently washed under running DI water to eradicate any residual chemicals. Lastly, the prepared PA TFC membranes were immersed and stored in DI water at 4 °C before testing their performance.

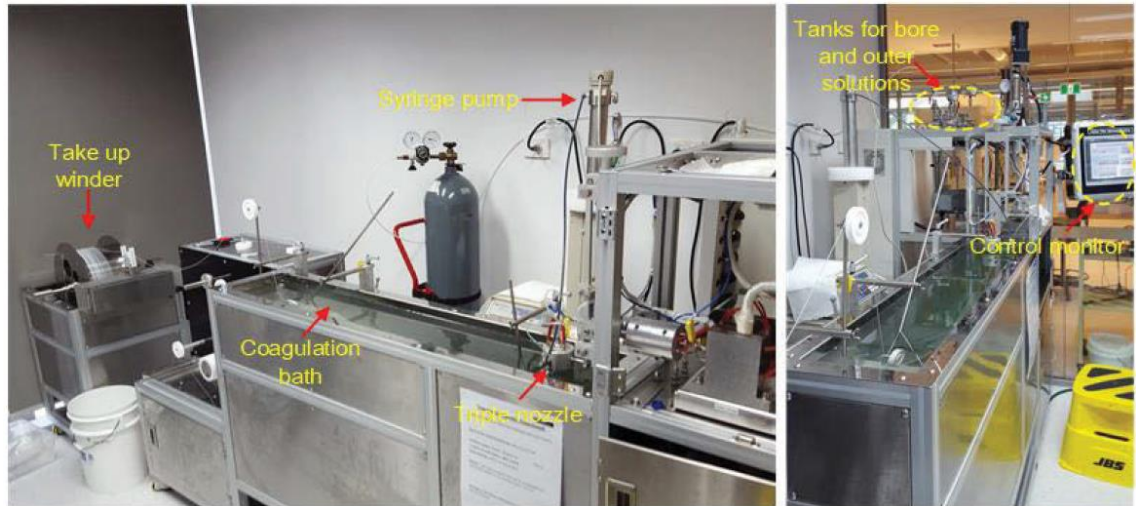
### **3.2.2 TFC FO OSHF membranes preparation**

#### *3.2.2.1 HF membrane substrate*

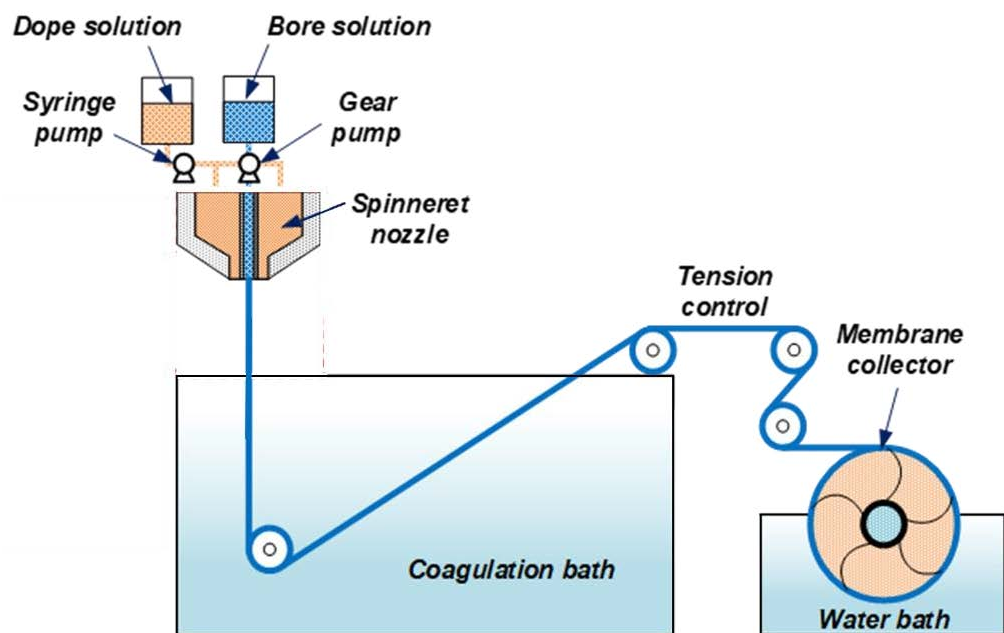
The polymer dope solution was prepared by dissolving 16.5 wt% poly(ethersulfone) (PES) powder (polymer) and 5 wt% polyethylene glycol (PEG, additive) in 78.5 wt% NMP (solvent) at 60°C for 12 h using a magnetic stirrer. PEG was added to the polymer dope solution as a hydrophilic non-solvent to facilitate pore formation and create a sponge-like porous morphology in the substrate (Cheng et al. 2016). The homogenous polymer dope solution was then poured into the syringe pump (500D, Teledyne ISCO) and left to degas overnight at room temperature before HF spinning to prevent pinhole formations in the HF substrates. The PES HF membrane substrates were prepared through the dry-jet wet PI technique at room temperature using a conventional HF spinneret assembly, as shown in **Fig. 3.2**. The degassed dope solution and the bore fluid (20 wt% NMP in DI water) were pumped into the double spinneret nozzle followed by an air-gap distance of 8 cm before being immersed in tap water coagulation bath to solidify the HF substrates via the PI process as depicted in **Fig. 3.3**. The prepared HF substrates were rolled onto a winder or membrane collector at a certain tension and stored in DI water for 24 h to eradicate the residual solvent and PEG. The substrates were later submerged in 50 wt% aqueous glycerol solution for 48 h. Subsequently, the HF membrane substrates were dried in ambient conditions before modulation to prevent the substrate pores from collapsing during storage. The specific



spinning conditions of HF substrates, as optimized in our previous study (Lim et al. 2019), are listed in **Table 3.1**.



**Fig. 3.2** HF spinneret assembly used to prepare HF substrates via dry-jet wet PI technique.



**Fig. 3.3** Representation of HF membrane substrate development using a conventional dry-jet wet spinneret assembly (Lim et al. 2019).

**Table 3.1** Spinning conditions of HF membrane substrates.

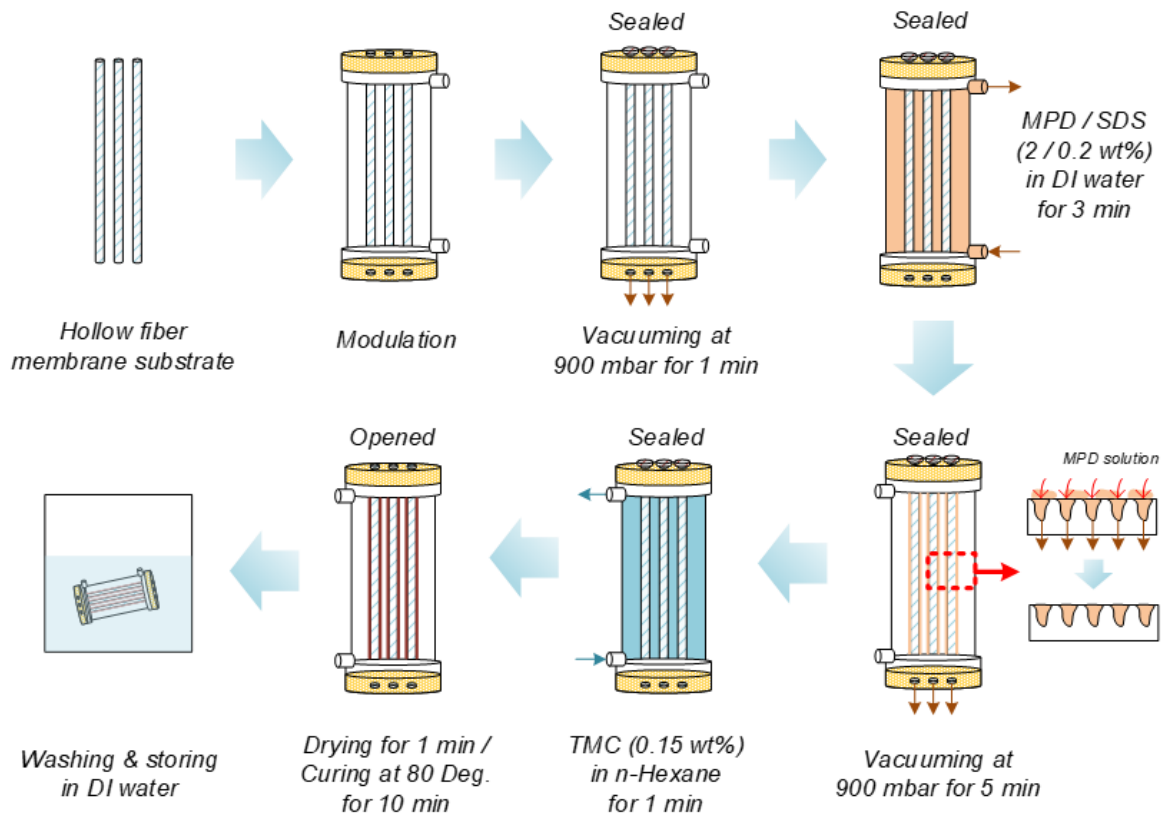
Spinning parameter	Value
Take-up speed ( $\text{m}\cdot\text{min}^{-1}$ )	0.61
Air gap (cm)	6
Bore fluid composition (wt%)	NMP/DI water: 20/80
Bore fluid flow rate ( $\text{mL}\cdot\text{min}^{-1}$ )	3
Polymer dope solution flow rate ( $\text{mL}\cdot\text{min}^{-1}$ )	1.8
External coagulant	Tap water

### 3.2.2.2 OSHF modulation and PA selective layer formation

The vacuum-assisted interfacial polymerization (VAIP) technique was employed to create PA selective layers on the outer surface of PES HF membrane substrates to develop OSHF TFC membranes using aqueous MPD and organic TMC solutions, as illustrated in **Fig. 3.4**. The detailed procedures for OSHF TFC membrane fabrication using the VAIP process are listed below:

- 1) The prepared modules containing two HF substrates were first immersed in DI water for at least a day to eradicate the remaining glycerol from the HF surface.
- 2) Excess water was then removed from the substrates by applying a vacuum at 900 mbar for 1 min.
- 3) An aqueous amine solution prepared by mixing 2 wt% MPD and 0.2 wt% sodium dodecyl sulfate (SDS) in DI water for 30 min was contacted with the outer surface of the HF substrates for 3 min.
- 4) Vacuum pressure at 900 mbar was applied for 5 min to eliminate the excess MPD solution from the shell side to the bore side of the HF.
- 5) The IP reaction was then initiated by exposing the amine saturated HF substrate to 0.15 wt% TMC/n-hexane organic solution for 1 min.

- 6) The prepared membrane modules with OSHF TFC membranes were then left to cure at room temperature for 1 min, followed by heat treatment at 80°C for 10 min to improve the PA cross-linking degree.
- 7) Lastly, the OSHF TFC membrane modules were rinsed with and stored in DI water at 4 °C before testing their performance.



**Fig. 3.4** Schematic representation of the modified VAIP technique for the development of OSHF TFC FO membrane (Lim et al. 2019).

### 3.3 Membrane characterisation

The membranes developed in this study were characterized using various techniques as listed in **Table 3.2**. More information on the specific characterisation techniques employed to investigate particular membrane properties can be found in the respective chapters.

**Table 3.2** A summary of the membrane characterisations and instruments employed in this study.

<b>Parameter</b>	<b>Instrument</b>
Membrane cross-section and surface morphology	FE-SEM (Field Emission Scanning Electron Microscope)
Membrane surface roughness	Atomic force microscopy (AFM)
Membrane surface chemistry	Attenuated Total Reflection-Fourier Transform Infrared Spectroscopy (ATR-FTIR)
Membrane surface wettability/ Contact angle measurement	Optical tensiometer
Membrane surface zeta potential	Electrokinetic analyser

### **3.3.1 Membrane cross-section and surface morphology**

Field Emission-Scanning Electron Microscope (FE-SEM, Zeiss Supra 55VP, Carl Zeiss AG) was operated at 5-10 kV to study the cross-sectional and surface morphologies of the prepared membranes. Membrane cross-section samples for SEM imaging were prepared by soaking dry membrane samples in ethanol before rupturing them in liquid nitrogen. The membrane samples were attached to stubs using copper tape and sputter-coated with 10 nm thick Au/Pd layer using a sputter coater (EM ACE600, Leica Microsystems) before conducting the SEM analysis.

### **3.3.2 Membrane surface roughness**

Atomic Force Microscopy (AFM, Dimension 3100 Scanning Probe Microscope, Bruker) was employed in tapping mode (scanning area  $5 \mu\text{m} \times 5 \mu\text{m}$ ) under ambient conditions to examine the membrane surface roughness and morphology. Dry membrane samples were fixed on metal specimen discs using double-sided adhesive tape and cleaned with a nitrogen knife before analysis. All membrane samples were scanned at least three times at randomly selected positions to obtain the average surface roughness values.

### **3.3.3 Membrane surface chemistry**

Attenuated total reflection–Fourier transform infrared spectroscopy (ATR-FTIR, IRAffinity-1 FTIR equipped with MIRacle 10 single reflection ATR accessory, Shimadzu) was used to assess changes in surface chemistries of the fabricated pristine and modified membranes. All membrane samples were dried in a vacuum desiccator for more than 48 h to remove moisture from samples before analysis. All the FTIR spectra were obtained at room temperature for the wavenumber range of 500 to 4000  $\text{cm}^{-1}$  with 20 scans at a resolution of 2  $\text{cm}^{-1}$ .

### **3.3.4 Membrane hydrophilicity**

An optical tensiometer equipped with a camera and image processing software (Attension Theta Lite 100, Biolin Scientific) was used to measure the contact angles on the membrane surfaces and assess the hydrophilicity of the membranes. Dry membrane samples were attached on microscope glass slides using a double-sided tape and placed on the sample platform. A 6  $\mu\text{L}$  droplet was then dropped on the membrane sample surface, and the contact angle measurement was made by the software using the sessile drop method. The contact angles were measured on at least six randomly selected locations for each sample to acquire the average value.

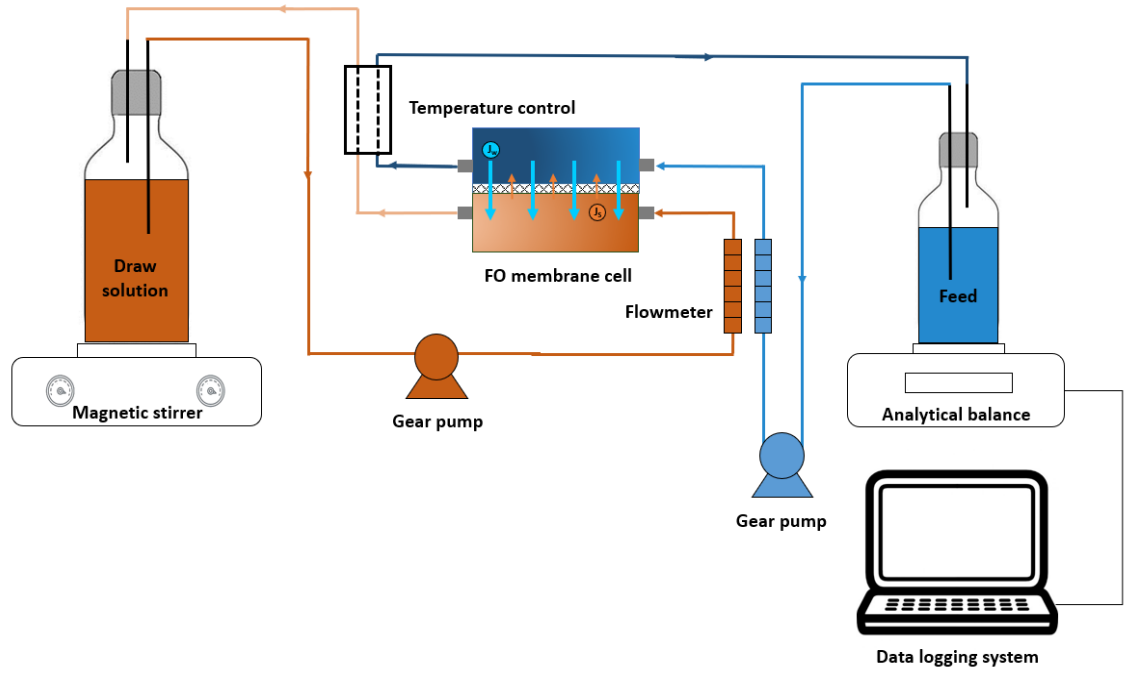
### **3.3.5 Membrane surface charge**

An electro-kinetic analyser (SurPASS™ 3, Anton Paar) was utilised to verify the membrane surface charge by measuring the zeta potential of the membranes over a pH range of 3 to 10 using an adjustable gap cell of size 20  $\times$  10 mm. The membranes were attached to the sample holder with the gap height fixed to about 100  $\mu\text{m}$ . The concentration of KCl electrolyte solution was maintained at about 1 mM and its pH was adjusted between 3 and 10 by dosing with 0.05 M NaOH and HCl solutions. The obtained streaming potential was utilized to verify the membrane surface zeta-potential by using the Helmholtz-Smoluchowski equation.

### **3.4 Membrane performance evaluation**

#### **3.4.1 FO experimental setup**

The performances of the TFC FO membranes were evaluated using a laboratory-scale FO experimental setup, as illustrated in **Fig. 3.5**. The FS and DS were circulated inside the FO cell using two variable speed gear pumps (Cole Parmer, USA) under the co-current flow mode. The temperature of both FS and DS was maintained around 22 °C throughout the performance tests using a temperature control unit. DI water was used as FS, while NaCl aqueous solution was used as DS. The membranes were tested under AL-FS (active layer facing FS) and AL-DS (active layer facing DS) orientations. The water flux ( $J_w$ ) of the membranes was determined by measuring the weight of FS at a constant interval using a digital weight balance (CAS, South Korea). The reverse salt flux ( $J_s$ ) of the membranes was obtained by monitoring the conductivity of FS using a conductivity meter (LAQUAact, Horiba Scientific, Japan). The FS weight and conductivity were recorded automatically at a constant interval using a data logging system.



**Fig. 3.5** Schematic of the lab-scale FO experimental setup used for testing membrane performance.

### 3.4.2 FO membrane performance

The membrane water flux ( $J_w$ ,  $L \cdot m^{-2} \cdot h^{-1}$ ) was determined using Eq. 3.1 from the weight of feed solution (FS), which was logged automatically at a constant time interval, where  $\Delta V_{FS}$  (L) is the change in the feed solution (FS) volume during the performance test,  $A_m$  is the effective membrane surface area ( $m^2$ ) and  $\Delta t$  (h) is the duration of the performance test.

$$J_w(L \cdot m^{-2} \cdot h^{-1}) = \frac{\Delta V_{FS}}{A_m \Delta t} \quad (3.1)$$

The reverse solute flux ( $J_s$ ,  $g \cdot m^{-2} \cdot h^{-1}$ ) through the membrane was calculated using Eq. 3.2 by monitoring the FS salinity, where  $\Delta C_{FS}$  ( $g \cdot L^{-1}$ ) is the change in FS concentration after an interval of  $\Delta t$  (h).

$$J_s(g \cdot m^{-2} \cdot h^{-1}) = \frac{\Delta C_{FS} V_{FS}}{A_m \Delta t} \quad (3.2)$$

The specific reverse solute flux (*SRSF*,  $g \cdot L^{-1}$ ), which indicates membrane selectivity, was obtained using Eq. 3.3.

$$SRSF(g \cdot L^{-1}) = \frac{J_s}{J_w} \quad (3.3)$$

### 3.4.3 Membrane intrinsic transport parameters

The pure water permeability coefficient (*A*), solute permeability coefficient (*B*) and intrinsic selectivity (*B/A*) of the pristine and modified FO membranes were predicted based on the 4-stages non-linear regression model developed for FO membranes by Tiraferri et al. (2013). The water and reverse solute fluxes of all the FO membranes required by the numerical model were obtained at four distinct DS concentrations (0.5, 1.0, 1.5, and 2.0 M NaCl).



# **CHAPTER 4**

## **SURFACE MODIFICATION OF THIN-FILM COMPOSITE FORWARD OSMOSIS MEMBRANES WITH POLYVINYL ALCOHOL–GRAPHENE OXIDE COMPOSITE HYDROGELS FOR ANTIFOULING PROPERTIES**

## STATEMENT OF CONTRIBUTION OF AUTHORS

Title of Paper	Surface modification of thin-film composite forward osmosis membranes with polyvinyl alcohol–graphene oxide composite hydrogels for antifouling properties		
Publication Status	<input checked="" type="checkbox"/> Published <input type="checkbox"/> Accepted for Publication <input type="checkbox"/> Submitted for Publication <input type="checkbox"/> Unpublished and Unsubmitted work written in manuscript style		
Publication Details	Akther, N., Ali, S.M., Phuntsho, S. & Shon, H.K. 2020, ‘Surface modification of thin-film composite forward osmosis membranes with polyvinyl alcohol–graphene oxide composite hydrogels for antifouling properties’, <i>Desalination</i> , vol. 491, p. 114591.		
<b>PRINCIPAL AUTHOR</b>			
Name of Principal Author (Candidate)	Nawshad Akther		
Contribution to the paper	Conceptualization, Data curation, Formal analysis, Investigation, Methodology, Validation, Writing – original draft.		
Certification	This paper reports on original research I conducted during the period of my Higher Degree by Research candidature and is not subject to any obligations or contractual agreements with a third party that would constrain its inclusion in this thesis. I am the primary author of this paper.		
Signature	Production Note: Signature removed prior to publication.	Date	04/09/2020
<b>CO-AUTHOR CONTRIBUTIONS</b>			
By signing the Statement of Contribution of Authors, each author certifies that:			
i. the candidate’s stated contribution to the publication is accurate (as detailed above); and ii. permission is granted for the publication to be included in the candidate’s thesis.			
Name of Co-Author 1	Syed Muztuza Ali		
Contribution to the paper	Methodology, Formal analysis.		
Signature	Production Note: Signature removed prior to publication.	Date	04/09/2020
Name of Co-Author 2	Dr. Sherub Phuntsho		
Contribution to the paper	Writing - review and editing, Funding acquisition, Supervision.		
Signature	Production Note: Signature removed prior to publication.	Date	04/09/2020
Name of Co-Author 3	Prof. Ho Kyong Shon		
Contribution to the paper	Supervision, Project administration, Resources, Funding acquisition, Validation, Writing - review and editing.		
Signature	Production Note: Signature removed prior to publication.	Date	04/09/2020

#### **4. CHAPTER 4 Surface modification of thin-film composite forward osmosis membranes with polyvinyl alcohol–graphene oxide composite hydrogels for antifouling properties**

##### **Abstract**

In this study, the polyamide (PA) layers of commercial thin-film composite (TFC) forward osmosis (FO) membranes were coated with glutaraldehyde cross-linked polyvinyl alcohol (PVA) hydrogel comprising of graphene oxide (GO) at various loadings to enhance their fouling resistance. The optimal GO concentration of 0.02 wt% in hydrogel solution was confirmed from the FO membrane performance, and its influence on membrane antifouling properties was studied. The properties of the modified membranes, such as surface morphology, surface charge and wettability, were also investigated. PVA/GO coating was observed to increase the smoothness and hydrophilicity of the membrane surface. The foulant resistances of the pristine, PVA-coated and PVA/GO-coated membranes were also reported. PVA hydrogel-coated TFC membrane with a GO loading of 0.02 wt% showed a 55% reduction in specific reverse solute flux, only a marginal reduction in the water flux, and the best antifouling property with a 58% higher flux recovery than the pristine TFC membrane. The significant improvement in the selectivity of the modified membranes meant that the hydrogel coating could be used to seal PA defects. The biocidal GO flakes in PVA hydrogel coating also improved the biofouling resistance of the modified membranes, which could be attributed to their morphologies and superior surface properties.

**Keywords:** Forward osmosis (FO); Graphene oxide (GO); Thin-film composite (TFC) membrane; Polyvinyl alcohol; Antifouling; Biofouling

## 4.1 Introduction

Water pollution from the discharge of large quantities of contaminants produced from human activities is one of the primary reasons for making water shortage a severe global problem. Consequently, treatment and safe reclamation of industrial and municipal wastewater are necessary as a sustainable solution to meet the growing freshwater demand and protect human health and the environment from harmful pollutants (Shannon et al. 2008). Stringent water guidelines and the need to treat wastewater with robust, energy-efficient and low-cost methods that require minimal chemicals have made membrane technology popular for wastewater reclamation and reuse (Chen et al. 2014; Kim et al. 2004; Mozia 2010). Pressure-driven membrane processes, such as nanofiltration (NF) and reverse osmosis (RO), have been studied for high-quality clean water production (Kim et al. 2004). Nonetheless, the efficiency of these processes is hampered with complex feed types that increase membrane fouling propensity and consequently lead to high energy consumption.

Forward osmosis (FO) process, on the other hand, uses the osmotic pressure difference between the feed solution (FS) and draw solution (DS), rather than the hydraulic pressure, to transport water molecules from FS to DS across a selective membrane (Akther et al. 2015; Ali, Kim, et al. 2018). Fouling in FO processes is more reversible than pressure-driven processes due to the absence of hydraulic pressure, thus, forming a less compact organic fouling layer that can be removed by simple backwashing and flushing. Hence, membrane cleaning in FO is much simpler than the pressure-driven processes without significant chemical cleaning requirements (Akther, Daer, et al. 2019; Akther et al. 2015; Mi & Elimelech 2010). Therefore, FO membranes have been extensively researched for application in osmotic membrane bioreactor (OMBR) for wastewater treatment and reuse (Tran et al. 2019); and can produce high-quality water by rejecting pathogens, particles and total dissolved solids (TDS).

Additionally, FO processes are more energy-efficient than RO when DS recovery is not required. For instance, they can be used for fertigation (Kim et al. 2019), treating wastewater (Tran et al. 2019), dewatering sludge (Zhu et al. 2012) and concentrating juice (Petrotos & Lazarides 2001) without needing DS recovery. Moreover, FO can be implemented in hybrid systems for treating highly saline feeds that cannot be treated by RO (Akther, Daer & Hasan 2018; Lutchmiah et al. 2014), and is suitable for directly pretreating complex feed and wastewaters (Ly et al. 2019). Consequently, it is essential to develop highly selective FO membranes with excellent antifouling properties, which will not only reduce the use of chemical cleaning reagents and maintenance costs but will also increase the membrane lifetime and offer consistent membrane performance.

The thin-film composite (TFC) membranes are most widely used for FO applications, and they comprise of a thin polyamide (PA) selective layer supported on a highly porous substrate. Both the selectivity and antifouling properties of the TFC membranes are primarily governed by the membrane selective layer properties (Akther, Lim, et al. 2019). For example, a smoother membrane surface can minimise foulant accumulation within the ridge-and-valley structures of the PA active layer (Lim et al. 2019). Whereas, a hydrophilic surface can prevent the adsorption of hydrophobic foulants by creating a water layer barrier between the foulants and the hydrophilic active layer (Emadzadeh, Lau, Matsuura, Hilal, et al. 2014). Consequently, several strategies like nanomaterial addition and polymer coating on the membrane active layer have been examined to enhance the antifouling properties of the membranes (Akther, Phuntsho, et al. 2019; Lim, Akther, et al. 2020; Lim, Park, et al. 2020b). Gao's group grafted polyvinyl alcohol (PVA) on PA TFC membrane to obtain chlorine resistant and antifouling membranes (Liu et al. 2015). The hydrophilic PVA layer acted as a protective barrier to hinder chlorine attack on the PA chain and minimised adsorption of hydrophobic foulants on the membrane surface. Zhang et al. also reported similar results by

optimising the process conditions of PVA film coating on PA TFC RO membranes. The optimal membrane demonstrated improved solute rejection and good antifouling properties towards dodecyl trimethyl ammonium bromide (Zhang et al. 2016).

Graphene oxide (GO) has gained much attention for its inherent hydrophilicity and biocidal properties and has been used as a filler to enhance membrane properties for several applications like desalination and wastewater treatment (Akther, Phuntsho, et al. 2019; Giwa et al. 2016; Inurria et al. 2018; Lim, Park, et al. 2020b; Qian et al. 2019). Hegab et al. coated GO flakes on the surface of PA TFC FO membranes using the bioadhesive polydopamine (pDA) facilitated the immobilisation method. The GO-modified membrane achieved 80% and 22% improvement in selectivity and water flux, respectively, in addition to demonstrating significant anti-biofouling properties compared to the pristine membrane (Hegab, ElMekawy, Barclay, et al. 2016). Yin et al., on the other hand, embedded multilayer GO flake structure with an interlayer spacing of  $\sim 0.83$  nm into the PA layer of the thin-film nanocomposite (TFN) membranes during the interfacial polymerisation (IP) reaction (Yin, Zhu & Deng 2016). Results indicated that, in comparison to the pristine membrane, the addition of 0.015 wt% of GO flakes in the organic phase during IP process improved the permeate flux by 52% while slightly reducing the sodium chloride (NaCl) rejection by 2% under 300 psi. The improved water permeability was attributed to the GO interlayer spacing that may have worked as water channels.

Owing to the desirable properties of both PVA and GO flakes as membrane coating, this work sought to systematically explore the influence of cross-linked hydrophilic PVA hydrogel and GO flake composite coating on the physicochemical properties, selectivity and antifouling properties of commercially-available TFC PA FO membranes. The PVA/GO hydrogel was coated on TFC membranes using a simple dip-coating method. For the first time, this study shows a facile and efficient method to improve the performance and

antifouling properties of commercial FO membrane by benefiting from the synergistic effects of intrinsically antifouling GO-modified PVA hydrogel coating, which could increase the effectiveness of TFC FO membranes in wastewater treatment.

## **4.2 Materials and methods**

### **4.2.1 Chemicals**

Commercially available PA TFC FO flat-sheet membranes from Toray Industries were used for surface modification in this study. PVA (96% hydrolysed, average MW 85,000–124,000  $\text{g}\cdot\text{mol}^{-1}$ ), sodium alginate (SA, low viscosity), calcium chloride dihydrate ( $\geq 99\%$ ) and glutaraldehyde solution (GA, grade II, 25% in water) were procured from Sigma Aldrich. Sulfuric acid ( $\text{H}_2\text{SO}_4$ , 98%) and sodium chloride ( $\text{NaCl}$ ,  $> 99.7\%$ ) were supplied by RCI Labscan Ltd. and Chem Supply, respectively. Monolayer GO with particle size  $\leq 10 \mu\text{m}$  was obtained from Graphenea (4  $\text{mg}\cdot\text{mL}^{-1}$  dispersion in water). Deionised water (DI, Milli-Q) with a resistivity of approximately  $18 \text{ M}\Omega\cdot\text{cm}^{-1}$  was used for FS and DS preparation. All reagents purchased were of analytical grade and used as received.

### **4.2.2 Hydrogel preparation and coating on PA TFC membrane**

The PVA hydrogel solution was prepared using a previously reported method (Peng, Jiang & Hoek 2011). Briefly, PVA crystalline powder was added to DI water at  $90 \text{ }^\circ\text{C}$  and dissolved by stirring for 8 h to obtain 0.25 wt% PVA aqueous solution. After cooling the PVA solution to room temperature, GA and 2 M  $\text{H}_2\text{SO}_4$  were added simultaneously as a cross-linking agent and catalyst, respectively, under vigorous stirring for 15 min at  $60 \text{ }^\circ\text{C}$  to prepare hydrogel solution. The catalyst concentration was adjusted to 1 wt% of the hydrogel solution; whereas, the GA weight was determined using Eq. 4.1 to achieve a theoretical cross-linking degree of 30%:

$$\chi_{CL}(\%) = 2 \left( \frac{MW_{PVA\ unit} W_{CL}}{W_{PVA} MW_{CL}} \right) 100\% \quad (4.1)$$

where  $\chi_{CL}$ ,  $MW_{PVA\ unit}$ ,  $W_{CL}$ ,  $W_{PVA}$  and  $MW_{CL}$  denote the theoretical cross-linking degree, molecular weight of one PVA unit, weight of cross-linking agent, weight of PVA, and molecular weight of the cross-linking agent, respectively.

PVA hydrogel solutions with various GO loadings (0.01, 0.02 and 0.04 wt%) were prepared using the same protocol as above except for the addition of GO to PVA aqueous solution at room temperature followed by stirring and sonication for 30 min each. GA and catalyst were then added to the PVA/GO aqueous solutions to prepare the PVA/GO composite hydrogel solutions. The starting GO concentration was chosen as 0.01 wt% as it was found to be the optimal GO concentration in our previous study (Akther, Yuan, et al. 2020).

The hydrogel was coated on the PA TFC FO membrane by first fixing the membrane in a rectangular frame with the PA layer exposed for coating. The exposed PA membrane surface was then immersed in the hydrogel solution for 4 min. Next, the surplus hydrogel solution was poured out from the membrane surface, and any remaining solution was gently removed using an air knife. The hydrogel coated membranes were later cured in an oven at 60 °C for 10 min. Finally, the membranes were rinsed with DI water to eradicate the unreacted PVA molecules and stored in DI water at 4 °C. **Table 4.1** presents the surface modification conditions and the abbreviation of the various membranes prepared in this study.



**Table 4.1** Surface modification conditions of PA TFC FO membranes.

Membrane	PVA (wt%)	GO (wt%)
TFC	0	0
TFC-P	0.25	0
TFC-PGO1	0.25	0.01
TFC-PGO2	0.25	0.02
TFC-PGO4	0.25	0.04

### 4.2.3 Membrane characterisation

Fourier transform infrared spectra (FTIR, Shimadzu MIRacle 10ATR-FTIR) of the membrane samples was analysed to confirm the PVA hydrogel grafting and GO flake integration on the membrane surface. All membrane samples were dried under ambient conditions before analysis. A scanning electron microscope (SEM, Zeiss Supra 55VP) was utilised to investigate the morphology of the PVA-coated membrane surface. The dry membrane samples were fixed on stubs with copper tape followed by sputter-coating with a gold layer at a thickness of 8 nm before SEM analysis. Atomic force microscopy (AFM, Dimension 3100, Bruker) was employed in tapping mode to determine the membrane surface roughness. The contact angles on the membrane surfaces were measured at ambient conditions with Attension Theta Lite 100 optical tensiometer from Biolin Scientific to ascertain the membrane hydrophilicity. At least seven measurements were made randomly for each membrane sample, and the average contact angle was reported. The membrane surface zeta potential was assessed via an electrokinetic analyser (SurPASS<sup>TM</sup> 3, Anton Paar). The membrane samples were fixed to the holder with a gap height of ~100  $\mu\text{m}$ . Zeta-potentials were determined using a 1 mM KCl electrolyte solution over a pH range of 3 to 10 adjusted with 0.05 M NaOH and HCl solutions by an automated titration system.

#### 4.2.4 Membrane performance evaluation

A laboratory-scale FO experimental setup, as described in Section 3.4.1, was used to determine the performance of membrane samples with an effective area of 20 cm<sup>2</sup>. The FO cell used for testing the membranes had a 3 mm deep flow channel on each side of the membrane. The co-current flow rate of both the FS and DS was maintained at 0.5 L·min<sup>-1</sup> (12.6 cm·s<sup>-1</sup>) at 22 °C, unless otherwise stated, during the FO membrane performance tests. The membranes were tested in AL-FS (active layer facing the feed solution) orientation with 1 M NaCl and DI water used as DS and FS, respectively. The membrane water flux ( $J_w$ , L·m<sup>-2</sup>·h<sup>-1</sup>) was determined from the weight of FS, which was automatically logged at a constant time interval by a digital weight balance (Eq. 3.1). The reverse solute flux ( $J_s$ , g·m<sup>-2</sup>·h<sup>-1</sup>) through the membrane was calculated by monitoring the FS salinity using a conductivity meter (Eq. 3.2). The specific reverse solute flux ( $SRSF$ , g·L<sup>-1</sup>) for all membranes was calculated from water and reverse solute flux values to indicate the membrane selectivity (Eq. 3.3). All the equations used for calculating the membrane performance parameters are provided in Section 3.4.2.

The pure water permeability coefficient ( $A$ ), solute permeability coefficient ( $B$ ) and intrinsic selectivity ( $B/A$ ) of the membranes were evaluated with the 4-stages non-linear regression model developed by Tiraferri et al. (2013) for FO membranes. The water and reverse solute fluxes of the FO membranes were determined at the four different NaCl DS concentrations (0.5, 1, 1.5 and 2) using the same experimental conditions as the FO performance tests. The average FO performance results of at least three samples from each membrane type was used to acquire the intrinsic transport parameters.

#### 4.2.5 Membrane fouling test

The FO membrane fouling experiments were conducted in AL-FS orientation with the same protocol used in our previous work (Akther, Yuan, et al. 2020). Firstly, the FO test was conducted for 1 h at a flow rate of  $0.5 \text{ L}\cdot\text{min}^{-1}$  to set the initial baseline water flux ( $J_{w,0}$ ) for each membrane at  $\sim 22 \text{ L}\cdot\text{m}^{-2}\cdot\text{h}^{-1}$  by adjusting the DS concentration between 0.5 M and 1 M. Secondly, a fouling study was performed for 5 h at a flow rate of  $0.5 \text{ L}\cdot\text{min}^{-1}$  by adding 1 mM calcium chloride and 200 ppm SA as foulants to the FS. The DS concentration was maintained throughout the fouling test to prevent flux decline from the DS dilution effect. Thirdly, the membranes were cleaned for 1 h after the fouling tests by circulating DI water at an increased flow rate of  $0.7 \text{ L}\cdot\text{min}^{-1}$  in DS and FS channels without using any chemical reagents. Finally, the cleaned membranes were tested with the baseline conditions to determine the flux recovery.

#### 4.2.6 Foulant resistance evaluation

The transient foulant resistances of the pristine and hydrogel-coated FO membranes were attained using the detailed procedure described by Siddiqui et al. (Siddiqui et al. 2018). Foulant resistance was reported to describe the membrane fouling behaviour more accurately than the typical permeate flux decline method. This is because the proposed method considers the foulant accumulation effect and the internal concentration polarisation self-compensation effect. The foulant resistance ( $R_f$ ) was determined using Eq. 4.2:

$$R(m^{-1}) = R_m + R_f = \frac{F}{\mu J_w} \quad (4.2)$$

where  $F$  is the osmotic driving force across the membrane,  $\mu$  denotes the solution viscosity,  $J_w$  represents the water flux, and  $R$  is the overall hydraulic resistance against the water permeation obtained by adding the membrane resistance ( $R_m$ ) and foulant resistance ( $R_f$ ).

Detailed information on the evaluation of foulant resistance for the fouled membranes is provided in Section 4.5.2.

#### **4.2.7 Static bacterial adhesion test**

Static bacterial adhesion tests were conducted using gram-positive *Bacillus subtilis* as model bacteria to examine the anti-biofouling properties of the membranes. First, the bacteria were inoculated in tryptic soy broth (TSB) medium from a single *Bacillus subtilis* colony by shaking at 120 rpm for 18 h at 37 °C. Second, the TSB medium was used to dilute the bacterial suspension 50 times prior to culturing it for 4 h at 30 °C. TSB medium was used again to adjust the bacterial suspension to acquire an optical density of 0.05 at a wavelength of 450 nm with a spectrophotometer (V-650, Jasco, Japan). Third, membranes (0.5 cm × 3 cm) were immersed in the bacterial suspension for 24 h at 30 °C to determine the bacterial growth. The soaked membranes were then rinsed twice with 0.85 wt% NaCl solution to remove weakly attached bacteria. Fourth, a NaCl solution (0.85 wt%) with SYTO9 (Life Technologies Corporation, Carlsbad, CA) was used to stain the adhered bacteria on the membrane surface for 20 min. A GA solution (2.5 wt%) was then used for 2 min to fix the stained bacteria on the membrane surface. Lastly, the membrane samples were examined by confocal laser scanning microscopy (CLSM; FV1000D, Olympus, Japan) and the obtained images were studied by ImageJ software (National Institutes of Health, USA) to quantify bacterial coverage.

### **4.3 Results and discussion**

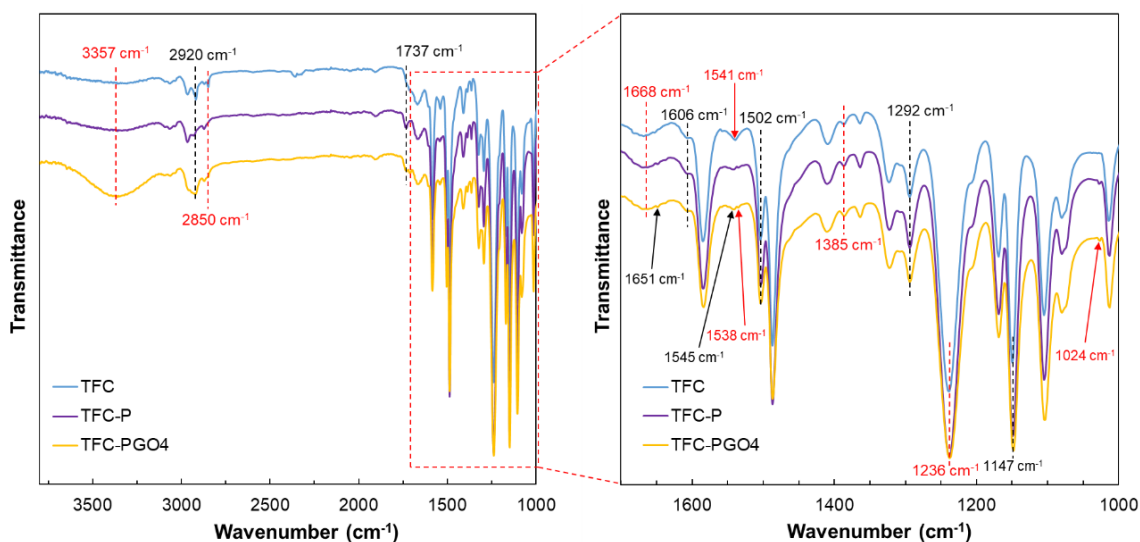
#### **4.3.1 Membrane characterisation**

In this study, the active layers of commercial PA TFC FO membranes were coated with GA cross-linked PVA hydrogels containing different concentrations of GO flakes to improve the antifouling properties of the membrane. To verify the existence of hydrogel coating on the

membrane surfaces, the surface chemistry of the pristine, PVA-coated and PVA/GO-coated TFC membranes were examined from the ATR-FTIR spectra as presented in **Fig. 4.1**. The full ATR-FTIR spectra of the pristine and modified TFC membranes show the typical peaks associated with the polysulfone (PSf) support layer and thin PA active layer. The characteristic strong peaks at  $1502\text{ cm}^{-1}$ ,  $1385\text{ cm}^{-1}$  and  $1236\text{ cm}^{-1}$  relate to the C=C in-plane aromatic ring bend stretching vibration, symmetric C–H deformation of  $\text{C}(\text{CH}_3)_2$ , and asymmetric C–O–C stretching vibration of the aryl–O–aryl group; whereas, the peaks at  $1292\text{ cm}^{-1}$  and  $1147\text{ cm}^{-1}$  represent the asymmetric and symmetric stretching vibrations of the O=S=O bonds found in PSf, respectively (Lai et al. 2018; Tang, Kwon & Leckie 2009a).

The spectra for all the membranes demonstrate the characteristic peaks of PA at  $1668\text{ cm}^{-1}$  and  $1606\text{ cm}^{-1}$ , which are attributed to the amide I and the aromatic amide band, respectively. The pristine TFC membrane also reveals a peak at  $1541\text{ cm}^{-1}$  conforming to the C–N stretching and N–H in-plane bending vibration of the amide group in PA (amide II band), which splits into two peaks at  $1545\text{ cm}^{-1}$  and  $1538\text{ cm}^{-1}$  for the pristine PVA-coated (TFC–P) and PVA/GO-coated (TFC–PGO) TFC membranes due to the reaction between GA's aldehyde groups and PA's amide bonds (–CO–NH–) (Hu et al. 2016; Tang, Kwon & Leckie 2009a). Additionally, the relative peak intensities at  $1651\text{ cm}^{-1}$ , ascribed to the C=N stretching, increased for the modified membranes due to the reaction between the end amino groups of the PA and the aldehyde groups of GA (Hu et al. 2016). The peak at  $1737\text{ cm}^{-1}$  is ascribed to the ester group (O=C–O) present in the PVA coating on the membrane surface, and the residual aldehyde groups of GA that remained unreacted during the acetalisation cross-linking reaction (Hu et al. 2016; Nisola et al. 2015). The presence of a new peak at  $1024\text{ cm}^{-1}$  on the spectra of the modified membranes indicates the formation of an ether group (C–O–C) during the reaction between the hydroxyl and aldehyde group of PVA and GA, respectively (Mansur et al. 2008).

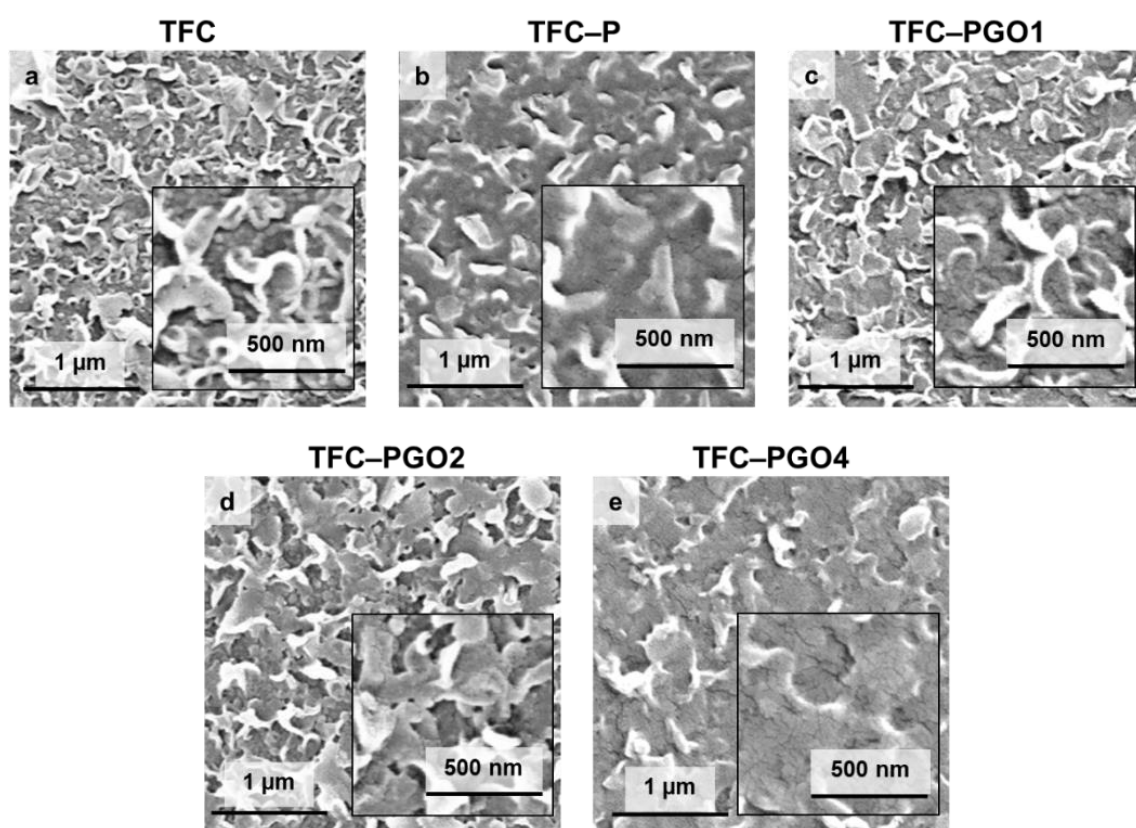
The relative intensities of peaks at  $2920\text{ cm}^{-1}$  and  $2850\text{ cm}^{-1}$  assigned to the C–H asymmetric and symmetric stretching vibration, respectively, are weaker for TFC–P than the TFC membrane because of the dilution effect of the PVA coating layer. On the contrary, TFC–PGO shows more intense peaks at  $2920\text{ cm}^{-1}$  and  $2850\text{ cm}^{-1}$  than the TFC–P membrane due to the asymmetric and symmetric stretch of C–H bonds in GO flakes (Akther, Yuan, et al. 2020). The broad peak from  $3100$  to  $3700\text{ cm}^{-1}$  results from the coinciding peaks that are attributed to the carboxyl group and N–H stretching of the PA, and hydroxyl groups (O–H) stretching of the PVA and GO flakes. Consequently, the peak intensity at  $3357\text{ cm}^{-1}$  is the highest for the TFC–PGO membrane due to abundant O–H groups in both GO flakes and cross-linked PVA. Overall, ATR-FTIR analysis results validate the effective coating of GA cross-linked PVA on the PA layer surface and the GO flakes integration into the PVA hydrogel coating.



**Fig. 4.1** ATR-FTIR spectra of the pristine and modified TFC membranes.

The morphologies of the pristine and modified TFC membrane surfaces were examined from the SEM (**Fig. 4.2**) and AFM (**Fig. 4.3**) micrographs that clearly show the changes in membrane morphologies following the surface modification. The SEM images show a uniform distribution of the typical ridge-and-valley PA formations on the pristine TFC

membrane surface (**Fig. 4.2a**); however, more distinct physical irregularities can be observed for the modified membranes (**Fig. 4.2b-e**). Coating the PA layer with cross-linked PVA (TFC-P), as shown in **Fig. 4.2b** made the TFC membrane surface denser and considerably smoother than the pristine TFC membrane. However, the surfaces of the PVA-coated TFC membranes became more inconsistent after incorporating GO flakes, forming patches that eventually covered the PA protrusions completely at a GO loading of 0.04 wt% (**Fig. 4.2e**).

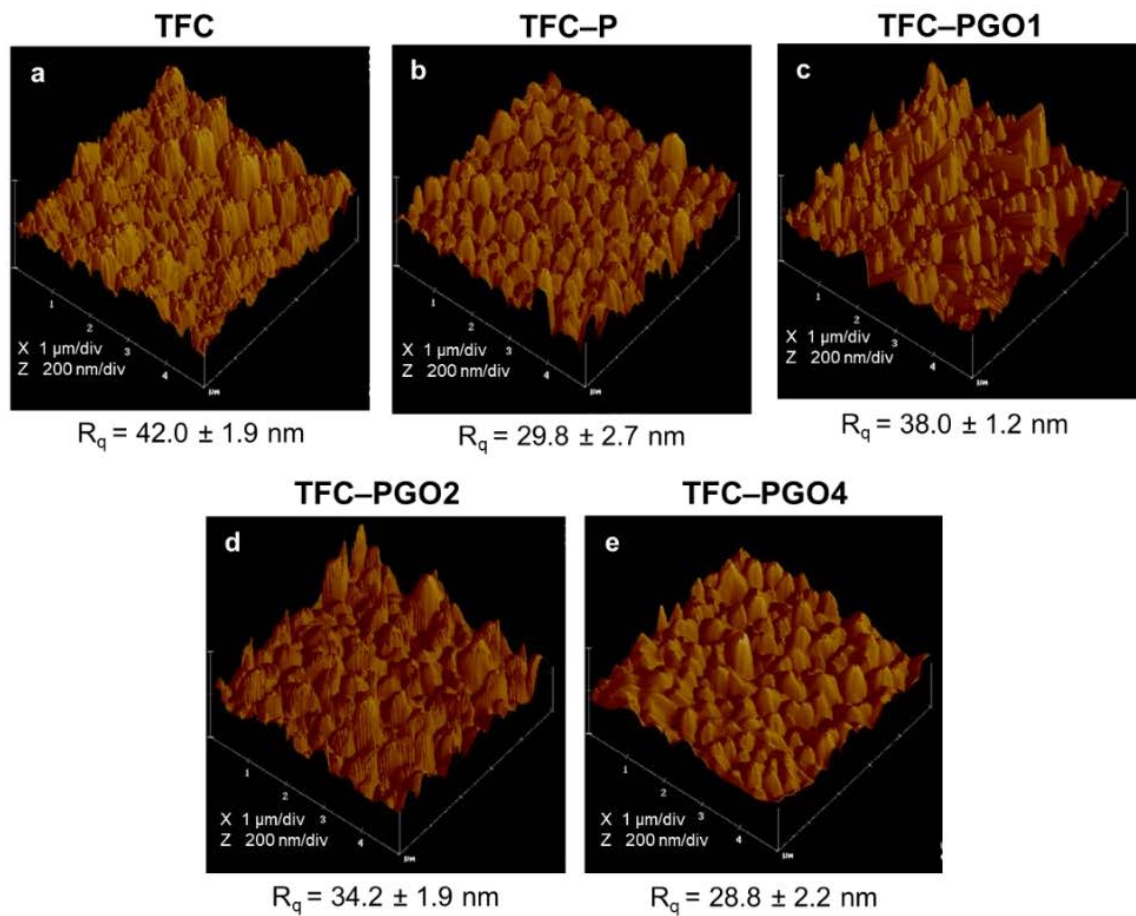


**Fig. 4.2** SEM images revealing the surface morphology of the (a) pristine TFC membrane; and PVA hydrogel coated TFC membranes with different GO loadings: (b) 0, (c) 0.01, (d) 0.02, and (e) 0.04 wt%.

The membrane surface roughness was quantitatively characterised using AFM (**Fig. 4.3**). The average ( $R_a$ ), maximum ( $R_{max}$ ) and root mean square values ( $R_q$ ) of the membrane surface roughness are provided in **Table S4.1**. The  $R_q$  values of the pristine TFC membrane and modified TFC-P, TFC-PGO1, TFC-PGO2 and TFC-PGO4 were 42.0 nm, 29.8 nm, 38.0 nm, 34.2 nm and 28.8 nm, respectively. The membrane roughness decreased after

coating the TFC membrane surface with PVA hydrogel (**Fig. 4.3b**). However, the roughness of the modified membranes increased after the addition of GO flakes in the PVA hydrogel, which eventually decreased with an increase in GO loading (**Fig. 4.3c-e**). It can be seen from both the SEM and AFM images that PVA hydrogel without GO flakes uniformly coated the membrane surface. On the contrary, the addition of GO flakes in PVA hydrogel formed irregular patches of PVA hydrogel aggregates on the membrane surfaces. A GO loading of 0.01 wt% formed smaller hydrogel aggregates resulting in a rougher membrane surface; whereas, the highest GO loading of 0.04 wt% formed large hydrogel aggregates that completely covered the membrane surface to provide the smoothest surface. The changes in membrane morphology could occur from the interaction between GO and PVA, where the non-uniform coating may most likely result from the solidification of PVA hydrogel directly on top of the GO flakes instead of the PA layer itself. Overall, the coated membranes were much smoother than the pristine TFC membranes because of the preferential deposition of PVA over the valley regions of the PA layer, which may improve the antifouling property of the membranes by reducing the surface area for foulant adhesion (Tang, Kwon & Leckie 2009b).





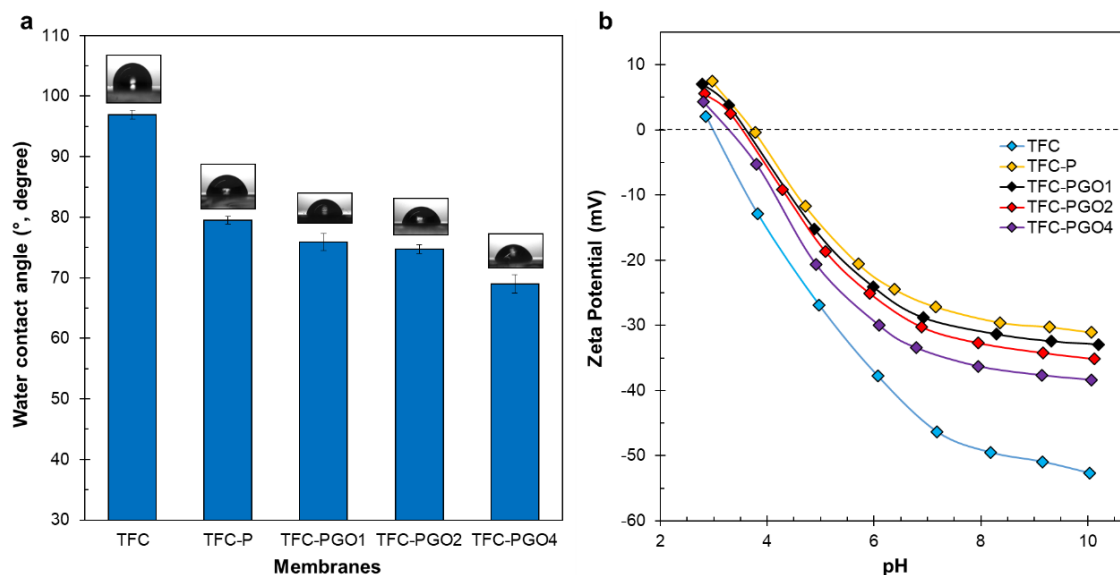
**Fig. 4.3** AFM images revealing the surface roughness of the (a) pristine TFC membrane; and PVA hydrogel coated TFC membranes with different GO loadings: (b) 0, (c) 0.01, (d) 0.02, and (e) 0.04 wt%. Error bars for membrane surface roughness represent one standard error obtained from at least four membrane samples for each condition.

The wettability of membrane surfaces before and after surface modification was determined from water contact angle measurements made at the air-water interface. As presented in **Fig. 4.4a**, the average water contact angle on the membrane surface significantly reduced from  $96.9^\circ$  for the pristine TFC membrane to  $79.5^\circ$ ,  $75.9^\circ$ ,  $74.7^\circ$  and  $69.0^\circ$  for the hydrogel-coated membranes TFC-P, TFC-PGO1, TFC-PGO2 and TFC-PGO4, respectively, which confirms the enhancement in membrane hydrophilicity after surface modification. The improved hydrophilicity of the modified membranes could be ascribed to the hydrophilic nature of PVA and GO flakes arising from the presence of oxygen-containing functional groups. Membrane surface hydrophilicity is critical as it can significantly affect membrane

performance. Increased membrane surface wettability could help improve water permeation and reduce adsorption of hydrophobic foulants on membrane surfaces by creating a water barrier between the hydrophilic membrane surface and the hydrophobic foulants (Rastgar et al. 2018).

The surface charges of the pristine and modified membranes were determined by measuring their surface zeta potentials over a pH range of 3 to 10. As can be observed from **Fig. 4.4b**, all membrane surfaces were negatively-charged at pH higher than 3.8 due to the deprotonation of the amino and carboxyl functional groups of the PA layer (Lau, Ismail, et al. 2015). Besides, the increasing surface negative charge of all the membranes at higher pH could be attributed to the adsorption of chloride ions from the electrolyte solution on the membrane surface (Akther, Yuan, et al. 2020). At lower pH, the membranes revealed positively-charged surfaces because of the protonation of the PA end amino groups. The pristine TFC membrane was the most negatively-charged due to the existence of abundant carboxyl groups. The modified TFC membranes, on the other hand, demonstrated lower surface negative charge than the pristine TFC membrane because the shielding effect of the hydrogel coating on membrane surface diminished the exposure of PA carboxyl groups (Liu et al. 2015). These results are expected due to the neutral properties of the PVA molecules. Finally, the zeta potential of the PVA/GO-coated membranes was higher than the pristine TFC membrane but lower than the PVA-coated (TFC-P) membrane. The surface negative charge of PVA/GO-coated membranes increased with an increase in GO loading because GO flakes contain abundant oxygen-containing functional groups, such as the carboxyl groups, that increase negative charges by deprotonating at alkaline conditions. **Fig. 4.4b** also reveals the isoelectric point (IEP), where the membrane surface carries no net charge. The IEPs of the modified membranes move to lower pH after incorporating GO flakes in the

PVA hydrogel due to the increasing amount of acidic functional groups from GO (Akther, Yuan, et al. 2020; Dimiev, Alemany & Tour 2013).



**Fig. 4.4** Water contact angle measurements, and (b) zeta potentials as a function of pH for the pristine and modified TFC membrane surfaces. Error bars for water contact angle measurements represent one standard error obtained from at least seven measurements for each membrane sample.

Overall, the changes in membrane surface chemistry, morphology, wettability and charge after modification confirm the successful coating of the cross-linked PVA and GO on the PA layer of the commercial TFC FO membrane. The above characterisation results also established that the physicochemical properties of the PVA-coated membranes could be adjusted by changing the GO loading in PVA hydrogel.

### 4.3.2 Membrane performance evaluation

The FO membrane performance, including the water flux, reverse solute flux and *SRSF* were evaluated for the pristine and modified membranes in AL-FS orientation using DI water as FS and 1 M NaCl as DS (**Fig. 4.5**). As expected, the modified membranes demonstrated lower water and reverse solute flux than the pristine TFC membranes as a result of the increased hydraulic resistance from the PVA or PVA/GO cross-linked hydrogel layer that

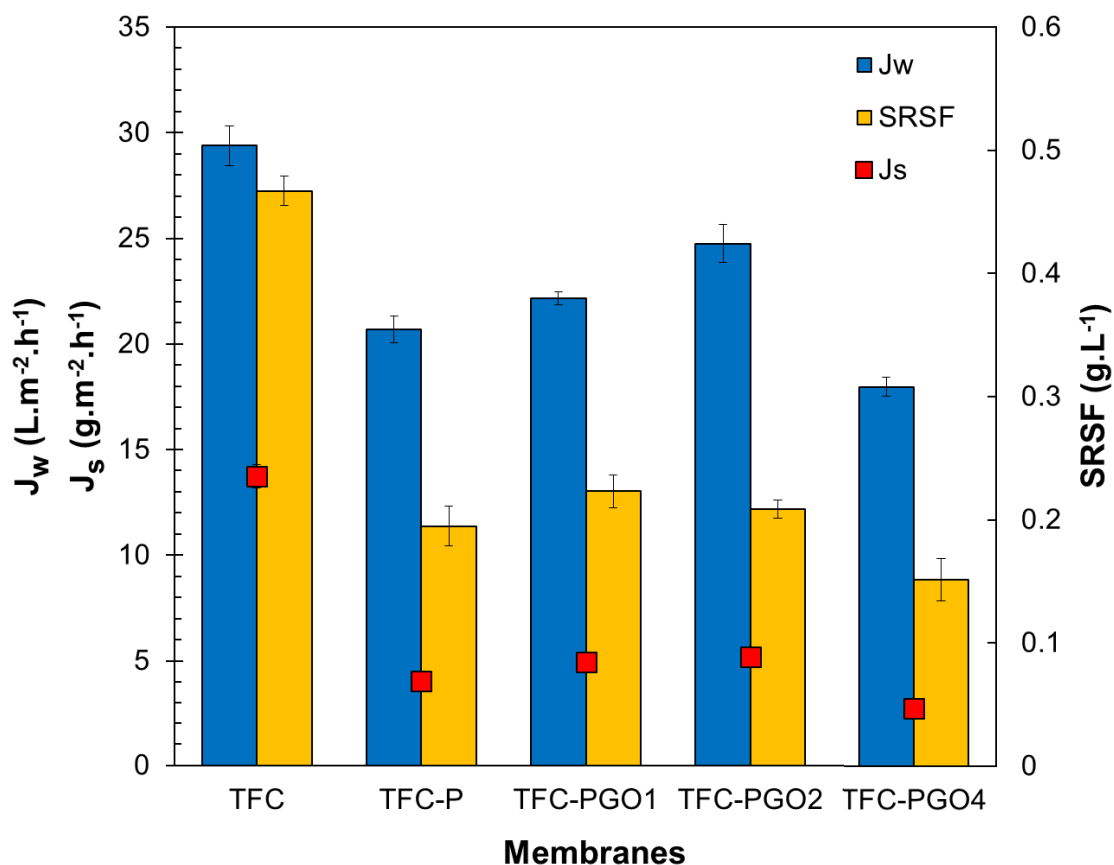
impeded water permeation. While the PVA coating improved the membrane surface wettability, which is essential to promote water permeability, the reduction in water flux occurred as the negative effect of additional hydraulic resistance transcends the positive influence of increased hydrophilicity. The dense PVA or PVA/GO coating improved the TFC membrane selectivity by augmenting the effect of size exclusion to draw solute; thus, decreasing the reverse solute flux across the modified membranes.

Conversely, the water flux through the modified membranes increased after GO flake addition up to a loading of 0.02 wt% (TFC-PGO2), while retaining membrane selectivity. Both the water flux and reverse solute flux were observed to decrease on further increasing the GO loading to 0.04 wt%. The higher water flux of TFC-PGO1 and TFC-PGO2 compared to the TFC-P could be ascribed to their reduced hydraulic resistance owing to more PA surface exposure from the uneven PVA coating on their surfaces as discussed earlier (**Fig. 4.3b-d**). Additionally, the improved hydrophilicity of the TFC-PGO1 and TFC-PGO2 could have also contributed to enhancing their water flux than the TFC-P membrane. The rougher membrane surfaces and the slight increase in the reverse solute flux of the TFC-PGO1 and TFC-PGO2 than the TFC-P membrane further confirmed that the discontinuous PVA/GO coating contributed to their water flux enhancement. The TFC-PGO4 demonstrated a significant decline in both the water and reverse solute flux due to the creation of a very dense hydrogel layer that covered almost the entire PA surface, as evident from its smoother surface (**Fig. 4.3e**) compared to that of the TFC-P membrane (**Fig. 4.3b**). The nonporous GO flakes at a loading of 0.04 wt% also created impervious regions in the PVA hydrogel matrix, which could have inhibited both water and solute permeation across the TFC membrane (Yu et al. 2016). Consequently, the TFC-PGO4 demonstrated the lowest water flux ( $18.0 \text{ L}\cdot\text{m}^{-2}\cdot\text{h}^{-1}$ ) and reverse solute flux ( $2.7 \text{ g}\cdot\text{m}^{-2}\cdot\text{h}^{-1}$ ) compared to the other modified membranes. Besides, the high concentration of GO flakes in the PVA hydrogel

could increase the composite hydrogel layer's tortuosity by forming numerous water channels at the GO-PVA interface (Chong, Wang & Li 2016).

The *SRSF* is an essential parameter for evaluating the FO membrane selectivity, where a more selective membrane exhibits a smaller *SRSF* value. The modified membranes exhibited at least 56% lower *SRSF* than the pristine TFC membrane due to the dense PVA or PVA/GO layer formation. The pristine TFC membrane showed the highest *SRSF* value ( $0.47 \text{ g}\cdot\text{L}^{-1}$ ) because of the looser dynamic pore structure of the PA layer that allowed comparatively more solute to diffuse from the DS to the FS. The *SRSF* values of TFC-P ( $0.19 \text{ g}\cdot\text{L}^{-1}$ ), TFC-PGO1 ( $0.22 \text{ g}\cdot\text{L}^{-1}$ ) and TFC-PGO2 ( $0.21 \text{ g}\cdot\text{L}^{-1}$ ) were similar, but that of TFC-PGO4 ( $0.15 \text{ g}\cdot\text{L}^{-1}$ ) was much lower, possibly due to the additional resistance from nonporous GO flakes. The TFC-PGO2 was chosen as the optimal membrane as it showed the highest water flux among the other modified TFC membranes without affecting the membrane selectivity. Moreover, the enhanced selectivity of the modified membranes makes them promising for application in wastewater reclamation and desalination.

The intrinsic transport properties of the pristine and modified TFC membranes examined in this work were evaluated from the pure water permeability coefficient (*A*) and solute permeability coefficient (*B*), which are listed in **Table 4.2**.



**Fig. 4.5** FO performance of the pristine and modified TFC membranes. Operating conditions: FS, DI water; DS, 1 M NaCl; cross-flow velocity, 12.6 cm·s<sup>-1</sup>; membrane orientation, AL-FS. Error bars represent one standard error obtained from at least three membrane samples for each condition.

**Table 4.2** Intrinsic transport parameters of the membranes.

Membrane	$A$ (L·m <sup>-2</sup> ·h <sup>-1</sup> ·bar <sup>-1</sup> )	$B$ (L·m <sup>-2</sup> ·h <sup>-1</sup> )	$B/A$ (bar)
TFC	6.41	1.15	0.18
TFC-P	3.41	0.22	0.06
TFC-PGO1	3.98	0.30	0.08
TFC-PGO2	4.75	0.31	0.07
TFC-PGO4	2.97	0.12	0.04

The modified membranes demonstrated lower  $A$  and  $B$  values than the pristine TFC membrane (6.41 L·m<sup>-2</sup>·h<sup>-1</sup>·bar<sup>-1</sup> and 1.15 L·m<sup>-2</sup>·h<sup>-1</sup>, respectively). The additional dense PVA or PVA/GO hydrogel layer on the TFC membrane surface lessened the permeability

and increased the selectivity of the modified membranes by increasing the hydraulic resistance across the membrane. The modified membranes TFC–PGO1 ( $3.98 \text{ L}\cdot\text{m}^{-2}\cdot\text{h}^{-1}\cdot\text{bar}^{-1}$ ) and TFC–PGO2 ( $4.75 \text{ L}\cdot\text{m}^{-2}\cdot\text{h}^{-1}\cdot\text{bar}^{-1}$ ) demonstrated higher  $A$  values than the TFC–P ( $3.41 \text{ L}\cdot\text{m}^{-2}\cdot\text{h}^{-1}\cdot\text{bar}^{-1}$ ) membrane due to their enhanced hydrophilicity and less dense PVA/GO layer resulting from the uneven hydrogel coating. The TFC–PGO4; however, exhibited the lowest  $A$  value ( $2.97 \text{ L}\cdot\text{m}^{-2}\cdot\text{h}^{-1}\cdot\text{bar}^{-1}$ ) due to the formation of a very dense, tortuous and partially nonporous PVA/GO hydrogel layer coating. The dense hydrogel layers reduced the  $B$  values of the modified membranes than the pristine TFC membrane through the size exclusion effect. The intrinsic membrane selectivity ratio ( $B/A$ ) is shown in **Table 4.2**, where a more selective membrane is represented by a smaller  $B/A$  ratio and vice versa. The pristine TFC membrane revealed the largest  $B/A$  ratio of 0.18 bar; while TFC–PGO4 revealed the highest selectivity with the lowest  $B/A$  ratio of 0.04 bar. The intrinsic transport parameters of the membranes are in good conformity with the FO test results shown in **Fig. 4.5**, and demonstrated that their separation performance could be tuned by simply adjusting the GO loading in the PVA hydrogel coating. Moreover, the improved selectivity of the modified membranes suggests that the PVA hydrogel coating could be used to seal defects on the PA TFC membrane.

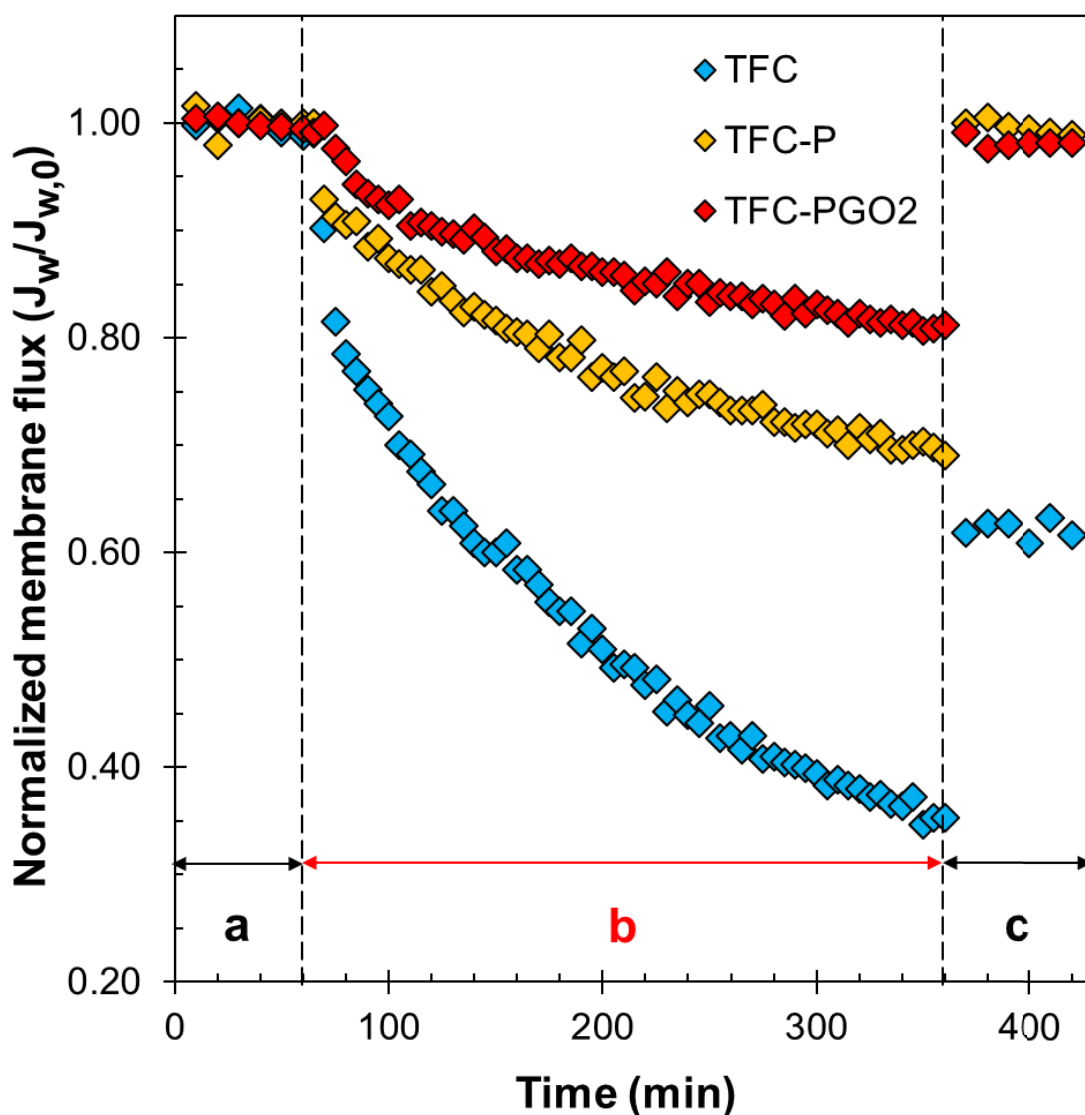
### 4.3.3 Membrane fouling study

The antifouling properties of the pristine and hydrogel-coated TFC membranes were assessed from the FO fouling tests with the membranes placed in AL-FS orientation. The TFC, TFC–P and TFC–PGO2 were utilised to study the influence of PVA hydrogel and GO flakes on the fouling tendency of the TFC membranes. **Fig. 4.6** presents the normalised membrane water flux ( $J_w/J_{w,0}$ ) obtained throughout the fouling experiment. The initial water flux ( $J_{w,0}$ ) for all the membranes was set to  $\sim 22 \text{ L}\cdot\text{m}^{-2}\cdot\text{h}^{-1}$ . Baseline tests were conducted for 1 h with foulant-free FS that resulted in stable water flux through the membranes (**Fig. 4.6a**).

The normalised water flux for the membranes immediately declined after foulants were added to the FS as they experienced increased transport resistance from foulant build-up on their surfaces, which eventually hindered water permeability across the membranes (**Fig. 4.6b**). Despite possessing the most negatively charged surface (**Fig. 4.6b**), the pristine TFC membrane failed to repel the negatively charged alginate molecules effectively and experienced the maximum flux decline at the end of the fouling study, which reached a normalised flux of 0.35. The observed fouling behaviour can be attributed to the bridging effects of the calcium ions between the PA layer and alginate chains to form a gel-like alginate layer on the TFC membrane surface (Hu, Zheng & Mi 2016; Yadav 2020). Besides, the comparatively rougher and less hydrophilic surface of the pristine TFC membrane promoted more foulant adhesion on its surface than the modified TFC-P and TFC-PGO2 membranes. Moreover, the relatively poor selectivity of the TFC membrane could have accelerated its fouling from the existence of electrostatic attraction amid the DS ions and the charged foulants (Lim et al. 2019).

On the other hand, the modified membranes showed significantly better antifouling properties than the pristine TFC membrane with the TFC-PGO2 exhibiting the lowest flux decline (**Fig. 4.6b**). The TFC-P and TFC-PGO2 membranes reached normalised fluxes of 0.69 and 0.81, respectively, at the end of the 5 h fouling test. The improved antifouling properties of the modified membranes could be attributed to their smooth surfaces that restrained hydrophobic foulant attachment on their surfaces by offering lesser adhesion sites. The hydrophilic modified membranes prevented the attachment of hydrophobic alginate molecules by forming a layer of hydrogen-bonded water molecules on their surfaces (Tiraferri et al. 2012b). The better fouling resistance of the TFC-PGO2 membrane than the TFC-P membrane could be attributed to its improved hydrophilicity.





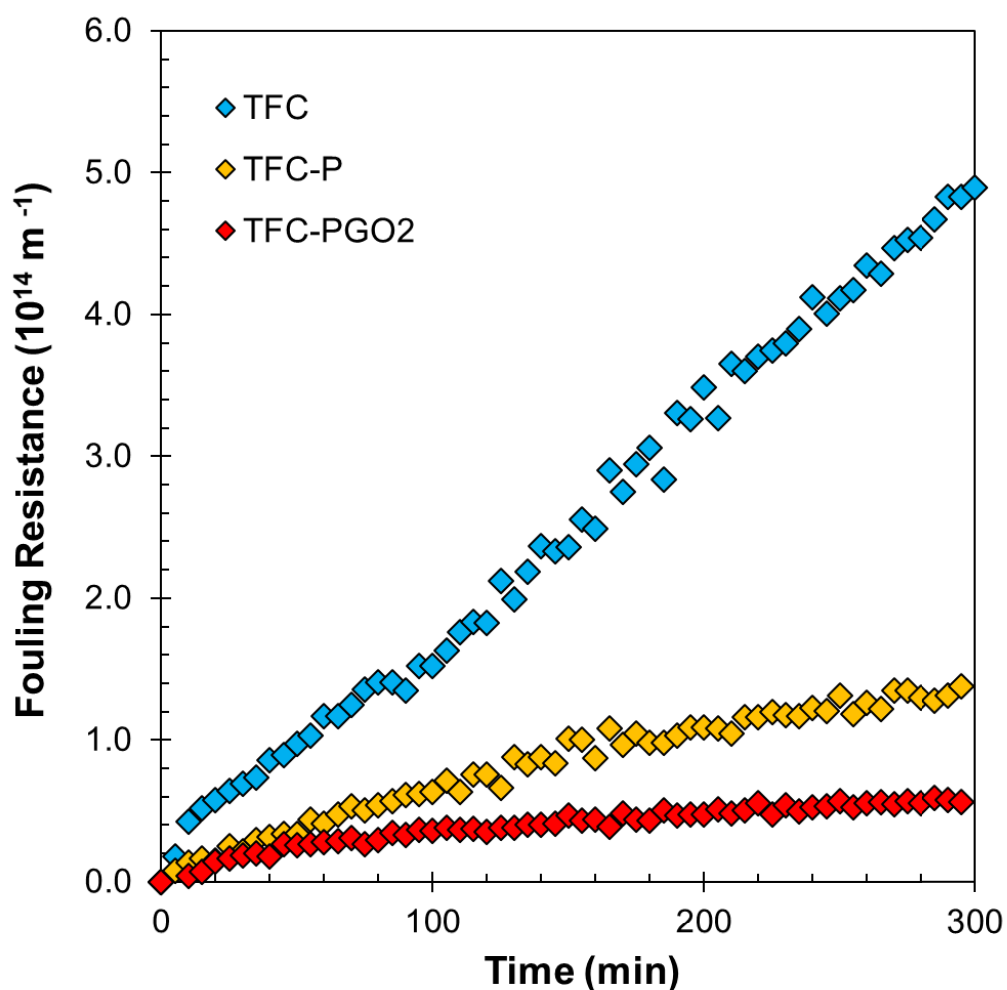
**Fig. 4.6** Normalised flux of the pristine and modified TFC membranes during the FO (a) baseline test, (b) fouling test and (c) after hydraulic cleaning. Operating conditions: Initial baseline water flux ( $J_{w,0}$ ),  $\sim 22 \text{ L}\cdot\text{m}^{-2}\cdot\text{h}^{-1}$ ; DS, 0.5 M to 1 M NaCl; flow rate (baseline and fouling test),  $0.5 \text{ L}\cdot\text{min}^{-1}$ ; flow rate (physical cleaning),  $0.7 \text{ L}\cdot\text{min}^{-1}$ ; membrane orientation, AL-FS; foulants, 1 mM calcium chloride and 200 ppm SA.

After finishing the fouling tests, the membranes were rinsed physically with DI water for 1 h and tested under baseline conditions to determine their flux recovery. As can be seen from **Fig. 4.6c**, the normalised flux increased for the membranes following the cleaning procedure, which signifies that the membranes demonstrated reversible fouling to a certain degree. The pristine TFC membrane achieved a low flux recovery of 62%; thus, showing

significant irreversible fouling due to strong fouling layer adhesion on the membrane surface. In contrast, the modified TFC–P and TFC–PGO2 membranes demonstrated comparatively high flux recoveries of 99% and 98%, respectively, which can be associated with their smoother surfaces that allowed simpler foulant removal owing to the existence of less foulant adhesive sites on their surfaces. Moreover, the improved hydrophilicity of the TFC–P and TFC–PGO2 membranes diminished the interaction between foulant and their surfaces that led to the development of a loosely bound foulant layer that could be removed effortlessly using a high cross-flow velocity in the cleaning stage. Hence, it can be established from the fouling results that the fouling was partially reversible by physical cleaning for the pristine TFC membrane but almost completely reversible for the TFC–P and TFC–PGO2 membranes.

#### 4.3.4 Membrane foulant resistance

The transient foulant resistances ( $R_f$ ) of the pristine TFC, TFC–P and TFC–PGO2 membranes were established from the osmotic-resistance filtration models using the experimentally determined membrane resistance ( $R_m$ ) (Table S4.2), structural parameter of 409  $\mu\text{m}$ , water flux and osmotic driving force. The water flux was obtained from the FO fouling experiment, as shown in Fig. 4.6. The  $R_f$  for pristine TFC membrane increased more rapidly as the fouling progressed than that for the modified membranes (Fig. 4.7). At the end of the fouling test, the  $R_f$  for TFC membrane ( $4.89 \times 10^{14} \text{ m}^{-1}$ ) was over 3.5 and 8.7 times greater than that for TFC–P ( $1.38 \times 10^{14} \text{ m}^{-1}$ ) and TFC–PGO2 ( $0.56 \times 10^{14} \text{ m}^{-1}$ ) membranes, respectively. The comparison of foulant resistances demonstrates that the pristine TFC membrane is the most susceptible to foulant deposition, whereas the GO-incorporated TFC–PGO2 membrane is the least prone to fouling.

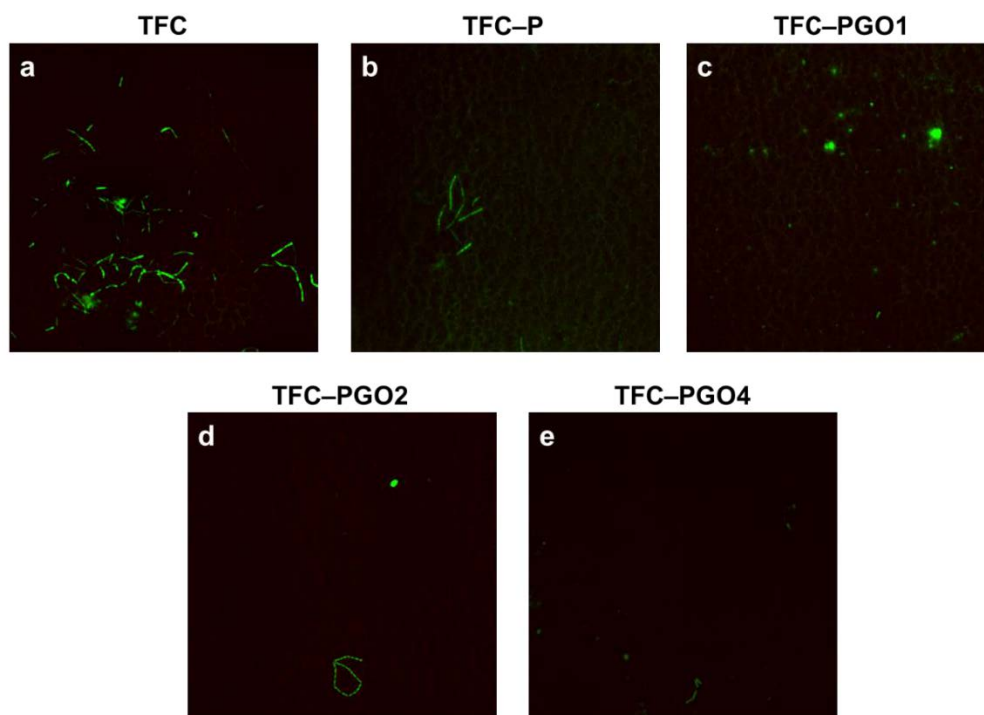


**Fig. 4.7** Fouling resistance of pristine and modified TFC membranes during the FO fouling test.

#### 4.3.5 Bacterial anti-adhesion performance

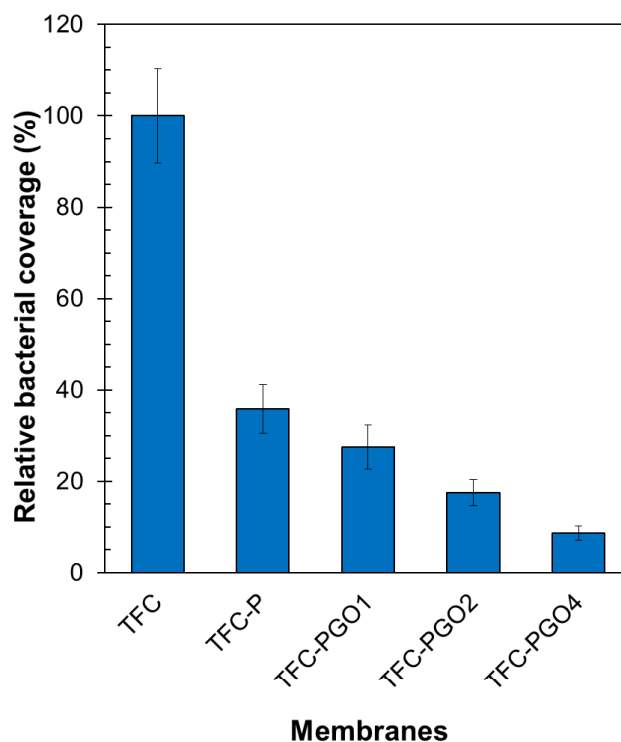
The anti-biofouling performance of the membrane samples was examined via static bacterial adhesion tests using *Bacillus subtilis* as the model bacteria. **Fig. 4.8** shows the epifluorescent images of *Bacillus subtilis* biofilms on the control pristine TFC membrane and the modified TFC membranes. After 24 h exposure to the bacterial solution, the pristine TFC membrane showed maximum bacterial adhesion (**Fig. 4.8a**). The bacterial adhesion on the modified membranes was normalised with that on the pristine TFC membrane. The modified TFC membranes (**Fig. 4.8b-e**) showed substantially lower relative bacterial coverage than the pristine TFC membrane as they possess a smoother and more hydrophilic surface than the

pristine TFC membrane. The smoother surfaces of the modified membranes provided fewer sites for bacterial adhesion. At the same time, the improved membrane surface hydrophilicity weakened the adsorption of hydrophobic bacteria to the surface by creating a hydration layer on the membrane surface (Perreault et al. 2016).



**Fig. 4.8** Static bacterial adhesion on (a) pristine and modified TFC membranes with different GO loadings: (b) 0, (c) 0.01, (d) 0.02, and (e) 0.04 wt%.

The PVA/GO-coated TFC membranes exhibited superior antibacterial activity compared to the TFC and TFC-P membranes, and the relative bacterial coverage on the PVA/GO-coated TFC membranes decreased with increasing GO loading (**Fig. 4.8c-e**). The relative bacterial adhesion of the PVA/GO-modified membrane decreased from 27% to 9% when the GO loading was increased from 0.01 wt% to 0.04%, which proves the biocidal effect of PVA/GO coating (**Fig. 4.9**).



**Fig. 4.9** Relative bacterial coverage on the pristine and modified TFC membrane surfaces. The bacterial adhesion on each membrane surface was normalised with respect to the pristine TFC membrane. Error bars represent one standard error obtained from at least three membrane samples for each condition.

In addition to the membrane hydrophilicity, the enhanced antibacterial properties of the PVA/GO-modified membranes could be attributed to their negatively charged membrane surfaces and the biocidal effect of the exposed GO flakes (Hegab, ElMekawy, Barclay, et al. 2016). The more negatively-charged surface of the PVA/GO-modified membranes arising from the epoxide, hydroxyl and carboxyl groups of the GO flakes could mitigate bacterial adhesion on their surfaces by electrostatically repelling the negatively-charged bacteria and extracellular polymeric substance, which is closely associated with biofilm development (Costerton et al. 1995). The biocidal activity of the exposed GO flakes is associated to their reactive edges that damage bacterial cell by creating oxidative stress or rupturing the cell membrane; thereby, leading to viability loss and death of the bacterial cell (Hu et al. 2010). The results suggest that addition on GO in PVA hydrogel can effectively suppress the

bacterial adhesion and growth on the membrane surface, thereby, considerably augmenting the anti-biofouling property of the membranes.

## **4.4 Conclusions**

Commercial PA TFC FO membranes were coated with a thin layer of cross-linked PVA and PVA/GO hydrogel to increase the selectivity, antifouling and anti-biofouling properties of the membranes. The hydrogel coating smoothened and improved the wettability of the membrane surface, while slightly declining the water flux. The membrane surface properties, performances and antibacterial properties were tuned by adjusting the GO loading in the PVA hydrogel coating. The modified TFC membrane with a GO loading of 0.02 wt% (TFC–PGO2) is chosen as the optimal membrane as it revealed the highest water flux among the modified membranes without sacrificing membrane selectivity. The TFC–PGO2 membrane exhibited improved solute rejection, cleaning efficiency and bacterial resistance with a 55% lower *SRSF*, 36% higher flux recovery and 82% lower relative bacterial coverage compared to the pristine TFC membrane. Consequently, the facile PVA/GO modification technique demonstrated in this study could be used to effectively seal the membrane defects and improve antifouling and anti-biofouling performance for potential application in wastewater reclamation and desalination.

## **4.5 Supporting Information**

### **4.5.1 Membrane surface roughness**

The effect of PVA/GO hydrogel coating on the PA layer surface roughness was analysed from the surface topography obtained using AFM. The maximum ( $R_{max}$ ), mean ( $R_a$ ) and root mean square ( $R_q$ ) membrane roughness of the membranes are listed in **Table S4.1**.

**Table S4.1** Surface roughness parameters of the pristine and coated TFC membranes obtained from examining at least three arbitrarily chosen membrane areas ( $5 \mu\text{m} \times 5 \mu\text{m}$ ) using AFM.

Membrane	$R_q$ (nm)	$R_a$ (nm)	$R_{max}$ (nm)
TFC	$42.0 \pm 1.9$	$32.9 \pm 1.3$	$338.5 \pm 25.4$
TFC-P	$29.8 \pm 2.7$	$22.9 \pm 1.9$	$253.7 \pm 48.3$
TFC-PGO1	$38.0 \pm 1.2$	$30.2 \pm 1.1$	$293.1 \pm 16.8$
TFC-PGO2	$34.2 \pm 2.0$	$26.3 \pm 1.2$	$316.7 \pm 31.2$
TFC-PGO4	$28.8 \pm 2.2$	$22.5 \pm 1.4$	$264.0 \pm 54.5$

#### 4.5.2 Foulant resistance evaluation

The overall hydraulic resistance against the water permeation ( $R$ ) experienced by a fouled membrane occurs as a result of both the foulant resistance ( $R_f$ ) and clean membrane resistance ( $R_m$ ) as shown by Eq. S4:1

$$R (m^{-1}) = R_m + R_f = \frac{F}{\mu J_w} \quad (\text{S4.1})$$

where  $F$  is the osmotic driving force across the membrane,  $\mu$  denotes the solution viscosity and  $J_w$  represents the water flux. The osmotic driving force is a function of the effective concentration difference across the selective layer of the membrane and can be determined using the modified van't Hoff formula, as shown by Eq. S4.2:

$$F (Pa) = \frac{N_{ion} R_g T \Delta C}{MW} \quad (\text{S4.2})$$

where  $N_{ion}$  stands for the ionization number in water,  $R_g$  is the universal gas constant,  $T$  represents the temperature of the solution,  $MW$  means the molecular weight and  $\Delta C$  is the concentration difference across the selective layer of the membrane. The effective

concentration difference ( $\Delta C$ ), considering the internal concentration polarization, is evaluated using Eq. S4.3:

$$\Delta C (M) = C_{DS} \exp\left(-\frac{J_w \cdot S}{D}\right) - C_{FS} \quad (S4.3)$$

where,  $C_{DS}$  and  $C_{FS}$  denote the bulk concentrations of the draw solution (DS) and FS; S and D represent the structural parameter and the diffusion coefficient of the NaCl DS, respectively. The overall hydraulic resistance increases with the increase in filtration operation time due to foulant accumulation on the membrane surface, which increases the foulant resistance. Differentiating Eq. S4.1, the overall transient resistance denoted by Eq. S4.4 is discretised to evaluate the overall resistance iteratively at any time during the operation, as shown by Eq. S4.5:

$$\frac{\left(\frac{dR}{dt}\right)}{R} = \frac{\left(-\frac{dJ}{dt}\right)}{J} + \frac{\left(\frac{dF}{dt}\right)}{F} \quad (S4.4)$$

$$R_{i+1}(m^{-1}) = R_i \left[ \frac{J_i - J_{i+1}}{J_i} + \frac{F_{i+1} - F_i}{F_i} + 1 \right] \quad (S4.5)$$

where,  $i$  and  $i+1$  are indexes representing the filtration parameter values (flux, osmotic driving force and overall resistance) at specific time  $t$  and  $t + \Delta t$ , respectively. In this study,  $t$  varies from 0 to 5 h, and  $\Delta t$  is set to 5 min. Once the initial values of the overall resistance, water flux, and osmotic driving force are known at time  $t$ , and the values of the water flux and osmotic driving forces are measured experimentally at time  $t + \Delta t$ , the overall hydraulic resistance can be calculated using the Eq. S4.5. Finally, the foulant resistance as a function of time was determined using Eq. S4.6 as follows:



$$R_{f,i+1}(m^{-1}) = R_{i+1} - R_m \quad (\text{S4.6})$$

where the  $R_m$  remains unchanged as the operating time increases.  $R_m$  was evaluated experimentally via the RO method using DI water as FS to prevent the concentration polarization and fouling effects on the water permeation. The membrane resistance was evaluated using Eq. S4.7:

$$R_m(m^{-1}) = \frac{\Delta P}{\mu J_w} \quad (\text{S4.7})$$

where ( $\Delta P$ ) is the applied transmembrane pressure.

The experimentally evaluated  $R_m$  for the membranes used in the fouling study are presented in **Table S4.2**.

**Table S4.2** Membrane resistance determined from the RO method.

<b>Membrane</b>	<b><math>R_m (\times 10^{13} \text{ m}^{-1})</math></b>
TFC	5.53
TFC-P	12.03
TFC-PGO2	9.67

### **CRedit authorship contribution statement**

**Nawshad Akther:** Conceptualisation, Data curation, Formal analysis, Investigation, Methodology, Validation, Writing - original draft. **Syed Muztuza Ali:** Methodology, Formal analysis. **Sherub Phuntsho:** Writing - review & editing. **Hokyong Shon:** Supervision, Project administration, Resources, Funding acquisition, Validation, Writing - review & editing.

### **Declaration of competing interest**

The authors declare that they have no known competing financial interests or personal relationships that could have appeared to influence the work reported in this paper.

### **Acknowledgement**

The research reported in this paper was supported by the Australian Research Council Industrial Transformation Research Hub (IH170100009).

# **CHAPTER 5**

## **INFLUENCE OF GRAPHENE OXIDE LATERAL SIZE ON THE PROPERTIES AND PERFORMANCES OF FORWARD OSMOSIS MEMBRANE**

## STATEMENT OF CONTRIBUTION OF AUTHORS

Title of Paper	Influence of graphene oxide lateral size on the properties and performances of forward osmosis membrane		
Publication Status	<input checked="" type="checkbox"/> Published <input type="checkbox"/> Accepted for Publication <input type="checkbox"/> Submitted for Publication <input type="checkbox"/> Unpublished and Unsubmitted work written in manuscript style		
Publication Details	Akther, N., Yuan, Z., Chen, Y., Lim, S., Phuntsho, S., Ghaffour, N., Matsuyama, H. & Shon, H.K. 2020, 'Influence of graphene oxide lateral size on the properties and performances of forward osmosis membrane', <i>Desalination</i> , vol. 484, p. 114421.		
<b>PRINCIPAL AUTHOR</b>			
Name of Principal Author (Candidate)	Nawshad Akther		
Contribution to the paper	Data curation, Formal analysis, Investigation, Methodology, Writing - original draft.		
Certification	This paper reports on original research I conducted during the period of my Higher Degree by Research candidature and is not subject to any obligations or contractual agreements with a third party that would constrain its inclusion in this thesis. I am the primary author of this paper.		
Signature	Production Note: Signature removed prior to publication.	Date	04/09/2020
<b>CO-AUTHOR CONTRIBUTIONS</b>			
By signing the Statement of Contribution of Authors, each author certifies that:			
i. the candidate's stated contribution to the publication is accurate (as detailed above); and ii. permission is granted for the publication to be included in the candidate's thesis.			
Name of Co-Author 1	Ziwen Yuan		
Contribution to the paper	Data curation, Formal analysis, Investigation.		
Signature	Production Note: Signature removed prior to publication.	Date	04/09/2020
Name of Co- Author 2	Prof. Yuan Chen		
Contribution to the paper	Formal analysis, Investigation, Methodology.		
Signature	Production Note: Signature removed prior to publication.	Date	04/09/2020
Name of Co-Author 3	Dr. Sungil Lim		
Contribution to the paper	Data curation.		
Signature	Production Note: Signature removed prior to publication.	Date	04/09/2020
Name of Co-Author 4	Dr. Sherub Phuntsho		
Contribution to the paper	Writing - review & editing.		
Signature	Production Note: Signature removed prior to publication.	Date	04/09/2020
Name of Co-Author 5	Prof. Noreddine Ghaffour		
Contribution to the paper	Writing - review & editing.		
Signature	Production Note: Signature removed prior to publication.	Date	04/09/2020
Name of Co-Author 6	Prof. Hideto Matsuyama		
Contribution to the paper	Writing - review & editing.		

Signature	Production Note: Signature removed prior to publication.	Date	04/09/2020
Name of Co-Author 7	Prof. Ho Kyong Shon		
Contribution to the paper	Supervision, Project administration, Resources, Funding acquisition, Validation, Visualization, Writing - original draft, Writing - review & editing.		
Signature	Production Note: Signature removed prior to publication.	Date	04/09/2020

## 5. CHAPTER 5 Influence of graphene oxide lateral size on the properties and performances of forward osmosis membrane

### Abstract

Graphene oxide (GO) has been widely explored to improve thin-film composite (TFC) membrane performance. However, the influences of GO flake lateral size on the polyamide (PA) TFC membrane properties and performances have not been investigated. In this study, GO suspensions with an average flake size ranging from 0.01 to 1.06  $\mu\text{m}^2$  were prepared by varying the sonication duration between 0 and 8 h. The different sized GO flakes were embedded in the PA layer to examine the effect of their size on the morphology and performances of TFC forward osmosis (FO) membranes. The specific reverse solute flux and water flux of the GO-modified thin-film nanocomposite (TFN) membranes improved by over 60% and 50%, respectively, when the average GO flake size was reduced from 1.06 to 0.01  $\mu\text{m}^2$  due to the formation of a thinner and more uniform PA layer. Large GO flakes deteriorated membrane performance by creating impervious regions that obstructed the reaction between monomers during the interfacial polymerization process resulting in defective PA layer formation. Whereas, smaller GO flakes were distributed more uniformly in the PA layer, creating fewer defects and demonstrating better desalination performance and antifouling property than the TFN membranes modified with larger GO flakes. These results deliver strategies for future improvements in GO or 2D nanomaterial-based TFN membranes, where smaller flake size can be beneficial for minimizing PA layer defects.

**Keywords:** Forward osmosis (FO); Graphene oxide (GO); Lateral size, Thin-film nanocomposite (TFN) membrane; Interfacial polymerization (IP)

## 5.1 Introduction

Extensive studies have been conducted on osmotically-driven membrane processes like forward osmosis (FO) and pressure-retarded osmosis (PRO) for power generation (Lee, Baker & Lonsdale 1981), desalination (Thiruvengkatachari et al. 2016; Xu et al. 2019; Yang et al. 2017), resource recovery (Zhang et al. 2014), wastewater treatment (Lutchmiah et al. 2014), brine or seawater dilution (Akther, Daer & Hasan 2018; Cath et al. 2010), osmotic membrane bioreactors (Tran et al. 2019), concentration of aqueous products like fruit juice (Wrolstad et al. 1993) and dairy whey (Aydiner et al. 2013). The difference in osmotic potential between the draw solution (DS) and feed solution (FS) mainly drives the water through the semi-permeable membrane in FO processes without the need for hydraulic pressure (Akther, Daer, et al. 2019). As a result, these processes are associated with many desirable characteristics like (1) potential for high water recovery, (2) desirable rejection of numerous contaminants, (3) low fouling tendency, and (3) possibly less energy consumption depending on the type of application (Akther et al. 2015).

The fabrication of robust and highly selective osmotic membranes is among the most critical research areas in the field of engineered osmotic processes. A standard FO membrane should demonstrate low structural parameter, high solute rejection and water permeability, excellent antifouling property, good chemical resistance and mechanical strength (Akther, Phuntsho, et al. 2019). Numerous works have been done on polyamide (PA) based thin-film composite (TFC) membranes compared to other asymmetric membranes, such as cellulose triacetate, as they demonstrate much higher water permeability combined with superior selectivity over a wide pH range (Yip et al. 2010). However, TFC membranes can be highly susceptible to fouling, especially during their long-term operations, with very poor resistance to chlorine exposure. Thus, several researchers have tried to heighten the antifouling and antibacterial properties of the TFC membrane by modifying the membrane surface, such as by coating or

embedding nanomaterials like graphene oxide (GO), silver, metal-organic frameworks (MOF) and carbon nanotubes, to develop thin-film nanocomposite (TFN) membranes (Akther, Phuntsho, et al. 2019; Hegab, ElMekawy, Barclay, et al. 2016; Ma, Peh, et al. 2017; Song et al. 2015; Soroush et al. 2015; Teow & Mohammad 2019).

Over the last few years, GO has drawn researchers' attention because of its distinct structure, hydrophilicity, superior antibacterial properties, high chemical stability and low production cost (Dreyer et al. 2010; Hegab, ElMekawy, Zou, et al. 2016). GO flakes are two-dimensional single-atom-thick structures that exhibit exceptional hydrophilic properties owing to the occurrence of oxygen-containing hydroxyl, epoxy and carboxyl groups on their surfaces and edges (Goh et al. 2016). GO-modified membranes have been reported to demonstrate improved mechanical strength, thermal stability, water permeability, chlorine resistance and antifouling properties (Pang et al. 2019; Yang, Alayande, et al. 2018; Yuan et al. 2017). Shen et al. incorporated GO in the PA layer of the TFC membrane, which produced a much smoother and thinner PA layer than the unmodified membrane (Shen, Xiong & Wang 2016). They observed that GO-modified TFN membranes reduced sodium alginate fouling by reducing sites on the PA surface for foulant adhesion and electrostatically repelling the alginate molecules. Wu et al. chemically-modified GO with polyvinylpyrrolidone (PVP) to minimize GO accumulation in the polymer matrix and confirmed that GO could enhance the membrane permeability, selectivity and hydrophilicity (Wu et al. 2017). Hegab et al. reported that grafting GO nanosheets on the PA layer significantly improved the antibacterial property of the modified membranes (Hegab et al. 2015). The numerous studies published on GO-incorporated membranes proved that membrane modification using GO is a promising approach to augment membrane performance.

Since 2012, several articles have been published on GO-modified TFN membranes for numerous separation processes like nanofiltration (NF), reverse osmosis (RO) and FO. These



studies mainly considered the effect of concentration, nanocomposites, chemical modification and functionalization of GO on the membrane's antifouling properties and performance (Kang et al. 2019; Ma, Ping & Dong 2017; Qian et al. 2019). For example, Kang et al. modified GO with sulfonic acid to produce sulfonated graphene oxide (SGO). They observed that incorporating 0.3 wt% of SGO into the PA layer improved the hydrophilicity, surface negative charge, water flux, salt rejection and antifouling properties of the NF membranes. The SGO increased the PA cross-linking degree, increasing the water flux without deteriorating membrane selectivity (Kang et al. 2019).

Interestingly, the physicochemical properties of GO were also found to be strongly influenced by the GO flake size. Chen's group observed that the antibacterial property of GO was dependent on the lateral size of the GO flakes, where larger GO flakes exhibited stronger antibacterial activity than the smaller ones (Liu et al. 2012). Large GO flakes were easily able to cover the bacterial cells completely and prevent their proliferation, resulting in the loss of cell viability. However, the smaller GO flakes only attached to the bacterial surfaces without isolating the cells effectively. In another study, nano-GO flakes with a lateral width of few nanometers were observed to be photoluminescent in the visible and infrared regions, making them suitable for live-cell imaging and potential material for medical and biological applications (Sun et al. 2008). Tayyebi et al. demonstrated that graphene quantum dots (GQD) produced from the fragmentation of GO at supercritical condition could enhance the thermal conductivity, absorption coefficient and temperature uniformity of GQD-treated tissues compared to GO flakes, which supported their feasibility for photothermal therapeutic treatment applications (Tayyebi et al. 2018). However, the influence of GO lateral size on the PA layer morphology and TFN membrane performance is yet to be investigated.

Therefore, this study investigates the effect of GO lateral size on the PA layer formation during the interfacial polymerization (IP) reaction. The effects of different GO lateral sizes on the membrane morphology, surface properties and desalination performance were explored. The effect of GO size on the antifouling properties of the membranes was also evaluated using sodium alginate and colloidal silica as model foulants. To the best of our knowledge, this work is the first to study in detail the impact of GO flake lateral size on the PA layer development and the TFN FO membrane properties and performance.

## **5.2 Materials and methods**

### **5.2.1 Chemicals**

Monolayer GO dispersion in water was procured from Graphenea (4 mg·mL<sup>-1</sup>, particle size <10 μm). Polysulfone pellets (PSf, Udel® P-3500, Solvay) and 1-methyl-2 pyrrolidone (NMP, ≥99.5%, Merck) were employed for membrane substrate preparation. M-phenylenediamine flakes (MPD, 99%), 1,3,5-benzenetricarbonyl trichloride (TMC, 98%) and sodium alginate were bought from Sigma-Aldrich. Colloidal silica (40–41 wt%, particle size: 70–100 nm, ST-ZL, SNOWTEX®) was procured from Nissan Chemical. N-hexane (98.5%, Merck) was used as a TMC solvent. Deionized (DI) water (~18 MΩ·cm<sup>-1</sup>, Milli-Q®, Merck) was used to prepare FS and DS. Sodium chloride (NaCl, >99.7%) from Chem Supply was used as a draw solute.

### **5.2.2 Graphene oxide preparation**

Commercial GO water suspension was first diluted to 1 mg·mL<sup>-1</sup> with DI water and sonicated for 30 min using an ultrasonic bath (Powersonic 405, Hwashin Technology Co.) to obtain uniform GO dispersion, which was called “GO-0”. The GO flake lateral sizes were then reduced by sonicating GO-0 dispersion for 0.5, 4 and 8 h at 120 W using a digital tip sonicator (S-450D, Branson Ultrasonics Corp.) equipped with a 13 mm disruptor horn. The various GO samples obtained were called “GO-0.5”, “GO-4” and “GO-8” depending on the

duration of tip-sonication. The temperature of the GO dispersions was maintained constant throughout the sonication process by using an ice bath, and the tip sonication cooling interval was set to 5 s for every 30 s. The GO dispersions sonicated at various times showed good stability even after three months of storage.

### **5.2.3 TFC and TFN membrane fabrication**

#### *5.2.3.1 Membrane substrate*

The porous PSf substrates were prepared using the phase inversion technique as described elsewhere (Akther, Lim, et al. 2019). Briefly, a homogenous polymer solution was prepared by dissolving 12 wt% PSf in NMP at 60 °C and stirring at 500 rpm continuously for 24 h. The well-mixed PSf dope solution was then left for degassing overnight at 34 °C.

A flat-sheet casting machine (Elcometer 4340) and a casting blade with a gate height of 120 µm were employed to cast the polymer solution on a glass plate under ambient conditions. The phase inversion process was initiated by immediately immersing the PSf film-coated glass plate in a coagulation bath holding tap water at room temperature. The solidified PSf substrate was then rinsed thoroughly and stored in DI water at 4 °C for at least 24 h to eradicate the residual solvents.

#### *5.2.3.2 PA selective layer*

The fabricated substrate was first wetted with DI water and fixed on a rectangular frame. Any remaining water on the substrate surface was then eliminated with a gentle air knife. IP technique was used to create a selective PA layer on the PSf substrate. In short, the substrate was first submerged for 2.5 min in MPD aqueous solution (4 wt%). Nitrogen was then employed to gently eradicate the surplus MPD from the substrate, which was then immediately immersed for 1 min in TMC/n-hexane organic solution (0.1 wt%). Next, the membrane was cured at room temperature for 1 min and at 60 °C for 5 min to improve PA

cross-linking degree. The TFC FO membrane was then washed carefully under running DI water for 3 min to eradicate any residual chemical. Lastly, the membranes were immersed in DI water and stored at 4 °C before testing their performance.

GO-modified TFN membranes were fabricated using a similar protocol like TFC membranes. GO flakes were added to the MPD aqueous solution at a loading of 0.01 wt% and sonicated for 1 h in a bath sonicator to obtain a homogenous dispersion. The subsequent GO/MPD dispersion on the PSf substrate was brought in contact with the organic solution during the IP reaction to produce GO impregnated PA layer. The GO-modified TFN membranes were denoted as “MGO-0”, “MGO-0.5”, “MGO-4” and “MGO-8” depending on the duration of tip sonication received by the commercial GO dispersion.

#### **5.2.4 Graphene oxide and membrane characterisation**

The lateral size and height of GO flakes were analysed using the atomic force microscopy (AFM, Dimension 3100, Bruker). The AFM study samples were assembled by dropping 4  $\mu\text{L}$  of GO dispersions ( $0.1 \text{ g}\cdot\text{L}^{-1}$ ) on a freshly cleaved mica and spin coating at 2500 rpm for 150 s. The GO films were then air-dried for AFM analysis. Image J software was used to determine the GO lateral size distribution by measuring approximately 200 GO flakes from the AFM images of each sample. The average GO flake size for each sample was determined by dividing the total sampling area by the total number of GO flakes. AFM was also utilized to investigate the membrane morphology and surface roughness with a scan size of  $5 \mu\text{m} \times 5 \mu\text{m}$ .

A scanning electron microscope (SEM, Zeiss Supra 55VP) was used to study the cross-sectional and PA layer top surface morphology of all the membranes. Dry membrane samples were soaked in ethanol prior to rupturing them in liquid nitrogen to prepare the cross-section samples for SEM imaging. Subsequently, the samples were attached to stubs

using copper tape and sputter-coated with a 10 nm thick Au/Pd layer before conducting the SEM analysis. The membrane wettability or hydrophilicity was ascertained by assessing the initial water contact angles on the PA surface at room temperature with an optical tensiometer. The contact angles were assessed at 7 random positions for each sample to acquire the average value.

Fourier transform infrared spectroscopy (FTIR, Shimadzu MIRacle 10) was employed to confirm the successful integration of the GO flakes through surface chemistry analysis of the fabricated membranes at room temperature. The zeta potentials of the membrane surfaces were quantified at room temperature using an electrokinetic analyser (SurPASS<sup>TM</sup> 3, Anton Paar) over a pH range of 3 to 10 using an adjustable gap cell of size 20 × 10 mm. The membranes were attached to the sample holder with the gap height fixed to about 100 μm. 1 mM KCl solution was used as the electrolyte, and 0.05 M HCl and NaOH were used to adjust the pH of the electrolyte. The obtained streaming potential was utilized to verify the membrane surface zeta-potential.

### **5.2.5 Membrane performance evaluation**

The FO performance of fabricated membranes was established with a laboratory-scale FO system, as described in Section 3.4.1. The FO membrane cell with a membrane area of 15.4 cm<sup>2</sup> and a flow channel depth of 3 mm on each side of the membrane was used. DI water and 0.5 M NaCl were used as FS and DS, respectively. FS and DS were circulated at 12.6 cm·s<sup>-1</sup>, and the temperature was maintained at 22 °C during the performance tests. The membrane performance was determined under both AL-FS and AL-DS (active layer facing to FS and DS, respectively) orientations. The FS weight was recorded at a constant interval using a digital weight balance to calculate the membrane water flux ( $J_w$ , L·m<sup>-2</sup>·h<sup>-1</sup>) using Eq. 3.1. The reverse solute flux ( $J_s$ , g·m<sup>-2</sup>·h<sup>-1</sup>) through the membrane was calculated using Eq. 3.2 from the FS conductivity recorded with a conductivity meter. The specific reverse solute

flux ( $SRSF$ ,  $\text{g}\cdot\text{L}^{-1}$ ) for all membranes was calculated from water and reverse solute flux values to indicate the membrane selectivity (Eq. 3.3). All the equations used for calculating the membrane performance parameters are provided in Section 3.4.2.

The pure water and solute permeability coefficients ( $A$  and  $B$ , respectively) of the membranes were obtained using the 4-step non-linear regression protocol established for the FO membranes by Tiraferri et al. (2013). The FO performance data for all the membranes required by the numerical model were obtained at four different DS concentrations (0.5, 1.0, 1.5, and 2.0 M NaCl).

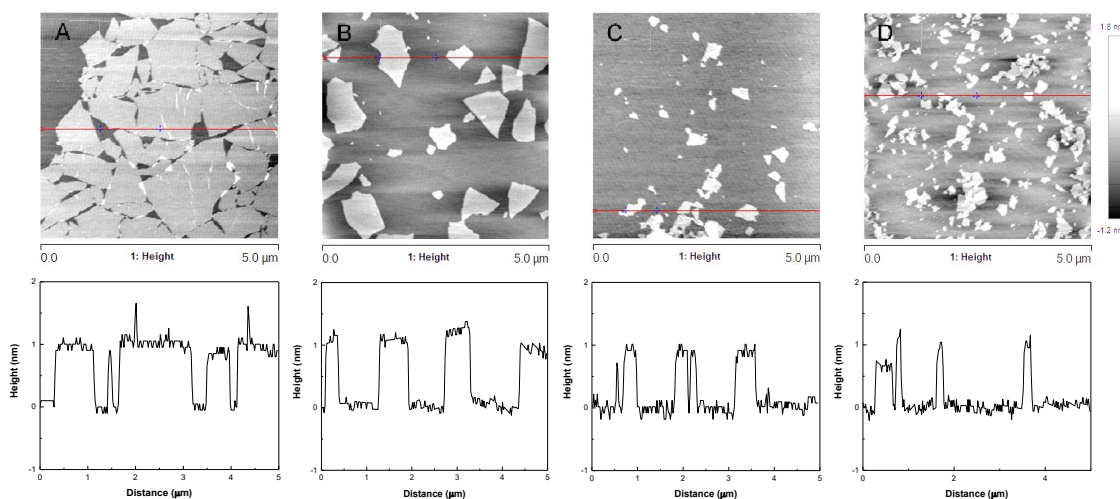
### 5.2.6 Membrane fouling test

The fouling tests for all the membranes were operated in the AL-FS configuration using the FO experimental system described in Section 3.4.1. Baseline experiments were first conducted at a cross-flow velocity of  $7.6 \text{ cm}\cdot\text{s}^{-1}$  with DI water as FS and NaCl as DS to account for the flux decline from the decrease in the osmotic driving force resulting from DS dilution and FS concentration. NaCl DS ranging between 0.75 M and 2 M were used to obtain an initial water flux ( $J_{w,0}$ ) of  $\sim 25 \text{ L}\cdot\text{m}^{-2}\cdot\text{h}^{-1}$ . The fouling experiments were then operated at a cross-flow velocity of  $7.6 \text{ cm}\cdot\text{s}^{-1}$  at the same initial baseline flux by introducing  $200 \text{ mg}\cdot\text{L}^{-1}$  of colloidal silica and sodium alginate into the FS. The flux decline detected in this case occurred due to the cumulative effect of DS dilution, reverse solute diffusion and membrane fouling. The baseline and fouling tests were run until a total permeate volume of 100 mL was collected. After completing the fouling tests, the membranes were physically cleaned for 1 h by circulating DI water in both FS and DS channels at  $12.6 \text{ cm}\cdot\text{s}^{-1}$ . The recovered water flux was then obtained by using the same conditions as the baseline study.

## 5.3 Results and discussion

### 5.3.1 GO characterisation

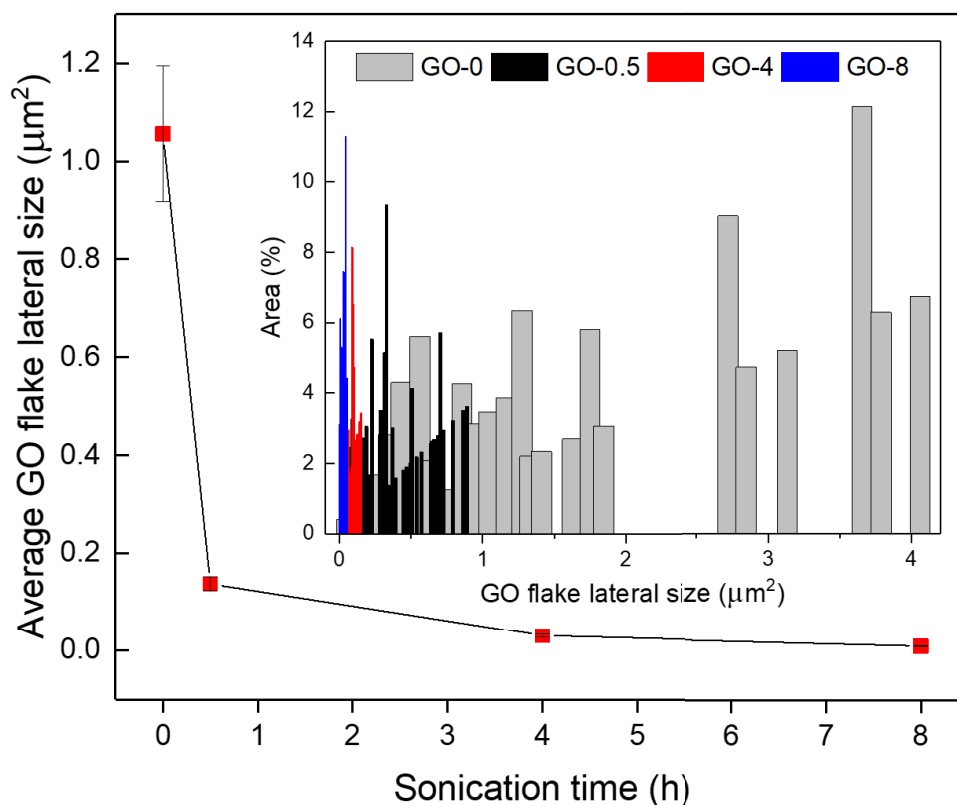
The lateral size of GO flakes was reduced via high power sonication without undermining their surface chemical properties. The lateral dimensions of GO flakes were up to several micrometres before sonication, as shown in **Fig. 5.1A**; however, increasing the sonication time reduced the average GO flake size to few nanometers as can be observed from **Fig. 5.1B to D**. This is also evident from the corresponding GO flake height profiles that indicate the lateral size of the GO flakes (the horizontal distance on top of plateaus) that fall along the red lines on the AFM images. The height profiles of GO flakes also showed that the flakes have a thickness of approximately 1 nm, which is the characteristic thickness of monolayer GO flakes, and verified the formation of single-layer GO aqueous dispersions without any aggregation.



**Fig. 5.1** AFM images of GO flakes deposited on mica sheets (top) and height profiles of GO flakes (bottom) along the red lines represented on AFM images at different sonication times (A) 0 h, (B) 0.5 h, (C) 4 h, and (D) 8 h.

The GO flake size distributions obtained at various sonication times are presented in **Fig. 5.2**. It can be seen that the average area of GO flakes is  $1.06 \mu\text{m}^2$  (0 h) prior to tip sonication but decreases to  $0.14 \mu\text{m}^2$ ,  $0.03 \mu\text{m}^2$  and  $0.01 \mu\text{m}^2$  after 0.5 h, 4 h and 8 h of sonication,

respectively. Although the GO-0 (representing 0 h of sonication) and GO-0.5 dispersions have a substantial proportion of larger GO flakes, their average size is much smaller than the larger flakes due to the presence of several smaller GO flakes in the dispersion. As a result, the average flake size by itself is insufficient to represent the difference in the GO flake size for various samples. However, it can be depicted from the size distributions that GO-4 and GO-8 dispersions are much less polydispersed than those of GO-0 and GO-0.5 dispersions; thus, confirming that the mean size of GO-4 and GO-8 flakes are maintained at  $<0.03 \mu\text{m}^2$  and  $0.01 \mu\text{m}^2$ , respectively. These GO dispersions were used to study the impact of GO size on the morphology and performance of PA TFN membranes.

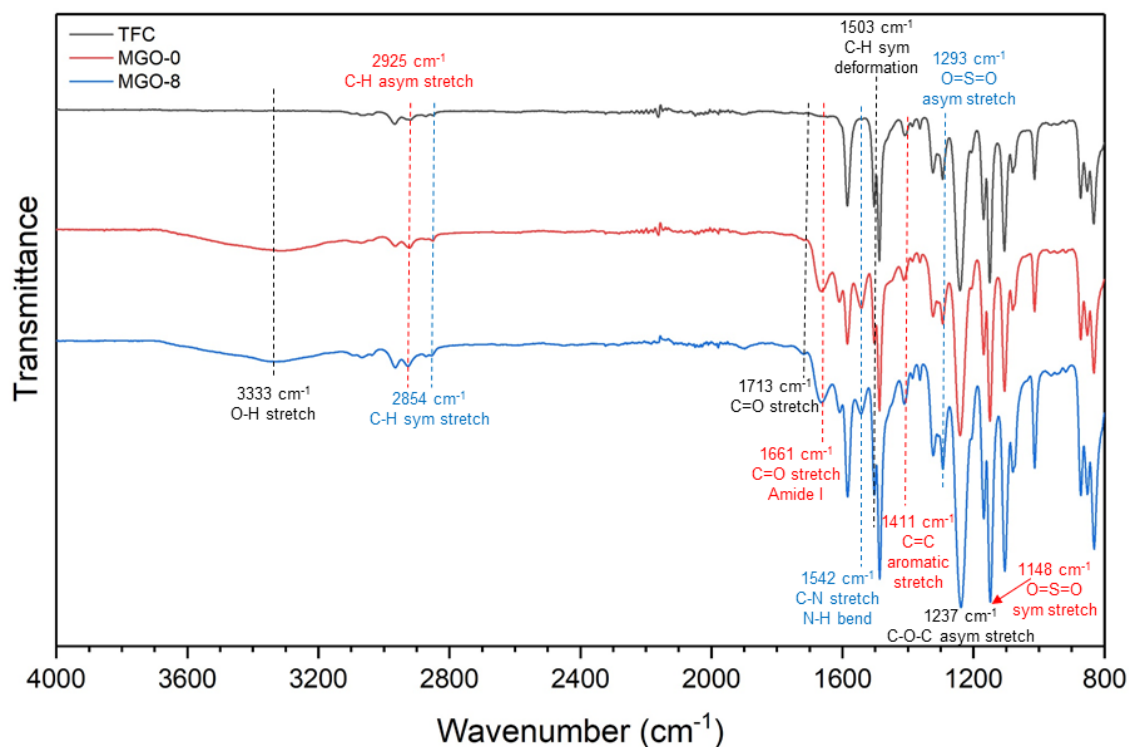


**Fig. 5.2** Average GO flake area at various durations of sonication. The size distributions were obtained from AFM images by measuring the area of nearly 200 GO flakes for each sample using the ImageJ software. Inset plot: Histograms depicting the GO flake size distributions at various durations of tip sonication.



### 5.3.2 Membrane characterisation

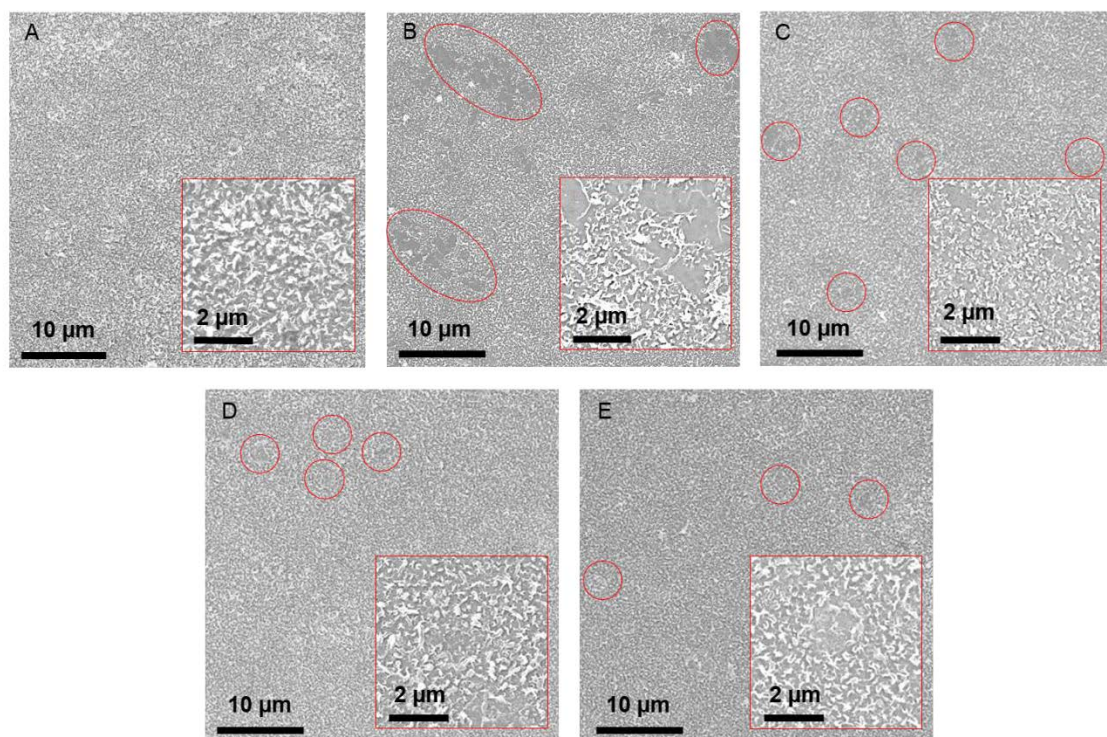
The changes in the surface chemistry of the fabricated membranes were observed using FTIR spectra, as shown in **Fig. 5.3**. The characteristic peaks of the PSf were detected at  $1503\text{ cm}^{-1}$ ,  $1411\text{ cm}^{-1}$ ,  $1237\text{ cm}^{-1}$ ,  $1293\text{ cm}^{-1}$  and  $1148\text{ cm}^{-1}$ , which are ascribed to the C–H symmetric deformation in  $\text{C}(\text{CH}_3)_2$ , C=C aromatic ring stretch, C–O–C asymmetric stretch of the aryl-O-aryl group, O=S=O asymmetric stretch and O=S=O symmetric stretch of the PSf, respectively (Ficai et al. 2013; Lai et al. 2018). The peaks at  $1542\text{ cm}^{-1}$  (C–N stretching and N-H bending of amide II) and  $1661\text{ cm}^{-1}$  (C=O stretching of amide I) validated the PA layer development on the substrate via the IP reaction. The increasing intensity of the  $1542\text{ cm}^{-1}$  band for the TFN membranes indicates possible interaction between GO flakes and PA, resulting in the formation of more amide bonds. The increasing transmission intensity at  $1661\text{ cm}^{-1}$  is evident for the TFN membranes and can be attributed to the development of new amide bonds due to the reaction between the GO flakes' carboxyl groups ( $-\text{COOH}$ ) with the amine groups ( $-\text{NH}_2$ ) of MPD. The peak at  $1713\text{ cm}^{-1}$  corresponds to the carboxyl groups (C=O) of GO, which explains its absence on the TFC membrane spectrum (Wu et al. 2017). In addition, the peak intensity at  $2854\text{ cm}^{-1}$  and  $2925\text{ cm}^{-1}$  (C-H symmetric and asymmetric stretching, respectively) increased upon GO flake incorporation due to the presence of more C–H bonds from GO flakes. Finally, the FTIR spectra of the TFN membranes demonstrated stronger peaks than the TFC membrane at  $3333\text{ cm}^{-1}$  because of the hydroxyl group ( $-\text{OH}$ ) stretching of GO flakes. Overall, the above FTIR results validated the successful integration of GO flakes inside the PA layer through covalent bonding during the IP reaction.



**Fig. 5.3** FTIR spectra of TFC and GO-modified TFN membranes.

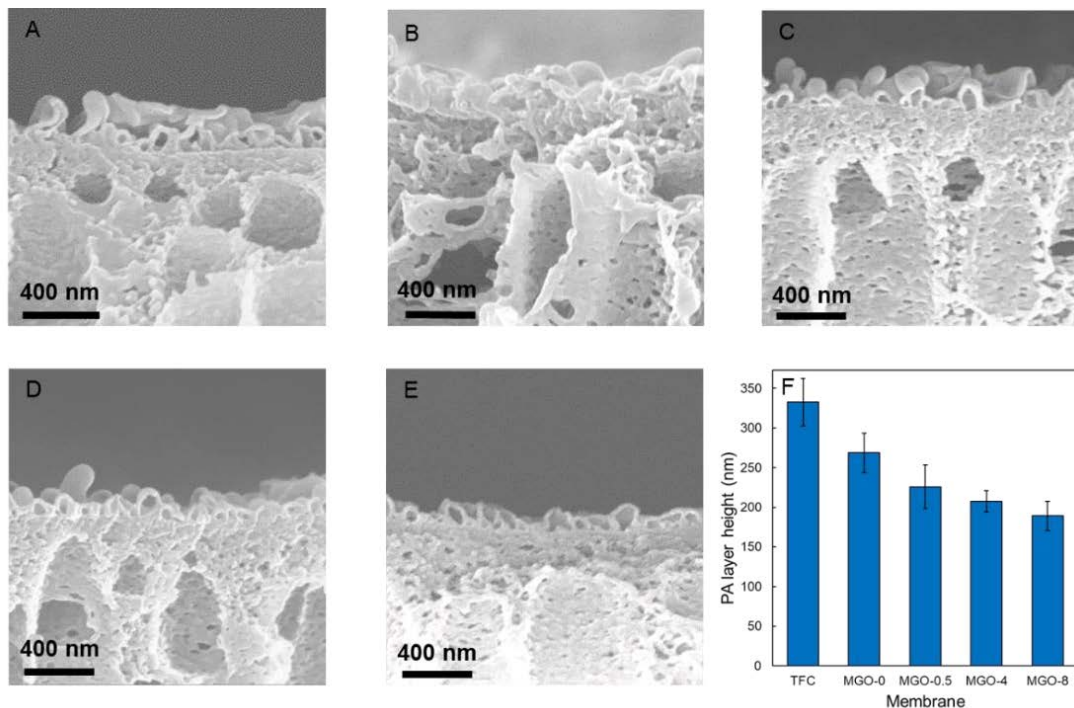
The SEM images of the PA surface and cross-section morphology of the TFC and GO-modified TFN membrane samples are presented in **Fig. 5.4** and **Fig. 5.5**, respectively. The characteristic ridge-and-valley structures of the PA layer are visible on the surfaces of all the membrane samples. However, the integration of GO flakes in the PA layer significantly altered the membrane surface morphology. It is evident from the top surface SEM (**Fig. 5.4**) and AFM images (**Fig. 5.6**) that the GO-modified TFN membranes have much smoother surfaces with smaller PA ridge height than the pristine TFC membrane. The PA layer ridge-and-valley structure develops when MPD diffuses from the aqueous to the organic phase and reacts with TMC. The GO-modified TFN membranes demonstrated a smoother PA surface mainly because the horizontally oriented GO flakes on the PSf substrate surface retarded MPD diffusion into the organic phase. The delay in IP reaction can be attributed to the steric-hindrance effect of the GO flakes. Additionally, both TMC and MPD can react with the oxygen functional groups of GO, which can reduce the reaction rate between them.

Unlike the TFC membrane, all the GO-modified TFN membranes can be observed to have some smooth patches with no ridge-and-valley structures, which are encircled in red borders (Fig. 5.4). These smooth patches result from the GO flakes obstructing the reaction between MPD and TMC. Hence, larger patches can be observed on membranes incorporated with larger GO flakes. For instance, MGO-0 exhibited the most defective PA layer with patches in the range of 2-10  $\mu\text{m}$  (Fig. 5.4B) followed by that of MGO-0.5 with smaller patches of 1-2  $\mu\text{m}$  (Fig. 5.4C). A more uniform distribution of patches that is significantly smaller in size than those of MGO-0 and MGO-0.5 can be noticed on the surfaces of MGO-4 and MGO-8 (Fig. 5.4D and E). This is because the number of GO flakes in the GO dispersion increases upon increasing the sonication time. Hence, 0.01 wt% dispersion of GO-8 has more GO flakes than that of GO-0 with much smaller lateral sizes that disperse more uniformly in the PA layer and create minimal defects in the selective layer.



**Fig. 5.4** SEM images of PA surface: (A) TFC, (B) MGO-0, (C) MGO-0.5 (D) MGO-4, and (E) MGO-8 membranes. The GO loading was fixed at 0.01 wt% for all the TFN membranes. The red borders present the smooth patches that form when GO flakes impede the IP reaction.

As apparent from the cross-section images (**Fig. 5.5**), the PA layer heights of the GO-modified membranes are smaller than those of the pristine membrane. It should be noted that the PA layer height here refers to the average height of the PA layer from the PSf substrate to the top of the PA ridge structure and not the thickness of PA skin. The cross-section SEM images were utilized to determine the average PA layer height for all the membranes, as presented in **Fig. 5.5F**. It can be observed that the overall height of the PA layer ridges decreases as the size of incorporated GO flakes decreases at higher sonication times. The GO flakes interrupt the growth of PA ridge-and-valley structures during the IP process (Yin, Zhu & Deng 2016). Additionally, the better distribution of smaller GO flakes in the PA leads to the development of thinner and more uniform selective layer. Therefore, it can be concluded that GO flakes with smaller lateral size are more desirable for less defective PA layer.



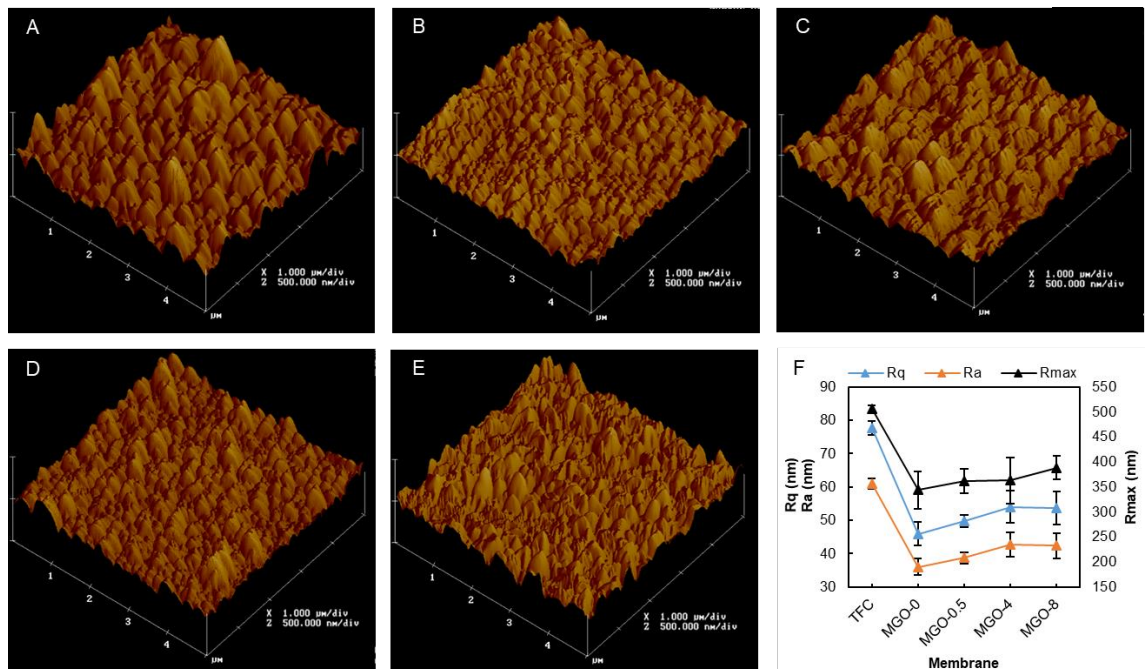
**Fig. 5.5** SEM images of membrane cross-section, (A) TFC, (B) MGO-0, (C) MGO-0.5 (D) MGO-4, and (E) MGO-8 membranes. (F) PA layer height of the TFC and GO-modified TFN membranes. The GO loading was fixed at 0.01 wt% for all the TFN membranes.

The GO flake size effect on the PA layer surface roughness was analysed from the surface topography obtained with AFM. **Fig. 5.6A–E** presents the 3-D AFM images of the fabricated membranes. The maximum ( $R_{max}$ ), mean ( $R_a$ ) and root mean square ( $R_q$ ) membrane roughness are shown in **Fig. 5.6F**. The pristine TFC membrane surface was the roughest with a  $R_a$  value of 61.0 nm. The GO-modified TFN membranes demonstrated much smoother surfaces than the TFC membrane due to GO flakes slowing down the IP reaction. Since the development of the PA layer's "ridge-and-valley" structures depends on the reaction between TMC and MPD, the retardation of MPD diffusion by GO flakes restricted the formation of the PA protrusions during the IP reaction.

The MGO-0 membrane demonstrated the smoothest surface ( $R_a = 36.0$  nm) because the GO-0 flakes with the largest lateral size ( $<5 \mu\text{m}$ ) inhibited MPD diffusion most effectively; thus, resulting in the formation of lesser and smaller PA protrusions (**Fig. 5.6B**). The roughness of GO-modified TFN membranes was observed to increase with a decrease in GO flake size (**Fig. 5.6F**) due to the better dispersion and reduced aggregation of smaller GO flakes. Hence, the reduced flake area of the smaller GO flakes could not impede the MPD diffusion as efficiently as the large GO flakes, which resulted in rougher PA layer formation. A higher surface roughness corresponds to a larger specific membrane surface area, which can promote water transport across the membrane.

To further assess membrane surface properties, the wettability of all the membrane samples was decided from the water contact angle measurements. Membrane surface wettability is a crucial factor as it can strongly influence membrane performance. Overall, the GO TFN membranes demonstrated much lower contact angles than the TFC membrane ( $82.8^\circ$ ) owing to the existence of hydrophilic oxygen-containing functional groups on GO flakes that significantly improved membrane wettability (**Fig. 5.7A**). The enhanced hydrophilicity of the GO-modified membranes is likely to promote water absorption and improve water flux

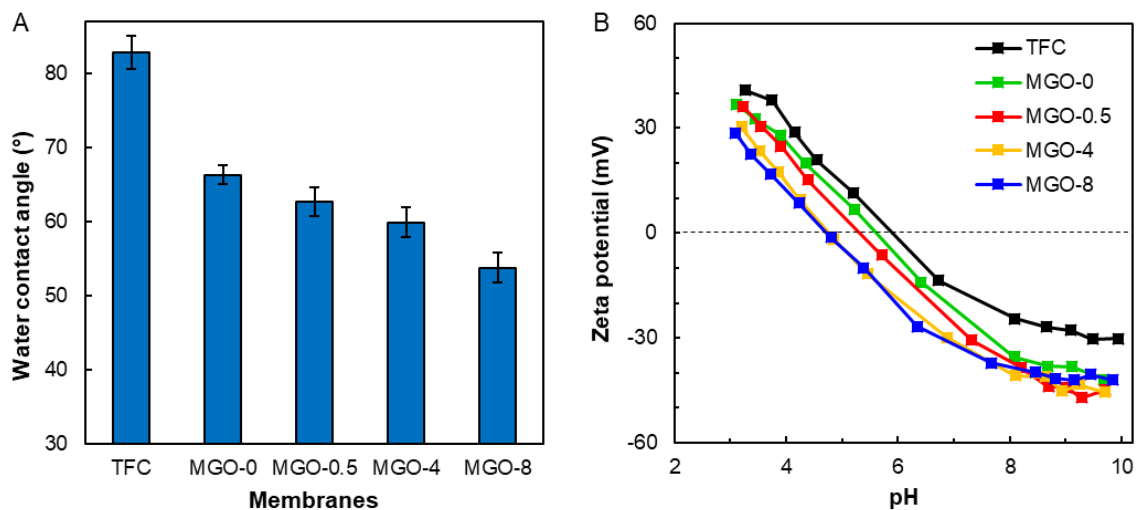
across the TFN membranes. As evident from **Fig. 5.7A**, the contact angle of the GO-modified membranes decreased slightly from  $66.3^\circ$  (MGO-0) to  $53.7^\circ$  (MGO-8) with decreasing GO flake size. The increased hydrophilicity of the GO-modified membranes with smaller GO flakes can be attributed to the uniform GO flake dispersion in the PA layer. Moreover, the diminished thickness (**Fig. 5.5F**) and increased roughness (**Fig. 5.6F**) of the PA layer with smaller GO flakes facilitated the easy permeation of water droplets through the PA layer.



**Fig. 5.6** AFM images representing PA surface topography of (A) TFC, (B) MGO-0, (C) MGO-0.5 (D) MGO-4, and (E) MGO-8 membranes. (F) Surface roughness parameters of the developed membranes obtained by examining three arbitrarily chosen membrane areas ( $5 \mu\text{m} \times 5 \mu\text{m}$ ).

The zeta potential of the fabricated membranes obtained as a function of the pH ranging from 3 to 10 is presented in **Fig. 5.7B**. It can be noticed that all the membranes were negatively-charged at  $\text{pH} \geq 5.9$  because of the carboxyl group dissociation and amine group deprotonation in the PA structure (Lau, Ismail, et al. 2015). The positive charge of the membranes at lower pH could be ascribed to the amine group protonation. It has been

previously reported that integration of GO inside the PA causes the TFN membrane surface to be more negatively charged than the TFC membrane owing to the existence of the plentiful oxygen-containing functional groups, like the carboxyl groups, on GO flakes that deprotonate at alkaline conditions to provide more negative charges. As a result, the TFC membrane has the least negatively-charged, and MGO-4 and MGO-8 have the most negatively-charged PA surfaces across the considered pH range. The isoelectric point (IEP) at which the PA layer is electrically neutral is shown in **Fig. 5.7B**. The IEPs of the membranes shift to lower pH values upon the addition of GO flakes in the PA layer because of the existence of the acidic functional groups on GO flakes (Dimiev, Alemany & Tour 2013). Additionally, the negative charge of all the membranes increases as the pH increases due to charge accumulation resulting from the adsorption of negatively-charged chloride ions on the membrane surface. Overall, the reduced zeta potentials of the GO-modified membranes established the successful integration of the GO flakes into the PA layer.



**Fig. 5.7** (A) Initial water contact angles and (B) surface charge measurements as a function of pH for fabricated TFC and GO-modified TFN membranes.

### 5.3.3 Membrane performance evaluation

The performance results of pristine TFC and GO-modified TFN FO membranes in both membrane orientations with DI water FS and 0.5 M NaCl DS are shown in **Fig. 5.8**. The water flux across all the GO-modified TFN membranes was greater than the pristine membrane as a result of their improved hydrophilicity and thinner PA active layer. Additionally, the water flux increased with a decrease in GO flake size (**Fig. 5.8A**) due to the increased roughness and reduced thickness of the PA layer that increased the membrane surface area and reduced the water transport resistance across the PA layer (Akther, Lim, et al. 2019). The low water flux of MGO-0 can be associated with its defective PA layer that failed to form a highly selective solute barrier; thus, reducing the effective osmotic driving force. The larger flakes of GO-0 likely resulted in more impervious area; thereby, reducing the effective PA area on the MGO-0 surface. MGO-8 exhibited the highest water flux of  $24.7 \text{ L}\cdot\text{m}^{-2}\cdot\text{h}^{-1}$  ( $41.9 \text{ L}\cdot\text{m}^{-2}\cdot\text{h}^{-1}$ ) in the AL-FS (AL-DS) orientations that corresponded to a flux enhancement of 89.6% (62.4%) than that of the pristine TFC membrane. Besides, the improvement in water flux with smaller GO flakes could be ascribed to the reduced tortuosity in the PA layer created by shorter water channels developed at the GO-PA interface (Bi et al. 2018).

The water flux obtained in the AL-DS arrangement was considerably higher than the AL-FS membrane orientation due to the absence of ICP when DI water was used as FS on the support layer side of the membrane. As indicated in several earlier studies, dilutive ICP significantly lowers the effective osmotic driving force at the membrane support layer and active layer interface in AL-FS orientation (Akther, Daer & Hasan 2018). The significant difference of water fluxes between AL-DS and AL-FS modes indicates the high degree of ICP effect in the synthesized membranes. This implies the potential of further improving the water flux performances of these membranes by optimizing the support layer structure.

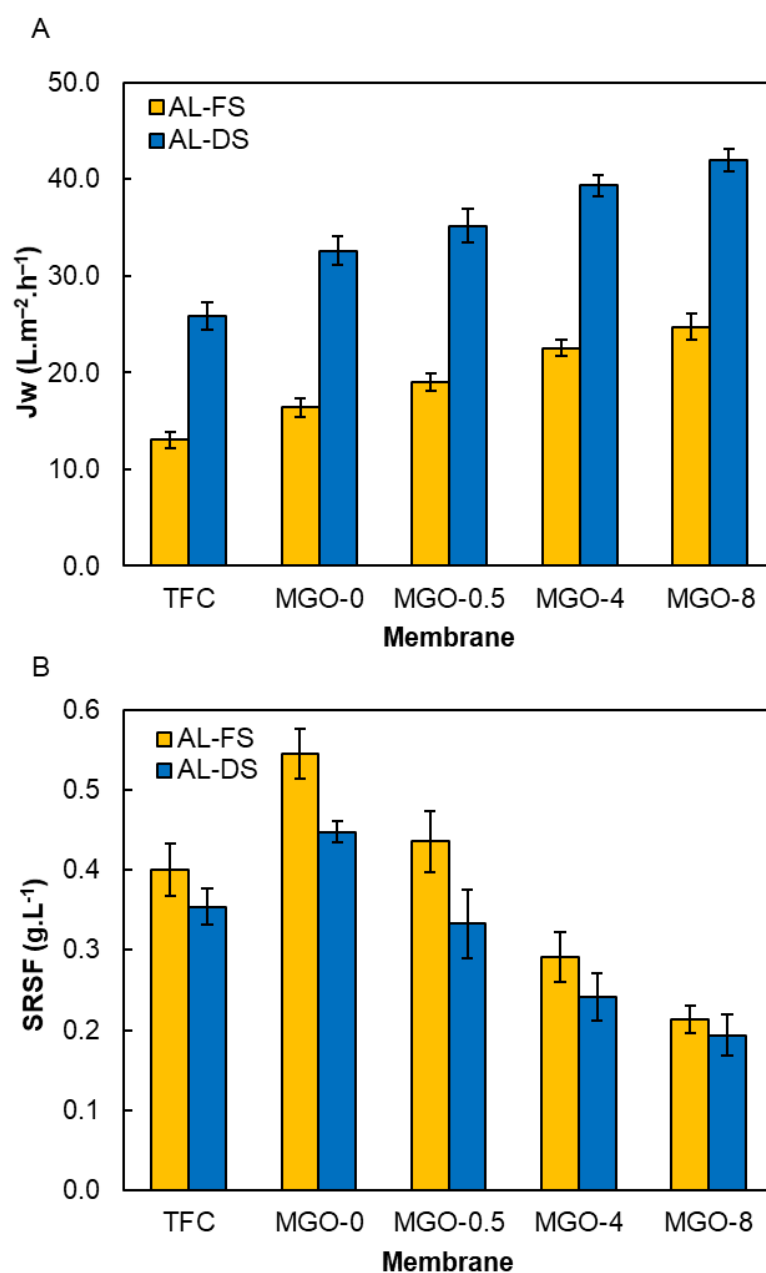


**Fig. 5.8B** exhibits the *SRSF* of the developed membranes. A smaller *SRSF* value indicates greater membrane selectivity, which is preferable for FO membranes. The *SRSF* of the MGO-0 membrane in both orientations was considerably higher than that of the TFC membrane because the largest GO flake size (GO-0) formed a defective non-uniform PA layer with large non-selective patches that likely enhanced the salt flux. As a result, MGO-0 demonstrated the highest *SRSF* value of  $0.54 \text{ g}\cdot\text{L}^{-1}$  in AL-FS mode compared to other membranes. The *SRSF* of MGO-0.5 was comparable to that of the TFC membrane; however, the *SRSF* values of the TFN membranes reduced with a decrease in GO flake size. The membrane selectivity improved with smaller GO flakes (GO-4 and GO-8) because they dispersed more uniformly in the PA layer and significantly reduced the PA defects compared to the GO-0 flakes.

The higher *SRSF* values for membranes with larger GO flakes indicate that the defective PA layer with a looser dynamic pore structure allowed relatively more draw solute to diffuse to the FS. Therefore, GO flakes with smaller lateral size are highly desirable for developing non-defective PA TFN membranes. The MGO-8 can be considered the best performing membrane among the other GO-modified TFN membranes based on the FO performance as it exhibited a substantial enhancement in water flux without deteriorating the membrane selectivity. MGO-8 demonstrated a 51% increment in water flux and a 61% decline in *SRSF* compared to the MGO-0 membrane, suggesting that the GO lateral size plays a vital role in the membrane performance.

The **intrinsic** selectivity ratio ( $B/A$ ) presented in **Table 5.1** is an essential factor for determining the selectivity of FO membranes. A higher membrane selectivity is denoted by a smaller  $B/A$  ratio. The MGO-0 exhibited the highest  $B/A$  value of 0.55 bar; whereas, MGO-8 demonstrated the best selectivity with the smallest  $B/A$  value of 0.24 bar. The  $B/A$  values of the membranes agree well with the previously discussed *SRSF* values (**Fig. 5.8B**).

**Table 5.1** lists the separation parameters of the membranes developed in this study. Both  $A$  and  $B$  parameters of the GO-modified TFN membranes were found to be higher than those of the pristine TFC membrane. TFN membrane with smaller GO flake lateral size showed higher  $A$  values and lower  $B$  values comparatively. For instance, the MGO-8 membrane with the smallest GO flake size demonstrated a 52% increase in the  $A$  value and a 33% decrease in the  $B$  value compared to the MGO-0 membrane with the largest GO flake size. A more uniform, hydrophilic and thinner PA layer formation with fewer defects and better GO dispersion resulted in the improved selectivity and permeability of membranes incorporated with GO of smaller flake size. The membrane separation parameters are in good agreement with the performance results presented in **Fig. 5.8**.



**Fig. 5.8** FO performance of the developed TFC and GO-modified TFN membranes in AL-FS/AL-DS arrangements: (A) water flux and (B) *SRSF*.

The intrinsic selectivity ratio ( $B/A$ ) presented in **Table 5.1** is an essential factor for determining the selectivity of FO membranes. A higher membrane selectivity is denoted by a smaller  $B/A$  ratio. The MGO-0 exhibited the highest  $B/A$  value of 0.55 bar; whereas, MGO-8 demonstrated the best selectivity with the smallest  $B/A$  value of 0.24 bar. The  $B/A$  values of the membranes agree well with the previously discussed *SRSF* values (**Fig. 5.8B**).

**Table 5.1** Separation parameters of the fabricated membranes determined using the algorithm established by Tiraferri et al. (2013).

Membrane	$A$ ( $\text{L}\cdot\text{m}^{-2}\cdot\text{h}^{-1}\cdot\text{bar}^{-1}$ )	$B$ ( $\text{L}\cdot\text{m}^{-2}\cdot\text{h}^{-1}$ )	$B/A$ (bar)
TFC	1.29	0.51	0.40
MGO-0	2.44	1.33	0.55
MGO-0.5	2.65	1.05	0.40
MGO-4	3.04	0.85	0.28
MGO-8	3.71	0.89	0.24

### 5.3.4 Membrane fouling study

The fouling propensity of the TFC and GO-modified TFN membranes during FO operation was examined via crossflow fouling tests in AL-FS membrane orientation while taking the DS dilution into consideration. MGO-0 and MGO-8 incorporated with the largest and smallest GO flakes, respectively, were chosen to evaluate the effect of GO flake size on the fouling propensity of the TFN membranes. The normalized water flux ( $J_w/J_{w,0}$ ) of the membranes during the fouling test, with synthetic wastewater as FS and initial water flux ( $J_{w,0}$ ) adjusted to  $\sim 25 \text{ L}\cdot\text{m}^{-2}\cdot\text{h}^{-1}$ , is presented in **Fig. 5.9**. A reduction in normalized water flux was observed for all membranes as soon as sodium alginate and silica were introduced into the FS due to foulant build-up on the membrane surfaces. The TFC membrane demonstrated a continuous and much rapid flux decline compared to the GO-modified membranes and reached a normalized flux of 0.77 for an accumulated permeate volume of 100 mL during the fouling test. The TFC membrane demonstrated the highest flux decline due to its rougher and less hydrophilic PA surface, which facilitated better adhesion of sodium alginate and silica to the membrane surface. The deposited foulant layer considerably reduced the flux by increasing transport resistance and decreasing permeability across the membrane.

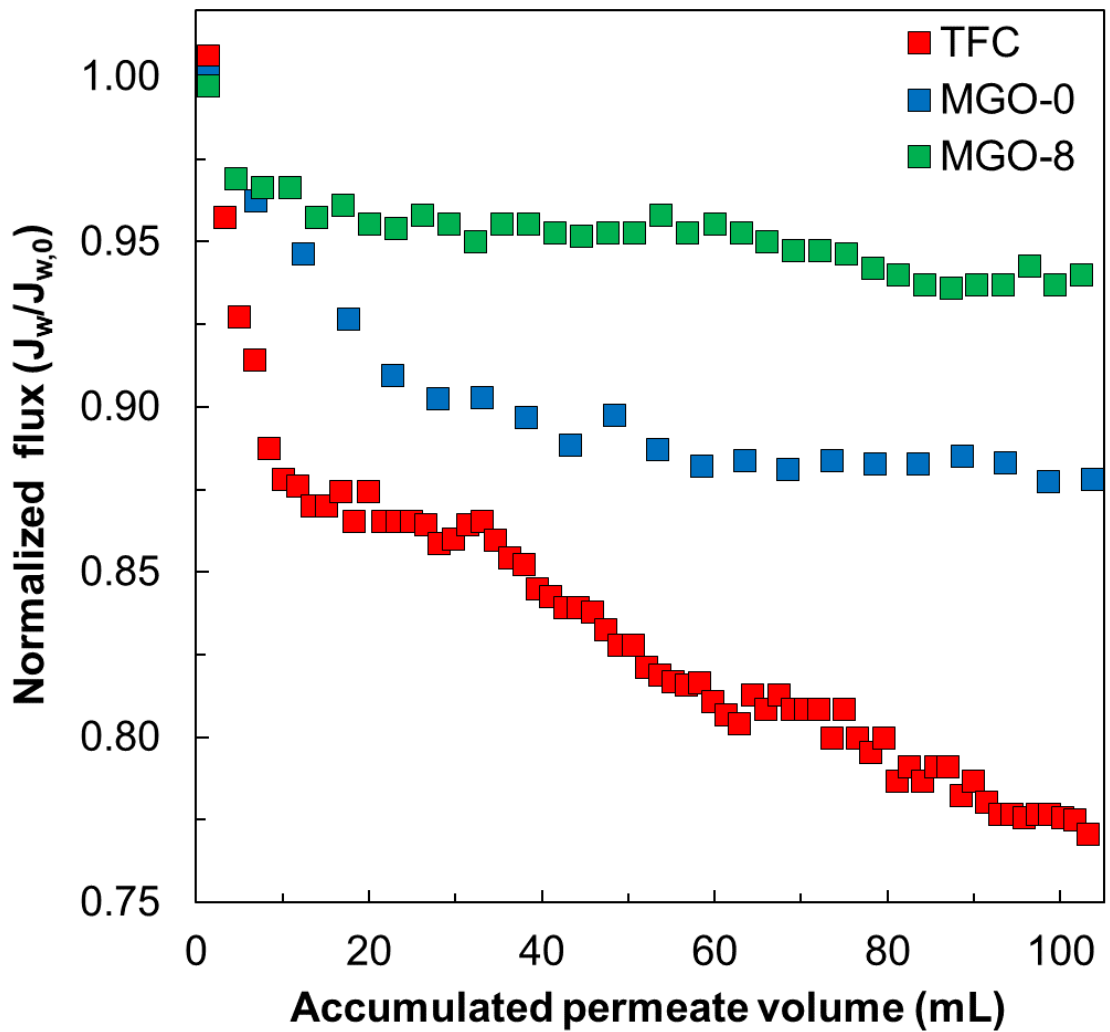
Conversely, the GO-modified membranes exhibited better antifouling property, and MGO-8 showed the lowest flux decline. The normalized flux of MGO-8 and MGO-0 membranes eventually stabilized at 0.94 and 0.88, respectively. As discussed in the previous sections, the increased smoothness, hydrophilicity and surface negativity of the TFN membranes, especially MGO-8, enhanced their fouling resistance and selectivity more than the pristine membrane by restraining hydrophobic foulant attachment on their surfaces and repelling negatively charged salt ions.

The GO TFN membranes created a thin film of water molecules on their hydrophilic surfaces through hydrogen bonding that minimized the adsorption of hydrophobic sodium alginate and silica cake layer on the membrane surfaces (Melián-Martel, Sadhwani Alonso & Ruiz-García 2018). The smooth PA surfaces of GO TFN membranes also minimized the accumulation of foulants by providing them with fewer adhesion sites. Finally, the negatively charged hydroxyl, epoxide and carboxyl functional groups on the GO flakes facilitated repulsion of the negatively charged foulants from the TFN membranes surfaces; thus, improving their antifouling property (Shen, Xiong & Wang 2016).

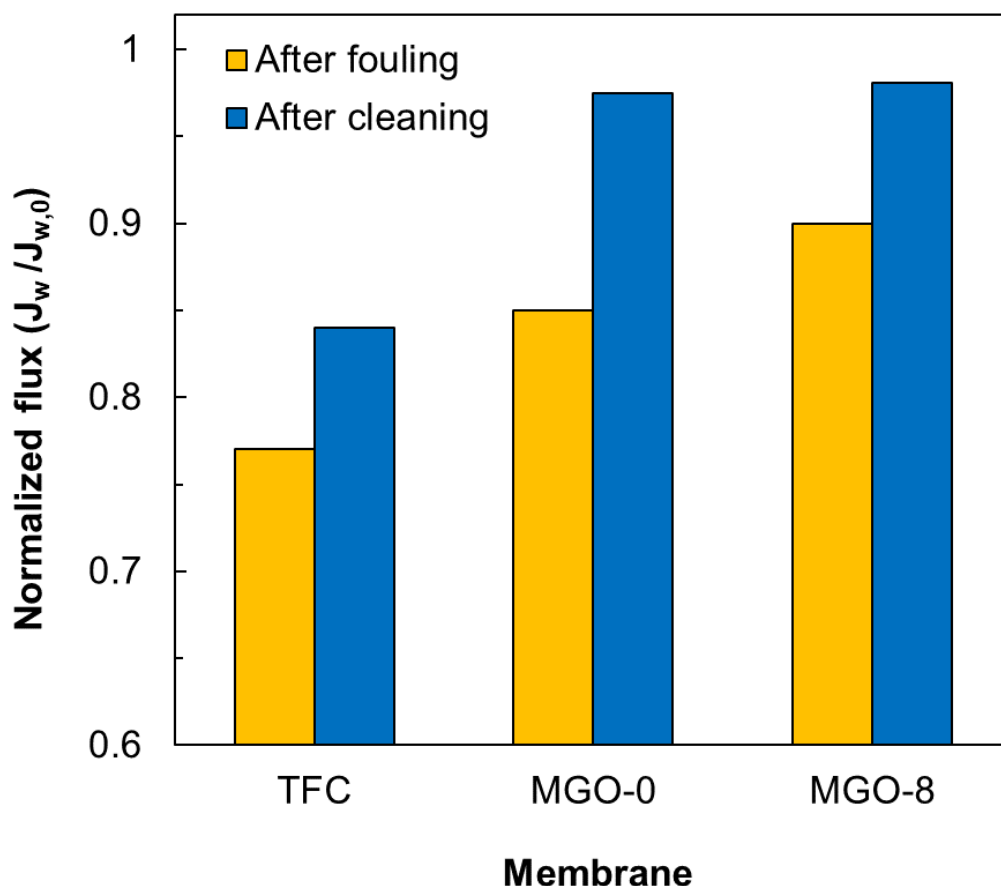
Moreover, it was observed that the fouling propensity of MGO-0 was higher than that of MGO-8. The higher flux decline with MGO-0 can be associated with its higher *SRSF* value compared to that of MGO-8. Although MGO-0 demonstrated a smoother surface than the MGO-8 membrane, its poor selectivity accelerated fouling on its surface because of electrostatic attraction between the charged foulants and the DS ions (Lim et al. 2019). Additionally, MGO-8 demonstrated a higher negative surface charge than the MGO-0 (**Fig. 5.7B**), which minimized the build-up of negatively charged sodium alginate molecules on its surface.

Following the fouling tests, the membranes were physically cleaned, and their flux recovery was obtained to determine the reversibility of the sodium alginate and silica fouling. The normalized membrane water flux before and after hydraulic cleaning is presented in **Fig. 5.10**. The normalized flux for all membranes increased after the cleaning process, which indicates that the fouling is reversible to a certain extent. The GO-modified TFN membranes (MGO-0 and MGO-8) achieved a high flux recovery of around 98%; whereas, the TFC membrane attained a relatively lower flux recovery of 80% after an hour of hydraulic rinsing at  $12.6 \text{ cm}\cdot\text{s}^{-1}$ . The much smoother surfaces of TFN membranes facilitated easier removal of foulants due to fewer adhesive sites on the PA layer.

Additionally, the increased surface negative charge and hydrophilicity of the TFN membranes decreased the foulant- membrane interaction leading to the formation of a loose foulant cake layer, which could be easily detached with the shear force from the high cross-flow velocity during the cleaning process. Therefore, it can be confirmed that the TFC membrane's fouling was partially reversible, while that of GO-modified TFN membranes was almost entirely reversible by physical cleaning. The above results suggest that TFN membranes incorporated with smaller GO flakes (MGO-8) possess better antifouling properties.



**Fig. 5.9** Normalized flux of the TFC, MGO-0 and MGO-8 membranes throughout the FO fouling test. The normalized flux was attained by dividing the water flux obtained after every 5 minute interval by the initial water flux ( $\sim 25 \text{ L}\cdot\text{m}^{-2}\cdot\text{h}^{-1}\cdot\text{bar}^{-1}$ ). NaCl (0.75 M to 2 M) and synthetic wastewater ( $200 \text{ mg}\cdot\text{L}^{-1}$  of sodium alginate and colloidal silica) were used as DS and FS, respectively.



**Fig. 5.10** Normalized flux of the TFC, MGO-0 and MGO-8 membranes before and after hydraulic cleaning (Hydraulic cleaning conditions: FS and DS, DI water; membrane orientation, AL-FS; cross-flow velocity,  $12.6 \text{ cm}\cdot\text{s}^{-1}$ ; physical rinsing duration, 1 h; temperature,  $22 \text{ }^\circ\text{C}$ ).

### 5.3.5 Benchmarking membrane performance

**Table 5.2** shows the performance of GO-incorporated TFN FO membranes developed in this study and those reported in the literature. An efficient FO membrane should demonstrate both high selectivity and permeability. The TFN membranes fabricated in this study exhibited a similar or better performance than those reported in the literature but at a much lower GO loading and DS concentration. The MGO-8 membrane incorporated with the smallest GO flakes exhibited higher water flux than other recently developed GO TFN FO membranes while maintaining membrane selectivity. Thus, the reduction of GO flake size can be a possible strategy for fabricating highly-efficient FO membranes.



**Table 5.2** FO performance summary of the various GO-modified PA TFN flat-sheet in AL-FS orientation.

Membrane	Filler	DS/ FS	$J_w$ (L·m <sup>-2</sup> ·h <sup>-1</sup> )	$SRSF$ (g·L <sup>-1</sup> )	Reference
TFC	N/A	0.5 M NaCl/DI water	13.04	0.40	This work
MGO-0	0.01 wt% GO (1.06 μm <sup>2</sup> )	0.5 M NaCl/DI water	16.38	0.54	This work
MGO-8	0.01 wt% GO (0.01 μm <sup>2</sup> )	0.5 M NaCl/DI water	24.72	0.21	This work
TFC-400	0.04 wt% GO	0.5 M NaCl/DI water	17.5	0.11	(Shen, Xiong & Wang 2016)
TFN 0.1	0.1 wt% GO	1.0 M NaCl/DI water	14.5	0.18	(Eslah et al. 2018)
TFC–PDA/GO-0.5	5 mL of 0.05 wt% GO dispersion	1.0 M NaCl/DI water	24.3	0.16	(Choi et al. 2019)
PA-GO2	2 mL of 0.05 wt% GO dispersion	0.3 M Na <sub>2</sub> SO <sub>4</sub> /DI water	10.5	1.78	(Jin et al. 2018b)
GO-FO-5	0.0175 wt% PVP modified GO	2 M NaCl/10 mM NaCl	14.6	1.0	(Wu et al. 2017)

## 5.4 Conclusions

This study explored the effect of GO flake lateral size on the TFN FO membrane performance. Different GO flake sizes were prepared by subjecting GO to different duration of sonication. GO was incorporated inside the PA layer during the IP process by dispersing 0.01 wt% of GO flakes in the amine solution. Generally, the GO-modified TFN membranes demonstrated better FO performance and antifouling property than the unmodified TFC membrane due to their thinner PA layer, improved membrane surface hydrophilicity, smoother and negatively charged surfaces. The largest GO flakes (GO-0, without tip sonication) were found to create a more defective PA layer by hindering the MPD diffusion into the organic phase and resulting in the formation of a low selective membrane (MGO-0) with a  $SRSF$  of 0.54 g·L<sup>-1</sup>. However, the TFN membrane performance enhanced on

incorporating smaller GO flakes due to a more uniform GO dispersion that reduced PA layer defects. The TFN membrane incorporated with the smallest GO flakes (MGO-8, tip sonicated for 8 h) showed a 51% higher water flux and 61% lower *SRSF* than the MGO-0 membrane when tested with 0.5 M NaCl DS and DI water FS in AL-FS orientation. MGO-8 also demonstrated better antifouling property than MGO-0 due to its augmented surface negativity, improved hydrophilicity and selectivity. These results confirm that the TFN membrane performance can be considerably influenced by GO flake lateral size and that smaller GO flakes can minimize PA defects; thus, improving membrane flux and selectivity. This study provides a guideline for future studies and highlights the significance of an accurate evaluation of the impact of nanomaterial physical properties on membrane performance rather than attributing the improvement in membrane performance solely to chemical modification of nanomaterials.

### **CRedit authorship contribution statement**

Nawshad Akther: Data curation, Formal analysis, Investigation, Methodology, Writing - original draft. Ziwen Yuan: Data curation, Formal analysis, Investigation. Yuan Chen: Formal analysis, Investigation, Methodology. Sungil Lim: Data curation. Sherub Phuntsho: Writing - review & editing. Noredine Ghaffour: Writing - review & editing. Hideto Matsuyama: Writing - review & editing. Hokyong Shon: Supervision, Project administration, Resources, Funding acquisition, Validation, Visualization, Writing – original draft, Writing - review & editing.

### **Declaration of competing interest**

The authors declare that they have no known competing financial interests or personal relationships that could have appeared to influence the work reported in this paper.

## **Acknowledgement**

The research reported in this paper was supported by King Abdullah University of Science and Technology (KAUST), Saudi Arabia through the Competitive Research Grant Program – CRG2017 (CRG6), Grant # URF/1/3404-01. H.K.S. and Y.C. acknowledge the support provided by the Australian Research Council under the Future Fellowships scheme (FT140101208 & FT160100107), Australian Research Council Industry Hub (IH170100009), Discovery Project (DP180102210) and Bhutan Trust Fund for Environmental Conservation (Grant No. MB0167Y16).

# **CHAPTER 6**

## **EMPLOYING THE SYNERGISTIC EFFECT BETWEEN AQUAPORIN NANOSTRUCTURES AND GRAPHENE OXIDE FOR ENHANCED SEPARATION PERFORMANCE OF THIN-FILM NANOCOMPOSITE FORWARD OSMOSIS MEMBRANES**

## STATEMENT OF CONTRIBUTION OF AUTHORS

Title of Paper	Employing the synergistic effect between aquaporin nanostructures and graphene oxide for enhanced separation performance of thin-film nanocomposite forward osmosis membranes		
Publication Status	<input checked="" type="checkbox"/> Published <input type="checkbox"/> Accepted for Publication <input type="checkbox"/> Submitted for Publication <input type="checkbox"/> Unpublished and Unsubmitted work written in manuscript style		
Publication Details	Akther, N., Sanahuja-Embuena, V., Górecki, R., Phuntsho, S., Helix-Nielsen, C. & Shon, H.K. 2021, 'Employing the synergistic effect between aquaporin nanostructures and graphene oxide for enhanced separation performance of thin-film nanocomposite forward osmosis membranes', <i>Desalination</i> , vol. 498, p. 114795.		
<b>PRINCIPAL AUTHOR</b>			
Name of Principal Author (Candidate)	Nawshad Akther		
Contribution to the paper	Conceptualization, Data curation, Formal analysis, Investigation, Methodology, Validation, Writing - original draft.		
Certification	This paper reports on original research I conducted during the period of my Higher Degree by Research candidature and is not subject to any obligations or contractual agreements with a third party that would constrain its inclusion in this thesis. I am the primary author of this paper.		
Signature	Production Note: Signature removed prior to publication.	Date	04/09/2020
<b>CO-AUTHOR CONTRIBUTIONS</b>			
By signing the Statement of Contribution of Authors, each author certifies that:			
i. the candidate's stated contribution to the publication is accurate (as detailed above); and ii. permission is granted for the publication to be included in the candidate's thesis.			
Name of Co-Author 1	Victoria Sanahuja-Embuena		
Contribution to the paper	Formal analysis, Validation, Writing - review and editing.		
Signature	Production Note: Signature removed prior to publication.	Date	04/09/2020
Name of Co-Author 2	Radosław Górecki		
Contribution to the paper	Consultation of the data in regards to AQN, Writing – review and editing.		
Signature	Production Note: Signature removed prior to publication.	Date	04/09/2020
Name of Co-Author 3	Dr. Sherub Phuntsho		
Contribution to the paper	Co-supervision, Writing - review and editing.		
Signature	Production Note: Signature removed prior to publication.	Date	04/09/2020
Name of Co-Author 4	Prof. Claus Helix-Nielsen		
Contribution to the paper	Writing - review and editing.		
Signature	Production Note: Signature removed prior to publication.	Date	04/09/2020

Name of Co-Author 5	Prof. Ho Kyong Shon		
Contribution to the paper	Supervision, Project administration, Resources, Funding acquisition, Validation, Writing - review and editing.		
Signature	Production Note: Signature removed prior to publication.	Date	04/09/2020

## 6. CHAPTER 6 Employing the synergistic effect between aquaporin nanostructures and graphene oxide for enhanced separation performance of thin-film nanocomposite forward osmosis membranes

### Abstract

In this study, novel thin-film nanocomposite (TFN) membranes were developed by incorporating graphene oxide (GO) and Aquaporin Z (AqpZ) reconstituting nanostructure (AQN) into the polyamide (PA) active layer to improve the forward osmosis (FO) performances of the PA TFN membranes. First, the AQN loading in the PA layer was optimized, followed by the GO addition in the PA layer at various loadings until the optimal FO process performance was attained. Experimental results showed that GO flakes increased membrane water flux but decreased selectivity by creating non-selective voids in the PA layer. Whereas, AQN increased membrane selectivity by healing the non-selective PA defects created by the GO flakes. The synergistic effect of GO-AQN improved the water flux without deteriorating the selectivity of the membrane. The TFN membrane with 0.2 wt% AQN and 0.005 wt% GO loading (TFN50) showed an almost 3 folds increase in water flux ( $24.1 \text{ L}\cdot\text{m}^{-2}\cdot\text{h}^{-1}$ ) in comparison to the TFC membrane ( $8.2 \text{ L}\cdot\text{m}^{-2}\cdot\text{h}^{-1}$ ) while retaining the membrane selectivity ( $0.37 \text{ g}\cdot\text{L}^{-1}$ ). Interestingly, the TFN50 membrane demonstrated a 27% lower specific reverse solute flux (*SRSF*) and a marginal increase in water flux than the TFN membrane embedded with 0.005 wt% GO and no AQN (TFNGO50). The overall experimental results confirmed that the addition of AQN into GO-based PA TFN membranes could improve the membrane selectivity by reducing the non-selective PA defects created by GO flakes. The results of this study could provide strategies to further enhance the selectivity of GO-based TFN membranes by preventing the formation of defective PA layer.

**Keywords:** Membrane; Thin-film nanocomposite (TFN); Graphene oxide (GO); Aquaporin, Forward osmosis (FO)

## 6.1 Introduction

Over the recent years, membrane separation operations have been recognized as a potential alternative to traditional processes owing to the possible benefits of their excellent separation efficiencies and lower operating and capital costs (Akther et al. 2015; Daer et al. 2020; Klaysom, Cath, et al. 2013; Marchetti et al. 2014). Since membrane processes that are osmotically-driven like forward osmosis (FO) possess higher water recovery and lower fouling tendency as opposed to pressure-driven membrane processes like reverse osmosis (RO), they have been intensely investigated for wastewater treatment (Tran et al. 2019), brine dilution (Akther, Daer & Hasan 2018), food processing (Sant'Anna, Marczak & Tessaro 2012) and resource recovery (Zhang et al. 2014). The main driving force in FO processes is the osmotic pressure difference existing between the feed solution (FS) and the more concentrated draw solution (DS), which allows water to flow across the semi-permeable membrane (Akther, Daer, et al. 2019; Akther et al. 2015). Consequently, FO processes have been found to consume lower energy than RO when employed in applications not requiring DS regeneration.

FO processes mainly rely on polyamide (PA) thin-film composite (TFC) membranes, which are prepared from the interfacial polymerization (IP) reaction between trimesoyl chloride (TMC) and m-phenylenediamine (MPD), due to their superior permeability-selectivity performance and broader pH tolerance range than that of the cellulose-based membranes (Giwa et al. 2016; Tiraferri, Vecitis & Elimelech 2011). The porous substrate of the TFC membrane provides mechanical support to the dense and ultrathin PA selective layer, which influences the separation property of the membrane. Although PA TFC membranes are currently recognized as the state-of-the-art membranes for use in wastewater treatment, desalination and other separation applications, they exhibit low water flux, and a trade-off between water permeability and solute selectivity,



which significantly inhibits the process separation efficiency (Akther, Phuntsho, et al. 2019). In addition, the inherently hydrophobic and rough surface of the PA layer promotes membrane fouling, which could impede their application for high-fouling wastewater treatment (Lu, Arias Chavez, et al. 2015). The declined membrane performance could reduce membrane life and increase the overall operating costs (Jirjis & Luque 2010; Maddah & Chogle 2017). Hence, the development of highly efficient PA TFC FO membranes is required to enhance the membrane performance and reduce the foulant deposition on the membrane surface.

To overcome the issues mentioned above, thin-film nanocomposite (TFN) membranes, which involves the addition of nanomaterials into the PA selective layer, have been extensively explored for enhancing the membrane separation efficiency (Akther, Phuntsho, et al. 2019; Giwa et al. 2016; Lim, Akther, et al. 2020). Since first reported by Hoek's group in 2017 (Jeong et al. 2007b), various nanomaterials like zeolites (Lind et al. 2009), carbon nanotubes (Song et al. 2015), graphene oxide (GO) (Akther, Yuan, et al. 2020; Lim, Park, et al. 2020b), graphene quantum dots (Shen et al. 2020a; Xu et al. 2019), silica (Daer et al. 2020; Niksefat, Jahanshahi & Rahimpour 2014), covalent/metal-organic frameworks (Akther, Lim, et al. 2019; Ma, Peh, et al. 2017) and titanium oxide (Amini, Rahimpour & Jahanshahi 2016) have been heavily studied for altering the membrane characteristics and performance depending on the physical and chemical properties of the embedded nanomaterial. For instance, porous nanomaterial like zeolites act as molecular sieves for size-selective separation of molecules and are suitable for pervaporation and gas separation (McLeary, Jansen & Kapteijn 2006); whereas, two-dimensional GO flakes have been widely used to improve the membrane hydrophilicity, antifouling and antimicrobial properties for

desalination and wastewater treatment (Akther, Ali, et al. 2020; Lim, Park, et al. 2020a; Mahmoud et al. 2015).

Nonetheless, TFN membranes often exhibit lower solute rejection compared to the TFC membranes due to the formation of non-selective interfacial voids between the nanoparticles and PA matrix. The defective non-uniform PA layer in TFN membranes form due to several reasons, such as the incompatibility of the nanofillers with the PA matrix, severe aggregation of nanofillers within the PA, and nanofillers impeding the reaction between monomers during the IP process (Akther, Phuntsho, et al. 2019; Akther, Yuan, et al. 2020). Therefore, it is imperative to select nanomaterials that are compatible with the PA and to design TFN membranes to improve the membrane water permeability without significantly deteriorating the selectivity.

It has been recently observed in one of our studies that GO flakes created non-selective patches when incorporated into the PA layer of the membrane (Akther, Yuan, et al. 2020), which reduced the membrane selectivity. To tackle this issue, this study considered the use of nanostructures incorporating aquaporin proteins, specifically Aquaporin Z (AqpZ). AqpZ is a transmembrane protein in charge of the selective transport of water through the cell membrane of *Escherichia coli* (*E. coli*). It is formed by a bundle of six  $\alpha$  helices, which leave a narrow opening inside, allowing only water molecules to pass through (Borgnia et al. 1999; Verkman 2013; Verkman & Mitra 2000). Thus, AqpZ were extensively studied to be used in membrane technology for developing advanced biomimetic membranes that could be more selective than conventional TFC membranes (Górecki et al. 2020; Sengur-Tasdemir et al. 2016; Xia et al. 2017). Since AqpZ can degrade or denature, they require a membrane cell structure or similar to function properly when embedded into the polymer membranes. Stabilization of these proteins is mostly done by

incorporating them into the bilayer membranes of vesicular nanostructures, such as liposomes made of phospholipids or polymersomes made of amphiphilic block copolymers (Garni et al. 2017; Itel et al. 2015; Zhao, Vararattanavech, et al. 2013). There is a preference for using polymer-based nanostructures to stabilise AqpZ as they are better suited in terms of stability for membrane manufacturing processes and industrial applications (Discher & Ahmed 2006; Discher & Eisenberg 2002). To further improve the incorporation of these nanostructures into the membrane, amino terminated chains could be introduced to covalently bond the nanostructures within the PA layer (Grzelakowski & Kita-Tokarczyk 2016; Xie et al. 2013). Therefore, in this study, we used AqpZ incorporated in Pluronic® based nanostructures of Poly(ethylene glycol)-block-poly(propylene glycol)-block-poly(ethylene glycol) (PEG-PPG-PEG) blend with poly(ether monoamine) (PMA). The PMA could facilitate the addition of nanostructures into the PA layer during the IP reaction, and AqpZ proteins will assist in maintaining the selectivity that may be lost from the incorporation of GO flakes.

To the best of our knowledge, this is the first study to present the synergistic use of AqpZ reconstituting nanostructure (AQN) with GO for the preparation of PA TFN membranes. Additionally, it is the first to describe the “healing” effect of AQN towards the non-selective defects created by GO flakes in the PA layer. We believe that the article will open the doors towards further research of the synergistic use of different nanostructures to prepare novel membrane materials.

## **6.2 Materials and methods**

### **6.2.1 Chemicals**

Commercial GO-water dispersion (particle size <10  $\mu\text{m}$ , 4  $\text{mg}\cdot\text{mL}^{-1}$ ) was supplied by Graphenea; and the GO properties and characteristics can be found on the supplier’s website.

Membrane substrates were prepared from polysulfone pellets (PSf, P-3500 Udel<sup>®</sup>, Solvay) using 1-methyl-2 pyrrolidone (NMP,  $\geq 99.5\%$ , Merck) as the polymer solvent. Trimesoyl chloride (TMC, 98%) and m-phenylenediamine flakes (MPD, 99%) were provided by Sigma-Aldrich. N-hexane (98.5%, Merck) was used as an organic solvent for TMC. Sodium chloride (NaCl,  $> 99.7\%$ , Chem Supply) was utilized as a draw solute. Deionized (DI) water (Milli-Q<sup>®</sup>, Merck) with a resistivity of  $\sim 18 \text{ M}\Omega\cdot\text{cm}^{-1}$  was used to prepare DS and FS. Polymer-based nanostructure solution incorporated with AqpZ was developed by and obtained from Aquaporin A/S (Denmark). The development and characteristics of the nanostructure solution can be found in the corresponding patent and our previous work (Górecki et al. 2020; Spulber et al. 2019).

### **6.2.2 TFC and TFN membrane fabrication**

The porous flat-sheet substrates were prepared from 12 wt% PSf dope solution using the phase inversion technique described in our previous work (Akther, Yuan, et al. 2020). More details are given in Section 3.2.1.1. IP was then conducted on the prepared PSf substrates to produce a TFC membrane. First, the substrate was treated with 2 wt% MPD aqueous amine solution for 2.5 min, and the excess amine solution was removed using a nitrogen knife. The amine-saturated substrate was then exposed to 0.1 wt% TMC organic solution for 1 min to initiate the IP reaction. More information is provided in Section 3.2.1.2. The AQN and GO incorporated TFN membranes were produced using the same procedure as that of the TFC membrane, except for the addition of AQNs and GO flakes in the MPD aqueous solution at the desired loadings. The GO flakes were first added to the amine solution and placed in a bath sonicator for 30 min to achieve uniform dispersion. AQNs were then added to the well-dispersed GO-containing amine solution and mixed for 1 h using a shaker, which was brought in contact with the PSf substrate. The subsequent amine-impregnated PSf substrate was reacted with TMC organic solution to produce the TFN membranes. **Table 6.1** presents

the AQN and GO loadings in MPD amine aqueous solution of the various membranes prepared in this study.

**Table 6.1** AQN and GO compositions of the pristine TFC and modified TFN membranes.

Membranes	Concentration in aqueous amine solution	
	AQN ( $\text{g}\cdot\text{L}^{-1}$ )	GO ( $\text{mg}\cdot\text{L}^{-1}$ )
TFC	0	0
TFN0	2	0
TFN25	2	25
TFN50	2	50
TFN75	2	75
TFNGO25	0	25
TFNGO50	0	50
TFNGO75	0	75

### 6.2.3 Membrane characterisation

Membrane surface morphology was studied using a scanning electron microscope (SEM, Zeiss Supra 55VP) and atomic force microscopy (AFM, Park XE7, Park Systems). Dry samples of the membranes were sputter-coated with an 8 nm thick Pd/Au layer before SEM investigation and examined at 5 or 10 kV. AFM scanning was repeated at least three times for each sample under tapping mode with a scan area of  $5\ \mu\text{m} \times 5\ \mu\text{m}$  and the average surface roughness measurements were reported. The surface chemistry of the TFC and TFN membranes were examined using Fourier transform infrared spectroscopy (FTIR, Shimadzu MIRacle 10). An optical tensiometer (Attension Theta Lite 100, Biolin Scientific) was used to verify the membrane surface hydrophilicity by randomly measuring at least seven water contact angles on the surface of each membrane sample and the average value was reported. The charge on the membrane surface was determined over a pH range of 3 to 10 by measuring the zeta potential using an electrokinetic analyzer (SurPASS<sup>TM</sup> 3, Anton Paar). The gap height of the membrane sample holder was adjusted to approximately  $100\ \mu\text{m}$ , and

1 mM KCl solution was used as the electrolyte. The electrolyte pH was varied using 0.05 M NaOH and HCl. The membrane surface zeta-potential was verified from the acquired streaming potential.

#### **6.2.4 Membrane performance evaluation**

As previously described in Section 3.4.1, a laboratory-scale FO setup was utilized to ascertain the membrane performance. During the FO tests, both the DS and FS were co-currently circulated across the membrane at a flow rate of  $0.5 \text{ Lmin}^{-1}$  ( $12.6 \text{ cm}\cdot\text{s}^{-1}$ ), unless stated otherwise, and their temperature was maintained at  $22 \text{ }^\circ\text{C}$  using a temperature controller. The membranes were placed in AL-FS (active layer facing FS) orientation while using DI water and  $0.5 \text{ M NaCl}$  as FS and DS, respectively. The water flux ( $J_w, \text{ L}\cdot\text{m}^{-2}\cdot\text{h}^{-1}$ ) and reverse solute flux ( $J_s, \text{ g}\cdot\text{m}^{-2}\cdot\text{h}^{-1}$ ) through the membrane was determined from Eqs. 3.1 and 3.2, respectively. The water and reverse solute flux values were employed to evaluate the specific reverse solute flux ( $SRSF, \text{ g}\cdot\text{L}^{-1}$ ) across the membrane to indicate the membrane selectivity (Eq. 3.3). Section 3.4.2 presents the equations that are employed to calculate the membrane performance parameters.

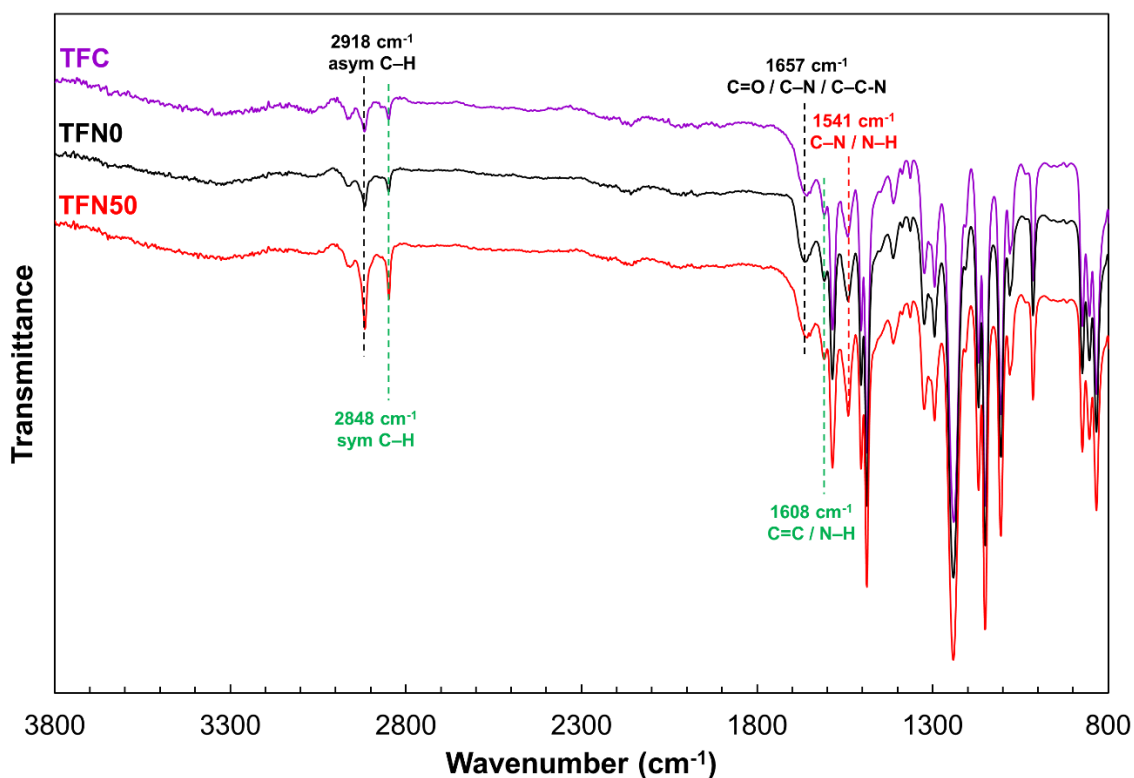
The non-linear regression model developed for FO membranes was used to establish the pure water permeability coefficients ( $A, \text{ L}\cdot\text{m}^{-2}\cdot\text{h}^{-1}\cdot\text{bar}^{-1}$ ), solute permeability coefficients ( $B, \text{ L}\cdot\text{m}^{-2}\cdot\text{h}^{-1}$ ) and intrinsic selectivities ( $B/A, \text{ bar}^{-1}$ ) of the membranes.

### **6.3 Results and discussion**

#### **6.3.1 Membrane characterisation**

In this study, AQNs and GO flakes were embedded in the PA layer to improve the separation performance of the PA TFN FO membranes. The FTIR spectra shown in **Fig. 6.1** were used to assess the surface chemistry of the prepared membranes. The spectra show distinctive fingerprints of the TFC and TFN membranes arising from their PA selective layers and PSf

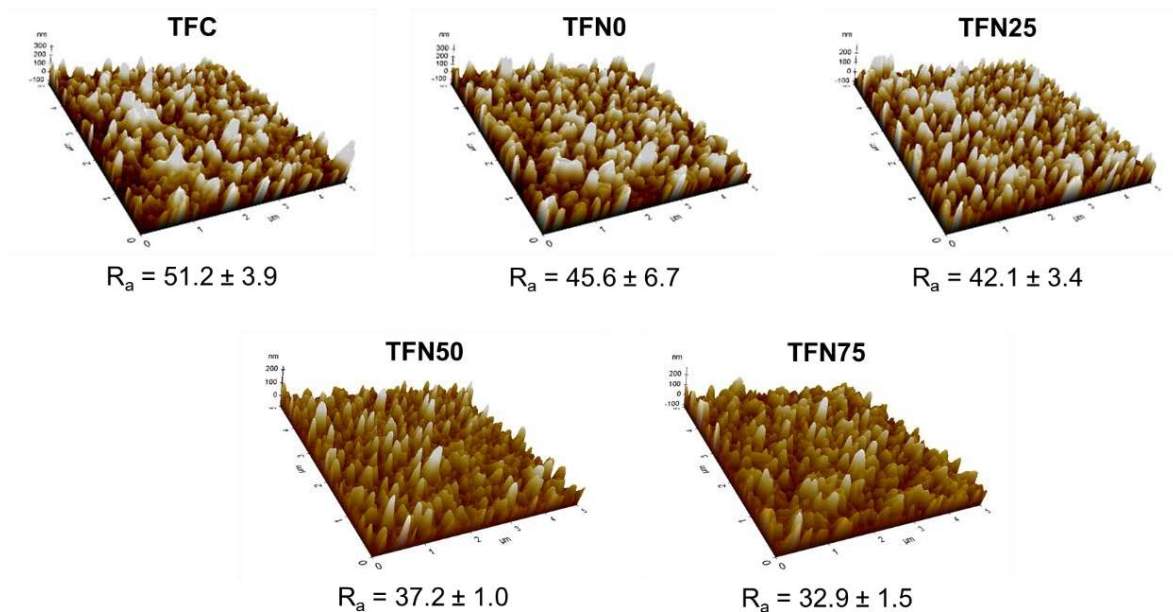
substrates (Tang, Kwon & Leckie 2009a). The typical peaks showing the functional groups of the PSf substrate occur at  $1294\text{ cm}^{-1}$  (asymmetric O=S=O bond stretching vibration),  $1151\text{ cm}^{-1}$  (symmetric O=S=O bond stretching vibration),  $1504\text{ cm}^{-1}$  (aromatic in-plane ring stretching vibration),  $1246\text{ cm}^{-1}$  (asymmetric C–O–C stretching vibration) and  $1385\text{ cm}^{-1}$  (symmetric C–H deformation) (Akther, Ali, et al. 2020; Tang, Kwon & Leckie 2009a). The distinctive peaks denoting the functional groups of PA appear at  $1657\text{ cm}^{-1}$  (C=O stretching, C–N stretching, and C–C–N deformation vibration in the secondary amide group of amide I band),  $1608\text{ cm}^{-1}$  (C=C ring stretching or N–H deformation vibration in aromatic amide), and  $1541\text{ cm}^{-1}$  (C–N stretching and N–H in-plane bending vibration in the –CO–NH– group of the amide II band) (Hu et al. 2016; Tang, Kwon & Leckie 2009a). The TFN50 membrane showed the most intense peaks at  $2848\text{ cm}^{-1}$  (symmetric C–H stretch), and  $2918\text{ cm}^{-1}$  (asymmetric C–H stretch) due to the presence of GO flakes in the PA layer (Akther, Yuan, et al. 2020; Kang et al. 2019). The broad absorption band from  $3150$  to  $3750\text{ cm}^{-1}$  arises from the overlapping peaks attributed to the PA structure's carboxyl group and N–H stretching and GO flakes' hydroxyl group stretching. As a result, the TFN50 demonstrated the most substantial peak at  $3310\text{ cm}^{-1}$  due to ample O–H groups from the GO flakes. Other groups related to the AQNs like C–H and N–H are found within the same range as that of the PSf and PA. The high intensity of these peaks masks those of the AQNs as they are present in low concentration; thus, making FTIR only a supporting analysis for identifying AQN incorporation. Even though some traces can be found indicating the presence of the AQNs, other analysis like membrane performance is more precise in displaying the effect and incorporation of the AQNs.



**Fig. 6.1** FTIR spectra of the pristine and modified TFC membranes.

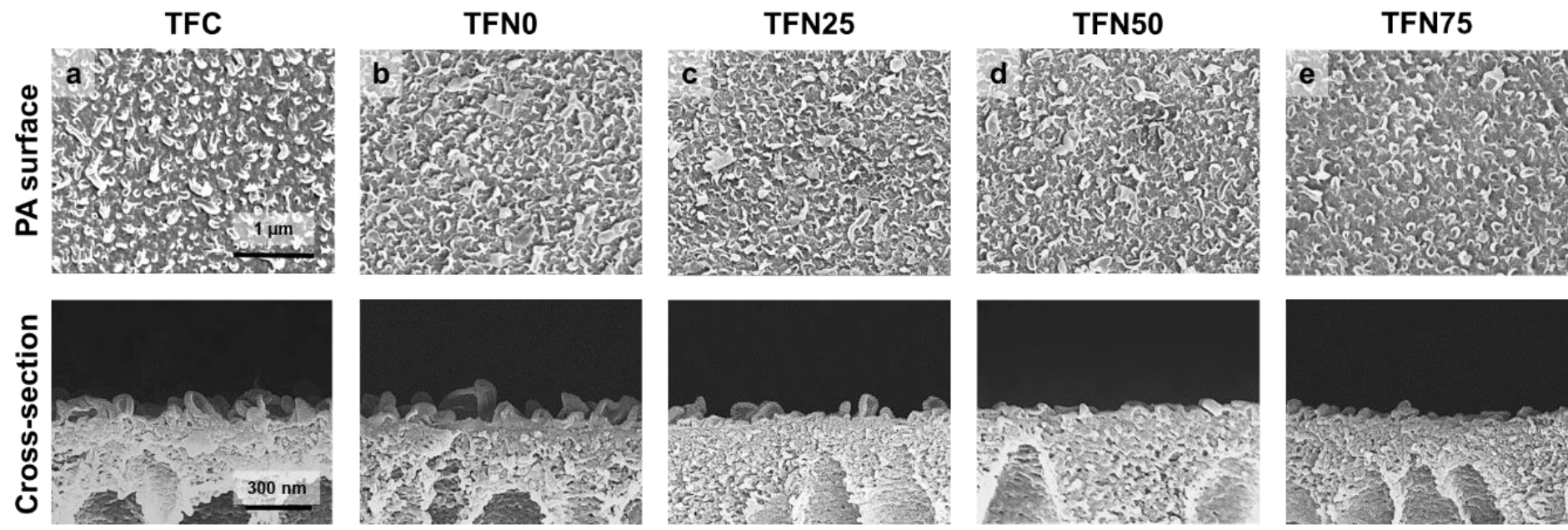
The surface roughness of the TFC and TFN membranes was examined using AFM topography. **Fig. 6.2** presents the AFM images of the fabricated TFC and TFN membranes, along with the mean membrane roughness ( $R_a$ ). The root mean square ( $R_q$ ) and maximum ( $R_{max}$ ) membrane surface roughness values are presented in **Table S6.1**. The TFC membrane exhibited the roughest PA surface with a  $R_a$  value of 51.2 nm. The  $R_a$  value reduced to 45.6 nm for TFN0 membranes due to the incorporation of AQNs. The addition of GO significantly decreased the membrane surface roughness due to GO restricting the PA growths during the IP reaction. The membrane surface smoothness increased with an increase in GO flake loading due to more effective retardation of MPD diffusion into the TMC/n-hexane organic phase. As a result, the TFN75 membrane revealed the smoothest surface ( $R_a = 32.9$  nm) as the GO sheets at a loading of  $75 \text{ mg}\cdot\text{L}^{-1}$  slowed down the IP reaction most effectively; thus, forming smaller PA protrusions.





**Fig. 6.2:** AFM images representing the PA surface roughness of the prepared TFC and TFN membranes. Error bars represent one standard error obtained from roughness measurements of at least three membrane samples for each condition.

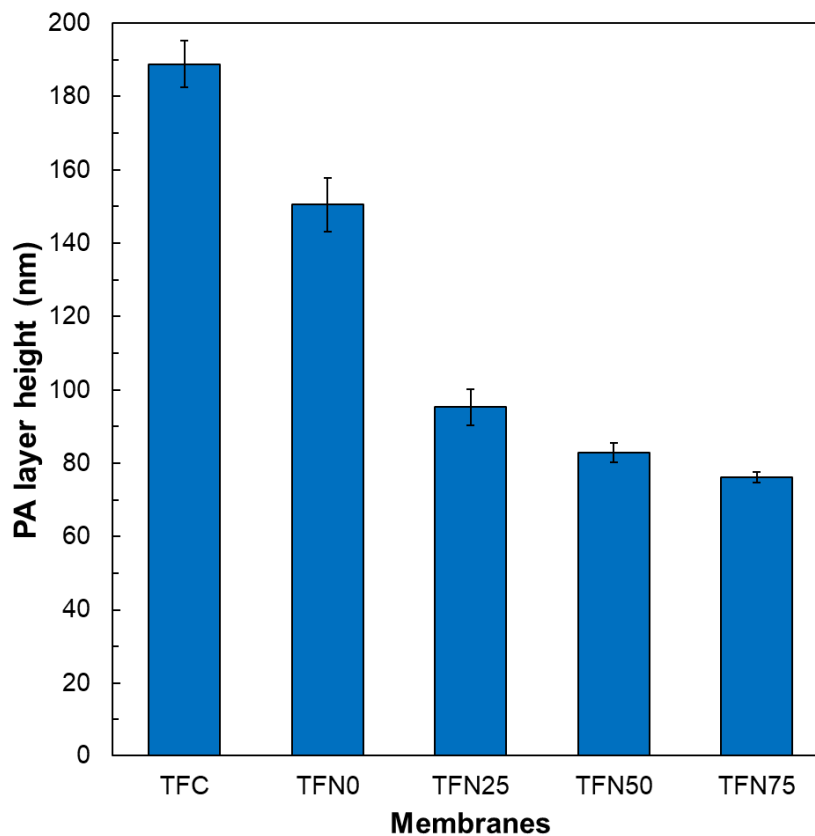
The PA surface and the membrane cross-section morphologies were examined using SEM, as shown in **Fig. 6.3**. All the membranes demonstrate the characteristic ridge-and-valley structures of the PA layer. Both the TFC and TFN0 membranes display a consistent distribution of the PA ridge-and-valley structures. Nonetheless, the PA structure of the pristine membrane shows compact globule-like formations; whereas, that of TFN0 is sparse with leaf-like formations. The AQNs compete with MPD as they can covalently bond with TMC via the amine groups of PMA chains during the IP reaction. We speculate that since less MPD can react with TMC, incorporating AQNs into the PA layer should reduce the PA cross-linking density and form sparser leaf-like structures compared to the TFC membrane. Additionally, AQNs consisting of PEG-PPG-PEG may affect the diffusion of MPD to the organic phase, which further alters the morphology of the PA layer.



**Fig. 6.3** SEM images demonstrating both the surface morphology of the PA layer (top) and cross-section of the prepared membranes (bottom): (a) pristine TFC, (b) TFN0, (c) TFN25, (d) TFN50 and (e) TFN75.

Interestingly, the incorporation of GO flakes into the PA layer considerably transformed the membrane morphology by forming much smaller ridges and smoother PA layer than those of the pristine TFC and TFN0 membranes, as evident from their AFM and SEM surface morphology images (**Fig. 6.2** and **Fig. 6.3**). As discussed in our previous study, GO-incorporated TFN membranes exhibited smoother PA surfaces compared to the TFC membranes because GO flakes prevented MPD from quickly diffusing into the TMC organic phase during the IP process (Akther, Yuan, et al. 2020). As a result, the IP reaction is delayed due to the effect of steric hindrance resulting from the GO flakes. GO can further reduce the reaction rate between MPD and TMC by preferentially reacting with the oxygen functional groups of both the monomers.

It can be observed from the cross-sectional SEM images that the height of the PA layer decreased with the addition of AQN and GO (**Fig. 6.3**). The PA layer height here does not indicate the PA skin thickness, but the average PA layer height from the top of the substrate to the PA ridge. The average PA layer height obtained from the SEM images is presented in **Fig. 6.4**. Both AQNs and GO flakes decrease the average PA layer height by intruding the development of PA ridge-and-valley formations during the IP reaction through steric hindrance and reacting with the acyl chloride groups of TMC (Yin, Zhu & Deng 2016). Consequently, the overall thickness of the PA layer diminishes with increasing GO flake loading.



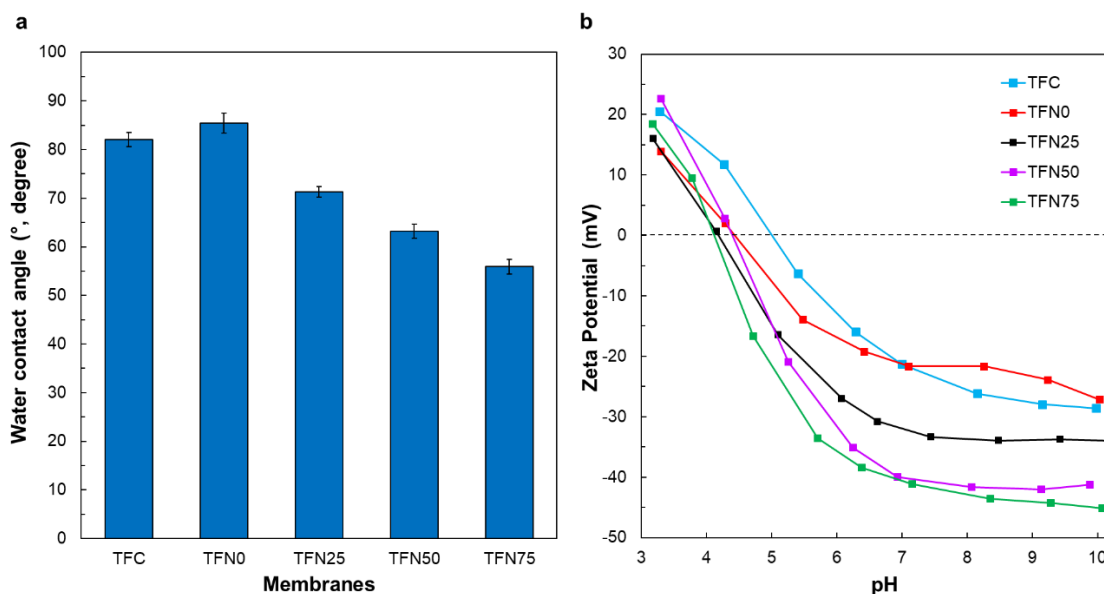
**Fig. 6.4:** PA layer height of the prepared pristine TFC and modified TFN membranes. Error bars represent one standard error obtained from at least three measurements for each membrane sample.

The membrane surface hydrophilicity was established from water contact angles measured at the air-water interface on the PA layer surface. As displayed in **Fig. 6.5a**, the mean water contact angles on the TFN0 surface was higher than that of the TFC membrane, suggesting that AQNs decrease the membrane surface wettability. AQNs used in this study contain the amino terminated PMA to allow covalent bonding within the PA layer. PMA is hydrophobic and its incorporation explains the increase in the contact angles measurements for TFN0. Additionally, AQNs have a hydrophobic part for the AQNs to stabilize in the membrane bilayer of the vesicle or nanostructures. The hydrophobic PMA chains may be exposed within the PA if the AQN is damaged during IP reaction, which can increase the hydrophobicity of the TFN0 membrane regardless of AQNs, increasing the membrane permeability.

In contrast, the water contact angles on the TFN membrane surfaces substantially decreased from 85.4° for the AQN-embedded TFN0 membrane to 71.3°, 63.2°, and 55.9° for the AQN-GO-embedded TFN25, TFN50 and TFN75 membranes, respectively, which confirms the improvement in membrane hydrophilicity after GO addition in the PA layer. The enhanced wettability of the GO-embedded TFN membranes could be attributed to the hydrophilic oxygen-containing functional groups of GO. Membrane surface hydrophilicity is considered to be an essential membrane property in assessing the membrane performance as it can influence both the water permeability and fouling behaviour of the membranes (Rastgar et al. 2018).

The surface charges of the TFC and TFN membranes were ascertained over a pH range of 3 to 10 by evaluating their surface zeta potentials. As can be seen from **Fig. 6.5b**, all membrane surfaces were negatively-charged at pH >5 because of the deprotonation of the PA layer's carboxyl and amino functional groups (Lau, Ismail, et al. 2015). The membrane surfaces become positively-charged at a lower pH due to the protonation of the end amino groups in the PA. The negative surface charge of TFN membranes augmented at a higher GO concentration owing to the oxygen-containing groups of GO that heighten the negative charges by deprotonating in alkaline conditions. **Fig. 6.5b** shows the isoelectric points (IEPs) of the membrane surfaces, where they carry no charge. The IEP of the TFC membrane occurs at pH 5, and the IEPs of the TFN membranes generally shift to lower pH following the addition of GO into the PA layer because of the increasing quantity of acidic groups from GO (Akther, Yuan, et al. 2020; Dimiev, Alemany & Tour 2013). The TFN0 membrane exhibits an increase in zeta potential between pH 7 and 9 due to the presence of PMA in AQN. PMA increases the pH of the AQN solution to 9 and alters the TFN0 membrane's zeta potential under high pH when it is incorporated into the PA layer. Generally, the changes in membrane surface properties after the addition of AQN and GO flakes in the PA layer

confirmed that the properties of the PA TFC membranes could be regulated by altering the composition of the GO flakes and AQNs in the PA active layer.



**Fig. 6.5:** (a) Water contact angle and (b) zeta potential measurements of the pristine TFC and modified TFN membrane surfaces. Error bars for water contact angle measurements represent one standard error obtained from at least seven measurements for each membrane sample.

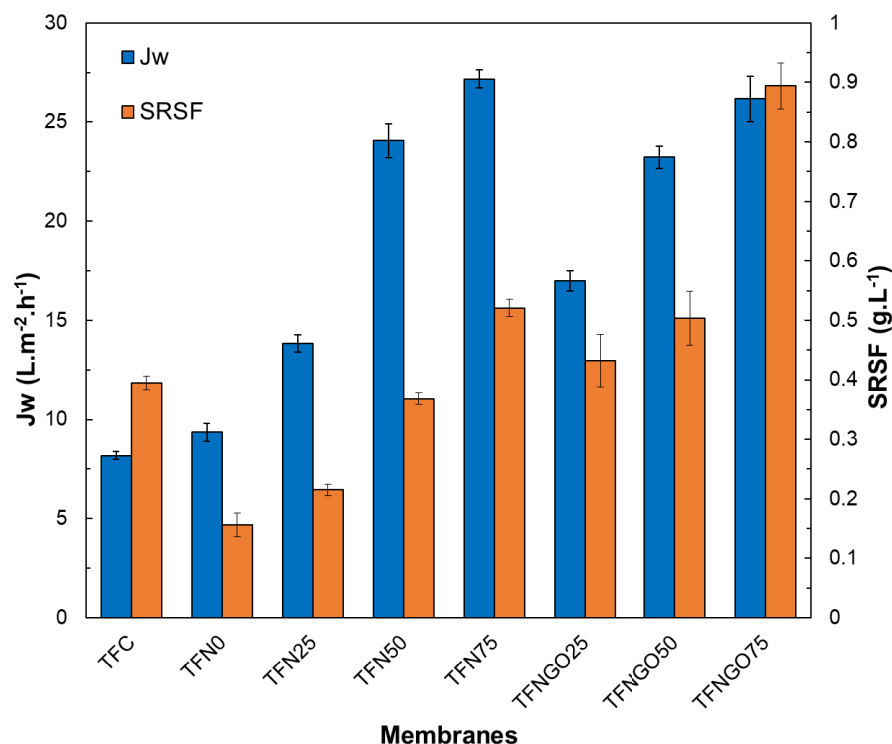
### 6.3.2 Membrane performance evaluation

The FO performances of the membranes were evaluated from the water flux and *SRSF* values obtained in AL-FS mode using 0.5 M NaCl as DS and DI water as FS (**Fig. 6.6**). The AQN-embedded TFN membrane (TFN0) showed only a slight improvement in water flux ( $9.4 \text{ L}\cdot\text{m}^{-2}\cdot\text{h}^{-1}$ ) compared to the pristine TFC membrane ( $8.2 \text{ L}\cdot\text{m}^{-2}\cdot\text{h}^{-1}$ ). However, TFN0 exhibited a 59% reduction in *SRSF* ( $0.16 \text{ g}\cdot\text{L}^{-1}$ ) than that of the TFC membrane ( $0.39 \text{ g}\cdot\text{L}^{-1}$ ). This observation confirms that AQN plays a role in improving the selectivity of the PA TFN membranes. We speculate that AQN incorporation reduces the cross-linking density of the PA, as AQNs are covalently bonded to the PA. Reduced cross-linking density is generally expected to reduce the membrane selectivity; however, the TFN0 membrane exhibited enhanced water permeability and selectivity. Based on previous studies, incorporating AqpZ

or polymersomes/nanostructures are known to improve membrane permeability (Gan et al. 2019; Kumar et al. 2007; Li, Qi, et al. 2019; Qi, Fang, et al. 2018; Tang et al. 2015). The improved selectivity of the TFN0 membrane suggests that the addition of AQN retained the integrity of the PA layer and created minimal or no PA defects. The slight improvement in the water flux of the TFN0 membrane can be attributed to the AqpZ protein and the comparatively thinner PA layer (**Fig. 6.3b** and **Fig. 6.4**), which facilitated faster water transport across the membrane.

On the other hand, both the water flux and SRSF across the AQN-incorporated TFN membranes increased with increasing GO addition (TFN25, TFN50 and TFN75) compared to the TFN0 membrane. The higher water flux of the AQN-GO incorporated TFN membranes could be ascribed to their thinner and sparser PA layers (**Fig. 6.3c-e** and **Fig. 6.4**), which reduced the water transport resistance across the membrane, and to their improved surface wettability (**Fig. 6.5a**). The *SRSF* values of the AQN-GO incorporated TFN membranes increased at higher GO loadings due to more defects formed in the PA layer, as discussed in our previous study (Akther, Yuan, et al. 2020). The loose pore structure of the PA layer at the highest GO loading of 75 mg·L<sup>-1</sup> (TFN75) permitted relatively more solute molecules to move from the DS to the FS. Nonetheless, it is interesting to note that the selectivity of AQN-GO incorporated TFN membranes is much better than that of the GO-only incorporated TFN membranes (TFNGO25, TFNGO50 and TFNGO75). Some of the non-selective PA defects in GO TFN membranes, which formed due to GO restricting the IP reaction, could be healed by reacting the exposed carboxyl groups with the amine groups of PMA chains in the AQNs. In addition, the amphiphilic composition of the AQN may enhance the MPD diffusion during the IP reaction, further improving selectivity and healing the defects induced by GO. The intrinsic selectivity of the AQNs, coupled with the disappearance of some of the defects, is responsible for the superior selectivity of the AQN-

GO TFN membranes compared to the GO TFN membranes. The performance results showed that AQNs could not completely eradicate PA defects formed by GO.



**Fig. 6.6:** FO performance of the pristine TFC and modified TFN membranes. Operating conditions: membrane orientation, AL-FS; DS, 0.5 M NaCl; FS, DI water; cross-flow velocity, 12.6 cm·s<sup>-1</sup>. Error bars represent one standard error obtained from the performance test results of at least three membrane samples for each condition.

Nevertheless, overall results suggest that AQNs in PA help to partially heal the defects created by GO in the PA layer. For instance, the TFN50 membrane (0.2 wt% AQN and 0.005 wt% GO) exhibited a 27% lower *SRSF* than that of the TFNGO50 membrane (0.005 wt% GO) while revealing similar water fluxes of ~23.5 L·m<sup>-2</sup>·h<sup>-1</sup>. The GO-incorporated TFN membranes demonstrated nearly similar water flux as that of the AQN-GO incorporated TFN membranes at the same GO loading, but those incorporated with AQN attained better selectivity to draw solutes. The TFN50 membrane was selected as the optimum membrane for this study as it exhibited substantial improvement in water flux with a similar *SRSF* value as that of the pristine membrane.



The intrinsic membrane transport properties were estimated from the  $A$  and  $B$  values, as presented in **Table 6.2**. All the TFN membranes exhibited higher  $A$  values; whereas, TFN0 and TFN25 showed lower  $B$  values in comparison to the pristine membrane. The GO flakes improved the membrane permeability by increasing membrane wettability, decreasing PA layer thickness and creating defects in the PA layer; whereas, AQNs enhanced membrane selectivity by healing PA defects. The  $B/A$  ratios of the prepared membranes are also shown in **Table 6.2**, where a smaller  $B/A$  ratio represents a more selective membrane and vice versa. The TFN75 membrane showed the highest  $B/A$  ratio of 0.63 bar; whereas, TFN0 was found to be the most selective by demonstrating the smallest  $B/A$  value of 0.19 bar. The intrinsic transport parameters agree well with the FO performance results displayed in **Fig. 6.6** and validated that the TFN membrane performance can be adjusted by varying the AQN and GO concentrations in the PA layer. Additionally, the enhanced selectivity of AQN-incorporated TFN membranes indicates that AQNs play an essential role in repairing the PA defects.

**Table 6.2** Intrinsic transport parameters of the membranes.

Membrane	$A$ ( $\text{L}\cdot\text{m}^{-2}\cdot\text{h}^{-1}\cdot\text{bar}^{-1}$ )	$B$ ( $\text{L}\cdot\text{m}^{-2}\cdot\text{h}^{-1}$ )	$B/A$ (bar)
TFC	1.02	0.47	0.46
TFN0	1.13	0.21	0.19
TFN25	1.59	0.41	0.26
TFN50	2.78	1.21	0.44
TFN75	3.06	1.93	0.63

## 6.4 Conclusions

In this study, TFN membranes were developed by incorporating both AQNs and GO flakes in the PA layers to improve the separation performance of the TFN membranes. The addition of AQNs in the TFN membranes improved the selectivity of the TFN membranes compared to the pristine TFC membrane. While the addition of GO enhanced the membrane permeability and reduced the membrane selectivity by creating non-selective defects in the

PA layer. However, the addition of AQN and GO led to synergies with AQN healing the PA defects formed by GO; thus, ultimately resulting in the development of promising PA TFN FO membranes with improved water flux and low *SRSF*. The selective characteristic of AQNs led to enhanced membrane selectivity, while GO improved the membrane surface wettability and water permeability. The TFN50 membrane with a GO and AQN loading of 0.005 wt% and 0.2 wt%, respectively, was found to be the optimum membrane in this study as it demonstrated the highest water flux with a *SRSF* value lower than that of the TFC membrane. The TFN50 membrane exhibited ~3 times higher water flux ( $24.1 \text{ L}\cdot\text{m}^{-2}\cdot\text{h}^{-1}$ ) than that of the pristine TFC membrane ( $8.2 \text{ L}\cdot\text{m}^{-2}\cdot\text{h}^{-1}$ ) with similar *SRSF* values using 0.5 M NaCl as DS and DI water as FS. Consequently, the synergy between AQN and GO demonstrated in this study could be used to effectively heal the non-selective membrane defects and improve the separation performance of the GO-incorporated PA TFN membranes for potential application in desalination and wastewater reclamation. Moreover, this study provides a guideline for future studies aiming to explore the synergistic use of different nanostructures/nanomaterials to prepare novel membrane materials.

## **6.5 Supporting Information**

### **6.5.1 Membrane surface roughness**

The effect of AQN and GO loading on the PA layer surface roughness was analysed from the surface topography obtained using AFM. The root mean square ( $R_q$ ) and maximum ( $R_{max}$ ) surface roughness values of the TFC and TFN membranes are listed in **Table S6.1**.

**Table S6.1** Surface roughness parameters of the pristine and coated TFC membranes obtained from examining at least three arbitrarily chosen membrane areas ( $5 \mu\text{m} \times 5 \mu\text{m}$ ) using AFM.

<b>Membrane</b>	<b><math>R_q</math> (nm)</b>	<b><math>R_{max}</math> (nm)</b>
TFC	$65.0 \pm 4.9$	$503.7 \pm 60.6$
TFN0	$57.9 \pm 7.3$	$462.2 \pm 55.6$
TFN25	$53.8 \pm 3.1$	$363.4 \pm 37.3$
TFN50	$45.4 \pm 3.0$	$322.0 \pm 5.3$
TFN75	$43.8 \pm 2.0$	$296.4 \pm 18.0$

### **CRedit authorship contribution statement**

**Nawshad Akther:** Conceptualization, Data curation, Formal analysis, Investigation, Methodology, Validation, Writing - original draft. **Victoria Sanahuja-Embuena:** Formal analysis, Validation, Writing - review & editing. **Radosław Górecki:** Consultation of the data in regards to AQN, Writing – review & editing. **Sherub Phuntsho:** Co-supervision, Writing - review & editing. **Claus Helix-Nielsen:** Writing - review & editing. **Hokyong Shon:** Supervision, Project administration, Resources, Funding acquisition, Validation, Writing - review & editing.

### **Declaration of competing interest**

The authors declare that they have no known competing financial interests or personal relationships that could have influenced the work reported in this paper.

### **Acknowledgement**

The research reported in this paper was supported by the Australian Research Council Industrial Transformation Research Hub (IH170100009) and the King Abdullah University of Science and Technology (KAUST), Saudi Arabia through the Competitive Research Grant Program–CRG2017 (CRG6), Grant # URF/1/3404-01.

# **CHAPTER 7**

## **EFFECT OF GRAPHENE OXIDE QUANTUM DOTS ON THE INTERFACIAL POLYMERIZATION OF A THIN-FILM NANOCOMPOSITE FORWARD OSMOSIS MEMBRANE: AN EXPERIMENTAL AND MOLECULAR DYNAMICS STUDY**

## STATEMENT OF CONTRIBUTION OF AUTHORS

Title of Paper	Effect of graphene oxide quantum dots on the interfacial polymerization of a thin-film nanocomposite forward osmosis membrane: An experimental and molecular dynamics study		
Publication Status	<input checked="" type="checkbox"/> Published <input type="checkbox"/> Accepted for Publication <input type="checkbox"/> Submitted for Publication <input type="checkbox"/> Unpublished and Unsubmitted work written in manuscript style		
Publication Details	Akther, N., Kawabata, Y., Lim, S., Yoshioka, T., Matsuyama, H., Phuntsho, S. & Shon, H.K. 'Effect of graphene oxide quantum dots on the interfacial polymerization of a thin-film nanocomposite forward osmosis membrane: An experimental and molecular dynamics study', <i>Journal of Membrane Science</i> , vol. 630, p. 119309.		
<b>PRINCIPAL AUTHOR</b>			
Name of Principal Author (Candidate)	Nawshad Akther		
Contribution to the paper	Conceptualization, Data curation, Formal analysis, Investigation, Methodology, Validation, Writing - original draft.		
Certification	This paper reports on original research I conducted during the period of my Higher Degree by Research candidature and is not subject to any obligations or contractual agreements with a third party that would constrain its inclusion in this thesis. I am the primary author of this paper.		
Signature	Production Note: Signature removed prior to publication.	Date	04/09/2020
<b>CO-AUTHOR CONTRIBUTIONS</b>			
By signing the Statement of Contribution of Authors, each author certifies that:			
i. the candidate's stated contribution to the publication is accurate (as detailed above); and ii. permission is granted for the publication to be included in the candidate's thesis.			
Name of Co-Author 1	Yuki Kawabata		
Contribution to the paper	Formal analysis, Investigation, Validation, Writing - review & editing.		
Signature	Production Note: Signature removed prior to publication.	Date	04/09/2020
Name of Co-Author 2	Dr. Sungil Lim		
Contribution to the paper	Consultation of the data in regards to OSHF membrane.		
Signature	Production Note: Signature removed prior to publication.	Date	04/09/2020
Name of Co-Author 3	Prof. Tomohisa Yoshioka		
Contribution to the paper	Validation, Writing - review & editing.		
Signature	Production Note: Signature removed prior to publication.	Date	04/09/2020
Name of Co-Author 4	Dr. Sherub Phuntsho		
Contribution to the paper	Co-supervision, Writing - review and editing.		
Signature	Production Note: Signature removed prior to publication.	Date	04/09/2020
Name of Co-Author 5	Prof. Hideto Matsuyama		
Contribution to the paper	Writing - review and editing.		

Signature	Production Note: Signature removed prior to publication.	Date	04/09/2020
Name of Co- Author 6	Prof. Ho Kyong Shon		
Contribution to the paper	Supervision, Project administration, Resources, Funding acquisition, Writing - review & editing.		
Signature	Production Note: Signature removed prior to publication.	Date	04/09/2020

## 7. CHAPTER 7 Effect of graphene oxide quantum dots on the interfacial polymerization of a thin-film nanocomposite forward osmosis membrane: An experimental and molecular dynamics study

### Abstract

We report an ultra-low loading of graphene oxide quantum dots (GQDs) into the polyamide (PA) layer of an outer-selective hollow fiber (OSHF) thin-film composite (TFC) membrane using the vacuum-assisted interfacial polymerization (VAIP) technique to improve the water permeability of OSHF TFC membranes without sacrificing membrane selectivity. Experimental results showed that GQD loading in the PA layer influenced membrane performance. The membrane with a GQD loading of  $5 \text{ mg}\cdot\text{L}^{-1}$  (TFN5) demonstrated an optimal water flux of  $30.9 \text{ L}\cdot\text{m}^{-2}\cdot\text{h}^{-1}$  and a specific reverse solute flux (*SRSF*) of  $0.12 \text{ g}\cdot\text{L}^{-1}$ . To investigate the effect of GQDs on the interfacial polymerization (IP) reaction and membrane performance, molecular dynamics (MD) simulation was employed at the water-hexane and water-PA interfaces. The simulation results showed that GQDs decreased the reaction rate during the IP process by reducing the diffusivities of *m*-phenylenediamine (MPD) and trimesoyl chloride (TMC). Additionally, GQDs reduced water permeability by acting as barriers to water molecules when present at a high concentration near the PA layer surface. At a very high loading, GQDs aggregated at the water-hexane interface and reduced the membrane selectivity by forming non-selective voids at the interface between the PA layer and GQDs. Together with the experimental findings, the MD simulation results delivered a good insight into the GQDs' effect on the TFC membrane's surface and transport properties at both macroscopic and microscopic levels.

**Keywords:** Forward osmosis (FO); Graphene oxide quantum dot (GQD); Outer-selective hollow fiber (OSHF); Thin-film nanocomposite (TFN); Interfacial polymerization (IP)

## **Introduction**

In recent decades, forward osmosis (FO) has been extensively recognized as an emerging technology for application in food processing (Sant'Anna, Marczak & Tessaro 2012), wastewater treatment (Tran et al. 2019), elimination of trace contaminants (Jin et al. 2012), resource recovery (Zhang et al. 2014), fertigation (Phuntsho et al. 2012) and brine dilution (Akther, Daer & Hasan 2018) due to its exceptional separation capabilities, and lower operating and capital costs. Moreover, FO processes demonstrate lower fouling tendency and higher water recovery in comparison to pressure-driven membrane processes like reverse osmosis (RO) as they are driven by the osmotic pressure gradient prevailing between the highly concentrated draw solution (DS) and more dilute feed solution (FS) across a semi-permeable membrane (Akther, Daer, et al. 2019; Akther et al. 2015). Subsequently, FO processes are more energy-efficient than RO when utilized for applications that do not demand DS regeneration, and for treating complex wastewaters with high membrane fouling potential and (Chekli et al. 2018). Regardless of having several promising characteristics, the lack of ideal FO membranes is among the key challenges that hinder the use of FO technology in water treatment. For a FO membrane to be ideal, it should demonstrate high water permeability, high selectivity to draw solutes and good anti-fouling performance to minimize the maintenance costs and extend the lifetime of the membranes.

The polyamide (PA) thin-film composite (TFC) flat sheet membranes are most widely used in FO separation processes owing to their unparalleled permeability-rejection performance, high degree of tunability and broader pH tolerance range in comparison to cellulose-based membranes (Giwa et al. 2016). The PA selective layer of a TFC membrane is developed on top of a porous and mechanically robust substrate via interfacial polymerization (IP) reaction. Several modification techniques, such as membrane surface coating and nanomaterial incorporation into the PA layer or membrane substrate, have been investigated



to improve the performances of PA TFC membranes or tailor their design for specific applications (Akther, Ali, et al. 2020; Akther, Phuntsho, et al. 2019; Akther, Sanahuja-Embuela, et al. 2021; Amini, Jahanshahi & Rahimpour 2013b). For instance, nanomaterials like carbon nanotubes (CNTs) (Amini, Jahanshahi & Rahimpour 2013a; Zhou et al. 2018), graphene oxide (GO) (Akther, Yuan, et al. 2020; Perreault, Tousley & Elimelech 2014), silica (Akther, Lin, et al. 2020; Daer et al. 2020; Shakeri et al. 2019), silver (Qiu & He 2018; Soroush et al. 2015), metal and covalent organic framework (MOF/COF) (Akther, Lim, et al. 2019; Lim, Akther, et al. 2020) have been used as nanofillers to improve the membrane porosity, hydrophilicity, surface charge, surface roughness and antifouling properties.

Graphene oxide quantum dots (GQDs) have recently drawn extensive attention as nanofillers in the membrane technology field due to their facile and inexpensive production and desirable physicochemical properties like small particle size, high chemical stability, good biocompatibility and superior antifouling characteristics. GQDs are zero-dimensional quasi-spherical nanoparticles with particle size ranging between 3 and 20 nm that possess outstanding hydrophilic properties due to the presence of substantial amounts of oxygen-rich carboxyl, hydroxyl and epoxy groups on their surfaces (Zhao & Chung 2018). These surface functional groups promote water solubility and aid further surface passivation and functionalization. Additionally, the small size and surface chemistry of GQDs facilitate their dispersion in polymer matrices and polar solvents like water, which are crucial properties for their application in membrane fabrication and separation processes. Due to these desirable properties of GQDs, researchers have employed them to enhance the performances and surface properties of membranes for various separation processes like nanofiltration (NF) (Zhang, Wei, et al. 2017), membrane distillation (MD) and reverse osmosis (RO) (Shen et al. 2020b).

Song et al. (Song, Zhou, et al. 2016) prepared GQD-modified thin-film nanocomposite (TFN) RO membranes by first depositing GQD/m-phenylenediamine (MPD) aqueous suspension on the membrane substrate via vacuum filtration, followed by the formation of PA layer through IP reaction between trimesoyl chloride (TMC) and MPD. The TFN membrane deposited with 5 mg of GQD demonstrated a 52% improvement in water flux than the nascent TFC membrane without deteriorating the solute rejection. The modified TFN membrane also exhibited stability over long-term RO testing, enhanced chlorine resistance and antifouling properties. Similarly, Zhang et al. (Zhang, Wei, et al. 2017) prepared TFN membranes by dispersing GQD in tannic acid for dye separation using low-pressure NF. The addition of GQD to the PA layer made the TFN membrane's surface more hydrophilic, smoother and negatively charged; thus, demonstrating high rejection to methylene blue and Congo red and 1.5 times higher water flux than that of the TFC membrane. Sun & Wu (2018) functionalized GQDs with amino, carboxyl and sulfonic acid groups and embedded them into the PA layer of TFN membranes. They found that the PA surface properties, separation performance and antifouling properties of the GQD-incorporated TFN membranes could be altered by tuning the functional groups of GQDs. The TFN membrane incorporated with GQDs containing sulfonic acid functional groups showed the highest permeate flux and the best antifouling performance. The various studies reported on GQD-modified TFC membranes confirm that GQD is a promising nanofiller to boost membrane performance by modifying their physicochemical structure, which eventually influences their water transport mechanism.

In our previous studies, we demonstrated the successful development of TFC and TFN outer-selective hollow fiber (OSHF) membranes for FO applications, where the dense PA active layer was developed on the outer surface of the hollow fiber (HF) instead of the lumen side (Lim, Akther, et al. 2020; Lim, Park, et al. 2020a; Lim et al. 2019). The OSHF membranes

are more suitable for treating feed with high foulant concentration than the inner-selective hollow fiber (ISHF) membranes as they do not clog easily and are simpler to clean post fouling. Besides, the OSHF membranes have a higher PA surface area in comparison to ISHF membranes. In general, HF membranes hold more potential than flat-sheet membranes because of their high packing density, improved separation performance and easy modulation. We also demonstrated that the large lateral size of non-porous GO flake creates PA defects by obstructing IP reaction; thereby, reducing the membrane selectivity to draw solutes (Akther, Yuan, et al. 2020; Lim, Park, et al. 2020a). Therefore, in this study, we incorporated GQDs into the PA layer via vacuum-assisted interfacial polymerization (VAIP) technique to improve the membrane separation performance of OSHF TFN membranes. The small size and abundant oxygen functional groups of GQDs could minimize the PA defects and effectively alter the PA layer surface characteristics for better separation performance.

Although previous experimental studies have exhibited that nanofillers could enhance PA TFN membrane's properties and performances, a comprehensive understanding of the interactions between the PA matrix and the embedded nanofillers at the molecular level is still lacking. As experimental techniques cannot predict the water transport behaviour inside the membranes at the microscopic level, molecular dynamics (MD) simulation could complement the experimental results to understand the microscopic structure of the PA and its nanocomposites. Hence, MD simulations can be useful in understanding the influence of microscopic membrane structural properties on macroscopic membrane transport properties. Previous MD simulations reported in the literature have primarily studied the PA membrane's local structures to assess the mechanisms that influence the formation, hydration and functioning of the PA membrane, which govern the water diffusivity behaviour within the PA structures (Goudeau et al. 2004; Kolev & Freger 2014; Wei et al. 2016). Some MD studies also investigated the effect of CNTs on the dynamics, structure and

hydration properties of PA TFN membrane (Araki et al. 2015; Eslami & Behrouz 2014). Recently, Salestan et al. (Salestan et al. 2020) assessed the effect of graphene quantum dot (GQD) nanofillers on the interaction energies, mean-square displacements (MSDs), densities, fractional free volumes and water transport behaviour of four likely PA/GQD nanocomposite chemical structures using MD simulation. However, the effect of GQDs on PA monomers' diffusivities during the IP reaction and water transport behaviour at the PA-water interface of the PA/GQD structure still needs to be investigated at the molecular-scale.

Therefore, in this study, we incorporated GQDs into the PA layer via the VAIP technique to improve the membrane separation performance of OSHF TFN membranes. The small size and abundant oxygen functional groups of GQDs could minimize the PA defects and effectively alter the PA layer surface characteristics for better separation performance. MD simulation was used to investigate the effect of GQDs on the diffusivities of (i) TMC and MPD at the water-hexane interface during IP reaction and (ii) water molecules at the PA-water interface at various GQD loadings inside the PA layer to complement experimental findings at the microscopic level. This study is expected to assist in the future design of GQD-embedded PA TFN membranes with improved performance.

## **7.1 Materials and methods**

### **7.1.1 Chemicals**

GQD dispersion in water was purchased from Sigma Aldrich ( $1 \text{ mg}\cdot\text{mL}^{-1}$ ), and the GQD properties and characteristics can be found on the supplier's website. Porous HF membrane substrates were prepared from poly(ethersulfone (PES,  $M_w = 62$  to  $64 \text{ kg}\cdot\text{mol}^{-1}$ , 3000P Veradel<sup>®</sup>, Solvay) using 1-methyl-2 pyrrolidone (NMP,  $\geq 99.5\%$ , Merck) as the polymer solvent. Polyethylene glycol (PEG,  $M_w = 400 \text{ g}\cdot\text{mol}^{-1}$ ), TMC (98%), sodium dodecyl sulfate (SDS,  $\geq 99\%$ ) and MPD flakes (99%) were provided by Sigma-Aldrich. N-hexane from

Merck (98.5%) was employed as an organic solvent for TMC. Sodium chloride (NaCl, >99.7%) from Chem Supply was used as a draw solute for the FO tests. Deionized water (DI,  $\sim 18 \text{ M}\Omega\cdot\text{cm}^{-1}$ , Milli-Q<sup>®</sup>, Merck) was used for making FS and DS. All chemicals were applied as obtained without further purification unless otherwise mentioned.

### 7.1.2 HF membrane substrate development

The porous HF membrane substrates were prepared with 16.5 wt% PES dope solution using a conventional dry-jet wet spinning technique (**Fig. 3.3**). The spinning parameters for preparing PES HF substrates were optimized in our previous study (Lim et al. 2019). Detailed HF substrate preparation methods and the optimized spinning parameters are provided in **Table 3.1**. The membrane modules were prepared by spacing two HF membrane substrates at a distance of 3 mm to prevent them from sticking to the module wall or with each other while conducting the IP reaction. The HFs were fixed inside the module by sealing the two modules with epoxy resin without blocking the HF bore holes. The length of each HF substrate inside the module was 13.5 cm, and together they possessed an effective surface area of around  $6.5 \text{ cm}^2$ . The prepared HF membrane modules were then stored in DI water at 4 °C.

### 7.1.3 OSHF TFC and TFN membrane development

The OSHF TFC membranes were made using the modified VAIP technique on our prepared PES HF substrates as presented elsewhere (Lim et al. 2019). A detailed experimental method for the OSHF membrane fabrication is provided in Section 3.2.2.2 and illustrated in **Fig. 3.4**. The OSHF TFN membranes were prepared using the same protocol as that of the OSHF TFC membrane, except for the addition of GQD in the aqueous amine solution at various loadings ranging between 0 and  $50 \text{ mg}\cdot\text{L}^{-1}$ . The GQDs were first added to the DI water and placed in a bath sonicator for 30 min to achieve uniform dispersion. The temperature in the bath sonicator was maintained using ice packs. The MPD flakes (2 wt%) and SDS (0.2 wt%)

were then added to the GQD dispersion and mixed gently for 30 min at room temperature using a magnetic stirrer. The GQD-dispersed amine solution was brought in contact with the PES HF substrate. Subsequently, the VAIP technique was employed to react the amine impregnated HF substrate with the 0.15 wt% TMC/n-hexane organic solution to produce a GQD-embedded PA layer on the outer surface of the HF substrate. The various loadings of GQDs in MPD aqueous solutions and the names of the resultant OSHF membranes prepared in this study are presented in **Table 7.1**.

**Table 7.1** Chemical compositions of OSHF TFC/TFN membranes.

Membranes	GQD in aqueous amine solution ( $\text{mg}\cdot\text{L}^{-1}$ )
TFC	0
TFN2	2.5
TFN5	5
TFN10	10
TFN25	25
TFN50	50

#### 7.1.4 Membrane characterisation

Membrane surface morphology was studied using a scanning electron microscope (SEM, Zeiss Supra 55VP) and atomic force microscopy (AFM, Park XE7, Park Systems). Dry samples of the membrane were sputter-coated with an 8 nm thick Pd/Au before SEM investigation and analysed with an accelerating voltage of 5 to 10 kV. AFM scanning was repeated four times for each sample under tapping mode with a scan area of  $5\ \mu\text{m} \times 5\ \mu\text{m}$  and the average surface roughness measurements were reported. The TFC and TFN membranes' surface chemistries were examined using Fourier Transform Infrared Spectroscopy (FTIR, Shimadzu MIRacle 10). An optical tensiometer (Attension Theta Lite 100, Biolin Scientific) was used to verify the membrane surface hydrophilicity by randomly

measuring at least 7 water contact angles on each sample's surface, and the average value was presented.

### 7.1.5 Membrane performance evaluation

The membranes were tested in AL-FS (active layer oriented towards FS) mode using 1 M NaCl solution and DI water as DS and FS, respectively, using a laboratory-scale FO set up as previously described in our work (Lim et al. 2019). The DS and FS were co-currently circulated across the OSHF membrane at a cross-flow velocity of 10.4 and 20.9  $\text{cm}\cdot\text{s}^{-1}$ , respectively, during the FO tests. A temperature controller was used to sustain the temperature of the DS and FS at 22 °C. The water flux ( $J_w$ ,  $\text{L}\cdot\text{m}^{-2}\cdot\text{h}^{-1}$ ) and reverse solute flux ( $J_s$ ,  $\text{g}\cdot\text{m}^{-2}\cdot\text{h}^{-1}$ ) through the membrane was determined from Eq. 3.1 and Eq. 3.2, respectively. The water and reverse solute flux values were employed to evaluate the specific reverse solute flux ( $SRSF$ ,  $\text{g}\cdot\text{L}^{-1}$ ) across the membrane to denote the selectivity of membranes (Eq. 3.3). The exact method for determining the FO performance is presented in Section 3.4.2. The non-linear regression model developed for FO membranes by Tiraferri et al. (2013) was used to establish the pure water permeability coefficient ( $A$ ), solute permeability coefficient ( $B$ ) and intrinsic selectivity ( $B/A$ ) of the membranes.

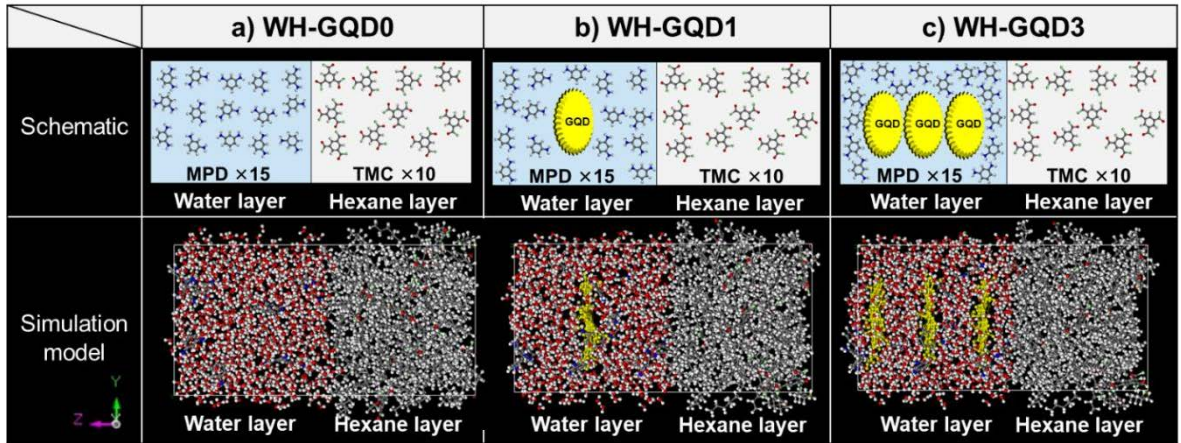
### 7.1.6 Molecular dynamics simulation

Molecular modelling and MD simulations were all carried out by utilizing the commercial software BIOVIA Material Studio<sup>®</sup> 2018. Energy minimization and MD calculations were all performed using the Condensed-phase Optimized Molecular Potential for Atomistic Simulation Studies II (COMPASS II) force field (Nussinov & van den Brink 2015; Sun 1998; Sun et al. 2016). The diffusivity of each chemical species was then calculated based on Einstein's equation (Tamai, Tanaka & Nakanishi 1994) and MSD of the molecule or GQD. The GQD model employed in this study has an area of 3.22  $\text{nm}^2$ , a width of 2.1964 nm and a height of 1.4669 nm, as presented in .

#### 7.1.6.1 Simulation cell of water-hexane interface

The effects of GQD on the diffusivity of TMC, MPD, hexane and water molecules were investigated. **Table S7.1** shows all the molecular models used in this study. A simulation cell with the dimensions  $30 \text{ \AA} \times 30 \text{ \AA} \times 60 \text{ \AA}$  was prepared with periodic boundaries in all directions, as shown in **Fig. 7.1**. Inside the simulation cell, an aqueous phase with a density of  $0.94 \text{ g.cm}^{-3}$  and an organic phase with a density of  $0.7 \text{ g.cm}^{-3}$  were modelled with 900 water and 123 hexane molecules. The organic hexane phase also comprised of 10 TMC molecules, and the aqueous phase contained 15 MPD molecules. The stoichiometric ratio of TMC: MPD was chosen as 2:3. Three types of simulation cell were prepared, which were identified as WH-GQD0, WH-GQD1 and WH-GQD3. The WH-GQD0 was a water-hexane interface system without GQD. WH-GQD1 was a water-hexane interface system that contained 1 GQD inside the water layer at a distance of  $5 \text{ \AA}$  from the water-hexane interface as the initial position of the GQD. The WH-GQD3 was a water-hexane interface system containing three GQDs inside the water layer at distances of  $5 \text{ \AA}$ ,  $15 \text{ \AA}$  and  $25 \text{ \AA}$  from the water-hexane interface as the initial position of the GQDs. MD simulations were implemented for 4 ns under an isothermal state of 298 K after structural optimization of these cells.



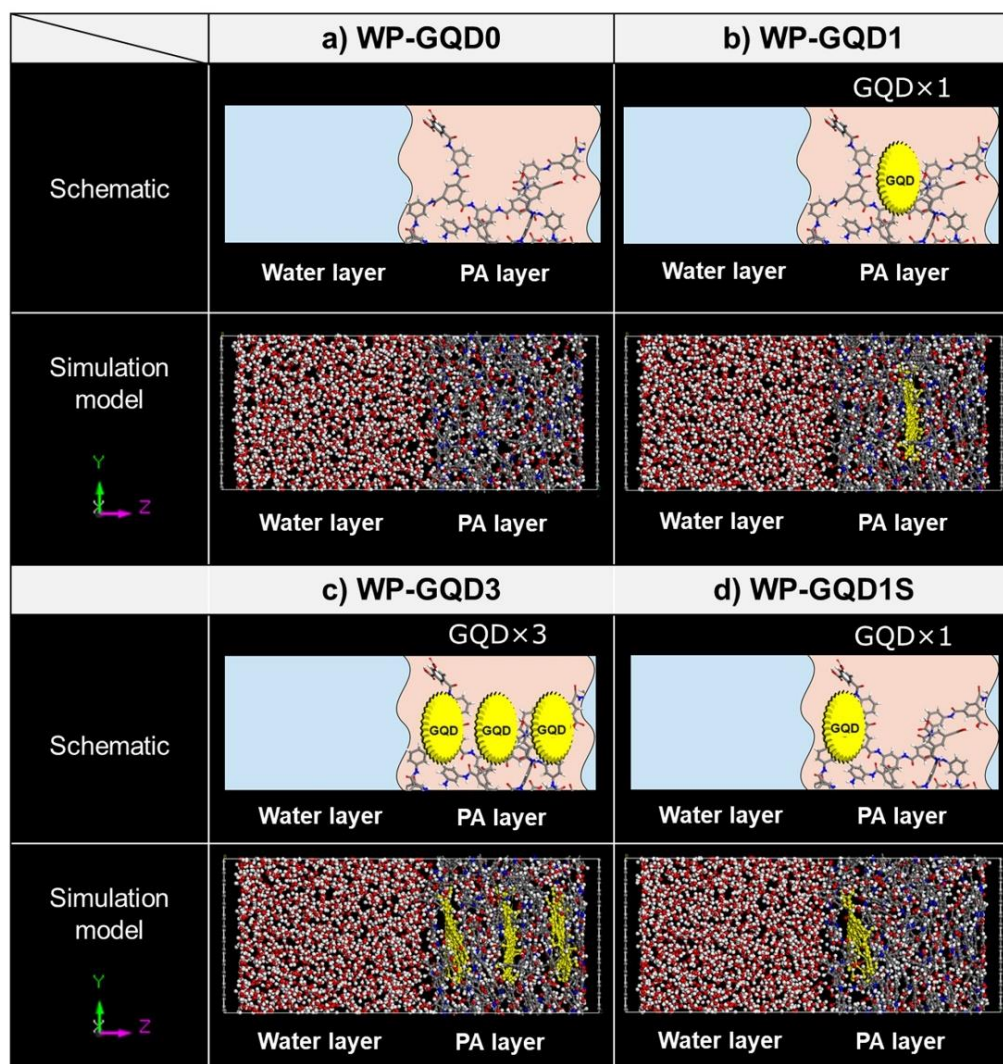


**Fig. 7.1** Schematic and simulation model of the water-hexane interface system. a) WH-GQD0, b) WH-GQD1 and c) WH-GQD3; blue: nitrogen atom, grey: carbon atom, white: hydrogen atom, red: oxygen atom and yellow: GQD.

#### 7.1.6.2 Simulation cell of water-PA interface

To study the influence of GQD on the adsorption and diffusion of water inside the PA layer on a molecular scale, a  $28.7 \text{ \AA} \times 28.7 \text{ \AA} \times 70 \text{ \AA}$  periodic boundary cell was modelled (Fig. 7.2). The PA used in this water-PA interface simulation cell was modelled to be composed of MPD and TMC molecules. The hydrogen atom of MPD and the chlorine atom of TMC were removed to form an amide bond. On the other hand, the chlorine atom that did not form an amide bond was replaced with a hydroxyl group. The PA membrane model was constructed by the same method as a hydrated PA with a crosslinking degree of 71% and a density of  $1.373 \text{ g}\cdot\text{cm}^{-3}$ , which are very close to the experimental values previously reported (Harder et al. 2009; Yoshioka et al. 2018). The cell contained 1073 water molecules necessary for a hydrated PA with a density of  $1.373 \text{ g}\cdot\text{cm}^{-3}$  and a pure water phase with a density of  $1 \text{ g}\cdot\text{cm}^{-3}$ . Four types of water-PA interface models were employed and named WP-GQD0, WP-GQD1, WP-GQD3, and WP-GQD1S. WP-GQD0 was a water-PA interface system without GQD. WP-GQD1 was a water-PA interface system that contained one GQD at a distance of  $15 \text{ \AA}$  from the water-PA interface on the PA side as the initial position of the GQD. WP-GQD3 was a water-PA interface system containing three GQDs at distances of 5

Å, 15 Å, and 25 Å from the water-PA interface on the PA phase side as the initial positions of the GQDs. Finally, WP-GQD1S was a water-PA interface system containing one GQD at a distance of 5 Å from the water-PA interface on the PA side as the initial position of the GQD. Furthermore, two graphene walls were placed and fixed at both ends (right and left ends of each cell as shown in **Fig. 7.2**) of the cell to prevent water molecules from diffusing into the PA from the opposite side of the water phase due to periodic boundary conditions. MD simulations were performed for 4 ns after structural optimization under an isothermal condition of 298 K.



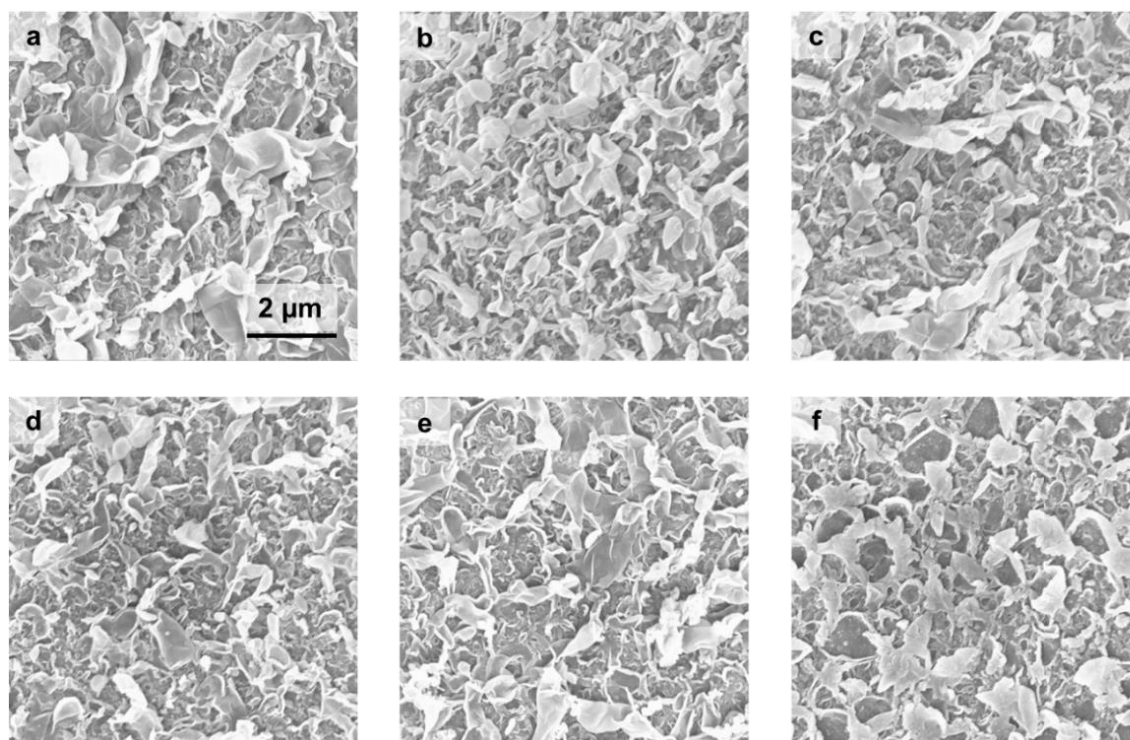
**Fig. 7.2** Schematic and simulation model of the water-PA interface system. a) WP-GQD0, b) WP-GQD1, c) WP-GQD3 and d) WP-GQD1S; blue: nitrogen atom, grey: carbon atom, white: hydrogen atom, red: oxygen atom and yellow: GQD.

## 7.2 Results and discussion

### 7.2.1 Membrane characterisation

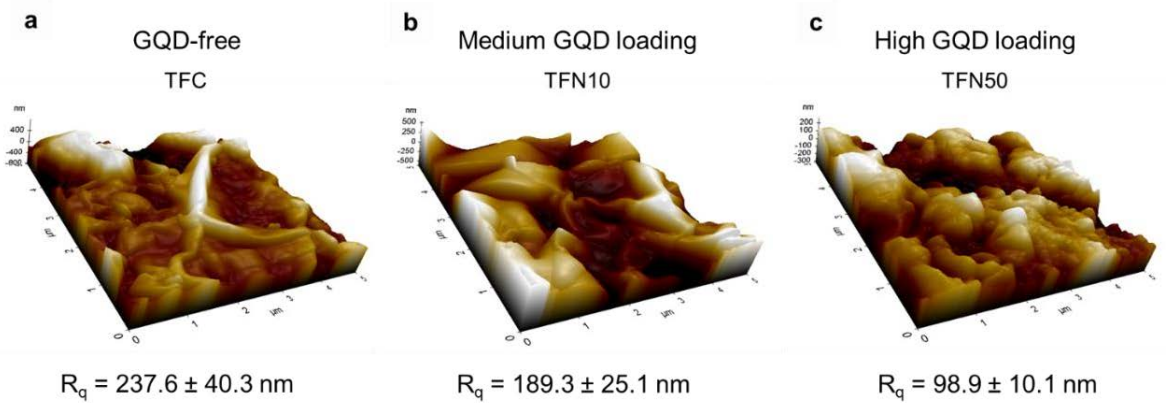
**Fig. 7.3** demonstrates the PA surface morphology of the prepared OSHF TFC/TFN membranes as observed by SEM. All the membranes exhibited the distinctive ridge-and-valley structures of the PA layer. The GQDs are not noticeable on the PA surface, suggesting that they are well-incorporated inside the PA layer. However, the PA layer looked sparser with the development of small leaf-like PA protrusions as the GQD loading was increased. The PA structure of TFN50 was very distinct from the other membranes and revealed more broad leaf-like PA structures with smooth patches (**Fig. 7.3f**). Such differences in PA morphological structure could arise from severe GQD agglomerations at high loadings due to the electrostatic interaction existing between their surface oxygen functional groups and hydrogen bonds. The steric hindrance effect of GQD aggregates impedes the IP reaction by preventing MPD from quickly diffusing into the TMC organic phase and delay the PA layer's ridge development, as discussed in our previous study (Akther, Yuan, et al. 2020).

Consequently, the PA layer grows around GQD aggregates and creates non-selective regions that easily allow DS ions to pass through the membrane to the FS. The GQDs could also block some pores on the membrane substrate's surface at high loading due to their small size (Bi et al. 2019). Additionally, the oxygen functional groups of GQDs could preferentially react with MPD and TMC; thereby, further reducing the IP reaction rate between the monomers. Based on the SEM images, TFN50 likely has a defective PA layer and is expected to demonstrate higher reverse solute flux than the other membranes.



**Fig. 7.3** SEM images of PA layer surface: (a) TFC, (b) TFN2, (c) TFN5 (d) TFN10, (e) TFN25 and (f) TFN50 OSHF membranes.

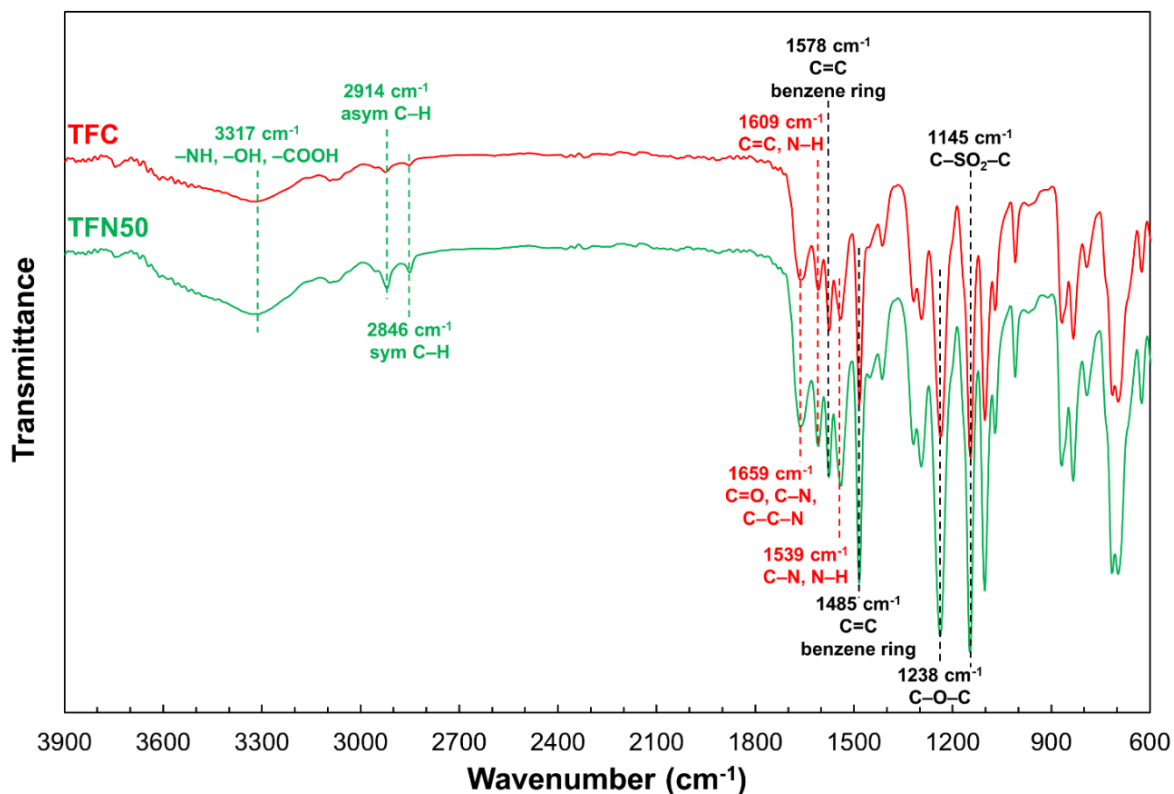
The root mean square surface roughness ( $R_q$ ) values of three selected OSHF TFC and TFN membranes (TFC, TFN10 and TFN50) were attained from AFM analysis, as shown in **Fig. 7.4**. The pristine TFC membrane exhibited the roughest surface with a  $R_q$  value of 237.6 nm. However, the membrane surface roughness decreased at higher GQD loading and TFN50 demonstrated the smoothest membrane surface with a  $R_q$  value of 98.9 nm (**Fig. 7.4c**). The change in membrane surface roughness is consistent with the SEM images (**Fig. 7.3**). The smoother PA layer surface at higher GQD loading could be ascribed to the GQDs more effectively slowing down the diffusion of MPD molecules and the IP reaction rate; thus, impeding the development of the PA ridge-and-valley structure (Zhang, Wei, et al. 2017).



**Fig. 7.4** AFM images signifying PA surface roughness of (a) TFC, (b) TFN10 and (c) TFN50 OSHF membranes. The  $R_q$  values of membrane surface roughness were acquired by inspecting four arbitrarily selected membrane areas.

The FTIR spectra of the prepared TFC and TFN membranes are presented in **Fig. 7.5** and were examined to assess the surface chemistry of OSHF TFN/TFN membranes. The spectra of both the TFC and TFN membranes show the characteristic peaks of PES substrate, which include the sulfone group stretching vibration at  $1145\text{ cm}^{-1}$ , asymmetric aromatic ether band vibration at  $1238\text{ cm}^{-1}$ , and C=C stretching vibration of the benzene ring at  $1485\text{ cm}^{-1}$  and  $1578\text{ cm}^{-1}$  (Ahmad, Shoparwe & Hanifa 2019; He et al. 2019). Both the membranes also exhibited the typical peaks corresponding to PA at  $1609\text{ cm}^{-1}$  (N–H deformation vibration and C=C ring stretching of aromatic amide),  $1659\text{ cm}^{-1}$  (amide I band) and  $1539\text{ cm}^{-1}$  (amide II band); thus, verifying the PA layer formation on the PES substrate (Tang, Kwon & Leckie 2009a). The TFN membrane showed more intense amide I and amide II peaks compared to the TFC membrane due to the development of new amide bonds through a reaction between the amine groups of MPD and carboxyl groups of GQDs. The carboxyl groups of GQDs also covalently bonded with the terminal carboxyl groups of TMC in the PA's linear portion during the IP process (Song, Zhou, et al. 2016). Additionally, the peak intensities at  $2846\text{ cm}^{-1}$  (symmetric C–H stretch) and  $2914\text{ cm}^{-1}$  (asymmetric C–H stretch) increased on the addition of GQDs to PA layer owing to the existence of plentiful C–H bonds from the GQDs. The broad peak at  $3317\text{ cm}^{-1}$ , which corresponds to the overlap of hydroxyl, carboxyl and

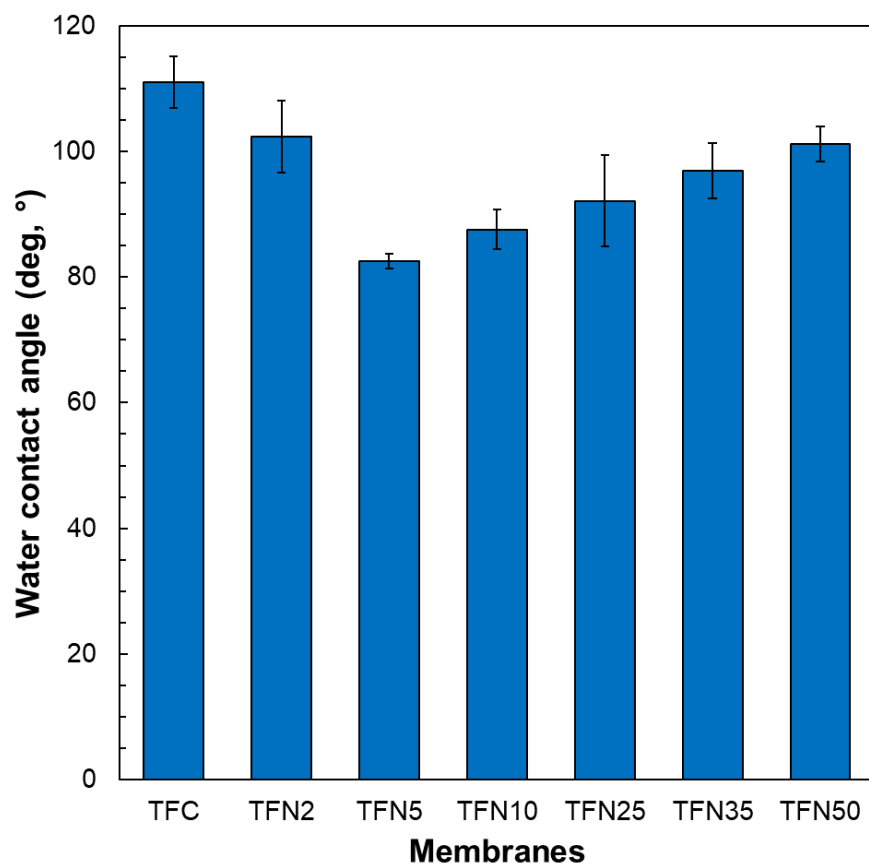
amine groups' stretching vibrations in the PA layer, intensified for the TFN membrane due to the stretching vibration of hydroxyl groups in GQDs (Xu et al. 2019); thus, confirming the successful integration of GQDs into the PA layer during the IP reaction.



**Fig. 7.5** FTIR spectra of the TFC and TFN membranes.

The surface hydrophilicity of the TFC/TFN membranes was established from the water contact angles measurements conducted at the PA surface's air-water interface. Membrane hydrophilicity is an essential parameter in assessing the membrane performance as it could impact both the water permeability and fouling behaviour of the membranes (Rastgar et al. 2018). Generally, a reduction in water contact angle signifies an increase in the hydrophilicity of the membrane surface. As can be observed from **Fig. 7.6**, the pristine TFC membrane exhibited the highest water contact angle of 111°; thus, indicating that it is the most hydrophobic membrane. The water contact angle gradually decreases from 102° for TFN2 membrane to 82.5° for TFN5 membrane, with increased GQDs loading from 2.5 to 5 mg·L<sup>-1</sup> in the amine aqueous phase. The increased wettability of the TFN membranes could

be attributed to the negatively charged hydrophilic carboxyl and hydroxyl groups on GQDs and the water channels forming inside the PA layer. However, membrane wettability decreased on increasing the GQD concentration beyond  $5 \text{ mg}\cdot\text{L}^{-1}$  due to agglomeration of GQDs and their uneven distribution inside the less hydrophilic PA layer. Severe GQD aggregation decreases the effective nanoparticle surface area; thus, reducing the number of GQDs' hydrophilic groups exposed on the PA surface. Moreover, GQD aggregates could obstruct water transport by blocking some substrate pores (Li, Li & Zhang 2017). Overall, incorporating a suitable GQD loading into the PA layer was observed to increase its affinity to the water molecules, which is expected to enhance the water flux of the TFN membranes.



**Fig. 7.6** Water contact angles of the OSHF PA TFC and TFN FO membranes.

### 7.2.2 Membrane performance evaluation

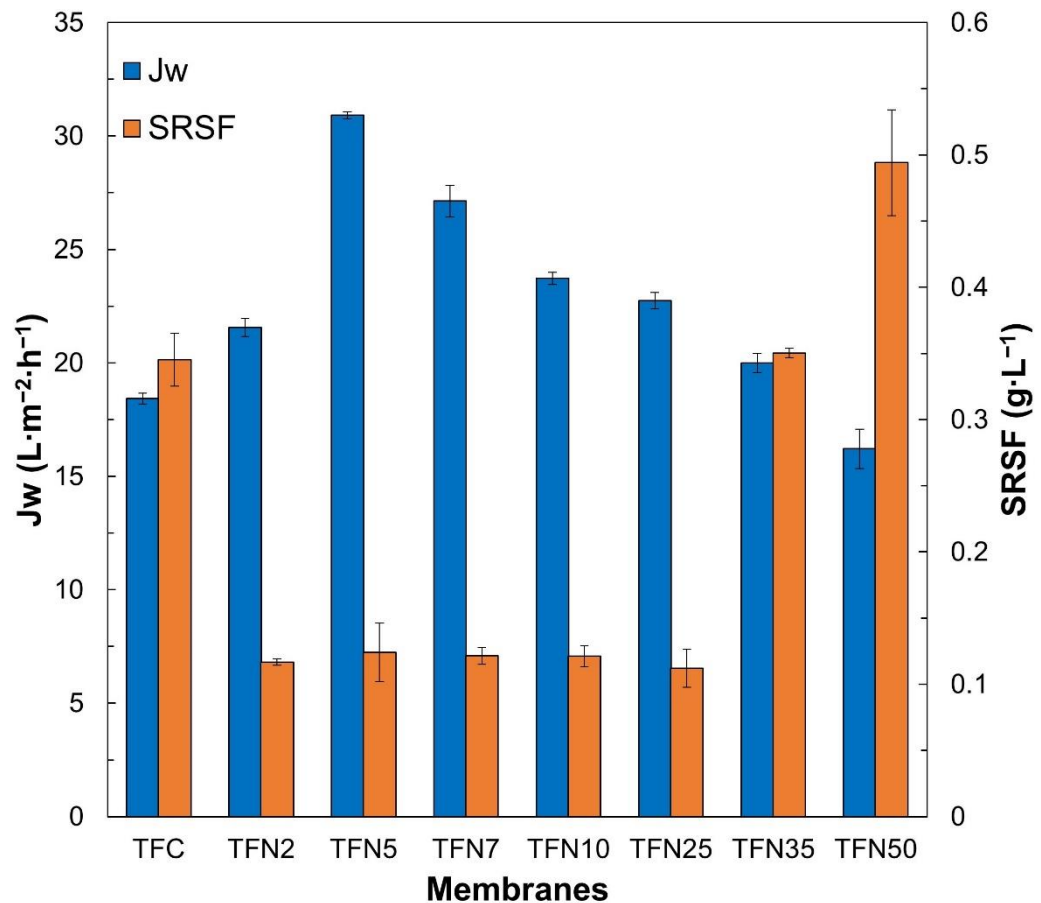
The FO performance of the prepared OSHF TFC and TFN membranes were tested under AL-FS orientation using DI water and 1M NaCl as FS and DS, respectively. As evident from

**Fig. 7.7**, all the GQD-incorporated TFN membranes, except TFN50, demonstrated higher water fluxes than that of the pristine TFC membrane. TFN5 exhibited the highest water flux of  $30.9 \text{ L}\cdot\text{m}^{-2}\cdot\text{h}^{-1}$ , which is 68% higher than the TFC membrane, and a *SRSF* of  $0.12 \text{ g}\cdot\text{L}^{-1}$ , indicating that the optimum GQD loading rate in this study is  $5 \text{ mg}\cdot\text{L}^{-1}$ . The enhanced water permeability of the TFN5 membrane could be ascribed to its improved hydrophilicity and the creation of more water channels inside the PA layer after the addition of GQDs. The abundant hydrophilic carboxyl and hydroxyl functional groups on the edges of GQDs increased water molecules' solubility on the membrane surface (Ma, Zhao, et al. 2013). Whereas, the small size of GQDs resulted in the formation of nanoscale water channels at the interface between the PA and the GQDs that contributed to improved water flux (Song, Zhou, et al. 2016). Additionally, the frictionless and smooth hydrophobic surfaces of the voids present between the GQD nanoaggregates facilitated the water molecules to flow through the channels rapidly (Bi et al. 2018; Bi et al. 2019). The enhanced water flux further resulted from the hydrogen bond interactions between the water molecules and the hydroxyl/carboxyl groups of GQDs that provided added driving force for transporting water molecules within the channels (Zhao & Chung 2018). Besides, good dispersion of GQDs in the PA layer could improve water flux by uniformly reducing the PA layer thickness by influencing the monomer diffusion rate (Akther, Yuan, et al. 2020).

On further increasing the GQD loading to  $10 \text{ mg}\cdot\text{L}^{-1}$  (TFN10) and  $25 \text{ mg}\cdot\text{L}^{-1}$  (TFN25), the water flux decreased, but the *SRSF* values remained nearly the same as that of TFN5. This unusual membrane performance could occur due to GQDs interfering with the water transport in the PA layer, which will be investigated later using MD simulation. The TFN50 demonstrated the worst performance with the highest *SRSF* of  $0.49 \text{ g}\cdot\text{L}^{-1}$  and the lowest water flux of  $16.2 \text{ L}\cdot\text{m}^{-2}\cdot\text{h}^{-1}$ . The poor selectivity of the TFN50 membrane could be attributed to its defective PA layer formed due to abundant GQD aggregates (**Fig. 7.3f**), that



reduced the osmotic driving force by accumulating the draw solutes in the FS and membrane substrate; which reduced the FO water flux by increasing the internal concentration polarization (Akther, Yuan, et al. 2020; Rezaei-DashtArzhandi et al. 2020). The low water permeability of the TFN50 membrane could also be attributed to its surface roughness, which is the smoothest compared to the other prepared membranes (**Fig. 7.4c**). A decrease in the PA surface roughness indicates a reduction in its surface area, which is undesirable for enhancing water flux. The observed water flux of the TFC/TFN membranes corresponds well with the contact angle measurements presented in **Fig. 7.6**.



**Fig. 7.7** FO performance of OSHF TFN membranes incorporated with GQD under AL-FS orientation with DI water as FS and 1 M NaCl as DS.

Overall, the results imply that the good dispersion of GQDs at the optimum loading improved the PA layer's separation performance by forming water channels and without

creating nonselective defects within the PA layer. In contrast, increasing the GQD loading over  $5 \text{ mg}\cdot\text{L}^{-1}$  reduced the water flux and membrane selectivity by hampering water transport and deteriorating PA layer integrity.

The intrinsic transport separation parameters of the pristine TFC and GQD-modified TFN membranes are listed in **Table 7.2**. The TFN5 membrane demonstrated the highest  $A$  value of  $2.24 \text{ L}\cdot\text{m}^{-2}\cdot\text{h}^{-1}\cdot\text{bar}^{-1}$  and the lowest  $B/A$  value of 0.13 bar owing to its improved hydrophilicity and selectivity to DS ions. On the contrary, the TFN50 membrane showed the highest  $B/A$  value of 0.42 bar because of the defective PA layer formation caused by GQD agglomeration. The formation of non-selective regions in the TFN50 membrane's PA layer possibly increased its  $B$  value by 31% compared to the pristine TFC membrane. Overall, an ideal FO membrane should exhibit a low  $B/A$  value to demonstrate a better permselectivity, which implies that a high  $A$  value and low  $B$  value are desirable for good membrane performance. Hence, it can be confirmed from the intrinsic transport parameters of the TFN5 OSHF membrane, especially its low  $B/A$  ratio that it demonstrated the optimal FO performance compared to the other membrane samples. The intrinsic transport parameters of the OSHF PA TFC/TFN membranes agree well with the FO test results shown in **Fig. 7.7** and confirmed that the membrane separation performance could be adjusted by altering the GQD concentration in the aqueous amine solution.

**Table 7.2** Intrinsic transport parameters of the pristine TFC and selected GQD-modified TFN membranes.

Membrane	$A \text{ (L}\cdot\text{m}^{-2}\cdot\text{h}^{-1}\cdot\text{bar}^{-1})$	$B \text{ (L}\cdot\text{m}^{-2}\cdot\text{h}^{-1})$	$B/A \text{ (bar)}$
TFC	1.60	0.48	0.30
TFN5	2.24	0.30	0.13
TFN50	1.51	0.63	0.42

### 7.2.3 Molecular dynamics simulation

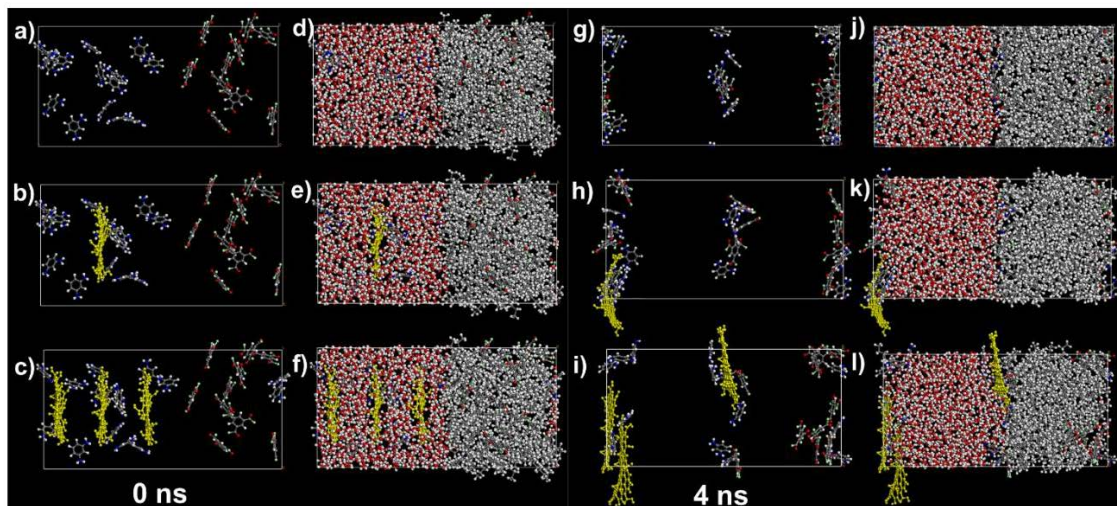
#### 7.2.3.1 Water-hexane interface simulation

The behaviour of GQD at the water-hexane interface was investigated using MD simulation. **Fig. 7.8** shows snapshots of the water-hexane interface at the initial state (0 ns) and 4 ns later after starting the MD simulation. The MPD and TMC molecules diffused towards and concentrated at the water-hexane interface (**Fig. 7.8g** and **j**), and the MPD molecules intruded slightly into the hexane phase. The GQD in the WH-GQD1 system also moved to the water-hexane interface (**Fig. 7.8h** and **k**), which indicated that GQD could be incorporated into the PA structure during the IP reaction between MPD and TMC. The snapshots of WH-GQD3 system at 4 ns (**Fig. 7.8i** and **l**) showed that the GQDs were closely well-aligned with each other and the water-hexane interface. This might be because the benzene ring portions of GQDs interacted with each other by  $\pi$ - $\pi$  stacking. This result shows that the GQDs would aggregate by interacting with each other, possibly around the water-hexane interface, if the GQD concentration is too high and could create non-selective defects in the PA layer. This result further confirmed the poor separation performance of TFN50, where a GQD loading of  $50 \text{ mg}\cdot\text{L}^{-1}$  deteriorated the PA layer integrity (**Fig. 7.7**).

The influence of GQD on the diffusivity of water, hexane, TMC, and MPD molecules was investigated using MSD and Einstein equation represented by Eq. 7.1:

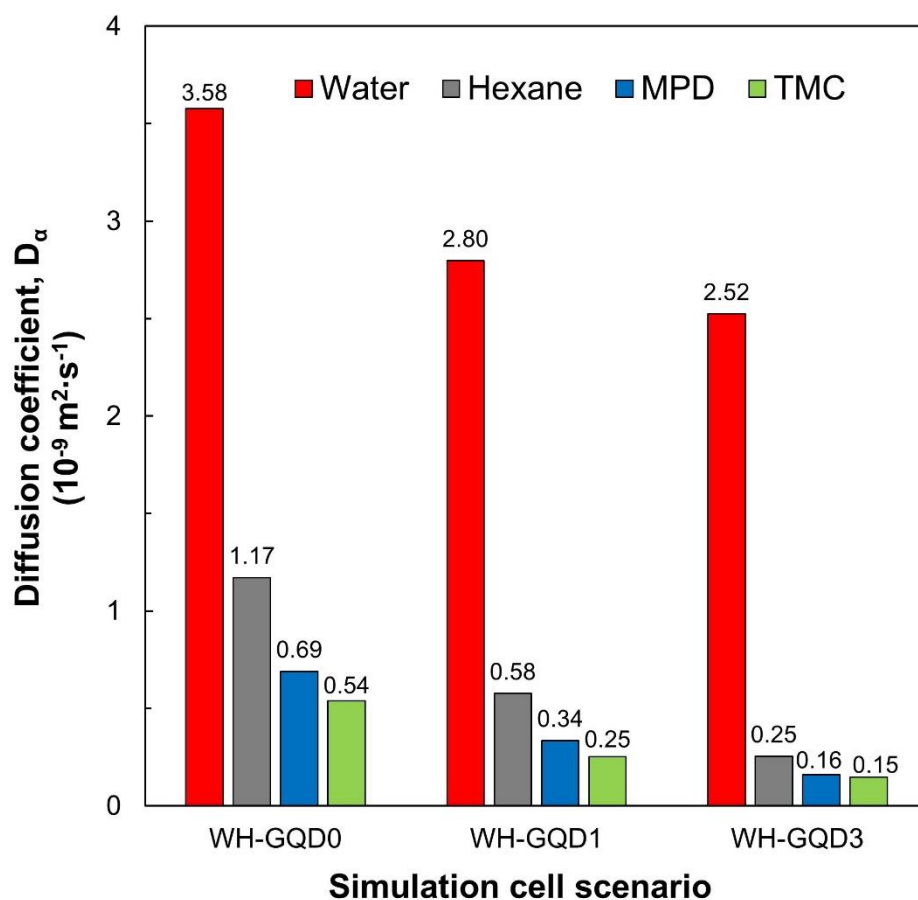
$$MSD = \frac{1}{N} \sum_{i=1}^N \langle [r_i(t + t_0) - r_i(t_0)]^2 \rangle = A + 6D_\alpha t \quad \text{Eq. 7.1}$$

where  $i$  denotes each particle for which the MSD is calculated,  $N$  is the total number of particles over which the sum is performed,  $r_i(t_0)$  and  $r_i(t)$  are the  $i$ -th particle positions (in three-dimensional space) at the initial time  $t_0$  and at time  $t$ , respectively,  $D_\alpha$  is the diffusion coefficient and  $A$  is a constant.



**Fig. 7.8** Snapshots of water-hexane interface system at 0 ns: (a, d), WH-GQD0, (b, e), WH-GQD1, (c, f), WH-GQD3; and at 4 ns: (g, j), WH-GQD0, (h, k), WH-GQD1, (i, l), WH-GQD3. Blue: nitrogen atom, grey: carbon atom, white: hydrogen atom, red: oxygen atom and yellow: GQD. In (a) to (c) and (g) to (i), water and hexane molecules are omitted to demonstrate GQD behaviour.

**Fig. 7.9** shows the diffusion coefficients calculated from Eq. 7.1 for particles under various scenarios. It was shown that the presence of GQD reduced the diffusivity of water, hexane, MPD, and TMC molecules. Since the diffusion coefficient of these molecules in WH-GQD3 was lower than that in WH-GQD1, it was considered that the respective diffusivities would be further reduced as the GQD concentration increases. This might be because the polar functional groups of GQD and the benzene ring attractively interacted with the benzene ring of MPD and TMC by Coulomb and  $\pi$ - $\pi$  stacking forces, respectively. It has been reported that the water permeability and solute rejection of RO membranes increased with increasing MPD diffusivity and decreasing MPD solubility (Ghosh et al. 2008). The above MD simulation results for molecular diffusion around the water-hexane interface suggested that the presence of GQD might reduce the diffusivity of MPD during an IP reaction; thus, causing a decrease in the IP reaction rate. Consequently, the presence of GQDs changes the “ridge-and-valley” structure of the PA layer.

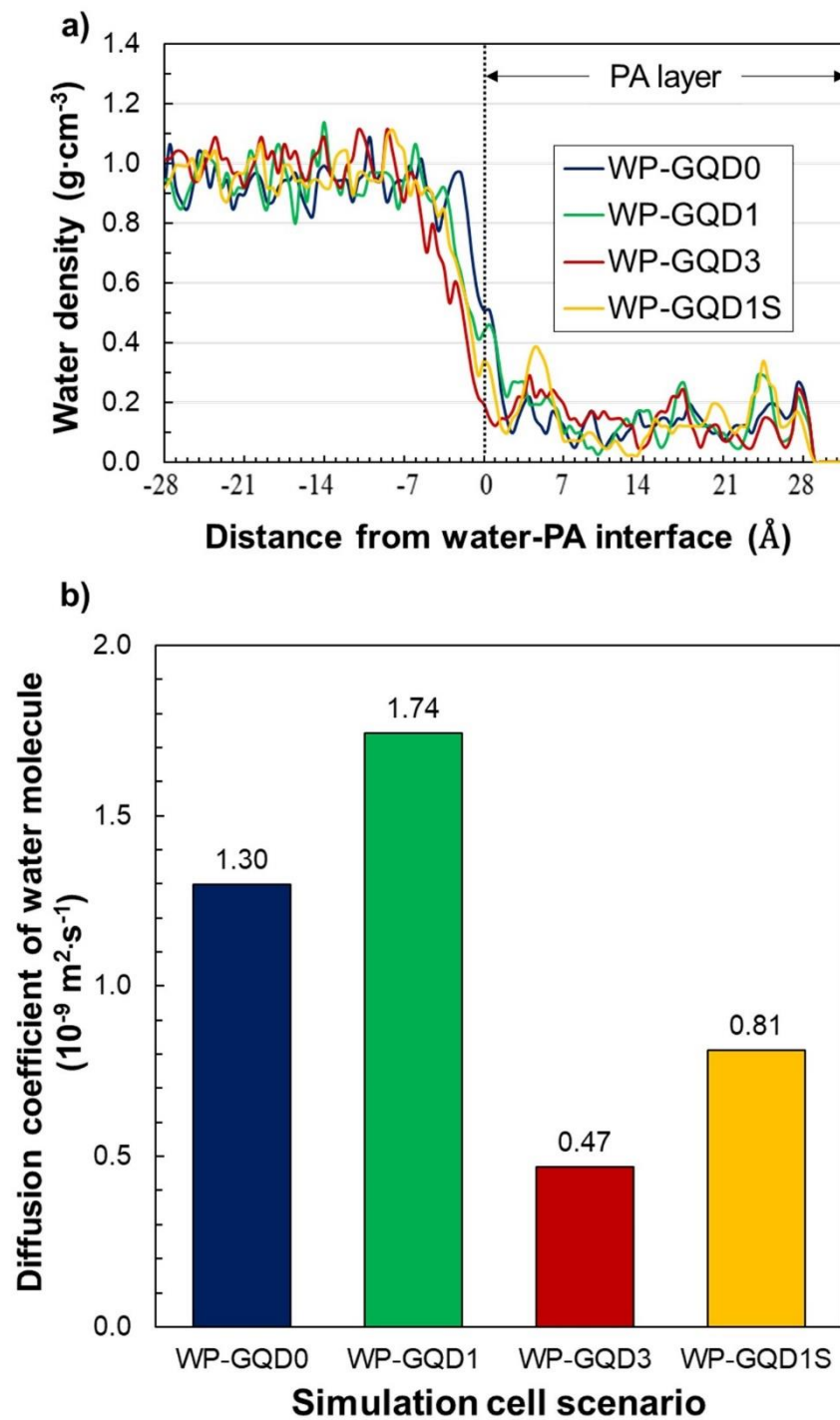


**Fig. 7.9** Diffusivity of water, hexane, MPD and TMC molecules.

### 7.2.3.2 Water-PA interface simulation

**Fig. 7.10a** shows the effect of GQD on the density distribution of the water molecule at the water-PA interface. Compared to the WP-GQD0 system without GQDs, water density decreased on the PA layer surface in the WP-GQD1, WP-GQD3, and WP-GQD1S systems containing GQDs. In addition, especially in WP-GQD3 and WP-GQD1S, where GQD existed on the PA side at a distance of 5 Å from the water-PA interface, the water density at a distance of about 6 Å from the membrane surface was lower than that of the WP-GQD0 by about 0.2 to 0.4 g·cm<sup>-3</sup>. It is considered that this would be caused by the hydrophobic portion of GQD present around the membrane surface. These results indicate that PA's hydrophilicity could be decreased when GQDs are present close to the PA layer's surface.

**Fig. 7.10b** shows the effect of GQD dispersion on the diffusivity of water molecules at the water-PA interface. The diffusion coefficient of water molecules without GQDs (WP-GQD0) was  $1.3 \times 10^{-9} \text{ m}^2 \cdot \text{s}^{-1}$ . In the case of WH-GQD1, which had one GQD at a distance of 15 Å from the water-PA interface on the PA phase, the diffusion coefficient of water molecules improved to  $1.74 \times 10^{-9} \text{ m}^2 \cdot \text{s}^{-1}$ . This might be because the presence of GQD inside the PA layer created a space around the hydrophobic portion of GQD where the water molecules could quickly move. A similar finding inside the GQD-modified PA membrane has already been reported by Salestan et al. (Salestan et al. 2020). However, in the case of WP-GQD3 with three GQDs, the diffusion coefficient of water molecules at the water-PA interface decreased to  $0.47 \times 10^{-9} \text{ m}^2 \cdot \text{s}^{-1}$ . As shown in **Fig. 7.10b**, the observed result is probably due to GQD existing close to the PA layer surface acting as a barrier and blocking the diffusion of water molecules into the PA layer. Even with WP-GQD1S, which contained one GQD like WH-GQD1, the diffusion coefficient of water at the water-PA interface was reduced from  $1.3 \times 10^{-9} \text{ m}^2 \cdot \text{s}^{-1}$  to  $0.81 \times 10^{-9} \text{ m}^2 \cdot \text{s}^{-1}$ . This occurrence could be attributed to the existence of a GQD very close to the PA layer surface. The overall results from the MD simulation suggested that the uniform dispersion of GQDs inside the PA layer could increase the water diffusivity at the water-PA interface and contribute to high water permeability. However, if the GQD density was too high and exposed close to the membrane surface, it might reduce the PA membrane's water permeability, which explains the sudden drop in water flux across TFN10 and TFN25 membranes without affecting membrane selectivity (**Fig. 7.7**).



**Fig. 7.10** (a) Effect of GQD on water molecular density distribution at the water-PA interface and (b) diffusivity of water molecules at the water-PA interface.

### 7.3 Conclusions

This study demonstrated the development of GQD-incorporated OSHF TFN membranes using the VAIP technique for FO applications. Experimental results showed that GQD

loading inside the PA layer influences membrane performance. The TFN5 membrane, with a GQD loading of  $5 \text{ mg}\cdot\text{L}^{-1}$ , demonstrated a *SRSF* of  $0.12 \text{ g}\cdot\text{L}^{-1}$  with the highest water flux of  $30.9 \text{ L}\cdot\text{m}^{-2}\cdot\text{h}^{-1}$ . The improved FO performance of the TFN5 membrane resulted from its improved hydrophilicity and uniform dispersion of GQDs inside the PA layer. MD simulation was employed at the water-hexane and water-PA interface to investigate the GQD loading effect on the IP reaction and membrane separation performance. The simulation results showed that a very high loading of GQDs caused them to aggregate at the water-hexane interface during the IP reaction and formed a defective PA layer.

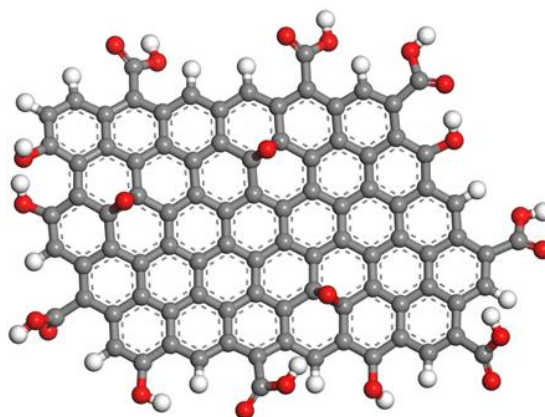
Additionally, that uniform dispersion of GQDs inside the PA layer increased the water diffusivity at the water-PA interface leading to high water permeability. However, too high GQD concentration at the PA layer surface reduced the membrane water permeability by acting as a barrier to water molecules. These results are expected to assist future studies aiming to improve the separation performance of GQD-embedded PA TFN membranes by tuning the interaction of GQDs with MPD, TMC and water molecules.

## **7.4 Supporting Information**

### **7.4.1 Molecular dynamics simulation**

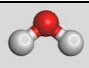

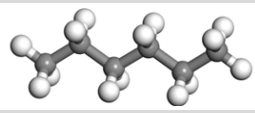
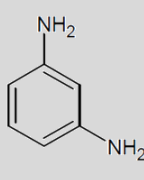

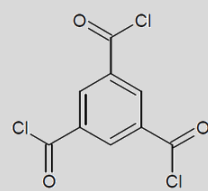
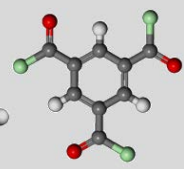
The GQD model employed in this study is shown in **Fig. S7.1** (Liu & Xu 2016). The GQD has an area of about  $3.22 \text{ nm}^2$ , a width of  $2.1964 \text{ nm}$  and a height of  $1.4669 \text{ nm}$ . In this study, a GQD model, which was not bonded to the PA membrane, was used as shown in previous studies (Salestan et al. 2020).





**Fig. S7.1** Structure of GQD; grey: carbon atom, red: oxygen atom, white: hydrogen atom.

**Table S7.1** Structural formula of water and hexane, *m*-phenylenediamine, and trimesoyl chloride.

Name	Molecular structural formula	Simulation model
Water	$\text{H}-\text{O}-\text{H}$	
Hexane		
<i>m</i> -phenylene diamine: MPD		
trimesoyl chloride: TMC		

### CRediT authorship contribution statement

**Nawshad Akther:** Conceptualization, Data curation, Formal analysis, Investigation, Methodology, Validation, Writing - original draft. **Yuki Kawabata:** Molecular dynamics simulation, Investigation, Validation, Writing - review & editing. **Sungil Lim:** Consultation of the data in regards to OSHF membrane, Writing – review & editing. **Tomohisa Yoshioka:** Molecular dynamics simulation, Validation, Writing - review & editing. **Sherub Phuntsho:** Writing - review & editing. **Hideto Matsuyama:** Writing - review & editing.

**Hokyong Shon:** Supervision, Project administration, Resources, Funding acquisition, Writing - review & editing.

### **Declaration of competing interest**

The authors declare that they have no known competing financial interests or personal relationships that could have appeared to influence the work reported in this paper.

### **Acknowledgement**

The research reported in this paper was supported by the Australian Research Council Industrial Transformation Research Hub (IH170100009) and the King Abdullah University of Science and Technology (KAUST), Saudi Arabia through the Competitive Research Grant Program–CRG2017 (CRG6), Grant # URF/1/3404-01.

# **CHAPTER 8**

## **CONCLUSIONS AND RECOMMENDATIONS**

## **8. CHAPTER 8 Conclusions and recommendations**

### **8.1 Conclusions**

PA TFC membranes have attained more preference than the cellulose acetate/triacetate membranes in recent years due to their enhanced physicochemical properties and permselectivity. However, conventional PA TFC membranes demonstrate a trade-off relationship between membrane selectivity and water permeability and are highly vulnerable to fouling that hamper their use in real applications. To overcome these issues, GO has been extensively used to improve the mechanical strength, thermal stability, chlorine resistance, antifouling properties, and separation performance of the TFC membranes. Nonetheless, very few studies provided an in-depth explanation of the possible interaction between GO and polymer matrix that alter the membrane chemical and physical properties or deteriorate membrane performance over time. It is, therefore, imperative to understand the polymer-nanomaterial interaction to enhance the stability and development of nanocomposite membranes.

Thus, the overall aim of this study was to develop high-performance PA TFC FO membranes by systematically investigating the effect of GO and its derivatives on the properties and performances of the modified membranes. Different TFC membrane fabrication and GO modification techniques, mainly surface coating and PA modification, have been employed and extensively characterized to understand possible interactions between GO and TFC membranes that govern water transport across the membranes. The effect of physicochemical properties of the prepared pristine and modified membranes on their desalination and antifouling performances has also been assessed to overcome the existing challenges and deliver strategies for future improvements in GO-based PA TFC membranes. The key conclusions from Chapters 4 to 7 are presented below.

Chapter 4 of this thesis showed the surface modification of commercial PA TFC FO membranes with a thin layer of cross-linked PVA and PVA/GO hydrogel coating that smoothed and improved the wettability of the membrane surface. Moreover, it was observed that the surface properties, performances and anti-bacterial properties of the membranes could be tuned by adjusting the GO loading in the PVA hydrogel coating. A GO loading of 0.02 wt% was optimal as it revealed the highest water flux amongst the modified membranes without sacrificing membrane selectivity. Membrane modification further resulted in improved solute rejection, higher fouling and bacterial resistance compared to the pristine TFC membrane. Consequently, the facile PVA/GO modification technique demonstrated in this study can be used to effectively seal membrane defects and potentially applied for wastewater reclamation and desalination.

Chapter 5 demonstrated the influence of GO flake lateral size on the properties and performances of the TFN FO membranes. Since PVA/GO coating explored in Chapter 4 increased the water transport resistance across the membrane, PA layers were modified in Chapter 5 by dispersing 0.01 wt% of GO flakes in the amine solution during the IP process. Overall, the GO-modified TFN membranes demonstrated better separation and antifouling properties than the unmodified TFC membrane due to their thinner PA layer, improved membrane surface hydrophilicity, smoother and negatively charged surfaces. The most important finding of this work was that the largest GO flakes (GO-0, without tip sonication) created a more defective PA layer and, consequently, a less selective membrane by hindering the MPD diffusion into the organic phase during the IP reaction. However, the TFN membrane performance enhanced on decreasing GO flake lateral size owing to a more uniform GO dispersion that reduced PA layer defects. The TFN membrane modified with the smallest GO flakes (MGO-8) demonstrated a 51% higher water flux and 61% lower *SRSF* than the MGO-0 membrane when tested with 0.5 M NaCl DS and DI water FS in AL-

FS orientation. MGO-8 also demonstrated better antifouling property than MGO-0 due to its augmented surface negativity, improved hydrophilicity and selectivity. These results confirmed that the TFN membrane performance can be considerably influenced by GO flake lateral size and that smaller GO flakes can minimize PA defects; thus, improving membrane flux and selectivity.

Chapter 6 of this thesis involved using AQN and GO flakes together as fillers to heal the PA defects created by GO, as shown in Chapter 5. The addition of AQN in the TFN membranes improved the selectivity of the TFN membranes with a slight increase in water flux compared to the pristine TFC membrane. On the other hand, the addition of GO enhanced the permeability of the membranes by creating defects in the PA layer, which in turn reduced the membrane selectivity. The synergistic effect of AQN and GO on the membrane separation performance was promising as they demonstrated augmented water flux without significantly compromising the membrane selectivity. The AQN repaired the defects created by GO in the PA layer to improve the membrane selectivity, while GO improved the membrane surface wettability and pore structure to increase water flux. The TFN50 membrane with a GO and AQN loading of 0.005 wt% and 0.2 wt%, respectively, was found to be the optimal membrane as it demonstrated the highest water flux with a *SRSF* value lower than that of the TFC membrane. The TFN50 membrane exhibited ~3 times higher water flux than the pristine TFC membrane with similar *SRSF*. Consequently, the AQN and GO could be used together to improve the separation performance of the PA TFN membranes.

Finally, Chapter 7 involved the development of GQD-incorporated OSHF TFN membranes using the VAIP technique for FO applications. GQD was used in this study as smaller GO flake lateral created less PA defects, as concluded in Chapter 5. Experimental results showed that GQD loading in the PA layer could influence membrane performance. TFN5, with a

GQD loading of  $5 \text{ mg}\cdot\text{L}^{-1}$ , demonstrated the highest water flux of  $30.9 \text{ L}\cdot\text{m}^{-2}\cdot\text{h}^{-1}$  with a *SRSF* value of  $0.12 \text{ g}\cdot\text{L}^{-1}$ . The improved FO performance of the TFN5 membrane could be ascribed to its improved hydrophilicity, good GQD dispersion and formation of nano water channels. MD simulation was also employed at the water-hexane and water-PA interface to investigate GQD loading effect on the IP reaction and membrane separation performance. The MD simulation results showed that uniform dispersion of GQDs inside the PA layer could increase the water diffusivity within the membrane leading to high water permeability. However, increasing the GQD loading beyond the optimal density could reduce the membrane water permeability while retaining selectivity due to hydrophobic sections of GQDs acting as a barrier to water transport. On increasing the GQD loading further, GQDs could aggregate at the water-hexane interface during the IP reaction and form a defective PA layer with very poor membrane selectivity.

**Table 8.1** summarizes the key details, including graphene oxide derivatives, modification methods and FO performances of the optimal membranes investigated in Chapters 4-7. While the PVA/GO-coated TFC membrane in Chapter 4 demonstrated the lowest water flux due to the increased hydraulic resistance from the PVA/GO cross-linked hydrogel layer, the GQD-modified OSHF membrane in Chapter 7 exhibited a better FO performance with a much lower nanomaterial loading than the other membranes prepared in this study due to the more uniform dispersion and smaller size of GQD, which reduced PA layer defects. Among the various strategies investigated in this project, the GO/AQN modification technique explored in Chapter 6 is the most beneficial and economical for the potential scale-up as commercial GO dispersion, and AQN can be used as received without further treatment for TFN membrane fabrication. Moreover, the GO/AQN-modified TFN membranes exhibit superior FO performance and can be prepared using the existing industrial membrane production line.

**Table 8.1** FO performance summary in AL-FS orientation of the various GO-modified PA TFN flat-sheet membranes prepared in this study.

Chapter	Nanomaterial (Particle size)	Modification method	Optimal particle loading	FO performance (AL-FS)			
				DS (FS)	CFV ( $\text{cm}\cdot\text{s}^{-1}$ )	$J_w$ (LMH)	$SRSF$ ( $\text{g}\cdot\text{L}^{-1}$ )
4	GO ( $\leq 10 \mu\text{m}$ )	PA layer surface dip- coated with PVA/GO hydrogel	0.02 wt% GO is PVA hydrogel	1 M NaCl (DI water)	12.6	24.7	0.21
5	GO ( $0.01 \mu\text{m}^2$ )	GO embedded in PA via IP reaction	0.01 wt% in in MPD solution	0.5 M NaCl (DI water)	12.6	24.7	0.21
6	GO/AQN ( $\leq 10 \mu\text{m}$ / n/a)	GO/AQN embedded in PA via IP reaction	0.005 wt% GO and 0.2 wt% AQN in MPD solution	0.5 M NaCl (DI water)	12.6	24.1	0.37
7	GQD (D: $\sim 30 \text{nm}$ )	GO embedded in PA via VAIP process	0.0005 wt% in MPD solution	1 M NaCl (DI water)	FS = 20.9 DS = 10.4	30.9	0.12

## 8.2 Recommendations

The PA TFN membrane modified with GO offers numerous advantages, such as high permeability, improved antifouling and antibiofouling properties, compared to the membranes modified with other types of fillers. As such, it is imperative to obtain a detailed understanding of the influence of GO properties on membrane properties and performance. Based on the results obtained from this study, the following recommendations in terms of further scientific research and commercial development are made:

- So far, researchers reported that the antibiofouling property of GO is contact-based, where the bacteria are inactivated by oxidation or their cell walls are ruptured by the sharp edges of GO. However, GO also demonstrates antibiofouling behaviour when embedded in the polymer matrix. Therefore, a more in-depth study is required to explain the antibiofouling behaviour of GO in membranes.
- GO improves water permeability by creating non-selective defects in the PA layer, which deteriorates membrane selectivity. More study is needed to find alternatives



like GO-AQN composites to overcome the membrane trade-off issues with their synergies.

- Smaller GO flakes are preferable for minimizing PA defects in TFN membranes. However, tip sonication and temperature regulation to break GO flakes and prevent GO reduction, respectively, could be energy-intensive for bulk GO production. Alternative affordable strategies for small-sized GO flake production could facilitate the production of GO-modified PA TFN membranes in a large-scale.
- PVA hydrogel creates a dense coating, which hinders the water permeability of the membranes. Consequently, strategies like using different cross-linking agents, polymer concentrations, coating conditions/methods or hydrophilic porous polymers could be investigated as alternatives for membrane surface modification.
- The OSHF TFN GQD membranes prepared using the VAIP technique in Chapter 7 demonstrated promising membrane performance at a very low GQD loading. Therefore, it will be interesting to develop large-scale OSHF TFN GQD membrane modules for application in various membrane processes like osmotic membrane bioreactor (OMBR). However, more methods need to be developed to apply the VAIP technique in large-scale OSHF membrane modules to minimize membrane defects. For instance, developing an open module design with optimal space between the HFs could prevent them from collapsing or sticking to each other during the VAIP process.

## References

- Ahmad, A.L., Shoparwe, N.F. & Hanifa, N. 2019, 'Equilibrium and Kinetic Study of Bovine Serum Albumin (BSA) Adsorption onto Fabricated Polyethersulfone (PES)/Hydroxyapatite (HAP) Adsorptive Mixed Matrix Membrane (MMM)', *Journal of Physical Science*, vol. 30.
- Akther, N., Ali, S.M., Phuntsho, S. & Shon, H. 2020, 'Surface modification of thin-film composite forward osmosis membranes with polyvinyl alcohol–graphene oxide composite hydrogels for antifouling properties', *Desalination*, vol. 491, p. 114591.
- Akther, N., Daer, S. & Hasan, S.W. 2018, 'Effect of flow rate, draw solution concentration and temperature on the performance of TFC FO membrane, and the potential use of RO reject brine as a draw solution in FO–RO hybrid systems', *Desalination and Water Treatment*, vol. 136, pp. 65-71.
- Akther, N., Daer, S., Wei, Q., Janajreh, I. & Hasan, S.W. 2019, 'Synthesis of polybenzimidazole (PBI) forward osmosis (FO) membrane and computational fluid dynamics (CFD) modeling of concentration gradient across membrane surface', *Desalination*, vol. 452, pp. 17-28.
- Akther, N., Kawabata, Y., Lim, S., Yoshioka, T., Phuntsho, S., Matsuyama, H. & Shon, H.K. 2021, 'Effect of graphene oxide quantum dots on the interfacial polymerization of a thin-film nanocomposite forward osmosis membrane: An experimental and molecular dynamics study', *Journal of Membrane Science*, vol. 630, p. 119309.
- Akther, N., Lim, S., Tran, V.H., Phuntsho, S., Yang, Y., Bae, T.-H., Ghaffour, N. & Shon, H.K. 2019, 'The effect of Schiff base network on the separation performance of thin film nanocomposite forward osmosis membranes', *Separation and Purification Technology*, vol. 217, pp. 284-93.
- Akther, N., Lin, Y., Wang, S., Phuntsho, S., Fu, Q., Ghaffour, N., Matsuyama, H. & Shon, H.K. 2020, 'In situ ultrathin silica layer formation on polyamide thin-film composite membrane surface for enhanced forward osmosis performances', *Journal of Membrane Science*, p. 118876.
- Akther, N., Phuntsho, S., Chen, Y., Ghaffour, N. & Shon, H.K. 2019, 'Recent advances in nanomaterial-modified polyamide thin-film composite membranes for forward osmosis processes', *Journal of Membrane Science*, vol. 584, pp. 20-45.
- Akther, N., Sanahuja-Embuela, V., Górecki, R., Phuntsho, S., Helix-Nielsen, C. & Shon, H.K. 2021, 'Employing the synergistic effect between aquaporin nanostructures and graphene oxide for enhanced separation performance of thin-film nanocomposite forward osmosis membranes', *Desalination*, vol. 498, p. 114795.
- Akther, N., Sodiq, A., Giwa, A., Daer, S., Arafat, H.A. & Hasan, S.W. 2015, 'Recent advancements in forward osmosis desalination: A review', *Chemical Engineering Journal*, vol. 281, pp. 502-22.
- Akther, N., Yuan, Z., Chen, Y., Lim, S., Phuntsho, S., Ghaffour, N., Matsuyama, H. & Shon, H. 2020, 'Influence of graphene oxide lateral size on the properties and performances of forward osmosis membrane', *Desalination*, vol. 484, p. 114421.
- Alejo, T., Arruebo, M., Carcelen, V., Monsalvo, V.M. & Sebastian, V. 2017, 'Advances in draw solutes for forward osmosis: Hybrid organic-inorganic nanoparticles and conventional solutes', *Chemical Engineering Journal*, vol. 309, pp. 738-52.
- Ali, A., Tufa, R.A., Macedonio, F., Curcio, E. & Drioli, E. 2018, 'Membrane technology in renewable-energy-driven desalination', *Renewable and Sustainable Energy Reviews*, vol. 81, Part 1, pp. 1-21.

- Ali, S.M., Kim, J.E., Phuntsho, S., Jang, A., Choi, J.Y. & Shon, H.K. 2018, 'Forward osmosis system analysis for optimum design and operating conditions', *Water Research*, vol. 145, pp. 429-41.
- Alsvik, I.L. & Hägg, M.-B. 2013, 'Pressure retarded osmosis and forward osmosis membranes: Materials and methods', *Polymers*, vol. 5, no. 1, pp. 303-27.
- Amini, M., Jahanshahi, M. & Rahimpour, A. 2013a, 'Synthesis of novel thin film nanocomposite (TFN) forward osmosis membranes using functionalized multi-walled carbon nanotubes', *Journal of Membrane Science*, vol. 435, no. Supplement C, pp. 233-41.
- Amini, M., Jahanshahi, M. & Rahimpour, A. 2013b, 'Synthesis of novel thin film nanocomposite (TFN) forward osmosis membranes using functionalized multi-walled carbon nanotubes', *Journal of Membrane Science*, vol. 435, pp. 233-41.
- Amini, M., Rahimpour, A. & Jahanshahi, M. 2016, 'Forward osmosis application of modified TiO<sub>2</sub>-polyamide thin film nanocomposite membranes', *Desalination and Water Treatment*, vol. 57, no. 30, pp. 14013-23.
- Ansari, A.J., Hai, F.I., Price, W.E., Drewes, J.E. & Nghiem, L.D. 2017, 'Forward osmosis as a platform for resource recovery from municipal wastewater - A critical assessment of the literature', *Journal of Membrane Science*, vol. 529, pp. 195-206.
- Araki, T., Cruz-Silva, R., Tejima, S., Takeuchi, K., Hayashi, T., Inukai, S., Noguchi, T., Tanioka, A., Kawaguchi, T., Terrones, M. & Endo, M. 2015, 'Molecular dynamics study of carbon nanotubes/polyamide reverse osmosis membranes: Polymerization, structure, and hydration', *ACS Applied Materials & Interfaces*, vol. 7, no. 44, pp. 24566-75.
- Attarde, D., Jain, M., Singh, P.K. & Gupta, S.K. 2017, 'Energy-efficient seawater desalination and wastewater treatment using osmotically driven membrane processes', *Desalination*, vol. 413, pp. 86-100.
- Aydiner, C., Topcu, S., Tortop, C., Kuvvet, F., Ekinci, D., Dizge, N. & Keskinler, B. 2013, 'A novel implementation of water recovery from whey: "Forward-reverse osmosis" integrated membrane system', *Desalination and Water Treatment*, vol. 51, no. 4-6, pp. 786-99.
- Baroña, G.N.B., Choi, M. & Jung, B. 2012, 'High permeate flux of PVA/PSf thin film composite nanofiltration membrane with aluminosilicate single-walled nanotubes', *Journal of Colloid and Interface Science*, vol. 386, no. 1, pp. 189-97.
- Baroña, G.N.B., Lim, J., Choi, M. & Jung, B. 2013, 'Interfacial polymerization of polyamide-aluminosilicate SWNT nanocomposite membranes for reverse osmosis', *Desalination*, vol. 325, no. Supplement C, pp. 138-47.
- Bell, E.A., Poynor, T.E., Newhart, K.B., Regnery, J., Coday, B.D. & Cath, T.Y. 2017, 'Produced water treatment using forward osmosis membranes: Evaluation of extended-time performance and fouling', *Journal of Membrane Science*, vol. 525, pp. 77-88.
- Bi, R., Zhang, Q., Zhang, R., Su, Y. & Jiang, Z. 2018, 'Thin film nanocomposite membranes incorporated with graphene quantum dots for high flux and antifouling property', *Journal of Membrane Science*, vol. 553, pp. 17-24.
- Bi, R., Zhang, R., Shen, J., Liu, Y.-n., He, M., You, X., Su, Y. & Jiang, Z. 2019, 'Graphene quantum dots engineered nanofiltration membrane for ultrafast molecular separation', *Journal of Membrane Science*, vol. 572, pp. 504-11.
- Bogler, A., Lin, S. & Bar-Zeev, E. 2017, 'Biofouling of membrane distillation, forward osmosis and pressure retarded osmosis: Principles, impacts and future directions', *Journal of Membrane Science*, vol. 542, pp. 378-98.

- Borgnia, M.J., Kozono, D., Calamita, G., Maloney, P.C. & Agre, P. 1999, 'Functional reconstitution and characterization of AqpZ, the E. coli water channel protein' Edited by W. Baumeister', *Journal of Molecular Biology*, vol. 291, no. 5, pp. 1169-79.
- Bui, N.-N. & McCutcheon, J.R. 2016, 'Nanoparticle-embedded nanofibers in highly permselective thin-film nanocomposite membranes for forward osmosis', *Journal of Membrane Science*, vol. 518, pp. 338-46.
- Buonomenna, M.G. & Bae, J. 2015, 'Membrane processes and renewable energies', *Renewable and Sustainable Energy Reviews*, vol. 43, pp. 1343-98.
- Car, A., Stropnik, C. & Peinemann, K.-V. 2006, 'Hybrid membrane materials with different metal-organic frameworks (MOFs) for gas separation', *Desalination*, vol. 200, no. 1, pp. 424-6.
- Cath, T.Y., Childress, A.E. & Elimelech, M. 2006, 'Forward osmosis: Principles, applications, and recent developments', *Journal of Membrane Science*, vol. 281, no. 1-2, pp. 70-87.
- Cath, T.Y., Elimelech, M., McCutcheon, J.R., McGinnis, R.L., Achilli, A., Anastasio, D., Brady, A.R., Childress, A.E., Farr, I.V., Hancock, N.T., Lampi, J., Nghiem, L.D., Xie, M. & Yip, N.Y. 2013, 'Standard Methodology for Evaluating Membrane Performance in Osmotically Driven Membrane Processes', *Desalination*, vol. 312, pp. 31-8.
- Cath, T.Y., Hancock, N.T., Lundin, C.D., Hoppe-Jones, C. & Drewes, J.E. 2010, 'A multi-barrier osmotic dilution process for simultaneous desalination and purification of impaired water', *Journal of Membrane Science*, vol. 362, no. 1, pp. 417-26.
- Chekli, L., Pathak, N., Kim, Y., Phuntsho, S., Li, S., Ghaffour, N., Leiknes, T. & Shon, H.K. 2018, 'Combining high performance fertiliser with surfactants to reduce the reverse solute flux in the fertiliser drawn forward osmosis process', *Journal of Environmental Management*, vol. 226, pp. 217-25.
- Chekli, L., Phuntsho, S., Kim, J.E., Kim, J., Choi, J.Y., Choi, J.-S., Kim, S., Kim, J.H., Hong, S., Sohn, J. & Shon, H.K. 2016, 'A comprehensive review of hybrid forward osmosis systems: Performance, applications and future prospects', *Journal of Membrane Science*, vol. 497, pp. 430-49.
- Chen, C., Yang, Q.H., Yang, Y., Lv, W., Wen, Y., Hou, P.X., Wang, M. & Cheng, H.M. 2009, 'Self-assembled free-standing graphite oxide membrane', *Advanced Materials*, vol. 21, no. 29, pp. 3007-11.
- Chen, L., Gu, Y., Cao, C., Zhang, J., Ng, J.-W. & Tang, C. 2014, 'Performance of a submerged anaerobic membrane bioreactor with forward osmosis membrane for low-strength wastewater treatment', *Water Research*, vol. 50, pp. 114-23.
- Chen, Q. & Peng, L.M. 2007, 'Structure and applications of titanate and related nanostructures', *International Journal of Nanotechnology*, vol. 4, no. 1-2, pp. 44-65.
- Cheng, Z.L., Li, X., Liu, Y.D. & Chung, T.-S. 2016, 'Robust outer-selective thin-film composite polyethersulfone hollow fiber membranes with low reverse salt flux for renewable salinity-gradient energy generation', *Journal of Membrane Science*, vol. 506, pp. 119-29.
- Chiao, Y.-H., Sengupta, A., Chen, S.-T., Huang, S.-H., Hu, C.-C., Hung, W.-S., Chang, Y., Qian, X., Ranil Wickramasinghe, S., Lee, K.-R. & Lai, J.-Y. 2018, 'Zwitterion augmented polyamide membrane for improved forward osmosis performance with significant antifouling characteristics', *Separation and Purification Technology*.
- Cho, Y.H., Han, J., Han, S., Guiver, M.D. & Park, H.B. 2013, 'Polyamide thin-film composite membranes based on carboxylated polysulfone microporous support

- membranes for forward osmosis', *Journal of Membrane Science*, vol. 445, pp. 220-7.
- Choi, H.-g., Shah, A.A., Nam, S.-E., Park, Y.-I. & Park, H. 2019, 'Thin-film composite membranes comprising ultrathin hydrophilic polydopamine interlayer with graphene oxide for forward osmosis', *Desalination*, vol. 449, pp. 41-9.
- Choi, H.-g., Son, M. & Choi, H. 2017, 'Integrating seawater desalination and wastewater reclamation forward osmosis process using thin-film composite mixed matrix membrane with functionalized carbon nanotube blended polyethersulfone support layer', *Chemosphere*, vol. 185, no. Supplement C, pp. 1181-8.
- Chong, J.Y., Wang, B. & Li, K. 2016, 'Graphene oxide membranes in fluid separations', *Current Opinion in Chemical Engineering*, vol. 12, pp. 98-105.
- Chun, Y., Mulcahy, D., Zou, L. & Kim, I. 2017, 'A Short Review of Membrane Fouling in Forward Osmosis Processes', *Membranes*, vol. 7, no. 2, p. 30.
- Chung, T.-S., Li, X., Ong, R.C., Ge, Q., Wang, H. & Han, G. 2012, 'Emerging forward osmosis (FO) technologies and challenges ahead for clean water and clean energy applications', *Current Opinion in Chemical Engineering*, vol. 1, no. 3, pp. 246-57.
- Chung, T.-S., Luo, L., Wan, C.F., Cui, Y. & Amy, G. 2015, 'What is next for forward osmosis (FO) and pressure retarded osmosis (PRO)', *Separation and Purification Technology*, vol. 156, pp. 856-60.
- Chung, T.-S., Zhang, S., Wang, K.Y., Su, J. & Ling, M.M. 2012, 'Forward osmosis processes: Yesterday, today and tomorrow', *Desalination*, vol. 287, no. 0, pp. 78-81.
- Corry, B. 2008, 'Designing carbon nanotube membranes for efficient water desalination', *The Journal of Physical Chemistry B*, vol. 112, no. 5, pp. 1427-34.
- Costerton, J.W., Lewandowski, Z., Caldwell, D.E., Korber, D.R. & Lappin-Scott, H.M. 1995, 'Microbial biofilms', *Annual Review of Microbiology*, vol. 49, no. 1, pp. 711-45.
- Cui, Y., Yue, Y., Qian, G. & Chen, B. 2012, 'Luminescent functional metal-organic frameworks', *Chemical Reviews*, vol. 112, no. 2, pp. 1126-62.
- Daer, S., Akther, N., Wei, Q., Shon, H.K. & Hasan, S.W. 2020, 'Influence of silica nanoparticles on the desalination performance of forward osmosis polybenzimidazole membranes', *Desalination*, vol. 491, p. 114441.
- Darabi, R.R., Peyravi, M., Jahanshahi, M. & Qhoreyshi Amiri, A.A. 2017, 'Decreasing ICP of forward osmosis (TFN-FO) membrane through modifying PES-Fe<sub>3</sub>O<sub>4</sub> nanocomposite substrate', *Korean Journal of Chemical Engineering*, vol. 34, no. 8, pp. 2311-24.
- Das, R., Abd Hamid, S.B., Ali, M.E., Ismail, A.F., Annuar, M.S.M. & Ramakrishna, S. 2014, 'Multifunctional carbon nanotubes in water treatment: The present, past and future', *Desalination*, vol. 354, pp. 160-79.
- Das, R., Ali, M.E., Hamid, S.B.A., Ramakrishna, S. & Chowdhury, Z.Z. 2014, 'Carbon nanotube membranes for water purification: A bright future in water desalination', *Desalination*, vol. 336, pp. 97-109.
- Deng, C., Zhang, Q.G., Han, G.L., Gong, Y., Zhu, A.M. & Liu, Q.L. 2013, 'Ultrathin self-assembled anionic polymer membranes for superfast size-selective separation', *Nanoscale*, vol. 5, no. 22, pp. 11028-34.
- Dimiev, A.M., Alemany, L.B. & Tour, J.M. 2013, 'Graphene Oxide. Origin of Acidity, Its Instability in Water, and a New Dynamic Structural Model', *ACS Nano*, vol. 7, no. 1, pp. 576-88.
- Ding, S.-Y., Gao, J., Wang, Q., Zhang, Y., Song, W.-G., Su, C.-Y. & Wang, W. 2011, 'Construction of covalent organic framework for catalysis: Pd/COF-LZU1 in

- Suzuki–Miyaura coupling reaction', *Journal of the American Chemical Society*, vol. 133, no. 49, pp. 19816-22.
- Ding, W., Li, Y., Bao, M., Zhang, J., Zhang, C. & Lu, J. 2017, 'Highly permeable and stable forward osmosis (FO) membrane based on the incorporation of Al<sub>2</sub>O<sub>3</sub> nanoparticles into both substrate and polyamide active layer', *RSC Advances*, vol. 7, no. 64, pp. 40311-20.
- Discher, D.E. & Ahmed, F. 2006, 'Polymersomes', *Annual Review of Biomedical Engineering*, vol. 8, no. 1, pp. 323-41.
- Discher, D.E. & Eisenberg, A. 2002, 'Polymer vesicles', *Science*, vol. 297, no. 5583, p. 967.
- Dreyer, D.R., Park, S., Bielawski, C.W. & Ruoff, R.S. 2010, 'The chemistry of graphene oxide', *Chemical Society Reviews*, vol. 39, no. 1, pp. 228-40.
- Dumée, L., Lee, J., Sears, K., Tardy, B., Duke, M. & Gray, S. 2013, 'Fabrication of thin film composite poly(amide)-carbon-nanotube supported membranes for enhanced performance in osmotically driven desalination systems', *Journal of Membrane Science*, vol. 427, pp. 422-30.
- Emadzadeh, D., Ghanbari, M., Lau, W.J., Rahbari-Sisakht, M., Matsuura, T., Ismail, A.F. & Kruczek, B. 2016, 'Solvothermal synthesis of nanoporous TiO<sub>2</sub>: The impact on thin-film composite membranes for engineered osmosis application', *Nanotechnology*, vol. 27, no. 34, p. 345702.
- Emadzadeh, D., Lau, W. & Ismail, A. 2013, 'Synthesis of thin film nanocomposite forward osmosis membrane with enhancement in water flux without sacrificing salt rejection', *Desalination*, vol. 330, pp. 90-9.
- Emadzadeh, D., Lau, W., Matsuura, T., Ismail, A. & Rahbari-Sisakht, M. 2014, 'Synthesis and characterization of thin film nanocomposite forward osmosis membrane with hydrophilic nanocomposite support to reduce internal concentration polarization', *Journal of Membrane Science*, vol. 449, pp. 74-85.
- Emadzadeh, D., Lau, W.J., Matsuura, T., Hilal, N. & Ismail, A.F. 2014, 'The potential of thin film nanocomposite membrane in reducing organic fouling in forward osmosis process', *Desalination*, vol. 348, no. Supplement C, pp. 82-8.
- Emadzadeh, D., Lau, W.J., Matsuura, T., Rahbari-Sisakht, M. & Ismail, A.F. 2014, 'A novel thin film composite forward osmosis membrane prepared from PSf–TiO<sub>2</sub> nanocomposite substrate for water desalination', *Chemical Engineering Journal*, vol. 237, pp. 70-80.
- Emadzadeh, D., Lau, W.J., Rahbari-Sisakht, M., Ilbeygi, H., Rana, D., Matsuura, T. & Ismail, A.F. 2015, 'Synthesis, modification and optimization of titanate nanotubes-polyamide thin film nanocomposite (TFN) membrane for forward osmosis (FO) application', *Chemical Engineering Journal*, vol. 281, pp. 243-51.
- Eslah, S.S., Shokrollahzadeh, S., Jazani, O.M. & Samimi, A. 2018, 'Forward osmosis water desalination: Fabrication of graphene oxide-polyamide/polysulfone thin-film nanocomposite membrane with high water flux and low reverse salt diffusion', *Separation Science and Technology*, vol. 53, no. 3, pp. 573-83.
- Eslami, H. & Behrouz, M. 2014, 'Molecular dynamics simulation of a polyamide-66/carbon nanotube nanocomposite', *The Journal of Physical Chemistry C*, vol. 118, no. 18, pp. 9841-51.
- Fan, X., Liu, Y. & Quan, X. 2018, 'A novel reduced graphene oxide/carbon nanotube hollow fiber membrane with high forward osmosis performance', *Desalination*.
- Faria, A.F., Liu, C., Xie, M., Perreault, F., Nghiem, L.D., Ma, J. & Elimelech, M. 2017, 'Thin-film composite forward osmosis membranes functionalized with graphene

- oxide–silver nanocomposites for biofouling control', *Journal of Membrane Science*, vol. 525, pp. 146-56.
- Farmer, V.C., Fraser, A.R. & Tait, J.M. 1977, 'Synthesis of imogolite: A tubular aluminium silicate polymer', *Journal of the Chemical Society, Chemical Communications*, no. 13, pp. 462-3.
- Fathizadeh, M., Aroujalian, A. & Raisi, A. 2011, 'Effect of added NaX nano-zeolite into polyamide as a top thin layer of membrane on water flux and salt rejection in a reverse osmosis process', *Journal of Membrane Science*, vol. 375, no. 1, pp. 88-95.
- Feng, X., Ding, X. & Jiang, D. 2012, 'Covalent organic frameworks', *Chemical Society Reviews*, vol. 41, no. 18, pp. 6010-22.
- Ficai, D., Ficai, A., Trusca, R., Vasile, B.S., Voicu, G., Guran, C. & Andronescu, E. 2013, 'Synthesis and characterization of magnetite-polysulfone micro- and nanobeads with improved chemical stability in acidic media', *Current Nanoscience*, vol. 9, no. 2, pp. 271-7.
- Furukawa, H., Cordova, K.E., O'Keeffe, M. & Yaghi, O.M. 2013, 'The chemistry and applications of metal-organic frameworks', *Science*, vol. 341, no. 6149.
- Gan, H.X., Zhou, H., Lee, H.J., Lin, Q. & Tong, Y.W. 2019, 'Toward a better understanding of the nature-inspired aquaporin biomimetic membrane', *Langmuir*, vol. 35, no. 22, pp. 7285-93.
- Ganesh, B.M., Isloor, A.M. & Ismail, A.F. 2013, 'Enhanced hydrophilicity and salt rejection study of graphene oxide-polysulfone mixed matrix membrane', *Desalination*, vol. 313, no. Supplement C, pp. 199-207.
- Garni, M., Thamboo, S., Schoenenberger, C.-A. & Palivan, C.G. 2017, 'Biopores/membrane proteins in synthetic polymer membranes', *Biochimica et Biophysica Acta (BBA) - Biomembranes*, vol. 1859, no. 4, pp. 619-38.
- Ghanbari, M., Emadzadeh, D., Lau, W.J., Lai, S.O., Matsuura, T. & Ismail, A.F. 2015, 'Synthesis and characterization of novel thin film nanocomposite (TFN) membranes embedded with halloysite nanotubes (HNTs) for water desalination', *Desalination*, vol. 358, pp. 33-41.
- Ghanbari, M., Emadzadeh, D., Lau, W.J., Matsuura, T., Davoody, M. & Ismail, A.F. 2015, 'Super hydrophilic TiO<sub>2</sub>/HNT nanocomposites as a new approach for fabrication of high performance thin film nanocomposite membranes for FO application', *Desalination*, vol. 371, pp. 104-14.
- Ghanbari, M., Emadzadeh, D., Lau, W.J., Matsuura, T. & Ismail, A.F. 2015, 'Synthesis and characterization of novel thin film nanocomposite reverse osmosis membranes with improved organic fouling properties for water desalination', *RSC Advances*, vol. 5, no. 27, pp. 21268-76.
- Ghanbari, M., Emadzadeh, D., Lau, W.J., Riazi, H., Almasi, D. & Ismail, A.F. 2016, 'Minimizing structural parameter of thin film composite forward osmosis membranes using polysulfone/halloysite nanotubes as membrane substrates', *Desalination*, vol. 377, pp. 152-62.
- Ghosh, A.K., Jeong, B.-H., Huang, X. & Hoek, E.M.V. 2008, 'Impacts of reaction and curing conditions on polyamide composite reverse osmosis membrane properties', *Journal of Membrane Science*, vol. 311, no. 1, pp. 34-45.
- Giwa, A., Akther, N., Dufour, V. & Hasan, S.W. 2016, 'A critical review on recent polymeric and nano-enhanced membranes for reverse osmosis', *RSC Advances*, vol. 6, no. 10, pp. 8134-63.
- Goh, K., Karahan, H.E., Wei, L., Bae, T.-H., Fane, A.G., Wang, R. & Chen, Y. 2016, 'Carbon nanomaterials for advancing separation membranes: A strategic perspective', *Carbon*, vol. 109, pp. 694-710.

- Goh, K., Setiawan, L., Wei, L., Jiang, W., Wang, R. & Chen, Y. 2013, 'Fabrication of novel functionalized multi-walled carbon nanotube immobilized hollow fiber membranes for enhanced performance in forward osmosis process', *Journal of Membrane Science*, vol. 446, no. Supplement C, pp. 244-54.
- Goh, K., Setiawan, L., Wei, L., Si, R., Fane, A.G., Wang, R. & Chen, Y. 2015, 'Graphene oxide as effective selective barriers on a hollow fiber membrane for water treatment process', *Journal of Membrane Science*, vol. 474, pp. 244-53.
- Goh, P.S., Ismail, A.F. & Ng, B.C. 2013, 'Carbon nanotubes for desalination: Performance evaluation and current hurdles', *Desalination*, vol. 308, pp. 2-14.
- Górecki, R., Reurink, D.M., Khan, M.M., Sanahuja-Embuena, V., Trzaskuś, K. & Hélix-Nielsen, C. 2020, 'Improved reverse osmosis thin film composite biomimetic membranes by incorporation of polymersomes', *Journal of Membrane Science*, vol. 593, p. 117392.
- Gorgojo, P., Karan, S., Wong, H.C., Jimenez-Solomon, M.F., Cabral, J.T. & Livingston, A.G. 2014, 'Ultrathin Polymer Films with Intrinsic Microporosity: Anomalous Solvent Permeation and High Flux Membranes', *Advanced Functional Materials*, vol. 24, no. 30, pp. 4729-37.
- Goudeau, S., Charlot, M., Vergelati, C. & Müller-Plathe, F. 2004, 'Atomistic simulation of the water influence on the local structure of polyamide 6,6', *Macromolecules*, vol. 37, no. 21, pp. 8072-81.
- Grzelakowski, M. & Kita-Tokarczyk, K. 2016, 'Terminal groups control self-assembly of amphiphilic block copolymers in solution', *Nanoscale*, vol. 8, no. 12, pp. 6674-83.
- Habel, J., Hansen, M., Kynde, S., Larsen, N., Midtgaard, S.R., Jensen, G.V., Bomholt, J., Ogbonna, A., Almdal, K., Schulz, A. & Hélix-Nielsen, C. 2015, 'Aquaporin-Based Biomimetic Polymeric Membranes: Approaches and Challenges', *Membranes*, vol. 5, no. 3, pp. 307-51.
- Han, G., Chung, T.-S., Toriida, M. & Tamai, S. 2012, 'Thin-film composite forward osmosis membranes with novel hydrophilic supports for desalination', *Journal of Membrane Science*, vol. 423–424, pp. 543-55.
- Harder, E., Walters, D.E., Bodnar, Y.D., Faibish, R.S. & Roux, B. 2009, 'Molecular dynamics study of a polymeric reverse osmosis membrane', *The Journal of Physical Chemistry B*, vol. 113, no. 30, pp. 10177-82.
- He, Y., Miao, J., Chen, S., Zhang, R., Zhang, L., Tang, H. & Yang, H. 2019, 'Preparation and characterization of a novel positively charged composite hollow fiber nanofiltration membrane based on chitosan lactate', *RSC Advances*, vol. 9, no. 8, pp. 4361-9.
- Hegab, H.M., ElMekawy, A., Barclay, T.G., Michelmore, A., Zou, L., Saint, C.P. & Ginic-Markovic, M. 2015, 'Fine-tuning the surface of forward osmosis membranes via grafting graphene oxide: Performance patterns and biofouling propensity', *ACS Applied Materials & Interfaces*, vol. 7, no. 32, pp. 18004-16.
- Hegab, H.M., ElMekawy, A., Barclay, T.G., Michelmore, A., Zou, L., Saint, C.P. & Ginic-Markovic, M. 2016, 'Effective in-situ chemical surface modification of forward osmosis membranes with polydopamine-induced graphene oxide for biofouling mitigation', *Desalination*, vol. 385, pp. 126-37.
- Hegab, H.M., ElMekawy, A., Zou, L., Mulcahy, D., Saint, C.P. & Ginic-Markovic, M. 2016, 'The controversial antibacterial activity of graphene-based materials', *Carbon*, vol. 105, pp. 362-76.
- Hegab, H.M. & Zou, L. 2015a, 'Graphene oxide-assisted membranes: Fabrication and potential applications in desalination and water purification', *Journal of Membrane Science*, vol. 484, pp. 95-106.



- Hegab, H.M. & Zou, L. 2015b, 'Graphene oxide-assisted membranes: Fabrication and potential applications in desalination and water purification', *Journal of Membrane Science*, vol. 484, no. Supplement C, pp. 95-106.
- Herron, J. 2008, *Asymmetric forward osmosis membranes*, US7445712 B2.
- Hu, M. & Mi, B. 2013, 'Enabling graphene oxide nanosheets as water separation membranes', *Environmental Science & Technology*, vol. 47, no. 8, pp. 3715-23.
- Hu, M. & Mi, B. 2014, 'Layer-by-layer assembly of graphene oxide membranes via electrostatic interaction', *Journal of Membrane Science*, vol. 469, pp. 80-7.
- Hu, M., Zheng, S. & Mi, B. 2016, 'Organic fouling of graphene oxide membranes and its implications for membrane fouling control in engineered osmosis', *Environmental Science & Technology*, vol. 50, no. 2, pp. 685-93.
- Hu, W., Peng, C., Luo, W., Lv, M., Li, X., Li, D., Huang, Q. & Fan, C. 2010, 'Graphene-based antibacterial paper', *ACS Nano*, vol. 4, no. 7, pp. 4317-23.
- Hu, Y., Lu, K., Yan, F., Shi, Y., Yu, P., Yu, S., Li, S. & Gao, C. 2016, 'Enhancing the performance of aromatic polyamide reverse osmosis membrane by surface modification via covalent attachment of polyvinyl alcohol (PVA)', *Journal of Membrane Science*, vol. 501, pp. 209-19.
- Huang, H., Qu, X., Dong, H., Zhang, L. & Chen, H. 2013, 'Role of NaA zeolites in the interfacial polymerization process towards a polyamide nanocomposite reverse osmosis membrane', *RSC Advances*, vol. 3, no. 22, pp. 8203-7.
- Huang, H., Ying, Y. & Peng, X. 2014, 'Graphene oxide nanosheet: An emerging star material for novel separation membranes', *Journal of Materials Chemistry A*, vol. 2, no. 34, pp. 13772-82.
- Huang, M., Chen, Y., Huang, C.-H., Sun, P. & Crittenden, J. 2015a, 'Rejection and adsorption of trace pharmaceuticals by coating a forward osmosis membrane with TiO<sub>2</sub>', *Chemical Engineering Journal*, vol. 279, no. Supplement C, pp. 904-11.
- Huang, M., Chen, Y., Huang, C.-H., Sun, P. & Crittenden, J. 2015b, 'Rejection and adsorption of trace pharmaceuticals by coating a forward osmosis membrane with TiO<sub>2</sub>', *Chemical Engineering Journal*, vol. 279, pp. 904-11.
- Huang, Y., Cay-Durgun, P., Lai, T., Yu, P. & Lind, M.L. 2018, 'Phenol removal from water by polyamide and AgCl mineralized thin-film composite forward osmosis membranes', *Industrial & Engineering Chemistry Research*, vol. 57, no. 20, pp. 7021-9.
- Huang, Y., Jin, H., Yu, P. & Luo, Y. 2016, 'Polyamide thin-film composite membrane based on nano-silica modified polysulfone microporous support layer for forward osmosis', *Desalination and Water Treatment*, vol. 57, no. 43, pp. 20177-87.
- Hung, W.S., An, Q.F., De Guzman, M., Lin, H.Y., Huang, S.H., Liu, W.R., Hu, C.C., Lee, K.R. & Lai, J.Y. 2014, 'Pressure-assisted self-assembly technique for fabricating composite membranes consisting of highly ordered selective laminate layers of amphiphilic graphene oxide', *Carbon*, vol. 68, pp. 670-7.
- Inurria, A., Cay-Durgun, P., Rice, D., Zhang, H., Seo, D.-K., Lind, M.L. & Perreault, F. 2018, 'Polyamide thin-film nanocomposite membranes with graphene oxide nanosheets: Balancing membrane performance and fouling propensity', *Desalination*, vol. 451, pp. 139-47.
- Ismail, A.F., Padaki, M., Hilal, N., Matsuura, T. & Lau, W.J. 2015, 'Thin film composite membrane — Recent development and future potential', *Desalination*, vol. 356, pp. 140-8.
- Itel, F., Najer, A., Palivan, C.G. & Meier, W. 2015, 'Dynamics of membrane proteins within synthetic polymer membranes with large hydrophobic mismatch', *Nano Letters*, vol. 15, no. 6, pp. 3871-8.

- Jeong, B.-H., Hoek, E.M.V., Yan, Y., Subramani, A., Huang, X., Hurwitz, G., Ghosh, A.K. & Jawor, A. 2007a, 'Interfacial polymerization of thin film nanocomposites: A new concept for reverse osmosis membranes', *Journal of Membrane Science*, vol. 294, no. 1, pp. 1-7.
- Jeong, B.H., Hoek, E.M.V., Yan, Y., Subramani, A., Huang, X., Hurwitz, G., Ghosh, A.K. & Jawor, A. 2007b, 'Interfacial polymerization of thin film nanocomposites: A new concept for reverse osmosis membranes', *Journal of Membrane Science*, vol. 294, no. 1, pp. 1-7.
- Jia, Y.-x., Li, H.-l., Wang, M., Wu, L.-y. & Hu, Y.-d. 2010, 'Carbon nanotube: Possible candidate for forward osmosis', *Separation and Purification Technology*, vol. 75, no. 1, pp. 55-60.
- Jin, H., Huang, Y., Li, H., Yu, P. & Luo, Y. 2015, 'Fabrication of BaSO<sub>4</sub>-based mineralized thin-film composite polysulfone/polyamide membranes for enhanced performance in a forward osmosis process', *RSC Advances*, vol. 5, no. 97, pp. 79774-82.
- Jin, H., Rivers, F., Yin, H., Lai, T., Cay-Durgun, P., Khosravi, A., Lind, M.L. & Yu, P. 2017, 'Synthesis of AgCl mineralized thin film composite polyamide membranes to enhance performance and antifouling properties in forward osmosis', *Industrial & Engineering Chemistry Research*, vol. 56, no. 4, pp. 1064-73.
- Jin, L., Wang, Z., Zheng, S. & Mi, B. 2018a, 'Polyamide-crosslinked graphene oxide membrane for forward osmosis', *Journal of Membrane Science*, vol. 545, no. Supplement C, pp. 11-8.
- Jin, L.M., Wang, Z.Y., Zheng, S.X. & Mi, B.X. 2018b, 'Polyamide-crosslinked graphene oxide membrane for forward osmosis', *Journal of Membrane Science*, vol. 545, pp. 11-8.
- Jin, X., She, Q., Ang, X. & Tang, C.Y. 2012, 'Removal of boron and arsenic by forward osmosis membrane: Influence of membrane orientation and organic fouling', *Journal of Membrane Science*, vol. 389, pp. 182-7.
- Jirjis, B.F. & Luque, S. 2010, 'Chapter 9 - Practical aspects of membrane system design in food and bioprocessing applications', in Z.F. Cui & H.S. Muralidhara (eds), *Membrane Technology*, Butterworth-Heinemann, Oxford, pp. 179-212.
- Kang, Y., Obaid, M., Jang, J. & Kim, I.S. 2019, 'Sulfonated graphene oxide incorporated thin film nanocomposite nanofiltration membrane to enhance permeation and antifouling properties', *Desalination*, vol. 470, p. 114125.
- Karan, S., Jiang, Z. & Livingston, A.G. 2015, 'Sub-10 nm polyamide nanofilms with ultrafast solvent transport for molecular separation', *Science*, vol. 348, no. 6241, pp. 1347-51.
- Kasik, A. & Lin, Y.S. 2014, 'Organic solvent pervaporation properties of MOF-5 membranes', *Separation and Purification Technology*, vol. 121, no. Supplement C, pp. 38-45.
- Khorshidi, B., Thundat, T., Fleck, B.A. & Sadrzadeh, M. 2015, 'Thin film composite polyamide membranes: parametric study on the influence of synthesis conditions', *RSC Advances*, vol. 5, no. 68, pp. 54985-97.
- Kim, B., Gwak, G. & Hong, S. 2017, 'Review on methodology for determining forward osmosis (FO) membrane characteristics: Water permeability (A), solute permeability (B), and structural parameter (S)', *Desalination*, vol. 422, pp. 5-16.
- Kim, H.J., Choi, K., Baek, Y., Kim, D.-G., Shim, J., Yoon, J. & Lee, J.-C. 2014, 'High-performance reverse osmosis CNT/polyamide nanocomposite membrane by controlled interfacial interactions', *ACS Applied Materials & Interfaces*, vol. 6, no. 4, pp. 2819-29.

- Kim, I.C., Ka, Y.H., Park, J.Y. & Lee, K.H. 2004, 'Preparation of fouling resistant nanofiltration and reverse osmosis membranes and their use for dyeing wastewater effluent', *Journal of Industrial and Engineering Chemistry*, vol. 10, no. 1, pp. 115-21.
- Kim, J.E., Kuntz, J., Jang, A., Kim, I.S., Choi, J.Y., Phuntsho, S. & Shon, H.K. 2019, 'Techno-economic assessment of fertiliser drawn forward osmosis process for greenwall plants from urban wastewater', *Process Safety and Environmental Protection*, vol. 127, pp. 180-8.
- Kim, S.G., Hyeon, D.H., Chun, J.H., Chun, B.-H. & Kim, S.H. 2013, 'Novel thin nanocomposite RO membranes for chlorine resistance', *Desalination and Water Treatment*, vol. 51, no. 31-33, pp. 6338-45.
- Klaysom, C., Cath, T.Y., Depuydt, T. & Vankelecom, I.F. 2013, 'Forward and pressure retarded osmosis: potential solutions for global challenges in energy and water supply', *Chem Soc Rev*, vol. 42, no. 16, pp. 6959-89.
- Klaysom, C., Hermans, S., Gahlaut, A., Van Craenenbroeck, S. & Vankelecom, I.F.J. 2013, 'Polyamide/Polyacrylonitrile (PA/PAN) thin film composite osmosis membranes: Film optimization, characterization and performance evaluation', *Journal of Membrane Science*, vol. 445, pp. 25-33.
- Kolev, V. & Freger, V. 2014, 'Hydration, porosity and water dynamics in the polyamide layer of reverse osmosis membranes: A molecular dynamics study', *Polymer*, vol. 55, no. 6, pp. 1420-6.
- Kong, C., koushima, A., Kamada, T., Shintani, T., Kanezashi, M., Yoshioka, T. & Tsuru, T. 2011, 'Enhanced performance of inorganic-polyamide nanocomposite membranes prepared by metal-alkoxide-assisted interfacial polymerization', *Journal of Membrane Science*, vol. 366, no. 1-2, pp. 382-8.
- Kresge, C.T., Leonowicz, M.E., Roth, W.J., Vartuli, J.C. & Beck, J.S. 1992, 'Ordered mesoporous molecular sieves synthesized by a liquid-crystal template mechanism', *Nature*, vol. 359, p. 710.
- Kuang, W., Liu, Z., Yu, H., Kang, G., Jie, X., Jin, Y. & Cao, Y. 2016, 'Investigation of internal concentration polarization reduction in forward osmosis membrane using nano-CaCO<sub>3</sub> particles as sacrificial component', *Journal of Membrane Science*, vol. 497, no. Supplement C, pp. 485-93.
- Kumar, M., Grzelakowski, M., Zilles, J., Clark, M. & Meier, W. 2007, 'Highly permeable polymeric membranes based on the incorporation of the functional water channel protein Aquaporin Z', *Proceedings of the National Academy of Sciences*, vol. 104, no. 52, pp. 20719-24.
- Kumar, R., Al-Jabli, H., Al-Haddad, S., Al-Rughaib, M. & Samuel, J. 2017, 'Modified titanate nanotubes incorporated polyamide layer for the fabrication of fouling control thin-film nanocomposite forward osmosis membranes', *Desalination and Water Treatment*, vol. 69, pp. 56-64.
- Lai, G.S., Lau, W.J., Goh, P.S., Ismail, A.F., Tan, Y.H., Chong, C.Y., Krause-Rehberg, R. & Awad, S. 2018, 'Tailor-made thin film nanocomposite membrane incorporated with graphene oxide using novel interfacial polymerization technique for enhanced water separation', *Chemical Engineering Journal*, vol. 344, pp. 524-34.
- Lai, G.S., Lau, W.J., Goh, P.S., Ismail, A.F., Yusof, N. & Tan, Y.H. 2016, 'Graphene oxide incorporated thin film nanocomposite nanofiltration membrane for enhanced salt removal performance', *Desalination*, vol. 387, no. Supplement C, pp. 14-24.
- Lai, G.S., Lau, W.J., Goh, P.S., Tan, Y.H., Ng, B.C. & Ismail, A.F. 2019, 'A novel interfacial polymerization approach towards synthesis of graphene oxide-

- incorporated thin film nanocomposite membrane with improved surface properties', *Arabian Journal of Chemistry*, vol. 12, no. 1, pp. 75-87.
- Lai, G.S., Lau, W.J., Gray, S.R., Matsuura, T., Gohari, R.J., Subramanian, M.N., Lai, S.O., Ong, C.S., Ismail, A.F., Emazadah, D. & Ghanbari, M. 2016, 'A practical approach to synthesize polyamide thin film nanocomposite (TFN) membranes with improved separation properties for water/wastewater treatment', *Journal of Materials Chemistry A*, vol. 4, no. 11, pp. 4134-44.
- Lau, W.J., Gray, S., Matsuura, T., Emadzadeh, D., Paul Chen, J. & Ismail, A.F. 2015, 'A review on polyamide thin film nanocomposite (TFN) membranes: History, applications, challenges and approaches', *Water Research*, vol. 80, pp. 306-24.
- Lau, W.J., Ismail, A.F., Goh, P.S., Hilal, N. & Ooi, B.S. 2015, 'Characterization methods of thin film composite nanofiltration membranes', *Separation & Purification Reviews*, vol. 44, no. 2, pp. 135-56.
- Le, N.L. & Nunes, S.P. 2016, 'Materials and membrane technologies for water and energy sustainability', *Sustainable Materials and Technologies*, vol. 7, pp. 1-28.
- Lee, E.-J., An, A.K., He, T., Woo, Y.C. & Shon, H.K. 2016, 'Electrospun nanofiber membranes incorporating fluorosilane-coated TiO<sub>2</sub> nanocomposite for direct contact membrane distillation', *Journal of Membrane Science*, vol. 520, no. Supplement C, pp. 145-54.
- Lee, J.-Y., Qi, S., Liu, X., Li, Y., Huo, F. & Tang, C.Y. 2014, 'Synthesis and characterization of silica gel–polyacrylonitrile mixed matrix forward osmosis membranes based on layer-by-layer assembly', *Separation and Purification Technology*, vol. 124, pp. 207-16.
- Lee, J.-Y., She, Q., Huo, F. & Tang, C.Y. 2015, 'Metal–organic framework-based porous matrix membranes for improving mass transfer in forward osmosis membranes', *Journal of Membrane Science*, vol. 492, pp. 392-9.
- Lee, J.-Y., Wang, Y., Tang, C.Y. & Huo, F. 2015, 'Mesoporous silica gel–based mixed matrix membranes for improving mass transfer in forward osmosis: Effect of pore size of filler', *Scientific reports*, vol. 5.
- Lee, K.L., Baker, R.W. & Lonsdale, H.K. 1981, 'Membranes for power generation by pressure-retarded osmosis', *Journal of Membrane Science*, vol. 8, no. 2, pp. 141-71.
- Lee, K.P., Arnot, T.C. & Mattia, D. 2011, 'A review of reverse osmosis membrane materials for desalination—Development to date and future potential', *Journal of Membrane Science*, vol. 370, no. 1, pp. 1-22.
- Lee, W.J., Goh, P.S., Lau, W.J., Ong, C.S. & Ismail, A.F. 2018, 'Antifouling zwitterion embedded forward osmosis thin film composite membrane for highly concentrated oily wastewater treatment', *Separation and Purification Technology*.
- Li, C., Li, S., Tian, L., Zhang, J., Su, B. & Hu, M.Z. 2019, 'Covalent organic frameworks (COFs)-incorporated thin film nanocomposite (TFN) membranes for high-flux organic solvent nanofiltration (OSN)', *Journal of Membrane Science*, vol. 572, pp. 520-31.
- Li, D., Yan, Y. & Wang, H. 2016, 'Recent advances in polymer and polymer composite membranes for reverse and forward osmosis processes', *Progress in Polymer Science*, vol. 61, pp. 104-55.
- Li, J.-R., Sculley, J. & Zhou, H.-C. 2012, 'Metal–organic frameworks for separations', *Chemical Reviews*, vol. 112, no. 2, pp. 869-932.
- Li, X., Sotto, A., Li, J. & Van der Bruggen, B. 2017, 'Progress and perspectives for synthesis of sustainable antifouling composite membranes containing in situ generated nanoparticles', *Journal of Membrane Science*, vol. 524, pp. 502-28.

- Li, X., Wang, K.Y., Helmer, B. & Chung, T.-S. 2012, 'Thin-film composite membranes and formation mechanism of thin-film layers on hydrophilic cellulose acetate propionate substrates for forward osmosis processes', *Industrial & Engineering Chemistry Research*, vol. 51, no. 30, pp. 10039-50.
- Li, Y., Li, S. & Zhang, K. 2017, 'Influence of hydrophilic carbon dots on polyamide thin film nanocomposite reverse osmosis membranes', *Journal of Membrane Science*, vol. 537, pp. 42-53.
- Li, Y., Qi, S., Tian, M., Widjajanti, W. & Wang, R. 2019, 'Fabrication of aquaporin-based biomimetic membrane for seawater desalination', *Desalination*, vol. 467, pp. 103-12.
- Li, Z.-Y., Yangali-Quintanilla, V., Valladares-Linares, R., Li, Q., Zhan, T. & Amy, G. 2012, 'Flux patterns and membrane fouling propensity during desalination of seawater by forward osmosis', *Water Research*, vol. 46, no. 1, pp. 195-204.
- Lim, S., Akther, N., Tran, V.H., Bae, T.-H., Phuntsho, S., Merenda, A., Dumée, L.F. & Shon, H.K. 2020, 'Covalent organic framework incorporated outer-selective hollow fiber thin-film nanocomposite membranes for osmotically driven desalination', *Desalination*, vol. 485, p. 114461.
- Lim, S., Park, K.H., Tran, V.H., Akther, N., Phuntsho, S., Choi, J.Y. & Shon, H.K. 2020a, 'Size-controlled graphene oxide for highly permeable and fouling-resistant outer-selective hollow fiber thin-film composite membranes for forward osmosis', *Journal of Membrane Science*, vol. 609, p. 118171.
- Lim, S., Park, K.H., Tran, V.H., Akther, N., Phuntsho, S., Choi, J.Y. & Shon, H.K. 2020b, 'Size-controlled graphene oxide for highly permeable and fouling-resistant outer-selective hollow fiber thin-film composite membranes for forward osmosis', *Journal of Membrane Science*, p. 118171.
- Lim, S., Park, M.J., Phuntsho, S., Tijing, L.D., Nisola, G.M., Shim, W.-G., Chung, W.-J. & Shon, H.K. 2017, 'Dual-layered nanocomposite substrate membrane based on polysulfone/graphene oxide for mitigating internal concentration polarization in forward osmosis', *Polymer*, vol. 110, no. Supplement C, pp. 36-48.
- Lim, S., Tran, V.H., Akther, N., Phuntsho, S. & Shon, H.K. 2019, 'Defect-free outer-selective hollow fiber thin-film composite membranes for forward osmosis applications', *Journal of Membrane Science*, vol. 586, pp. 281-91.
- Lind, M.L., Ghosh, A.K., Jawor, A., Huang, X., Hou, W., Yang, Y. & Hoek, E.M.V. 2009, 'Influence of zeolite crystal size on zeolite-polyamide thin film nanocomposite membranes', *Langmuir*, vol. 25, no. 17, pp. 10139-45.
- Liu, G., Jin, W. & Xu, N. 2015, 'Graphene-based membranes', *Chemical Society Reviews*, vol. 44, no. 15, pp. 5016-30.
- Liu, M., Chen, Q., Wang, L., Yu, S. & Gao, C. 2015, 'Improving fouling resistance and chlorine stability of aromatic polyamide thin-film composite RO membrane by surface grafting of polyvinyl alcohol (PVA)', *Desalination*, vol. 367, pp. 11-20.
- Liu, Q., Li, J., Zhou, Z., Xie, J. & Lee, J.Y. 2016, 'Hydrophilic mineral coating of membrane substrate for reducing internal concentration polarization (ICP) in forward osmosis', *Scientific Reports*, vol. 6.
- Liu, Q. & Xu, G.-R. 2016, 'Graphene oxide (GO) as functional material in tailoring polyamide thin film composite (PA-TFC) reverse osmosis (RO) membranes', *Desalination*, vol. 394, pp. 162-75.
- Liu, S., Hu, M., Zeng, T.H., Wu, R., Jiang, R., Wei, J., Wang, L., Kong, J. & Chen, Y. 2012, 'Lateral dimension-dependent antibacterial activity of graphene oxide sheets', *Langmuir*, vol. 28, no. 33, pp. 12364-72.

- Liu, X.-L., Li, Y.-S., Zhu, G.-Q., Ban, Y.-J., Xu, L.-Y. & Yang, W.-S. 2011, 'An organophilic pervaporation membrane derived from metal–organic framework nanoparticles for efficient recovery of bio-alcohols', *Angewandte Chemie International Edition*, vol. 50, no. 45, pp. 10636-9.
- Liu, X. & Ng, H.Y. 2015, 'Fabrication of layered silica–polysulfone mixed matrix substrate membrane for enhancing performance of thin-film composite forward osmosis membrane', *Journal of Membrane Science*, vol. 481, pp. 148-63.
- Liyanaarachchi, S., Shu, L., Muthukumar, S., Jegatheesan, V. & Baskaran, K. 2014, 'Problems in seawater industrial desalination processes and potential sustainable solutions: A review', *Reviews in Environmental Science and Bio/Technology*, vol. 13, no. 2, pp. 203-14.
- Low, Z.X., Liu, Q., Shamsaei, E., Zhang, X. & Wang, H. 2015, 'Preparation and characterization of thin-film composite membrane with nanowire-modified support for forward osmosis process', *Membranes*, vol. 5, no. 1, p. 136.
- Lu, P., Gao, Y., Umar, A., Zhou, T., Wang, J., Zhang, Z., Huang, L. & Wang, Q. 2015, 'Recent advances in cellulose-based forward osmosis membrane', *Science of Advanced Materials*, vol. 7, no. 10, pp. 2182-92.
- Lu, P., Liang, S., Qiu, L., Gao, Y. & Wang, Q. 2016, 'Thin film nanocomposite forward osmosis membranes based on layered double hydroxide nanoparticles blended substrates', *Journal of Membrane Science*, vol. 504, pp. 196-205.
- Lu, P., Liang, S., Zhou, T., Mei, X., Zhang, Y., Zhang, C., Umar, A. & Wang, Q. 2016, 'Layered double hydroxide/graphene oxide hybrid incorporated polysulfone substrate for thin-film nanocomposite forward osmosis membranes', *RSC Advances*, vol. 6, no. 61, pp. 56599-609.
- Lu, P., Liang, S., Zhou, T., Xue, T., Mei, X. & Wang, Q. 2017, 'Layered double hydroxide nanoparticle modified forward osmosis membranes via polydopamine immobilization with significantly enhanced chlorine and fouling resistance', *Desalination*.
- Lu, X., Arias Chavez, L.H., Romero-Vargas Castrillón, S., Ma, J. & Elimelech, M. 2015, 'Influence of active layer and support layer surface structures on organic fouling propensity of thin-film composite forward osmosis membranes', *Environmental Science & Technology*, vol. 49, no. 3, pp. 1436-44.
- Luo, H., Wang, Q., Zhang, T.C., Tao, T., Zhou, A., Chen, L. & Bie, X. 2014, 'A review on the recovery methods of draw solutes in forward osmosis', *Journal of Water Process Engineering*, vol. 4, pp. 212-23.
- Lutchmiah, K., Verliefde, A.R.D., Roest, K., Rietveld, L.C. & Cornelissen, E.R. 2014, 'Forward osmosis for application in wastewater treatment: A review', *Water Research*, vol. 58, pp. 179-97.
- Ly, Q.V., Hu, Y., Li, J., Cho, J. & Hur, J. 2019, 'Characteristics and influencing factors of organic fouling in forward osmosis operation for wastewater applications: A comprehensive review', *Environment International*, vol. 129, pp. 164-84.
- Ma, D., Han, G., Peh, S.B. & Chen, S.B. 2017, 'Water-Stable Metal–Organic Framework UiO-66 for Performance Enhancement of Forward Osmosis Membranes', *Industrial & Engineering Chemistry Research*, vol. 56, no. 44, pp. 12773-82.
- Ma, D., Peh, S.B., Han, G. & Chen, S.B. 2017, 'Thin-film nanocomposite (TFN) membranes incorporated with super-hydrophilic metal–organic framework (MOF) UiO-66: Toward enhancement of water flux and salt rejection', *ACS Applied Materials & Interfaces*, vol. 9, no. 8, pp. 7523-34.
- Ma, J., Ping, D. & Dong, X. 2017, 'Recent developments of graphene oxide-based membranes: A review', *Membranes*, vol. 7, no. 3, p. 52.

- Ma, J., Zhao, Y., Xu, Z., Min, C., Zhou, B., Li, Y., Li, B. & Niu, J. 2013, 'Role of oxygen-containing groups on MWCNTs in enhanced separation and permeability performance for PVDF hybrid ultrafiltration membranes', *Desalination*, vol. 320, pp. 1-9.
- Ma, N., Wei, J., Liao, R. & Tang, C.Y. 2012, 'Zeolite-polyamide thin film nanocomposite membranes: Towards enhanced performance for forward osmosis', *Journal of Membrane Science*, vol. 405, pp. 149-57.
- Ma, N., Wei, J., Qi, S., Zhao, Y., Gao, Y. & Tang, C.Y. 2013, 'Nanocomposite substrates for controlling internal concentration polarization in forward osmosis membranes', *Journal of Membrane Science*, vol. 441, no. Supplement C, pp. 54-62.
- Maddah, H. & Chogle, A. 2017, 'Biofouling in reverse osmosis: Phenomena, monitoring, controlling and remediation', *Applied Water Science*, vol. 7, no. 6, pp. 2637-51.
- Mahmoud, K.A., Mansoor, B., Mansour, A. & Khraisheh, M. 2015, 'Functional graphene nanosheets: The next generation membranes for water desalination', *Desalination*, vol. 356, no. Supplement C, pp. 208-25.
- Mansur, H.S., Sadahira, C.M., Souza, A.N. & Mansur, A.A.P. 2008, 'FTIR spectroscopy characterization of poly (vinyl alcohol) hydrogel with different hydrolysis degree and chemically crosslinked with glutaraldehyde', *Materials Science and Engineering: C*, vol. 28, no. 4, pp. 539-48.
- Marchetti, P., Jimenez Solomon, M.F., Szekely, G. & Livingston, A.G. 2014, 'Molecular separation with organic solvent nanofiltration: a critical review', *Chem Rev*, vol. 114, no. 21, pp. 10735-806.
- Martinetti, C.R., Childress, A.E. & Cath, T.Y. 2009, 'High recovery of concentrated RO brines using forward osmosis and membrane distillation', *Journal of Membrane Science*, vol. 331, no. 1-2, pp. 31-9.
- Mattia, D., Lee, K.P. & Calabrò, F. 2014, 'Water permeation in carbon nanotube membranes', *Current Opinion in Chemical Engineering*, vol. 4, pp. 32-7.
- McCutcheon, J.R. & Elimelech, M. 2006, 'Influence of concentrative and dilutive internal concentration polarization on flux behavior in forward osmosis', *Journal of Membrane Science*, vol. 284, no. 1, pp. 237-47.
- Mccutcheon, J.R. & Elimelech, M. 2007, 'Modeling water flux in forward osmosis: Implications for improved membrane design', *AIChE Journal*, vol. 53, no. 7, pp. 1736-44.
- McCutcheon, J.R., McGinnis, R.L. & Elimelech, M. 2005, 'A novel ammonia-carbon dioxide forward (direct) osmosis desalination process', *Desalination*, vol. 174, no. 1, pp. 1-11.
- McGovern, R.K. & Lienhard V, J.H. 2014, 'On the potential of forward osmosis to energetically outperform reverse osmosis desalination', *Journal of Membrane Science*, vol. 469, pp. 245-50.
- McLeary, E.E., Jansen, J.C. & Kapteijn, F. 2006, 'Zeolite based films, membranes and membrane reactors: Progress and prospects', *Microporous and Mesoporous Materials*, vol. 90, no. 1, pp. 198-220.
- Melián-Martel, N., Sadhwani Alonso, J.J. & Ruiz-García, A. 2018, 'Combined silica and sodium alginate fouling of spiral-wound reverse osmosis membranes for seawater desalination', *Desalination*, vol. 439, pp. 25-30.
- Mi, B. & Elimelech, M. 2010, 'Organic fouling of forward osmosis membranes: Fouling reversibility and cleaning without chemical reagents', *Journal of Membrane Science*, vol. 348, no. 1, pp. 337-45.
- Morales-Torres, S., Esteves, C.M.P., Figueiredo, J.L. & Silva, A.M.T. 2016, 'Thin-film composite forward osmosis membranes based on polysulfone supports blended

- with nanostructured carbon materials', *Journal of Membrane Science*, vol. 520, pp. 326-36.
- Motsa, M.M., Mamba, B.B., D'Haese, A., Hoek, E.M.V. & Verliefde, A.R.D. 2014, 'Organic fouling in forward osmosis membranes: The role of feed solution chemistry and membrane structural properties', *Journal of Membrane Science*, vol. 460, no. Supplement C, pp. 99-109.
- Mozia, S. 2010, 'Photocatalytic membrane reactors (PMRs) in water and wastewater treatment. A review', *Separation and Purification Technology*, vol. 73, no. 2, pp. 71-91.
- Niksefat, N., Jahanshahi, M. & Rahimpour, A. 2014, 'The effect of SiO<sub>2</sub> nanoparticles on morphology and performance of thin film composite membranes for forward osmosis application', *Desalination*, vol. 343, no. Supplement C, pp. 140-6.
- Nisola, G.M., Limjuco, L.A., Vivas, E.L., Lawagon, C.P., Park, M.J., Shon, H.K., Mittal, N., Nah, I.W., Kim, H. & Chung, W.-J. 2015, 'Macroporous flexible polyvinyl alcohol lithium adsorbent foam composite prepared via surfactant blending and cryo-desiccation', *Chemical Engineering Journal*, vol. 280, pp. 536-48.
- Nussinov, Z. & van den Brink, J. 2015, 'Compass models: Theory and physical motivations', *Reviews of Modern Physics*, vol. 87, no. 1, pp. 1-59.
- Obaid, M., Ghouri, Z.K., Fadali, O.A., Khalil, K.A., Almajid, A.A. & Barakat, N.A.M. 2016, 'Amorphous SiO<sub>2</sub> NP-incorporated poly(vinylidene fluoride) electrospun nanofiber membrane for high flux forward osmosis desalination', *ACS Applied Materials & Interfaces*, vol. 8, no. 7, pp. 4561-74.
- Ong, R.C., Chung, T.-S., de Wit, J.S. & Helmer, B.J. 2015, 'Novel cellulose ester substrates for high performance flat-sheet thin-film composite (TFC) forward osmosis (FO) membranes', *Journal of Membrane Science*, vol. 473, pp. 63-71.
- Pan, Y.-H., Zhao, Q.-Y., Gu, L. & Wu, Q.-Y. 2017, 'Thin film nanocomposite membranes based on imogolite nanotubes blended substrates for forward osmosis desalination', *Desalination*, vol. 421, pp. 160-8.
- Pang, J., Kang, Z., Wang, R., Xu, B., Nie, X., Fan, L., Zhang, F., Du, X., Feng, S. & Sun, D. 2019, 'Exploring the sandwich antibacterial membranes based on UiO-66/graphene oxide for forward osmosis performance', *Carbon*, vol. 144, pp. 321-32.
- Park, M.J., Phuntsho, S., He, T., Nisola, G.M., Tijging, L.D., Li, X.-M., Chen, G., Chung, W.-J. & Shon, H.K. 2015, 'Graphene oxide incorporated polysulfone substrate for the fabrication of flat-sheet thin-film composite forward osmosis membranes', *Journal of Membrane Science*, vol. 493, pp. 496-507.
- Pendergast, M.M., Ghosh, A.K. & Hoek, E.M.V. 2013, 'Separation performance and interfacial properties of nanocomposite reverse osmosis membranes', *Desalination*, vol. 308, no. Supplement C, pp. 180-5.
- Peng, F., Jiang, Z. & Hoek, E.M.V. 2011, 'Tuning the molecular structure, separation performance and interfacial properties of poly(vinyl alcohol)-polysulfone interfacial composite membranes', *Journal of Membrane Science*, vol. 368, no. 1, pp. 26-33.
- Perera, M.G.N., Galagedara, Y.R., Ren, Y., Jayaweera, M., Zhao, Y. & Weerasooriya, R. 2018, 'Fabrication of fullerenol-incorporated thin-film nanocomposite forward osmosis membranes for improved desalination performances', *Journal of Polymer Research*, vol. 25, no. 9, p. 199.
- Perreault, F., Jaramillo, H., Xie, M., Ude, M., Nghiem, L.D. & Elimelech, M. 2016, 'Biofouling mitigation in forward osmosis using graphene oxide functionalized thin-film composite membranes', *Environmental Science & Technology*, vol. 50, no. 11, pp. 5840-8.



- Perreault, F., Tousley, M.E. & Elimelech, M. 2014, 'Thin-film composite polyamide membranes functionalized with biocidal graphene oxide nanosheets', *Environmental Science & Technology Letters*, vol. 1, no. 1, pp. 71-6.
- Petrotos, K.B. & Lazarides, H.N. 2001, 'Osmotic concentration of liquid foods', *Journal of Food Engineering*, vol. 49, no. 2, pp. 201-6.
- Phuntsho, S., Shon, H.K., Majeed, T., El Saliby, I., Vigneswaran, S., Kandasamy, J., Hong, S. & Lee, S. 2012, 'Blended Fertilizers as Draw Solutions for Fertilizer-Drawn Forward Osmosis Desalination', *Environmental Science & Technology*, vol. 46, no. 8, pp. 4567-75.
- Qi, L., Hu, Y., Liu, Z., An, X. & Bar-Zeev, E. 2018, 'Improved anti-biofouling performance of thin -film composite forward-osmosis membranes containing passive and active moieties', *Environmental Science & Technology*, vol. 52, no. 17, pp. 9684-93.
- Qi, S., Fang, W., Siti, W., Widjajanti, W., Hu, X. & Wang, R. 2018, 'Polymersomes-based high-performance reverse osmosis membrane for desalination', *Journal of Membrane Science*, vol. 555, pp. 177-84.
- Qian, Y., Zhang, X., Liu, C., Zhou, C. & Huang, A. 2019, 'Tuning interlayer spacing of graphene oxide membranes with enhanced desalination performance', *Desalination*, vol. 460, pp. 56-63.
- Qin, D., Liu, Z., Delai Sun, D., Song, X. & Bai, H. 2015, 'A new nanocomposite forward osmosis membrane custom-designed for treating shale gas wastewater', *Scientific Reports*, vol. 5, p. 14530.
- Qiu, M. & He, C. 2018, 'Novel zwitterion-silver nanocomposite modified thin-film composite forward osmosis membrane with simultaneous improved water flux and biofouling resistance property', *Applied Surface Science*, vol. 455, pp. 492-501.
- Quist-Jensen, C.A., Macedonio, F. & Drioli, E. 2015, 'Membrane technology for water production in agriculture: Desalination and wastewater reuse', *Desalination*, vol. 364, pp. 17-32.
- Rahimpour, A., Jahanshahi, M., Khalili, S., Mollahosseini, A., Zirepour, A. & Rajaeian, B. 2012, 'Novel functionalized carbon nanotubes for improving the surface properties and performance of polyethersulfone (PES) membrane', *Desalination*, vol. 286, no. Supplement C, pp. 99-107.
- Rahimpour, A., Seyedpour, S.F., Aghapour Aktij, S., Dadashi Firouzjaei, M., Zirehpour, A., Arabi Shamsabadi, A., Khoshhal Salestan, S., Jabbari, M. & Soroush, M. 2018, 'Simultaneous improvement of antimicrobial, antifouling, and transport properties of forward osmosis membranes with immobilized highly-compatible polyrhodanine nanoparticles', *Environmental Science & Technology*, vol. 52, no. 9, pp. 5246-58.
- Ramezani Darabi, R., Jahanshahi, M. & Peyravi, M. 2018, 'A support assisted by photocatalytic Fe<sub>3</sub>O<sub>4</sub>/ZnO nanocomposite for thin-film forward osmosis membrane', *Chemical Engineering Research and Design*, vol. 133, pp. 11-25.
- Rastgar, M., Shakeri, A., Bozorg, A., Salehi, H. & Saadattalab, V. 2017, 'Impact of nanoparticles surface characteristics on pore structure and performance of forward osmosis membranes', *Desalination*, vol. 421, no. Supplement C, pp. 179-89.
- Rastgar, M., Shakeri, A., Bozorg, A., Salehi, H. & Saadattalab, V. 2018, 'Highly-efficient forward osmosis membrane tailored by magnetically responsive graphene oxide/Fe<sub>3</sub>O<sub>4</sub> nanohybrid', *Applied Surface Science*, vol. 441, pp. 923-35.
- Razmjou, A., Arifin, E., Dong, G., Mansouri, J. & Chen, V. 2012, 'Superhydrophobic modification of TiO<sub>2</sub> nanocomposite PVDF membranes for applications in membrane distillation', *Journal of Membrane Science*, vol. 415-416, no. Supplement C, pp. 850-63.

- Ren, J. & McCutcheon, J.R. 2014, 'A new commercial thin film composite membrane for forward osmosis', *Desalination*, vol. 343, pp. 187-93.
- Rezaei-DashtArzhandi, M., Sarrafzadeh, M.H., Goh, P.S., L{Rezaei-DashtArzhandi, a., W. J., Ismail, A.F. & Mohamed, M.A. 2018, 'Development of novel thin film nanocomposite forward osmosis membranes containing halloysite/graphitic carbon nitride nanoparticles towards enhanced desalination performance', *Desalination*, vol. 447, pp. 18-28.
- Rezaei-DashtArzhandi, M., Sarrafzadeh, M.H., Goh, P.S., Lau, W.J., Ismail, A.F., Wong, K.C. & Mohamed, M.A. 2020, 'Enhancing the desalination performance of forward osmosis membrane through the incorporation of green nanocrystalline cellulose and halloysite dual nanofillers', *Journal of Chemical Technology & Biotechnology*, vol. 95, no. 9, pp. 2359-70.
- Robeson, L.M. 1991, 'Correlation of separation factor versus permeability for polymeric membranes', *Journal of Membrane Science*, vol. 62, no. 2, pp. 165-85.
- Safarpour, M., Khataee, A. & Vatanpour, V. 2015, 'Thin film nanocomposite reverse osmosis membrane modified by reduced graphene oxide/TiO<sub>2</sub> with improved desalination performance', *Journal of Membrane Science*, vol. 489, no. Supplement C, pp. 43-54.
- Salehi, H., Rastgar, M. & Shakeri, A. 2017, 'Anti-fouling and high water permeable forward osmosis membrane fabricated via layer by layer assembly of chitosan/graphene oxide', *Applied Surface Science*, vol. 413, no. Supplement C, pp. 99-108.
- Salehian, P. & Chung, T.-S. 2017, 'Thermally treated ammonia functionalized graphene oxide/polyimide membranes for pervaporation dehydration of isopropanol', *Journal of Membrane Science*, vol. 528, pp. 231-42.
- Salestan, S.K., Seyedpour, S.F., Rahimpour, A., Shamsabadi, A.A., Tiraferri, A. & Soroush, M. 2020, 'Molecular dynamics insights into the structural and water transport properties of a forward osmosis polyamide thin-film nanocomposite membrane modified with graphene quantum dots', *Industrial & Engineering Chemistry Research*, vol. 59, no. 32, pp. 14447-57.
- Sant'Anna, V., Marczak, L.D.F. & Tessaro, I.C. 2012, 'Membrane concentration of liquid foods by forward osmosis: Process and quality view', *Journal of Food Engineering*, vol. 111, no. 3, pp. 483-9.
- Sengur-Tasdemir, R., Aydin, S., Turken, T., Genceli, E.A. & Koyuncu, I. 2016, 'Biomimetic approaches for membrane technologies', *Separation & Purification Reviews*, vol. 45, no. 2, pp. 122-40.
- Seyedpour, S.F., Rahimpour, A., Shamsabadi, A.A. & Soroush, M. 2018, 'Improved performance and antifouling properties of thin-film composite polyamide membranes modified with nano-sized bactericidal graphene quantum dots for forward osmosis', *Chemical Engineering Research and Design*, vol. 139, pp. 321-34.
- Shaffer, D.L., Werber, J.R., Jaramillo, H., Lin, S. & Elimelech, M. 2015, 'Forward osmosis: Where are we now?', *Desalination*, vol. 356, pp. 271-84.
- Shakeri, A., Razavi, R., Salehi, H., Fallahi, M. & Eghbalazar, T. 2019, 'Thin film nanocomposite forward osmosis membrane embedded with amine-functionalized ordered mesoporous silica', *Applied Surface Science*.
- Shannon, M.A., Bohn, P.W., Elimelech, M., Georgiadis, J.G., Mariñas, B.J. & Mayes, A.M. 2008, 'Science and technology for water purification in the coming decades', *Nature*, vol. 452, no. 7185, pp. 301-10.

- Sharma, A., Kumar, S., Tripathi, B., Singh, M. & Vijay, Y.K. 2009, 'Aligned CNT/Polymer nanocomposite membranes for hydrogen separation', *International Journal of Hydrogen Energy*, vol. 34, no. 9, pp. 3977-82.
- Shen, L., Xiong, S. & Wang, Y. 2016, 'Graphene oxide incorporated thin-film composite membranes for forward osmosis applications', *Chemical Engineering Science*, vol. 143, pp. 194-205.
- Shen, Q., Lin, Y., Kawabata, Y., Jia, Y., Zhang, P., Akther, N., Guan, K., Yoshioka, T., Shon, H. & Matsuyama, H. 2020a, 'Engineering heterostructured thin-film nanocomposite membrane with functionalized graphene oxide quantum dots (GOQD) for highly-efficient reverse osmosis', *ACS Applied Materials & Interfaces*, vol. 12, no. 34, pp. 38662-73.
- Shen, Q., Lin, Y., Kawabata, Y., Jia, Y., Zhang, P., Akther, N., Guan, K., Yoshioka, T., Shon, H. & Matsuyama, H. 2020b, 'Engineering heterostructured thin-film nanocomposite membrane with functionalized graphene oxide quantum dots (GOQD) for highly efficient reverse osmosis', *ACS Applied Materials & Interfaces*, vol. 12, no. 34, pp. 38662-73.
- Siddiqui, F.A., She, Q., Fane, A.G. & Field, R.W. 2018, 'Exploring the differences between forward osmosis and reverse osmosis fouling', *Journal of Membrane Science*, vol. 565, pp. 241-53.
- Sirinupong, T., Youravong, W., Tirawat, D., Lau, W.J., Lai, G.S. & Ismail, A.F. 2017, 'Synthesis and characterization of thin film composite membranes made of PSF-TiO<sub>2</sub>/GO nanocomposite substrate for forward osmosis applications', *Arabian Journal of Chemistry*.
- Song, X., Wang, L., Mao, L. & Wang, Z. 2016, 'Nanocomposite membrane with different carbon nanotubes location for nanofiltration and forward osmosis applications', *ACS Sustainable Chemistry & Engineering*, vol. 4, no. 6, pp. 2990-7.
- Song, X., Wang, L., Tang, C.Y., Wang, Z. & Gao, C. 2015, 'Fabrication of carbon nanotubes incorporated double-skinned thin film nanocomposite membranes for enhanced separation performance and antifouling capability in forward osmosis process', *Desalination*, vol. 369, pp. 1-9.
- Song, X., Zhou, Q., Zhang, T., Xu, H. & Wang, Z. 2016, 'Pressure-assisted preparation of graphene oxide quantum dot-incorporated reverse osmosis membranes: antifouling and chlorine resistance potentials', *Journal of Materials Chemistry A*, vol. 4, no. 43, pp. 16896-905.
- Soroush, A., Ma, W., Cyr, M., Rahaman, M.S., Asadishad, B. & Tufenkji, N. 2016, 'In situ silver decoration on graphene oxide-treated thin film composite forward osmosis membranes: Biocidal properties and regeneration potential', *Environmental Science & Technology Letters*, vol. 3, no. 1, pp. 13-8.
- Soroush, A., Ma, W., Silvino, Y. & Rahaman, M.S. 2015, 'Surface modification of thin film composite forward osmosis membrane by silver-decorated graphene-oxide nanosheets', *Environmental Science: Nano*, vol. 2, no. 4, pp. 395-405.
- Sorribas, S., Gorgojo, P., Téllez, C., Coronas, J. & Livingston, A.G. 2013, 'High Flux Thin Film Nanocomposite Membranes Based on Metal–Organic Frameworks for Organic Solvent Nanofiltration', *Journal of the American Chemical Society*, vol. 135, no. 40, pp. 15201-8.
- Spulber, M., Tvermoes, D.C., Gorecki, R. & Haugsted, F. 2019, *Vesicle incorporating transmembrane protein*, WO 2019/081371 A1.
- Stankovich, S., Dikin, D.A., Dommett, G.H.B., Kohlhaas, K.M., Zimney, E.J., Stach, E.A., Piner, R.D., Nguyen, S.T. & Ruoff, R.S. 2006, 'Graphene-based composite materials', *Nature*, vol. 442, p. 282.

- Subramani, A. & Jacangelo, J.G. 2015, 'Emerging desalination technologies for water treatment: A critical review', *Water Research*, vol. 75, pp. 164-87.
- Sukitpaneemit, P. & Chung, T.-S. 2012, 'High Performance Thin-Film Composite Forward Osmosis Hollow Fiber Membranes with Macrovoid-Free and Highly Porous Structure for Sustainable Water Production', *Environmental Science & Technology*, vol. 46, no. 13, pp. 7358-65.
- Sun, H. 1998, 'Compass: An ab initio force-field optimized for condensed-phase applications overview with details on alkane and benzene compounds', *The Journal of Physical Chemistry B*, vol. 102, no. 38, pp. 7338-64.
- Sun, H., Jin, Z., Yang, C., Akkermans, R.L.C., Robertson, S.H., Spensley, N.A., Miller, S. & Todd, S.M. 2016, 'COMPASS II: extended coverage for polymer and drug-like molecule databases', *Journal of Molecular Modeling*, vol. 22, no. 2, p. 47.
- Sun, H. & Wu, P. 2018, 'Tuning the functional groups of carbon quantum dots in thin film nanocomposite membranes for nanofiltration', *Journal of Membrane Science*, vol. 564, pp. 394-403.
- Sun, S.-P. & Chung, T.-S. 2013, 'Outer-Selective Pressure-Retarded Osmosis Hollow Fiber Membranes from Vacuum-Assisted Interfacial Polymerization for Osmotic Power Generation', *Environmental Science & Technology*, vol. 47, no. 22, pp. 13167-74.
- Sun, X., Liu, Z., Welsher, K., Robinson, J.T., Goodwin, A., Zaric, S. & Dai, H. 2008, 'Nano-graphene oxide for cellular imaging and drug delivery', *Nano Research*, vol. 1, no. 3, pp. 203-12.
- Tamai, Y., Tanaka, H. & Nakanishi, K. 1994, 'Molecular simulation of permeation of small penetrants through membranes. 1. Diffusion coefficients', *Macromolecules*, vol. 27, no. 16, pp. 4498-508.
- Tang, C., Wang, Z., Petrinić, I., Fane, A.G. & Hélix-Nielsen, C. 2015, 'Biomimetic aquaporin membranes coming of age', *Desalination*, vol. 368, pp. 89-105.
- Tang, C.Y., Kwon, Y.-N. & Leckie, J.O. 2009a, 'Effect of membrane chemistry and coating layer on physiochemical properties of thin film composite polyamide RO and NF membranes: I. FTIR and XPS characterization of polyamide and coating layer chemistry', *Desalination*, vol. 242, no. 1, pp. 149-67.
- Tang, C.Y., Kwon, Y.-N. & Leckie, J.O. 2009b, 'Effect of membrane chemistry and coating layer on physiochemical properties of thin film composite polyamide RO and NF membranes: II. Membrane physiochemical properties and their dependence on polyamide and coating layers', *Desalination*, vol. 242, no. 1, pp. 168-82.
- Tayyebi, A., Akhavan, O., Lee, B.-K. & Outokesh, M. 2018, 'Supercritical water in top-down formation of tunable-sized graphene quantum dots applicable in effective photothermal treatments of tissues', *Carbon*, vol. 130, pp. 267-72.
- Teow, Y.H. & Mohammad, A.W. 2019, 'New generation nanomaterials for water desalination: A review', *Desalination*, vol. 451, pp. 2-17.
- Thiruvenkatachari, R., Francis, M., Cunnington, M. & Su, S. 2016, 'Application of integrated forward and reverse osmosis for coal mine wastewater desalination', *Separation and Purification Technology*, vol. 163, pp. 181-8.
- Tian, M., Wang, Y.-N. & Wang, R. 2015, 'Synthesis and characterization of novel high-performance thin film nanocomposite (TFN) FO membranes with nanofibrous substrate reinforced by functionalized carbon nanotubes', *Desalination*, vol. 370, pp. 79-86.
- Tian, M., Wang, Y.-N., Wang, R. & Fane, A.G. 2017, 'Synthesis and characterization of thin film nanocomposite forward osmosis membranes supported by silica nanoparticle incorporated nanofibrous substrate', *Desalination*, vol. 401, pp. 142-50.

- Tiraferrri, A., Kang, Y., Giannelis, E.P. & Elimelech, M. 2012a, 'Highly hydrophilic thin-film composite forward osmosis membranes functionalized with surface-tailored nanoparticles', *ACS Applied Materials & Interfaces*, vol. 4, no. 9, pp. 5044-53.
- Tiraferrri, A., Kang, Y., Giannelis, E.P. & Elimelech, M. 2012b, 'Superhydrophilic thin-film composite forward osmosis membranes for organic fouling control: Fouling behavior and antifouling mechanisms', *Environmental Science & Technology*, vol. 46, no. 20, pp. 11135-44.
- Tiraferrri, A., Vecitis, C.D. & Elimelech, M. 2011, 'Covalent binding of single-walled carbon nanotubes to polyamide membranes for antimicrobial surface properties', *ACS Applied Materials & Interfaces*, vol. 3, no. 8, pp. 2869-77.
- Tiraferrri, A., Yip, N.Y., Straub, A.P., Romero-Vargas Castrillon, S. & Elimelech, M. 2013, 'A method for the simultaneous determination of transport and structural parameters of forward osmosis membranes', *Journal of Membrane Science*, vol. 444, no. Supplement C, pp. 523-38.
- Tiscornia, I., Kumakiri, I., Bredesen, R., Téllez, C. & Coronas, J. 2010, 'Microporous titanosilicate ETS-10 membrane for high pressure CO<sub>2</sub> separation', *Separation and Purification Technology*, vol. 73, no. 1, pp. 8-12.
- Tran, V.H., Lim, S., Han, D.S., Pathak, N., Akther, N., Phuntsho, S., Park, H. & Shon, H.K. 2019, 'Efficient fouling control using outer-selective hollow fiber thin-film composite membranes for osmotic membrane bioreactor applications', *Bioresource Technology*, vol. 282, pp. 9-17.
- Verkman, A.S. 2013, 'Aquaporins', *Current Biology*, vol. 23, no. 2, pp. R52-R5.
- Verkman, A.S. & Mitra, A.K. 2000, 'Structure and function of aquaporin water channels', *American Journal of Physiology-Renal Physiology*, vol. 278, no. 1, pp. F13-F28.
- Vos, K.D., Burris, F.O. & Riley, R.L. 1966, 'Kinetic study of the hydrolysis of cellulose acetate in the pH range of 2–10', *Journal of Applied Polymer Science*, vol. 10, no. 5, pp. 825-32.
- Wang, L., Song, X., Wang, T., Wang, S., Wang, Z. & Gao, C. 2015, 'Fabrication and characterization of polyethersulfone/carbon nanotubes (PES/CNTs) based mixed matrix membranes (MMMs) for nanofiltration application', *Applied Surface Science*, vol. 330, pp. 118-25.
- Wang, N., Ji, S., Li, J., Zhang, R. & Zhang, G. 2014, 'Poly(vinyl alcohol)–graphene oxide nanohybrid “pore-filling” membrane for pervaporation of toluene/n-heptane mixtures', *Journal of Membrane Science*, vol. 455, pp. 113-20.
- Wang, N., Ji, S., Zhang, G., Li, J. & Wang, L. 2012, 'Self-assembly of graphene oxide and polyelectrolyte complex nanohybrid membranes for nanofiltration and pervaporation', *Chemical Engineering Journal*, vol. 213, pp. 318-29.
- Wang, R., Jiang, G., Ding, Y., Wang, Y., Sun, X., Wang, X. & Chen, W. 2011, 'Photocatalytic activity of heterostructures based on TiO<sub>2</sub> and halloysite nanotubes', *ACS Applied Materials & Interfaces*, vol. 3, no. 10, pp. 4154-8.
- Wang, X., Zhao, Y., Yuan, B., Wang, Z., Li, X. & Ren, Y. 2016, 'Comparison of biofouling mechanisms between cellulose triacetate (CTA) and thin-film composite (TFC) polyamide forward osmosis membranes in osmotic membrane bioreactors', *Bioresource Technology*, vol. 202, no. Supplement C, pp. 50-8.
- Wang, Y., Li, X., Zhao, S., Fang, Z., Ng, D., Xie, C., Wang, H. & Xie, Z. 2019, 'Thin-Film Composite Membrane with Interlayer Decorated Metal–Organic Framework UiO-66 toward Enhanced Forward Osmosis Performance', *Industrial & Engineering Chemistry Research*, vol. 58, no. 1, pp. 195-206.

- Wang, Y., Ou, R., Ge, Q., Wang, H. & Xu, T. 2013a, 'Preparation of polyethersulfone/carbon nanotube substrate for high-performance forward osmosis membrane', *Desalination*, vol. 330, pp. 70-8.
- Wang, Y., Ou, R., Ge, Q., Wang, H. & Xu, T. 2013b, 'Preparation of polyethersulfone/carbon nanotube substrate for high-performance forward osmosis membrane', *Desalination*, vol. 330, no. Supplement C, pp. 70-8.
- Wang, Y., Ou, R., Wang, H. & Xu, T. 2015, 'Graphene oxide modified graphitic carbon nitride as a modifier for thin film composite forward osmosis membrane', *Journal of Membrane Science*, vol. 475, pp. 281-9.
- Wei, J., Qiu, C., Tang, C.Y., Wang, R. & Fane, A.G. 2011, 'Synthesis and characterization of flat-sheet thin film composite forward osmosis membranes', *Journal of Membrane Science*, vol. 372, no. 1-2, pp. 292-302.
- Wei, T., Zhang, L., Zhao, H., Ma, H., Sajib, M.S.J., Jiang, H. & Murad, S. 2016, 'Aromatic polyamide reverse-osmosis membrane: An atomistic molecular dynamics simulation', *The Journal of Physical Chemistry B*, vol. 120, no. 39, pp. 10311-8.
- WHO 2015, *Drinking water*, World Health Organization, <<http://www.who.int/mediacentre/factsheets/fs391/en/>>.
- Widjojo, N., Chung, T.-S., Weber, M., Maletzko, C. & Warzelhan, V. 2011, 'The role of sulphonated polymer and macrovoid-free structure in the support layer for thin-film composite (TFC) forward osmosis (FO) membranes', *Journal of Membrane Science*, vol. 383, no. 1-2, pp. 214-23.
- Wrolstad, R.E., Mcdaniel, M.R., Durst, R.W., Micheals, N., Lampi, K.A. & Beaudry, E.G. 1993, 'Composition and sensory characterization of red raspberry juice concentrated by direct-osmosis or evaporation', *Journal of Food Science*, vol. 58, no. 3, pp. 633-7.
- Wu, X., Field, R.W., Wu, J.J. & Zhang, K. 2017, 'Polyvinylpyrrolidone modified graphene oxide as a modifier for thin film composite forward osmosis membranes', *Journal of Membrane Science*, vol. 540, pp. 251-60.
- Wu, X., Shaibani, M., Smith, S.J.D., Konstas, K., Hill, M.R., Wang, H., Zhang, K. & Xie, Z. 2018, 'Microporous carbon from fullerene impregnated porous aromatic frameworks for improving the desalination performance of thin film composite forward osmosis membranes', *Journal of Materials Chemistry A*, vol. 6, no. 24, pp. 11327-36.
- Xia, L., Andersen, M.F., Hélix-Nielsen, C. & McCutcheon, J.R. 2017, 'Novel commercial aquaporin flat-sheet membrane for forward osmosis', *Industrial & Engineering Chemistry Research*, vol. 56, no. 41, pp. 11919-25.
- Xiao, J., Huang, Y. & Manke, C.W. 2010, 'Computational Design of Polymer Nanocomposite Coatings: A Multiscale Hierarchical Approach for Barrier Property Prediction', *Industrial & Engineering Chemistry Research*, vol. 49, no. 17, pp. 7718-27.
- Xie, M., Lee, J., Nghiem, L.D. & Elimelech, M. 2015, 'Role of pressure in organic fouling in forward osmosis and reverse osmosis', *Journal of Membrane Science*, vol. 493, pp. 748-54.
- Xie, W., He, F., Wang, B., Chung, T.-S., Jeyaseelan, K., Armugam, A. & Tong, Y.W. 2013, 'An aquaporin-based vesicle-embedded polymeric membrane for low energy water filtration', *Journal of Materials Chemistry A*, vol. 1, no. 26, pp. 7592-600.
- Xie, Z., Nagaraja, N., Skillman, L., Li, D. & Ho, G. 2017, 'Comparison of polysaccharide fouling in forward osmosis and reverse osmosis separations', *Desalination*, vol. 402, pp. 174-84.

- Xu, G.-R., Wang, J.-N. & Li, C.-J. 2013, 'Strategies for improving the performance of the polyamide thin film composite (PA-TFC) reverse osmosis (RO) membranes: Surface modifications and nanoparticles incorporations', *Desalination*, vol. 328, pp. 83-100.
- Xu, G.-R., Xu, J.-M., Feng, H.-J., Zhao, H.-L. & Wu, S.-B. 2017, 'Tailoring structures and performance of polyamide thin film composite (PA-TFC) desalination membranes via sublayers adjustment-a review', *Desalination*, vol. 417, pp. 19-35.
- Xu, S., Li, F., Su, B., Hu, M.Z., Gao, X. & Gao, C. 2019, 'Novel graphene quantum dots (GQDs)-incorporated thin film composite (TFC) membranes for forward osmosis (FO) desalination', *Desalination*, vol. 451, pp. 219-30.
- Xu, W., Chen, Q. & Ge, Q. 2017, 'Recent advances in forward osmosis (FO) membrane: Chemical modifications on membranes for FO processes', *Desalination*, vol. 419, pp. 101-16.
- Yadav, S.I., Ibrar; Bakly, Salam; Khanafer, Daoud; Altaee, Ali; Padmanaban, V. C.; Samal, Akshaya K.; Hawari, Alaa H. 2020, 'Organic Fouling in Forward Osmosis: A Comprehensive Review', *Water*, vol. 12, no. 5, p. 1505.
- Yang, D., Li, J., Jiang, Z., Lu, L. & Chen, X. 2009, 'Chitosan/TiO<sub>2</sub> nanocomposite pervaporation membranes for ethanol dehydration', *Chemical Engineering Science*, vol. 64, no. 13, pp. 3130-7.
- Yang, E., Alayande, A.B., Kim, C.-M., Song, J.-h. & Kim, I.S. 2018, 'Laminar reduced graphene oxide membrane modified with silver nanoparticle-polydopamine for water/ion separation and biofouling resistance enhancement', *Desalination*, vol. 426, pp. 21-31.
- Yang, E., Ham, M.-H., Park, H.B., Kim, C.-M., Song, J.-h. & Kim, I.S. 2018, 'Tunable semi-permeability of graphene-based membranes by adjusting reduction degree of laminar graphene oxide layer', *Journal of Membrane Science*, vol. 547, pp. 73-9.
- Yang, E., Kim, C.-M., Song, J.-h., Ki, H., Ham, M.-H. & Kim, I.S. 2017, 'Enhanced desalination performance of forward osmosis membranes based on reduced graphene oxide laminates coated with hydrophilic polydopamine', *Carbon*, vol. 117, pp. 293-300.
- Yang, S., Gu, J.-S., Yu, H.-Y., Zhou, J., Li, S.-F., Wu, X.-M. & Wang, L. 2011, 'Polypropylene membrane surface modification by RAFT grafting polymerization and TiO<sub>2</sub> photocatalysts immobilization for phenol decomposition in a photocatalytic membrane reactor', *Separation and Purification Technology*, vol. 83, no. Supplement C, pp. 157-65.
- Yin, J., Zhu, G. & Deng, B. 2016, 'Graphene oxide (GO) enhanced polyamide (PA) thin-film nanocomposite (TFN) membrane for water purification', *Desalination*, vol. 379, pp. 93-101.
- Yip, N.Y., Tiraferri, A., Phillip, W.A., Schiffman, J.D. & Elimelech, M. 2010, 'High performance thin-film composite forward osmosis membrane', *Environmental Science & Technology*, vol. 44, pp. 3812-8.
- Yoshioka, T., Kotaka, K., Nakagawa, K., Shintani, T., Wu, H.-C., Matsuyama, H., Fujimura, Y. & Kawakatsu, T. 2018, 'Molecular dynamics simulation study of polyamide membrane structures and RO/FO water permeation properties', *Membranes*, vol. 8, no. 4, p. 127.
- Yu, C., Zhang, B., Yan, F., Zhao, J., Li, J., Li, L. & Li, J. 2016, 'Engineering nano-porous graphene oxide by hydroxyl radicals', *Carbon*, vol. 105, pp. 291-6.
- Yu, L., Zhang, Y., Zhang, B., Liu, J., Zhang, H. & Song, C. 2013, 'Preparation and characterization of HPEI-GO/PES ultrafiltration membrane with antifouling and

- antibacterial properties', *Journal of Membrane Science*, vol. 447, no. Supplement C, pp. 452-62.
- Yuan, Y., Gao, X., Wei, Y., Wang, X., Wang, J., Zhang, Y. & Gao, C. 2017, 'Enhanced desalination performance of carboxyl functionalized graphene oxide nanofiltration membranes', *Desalination*, vol. 405, pp. 29-39.
- Zaidi, S.J., Mauritz, K.A. & Hassan, M.K. 2018, 'Membrane Surface Modification and Functionalization', in M.A. Jafar Mazumder, H. Sheardown & A. Al-Ahmed (eds), *Functional Polymers*, Springer International Publishing, Cham, pp. 1-26.
- Zhang, C., Huang, M., Meng, L., Li, B. & Cai, T. 2017, 'Electrospun polysulfone (PSf)/titanium dioxide (TiO<sub>2</sub>) nanocomposite fibers as substrates to prepare thin film forward osmosis membranes', *Journal of Chemical Technology & Biotechnology*, vol. 92, no. 8, pp. 2090-7.
- Zhang, C., Wei, K., Zhang, W., Bai, Y., Sun, Y. & Gu, J. 2017, 'Graphene oxide quantum dots incorporated into a thin film nanocomposite membrane with high flux and antifouling properties for low-pressure nanofiltration', *ACS Applied Materials & Interfaces*, vol. 9, no. 12, pp. 11082-94.
- Zhang, J., She, Q., Chang, V.W.C., Tang, C.Y. & Webster, R.D. 2014, 'Mining nutrients (N, K, P) from urban source-separated urine by forward osmosis dewatering', *Environmental Science & Technology*, vol. 48, no. 6, pp. 3386-94.
- Zhang, J., Xu, Z., Mai, W., Min, C., Zhou, B., Shan, M., Li, Y., Yang, C., Wang, Z. & Qian, X. 2013, 'Improved hydrophilicity, permeability, antifouling and mechanical performance of PVDF composite ultrafiltration membranes tailored by oxidized low-dimensional carbon nanomaterials', *Journal of Materials Chemistry A*, vol. 1, no. 9, pp. 3101-11.
- Zhang, J., Zhang, Y., Chen, Y., Du, L., Zhang, B., Zhang, H., Liu, J. & Wang, K. 2012, 'Preparation and characterization of novel polyethersulfone hybrid ultrafiltration membranes bending with modified halloysite nanotubes loaded with silver nanoparticles', *Industrial & Engineering Chemistry Research*, vol. 51, no. 7, pp. 3081-90.
- Zhang, Q., Zhang, C., Xu, J., Nie, Y., Li, S. & Zhang, S. 2016, 'Effect of poly(vinyl alcohol) coating process conditions on the properties and performance of polyamide reverse osmosis membranes', *Desalination*, vol. 379, pp. 42-52.
- Zhang, S., Qiu, G., Ting, Y.P. & Chung, T.-S. 2013, 'Silver-PEGylated dendrimer nanocomposite coating for anti-fouling thin film composite membranes for water treatment', *Colloids and Surfaces A: Physicochemical and Engineering Aspects*, vol. 436, no. Supplement C, pp. 207-14.
- Zhang, S., Wang, K.Y., Chung, T.-S., Chen, H., Jean, Y.C. & Amy, G. 2010, 'Well-constructed cellulose acetate membranes for forward osmosis: Minimized internal concentration polarization with an ultra-thin selective layer', *Journal of Membrane Science*, vol. 360, no. 1-2, pp. 522-35.
- Zhang, X., Shen, L., Guan, C.-Y., Liu, C.-X., Lang, W.-Z. & Wang, Y. 2018, 'Construction of SiO<sub>2</sub>@MWNTs incorporated PVDF substrate for reducing internal concentration polarization in forward osmosis', *Journal of Membrane Science*, vol. 564, pp. 328-41.
- Zhao, D., Chen, S., Guo, C.X., Zhao, Q. & Lu, X. 2016, 'Multi-functional forward osmosis draw solutes for seawater desalination', *Chinese Journal of Chemical Engineering*, vol. 24, no. 1, pp. 23-30.
- Zhao, D.L. & Chung, T.-S. 2018, 'Applications of carbon quantum dots (CQDs) in membrane technologies: A review', *Water Research*, vol. 147, pp. 43-9.



- Zhao, H., Wu, L., Zhou, Z., Zhang, L. & Chen, H. 2013, 'Improving the antifouling property of polysulfone ultrafiltration membrane by incorporation of isocyanate-treated graphene oxide', *Physical Chemistry Chemical Physics*, vol. 15, no. 23, pp. 9084-92.
- Zhao, S., Zou, L., Tang, C.Y. & Mulcahy, D. 2012, 'Recent developments in forward osmosis: Opportunities and challenges', *Journal of Membrane Science*, vol. 396, pp. 1-21.
- Zhao, W., Liu, H., Liu, Y., Jian, M., Gao, L., Wang, H. & Zhang, X. 2018, 'Thin-Film Nanocomposite Forward-Osmosis Membranes on Hydrophilic Microfiltration Support with an Intermediate Layer of Graphene Oxide and Multiwall Carbon Nanotube', *ACS Applied Materials & Interfaces*, vol. 10, no. 40, pp. 34464-74.
- Zhao, X., Li, J. & Liu, C. 2017, 'A novel TFC-type FO membrane with inserted sublayer of carbon nanotube networks exhibiting the improved separation performance', *Desalination*, vol. 413, pp. 176-83.
- Zhao, Y., Vararattanavech, A., Li, X., HélixNielsen, C., Vissing, T., Torres, J., Wang, R., Fane, A.G. & Tang, C.Y. 2013, 'Effects of proteoliposome composition and draw solution types on separation performance of aquaporin-based proteoliposomes: Implications for seawater desalination using aquaporin-based biomimetic membranes', *Environmental Science & Technology*, vol. 47, no. 3, pp. 1496-503.
- Zhou, Z., Hu, Y., Boo, C., Liu, Z., Li, J., Deng, L. & An, X. 2018, 'High-performance thin-film composite membrane with an ultrathin spray-coated carbon nanotube interlayer', *Environmental Science & Technology Letters*, vol. 5, no. 5, pp. 243-8.
- Zhu, H., Zhang, L., Wen, X. & Huang, X. 2012, 'Feasibility of applying forward osmosis to the simultaneous thickening, digestion, and direct dewatering of waste activated sludge', *Bioresource Technology*, vol. 113, pp. 207-13.
- Zinadini, S., Zinatizadeh, A.A., Rahimi, M., Vatanpour, V. & Zangeneh, H. 2014, 'Preparation of a novel antifouling mixed matrix PES membrane by embedding graphene oxide nanoplates', *Journal of Membrane Science*, vol. 453, no. Supplement C, pp. 292-301.
- Zirehpour, A., Rahimpour, A., Khoshhal, S., Firouzjaei, M.D. & Ghoreyshi, A.A. 2016, 'The impact of MOF feasibility to improve the desalination performance and antifouling properties of FO membranes', *RSC Advances*, vol. 6, no. 74, pp. 70174-85.
- Zirehpour, A., Rahimpour, A. & Ulbricht, M. 2017, 'Nano-sized metal organic framework to improve the structural properties and desalination performance of thin film composite forward osmosis membrane', *Journal of Membrane Science*, vol. 531, pp. 59-67.